Study of accessible ground states in two-dimensional disordered superconductors

Vincent Humbert

NNT : 2016SACLS149

THESE DE DOCTORAT
DE
L'UNIVERSITE PARIS-SACLAY
PREPAREE AU
"CENTRE DE SCIENCES NUCLEAIRES ET DE SCIENCES DE LA MATIERE"

ECOLE DOCTORALE
Physique en Île-de-France

Spécialité Physique de la Matière Condensée

Par

Vincent Humbert

Etude des états fondamentaux dans des systèmes supraconducteurs désordonnés de dimension 2

Study of accessible ground states in two-dimensional disordered superconductors

Thèse présentée et soutenue à Orsay, le 16 juin 2016

Composition du Jury :

M. Christian Glattli	Directeur de Recherche	Président
M. Claude Chapelier	Directeur de Recherche	Rapporteur
M. Thomas Lemberger	Professeur	Rapporteur
M. Olivier Bourgeois	Directeur de Recherche	Examinateur
M. Nicolas Dupuis	Directeur de Recherche	Examinateur
M. Dan Shahar	Professeur	Examinateur
Mme Claire Marrache-Kikuchi	Maître de Conférence	Directeur de thèse
M. Julien Gabelli	Chargé de Recherche	Invité

Contents

Introduction 1

I Low Frequency transport properties of disordered films 3

1 State of the Art/Theory 4
1.1 Introduction . . . 4
1.2 Basic description of a metal . . . 4
1.2.1 The Drude Model : A classical representation . . . 4
1.2.2 Matthiessen's rule . . . 5
1.2.3 The Fermi Gas Theory . . . 5
1.3 Localization by disorder . . . 7
1.3.1 Anderson localization . . . 7
1.3.2 Finite Size Scaling Theory of Localization . . . 9
1.3.2.1 Thouless's approach . . . 9
1.3.2.2 Abrahams, Anderson, Licciardello & Ramakrishnan : the Gang of Four . . . 10
1.3.2.3 Weak Localization . . . 11
1.4 Effects of interactions . . . 13
1.4.1 The Electron-Phonon Interaction . . . 13
1.4.2 Electron-Electron Interactions . . . 15
1.4.3 Discussion on the effects of interactions . . . 18
1.5 Conduction laws linked to localization . . . 19
1.5.1 Variable Range Hopping . . . 20
1.5.1.1 Nearest Neighbour Hopping . . . 20
1.5.1.2 Mott Variable Range Hopping . . . 21
1.5.1.3 Efros-Shklovskii Variable Range Hopping . . . 21
1.5.2 Electronic Transport in the weak localization regime . . . 22
1.6 Effect of disorder on superconductivity . . . 22
1.6.1 Superconductivity in the presence of (small) disorder . . . 23
1.6.1.1 Superconductivity : from H.K. Onnes to the BCS theory . . . 23
1.6.1.2 The dirty limit . . . 24
1.6.2 Possible effects of localization on 3D superconductivity . . . 24
1.6.3 Effects of a thickness reduction depending on the morphology . . . 26
1.7 Dimensional Effects on Superconductivity . . . 26
1.7.1 Surface effects . . . 27
1.7.2 The Berezinskii-Kosterlitz-Thouless Transition . . . 28
1.7.3 The Superconductor-to-Insulator Transition . . . 29
1.7.3.1 Fermionic models of the SIT . . . 29
1.7.3.1.a Maekawa & Fukuyama first order calculation . . . 29
1.7.3.1.b Finkel'stein's theory . . . 30
1.7.3.1.c Experiments pointing to a fermionic scenario in some materials . . . 31
1.7.3.2 Bosonic models of the transition . . . 32
1.7.3.2.a The "Dirty Boson Model" . . . 32
1.7.3.2.b Layered 2D superconductor . . . 34
1.7.3.2.c Numerical studies of the SIT . . . 35
1.7.3.2.d Some experiment supporting the Bosonic picture . . . 36
1.7.3.3 A link between the bosonic and fermionic pictures ? . . . 38
1.7.3.4 Possible metallic states . . . 39

1.7.3.4.a Experimental evidence . . . 39
1.7.3.4.b Fermionic theories of 2D metals . . . 41
1.7.3.4.c Bosonic theories of 2D metals . . . 41
1.8 Conclusion . . . 43

2 Low frequency transport properties of Nb_xSi_{1-x} 44
2.1 Introduction . . . 44
2.2 Sample fabrication and measurements . . . 44
2.2.1 Sample fabrication . . . 44
2.2.1.1 Evaporators . . . 44
2.2.1.1.a Principle of evaporation techniques . . . 44
2.2.1.1.b Co-deposition process for a-Nb_xSi_{1-x} . . . 45
2.2.1.2 Sample fabrication . . . 46
2.2.1.3 Heat Treatment Procedure . . . 47
2.2.2 Cryogenics . . . 47
2.2.2.1 Dilution refrigerator . . . 47
2.2.2.2 Thermometry . . . 49
2.2.3 Measurement Techniques . . . 49
2.2.3.1 Low-frequency AC technique . . . 49
2.2.3.2 DC technique . . . 50
2.2.3.3 Protection against parasitic power . . . 50
2.2.4 Sample homogeneity and morphological structure . . . 51
2.2.4.1 Rutherford Backscattering Spectrometry . . . 51
2.2.4.1.a Principle . . . 52
2.2.4.1.b Experiment . . . 52
2.2.4.2 Determination of the morphology . . . 54
2.2.4.2.a Structural characterisation techniques . . . 54
2.2.4.2.b Observation of as-deposited a-Nb_XSi_{1-x} thin films . . . 55
2.2.4.2.c Effect of heat treatment on the sample morphology . . . 56
2.3 Characteristics of a-NbSi . . . 57
2.3.1 Estimation of the Disorder . . . 58
2.3.2 External disorder-tuning parameters for 3D Nb_xSi_{1-x} . . . 58
2.3.2.1 Effects of a modification of the composition . . . 59
2.3.2.2 Heat treatment : fine-tuning of the disorder . . . 60
2.3.3 Approaching the 2 dimensional limit . . . 62
2.3.3.1 Characteristic length-scales and dimensions . . . 62
2.3.3.2 Effects of the modification of the thickness . . . 63
2.3.3.3 Comparison with other tuning parameters . . . 64
2.3.3.4 Different ground states . . . 66
2.3.4 Conclusion . . . 68

3 Experimental results 71
3.1 Relevant disorder parameter for transport measurement . . . 72
3.2 Thickness evolution of the properties of the samples . . . 73
3.2.1 As-deposited films . . . 73
3.2.2 Experimental artefacts . . . 74
3.2.3 Inclusion in other sets of data . . . 76
3.2.4 Evolution as a function of heat treatment . . . 76
3.3 Analysis of the insulating phase . . . 77
3.3.1 Brief overview of our results . . . 85
3.3.2 Identification of the different laws in the insulator . . . 85
3.3.2.1 Identification of the different parameters . . . 85
3.3.2.2 Application to our films . . . 87
3.3.2.3 Extraction of the parameters in the different regimes . . . 90
3.3.2.4 Parameters extracted from the crossover temperatures . . . 93
3.3.2.5 Extracted parameters from Mott VRH . . . 98
3.3.2.6 Extracted parameters from ES regime . . . 99
3.4 Analysis of metallic samples . . . 100
3.4.1 Brief overview of the results regarding metallic samples . . . 100
3.4.2 Weak localization in metallic samples . . . 101
3.4.2.1 3D weak localization . . . 102

3.4.2.2 Dimensional crossover for weak localization . . . 102
3.4.2.3 Evolution of the 2D weak localization law as a function of disorder 104
3.4.2.4 Toward a more localizing law . . . 106
3.4.3 Strong localization in the metallic samples . . . 106
3.4.3.1 Identification of the observed localization law . . . 106
3.4.3.2 Dependence as a function of the thickness and disorder . . . 108
3.4.3.3 Evolution of the insulating law close to the M2-to-Insulator transition . . . 109
3.4.4 The saturations . . . 111
3.4.4.1 Electron-phonon decoupling . . . 113
3.4.4.2 Evolution of the saturation as a function of disorder . . . 116
3.5 The MIT . . . 118
3.5.1 Identification of the first insulating sample in a series . . . 118
3.5.2 Comparison of the laws at both sides of the MIT . . . 119
3.6 Interpretation . . . 121

II Microwave measurements 127

4 State of the art : electrodynamics of superconductors 128
4.1 Frequency as a probe for Quantum Phase Transitions . . . 128
4.2 Theory of electrodynamics within the BCS model . . . 130
4.2.1 Two-fluid model . . . 130
4.2.2 Mattis-Bardeen theory . . . 131
4.2.3 Electrodynamics of disordered superconductors . . . 134
4.3 Experimental techniques . . . 134
4.3.1 Two-coil experiments . . . 135
4.3.2 Superconducting cavity resonators . . . 136
4.3.3 Broadband spectroscopy . . . 137
4.3.4 THz spectroscopy . . . 138
4.4 Measurements of electrodynamics of superconducting thin films . . . 138
4.4.1 Clean superconductors . . . 138
4.4.2 Superconducting fluctuations . . . 139
4.4.3 BKT transition . . . 140
4.5 Frequency measurements and the Superconductor-to-Insulator Transition . . . 141
4.5.1 Electrodynamics of fermionic insulators . . . 142
4.5.2 Electrodynamic characterization of Cooper pairs in the non-superconducting regime . . . 143
4.5.3 Electrodynamic characterization of Coulomb interactions . . . 143
4.6 Aim of our work . . . 145

5 Experimental results 147
5.1 Introduction . . . 147
5.2 Broadband measurement : principle . . . 147
5.2.1 Basics of broadband spectrometry . . . 147
5.2.2 The error sources . . . 148
5.2.3 Calibration . . . 151
5.2.3.1 Mathematical description of calibration . . . 151
5.2.3.2 Principle . . . 152
5.2.3.3 Non standard calibration techniques . . . 153
5.3 Calibration device . . . 153
5.3.1 Design of the lines on the dial . . . 154
5.3.2 Design of the calibration dial . . . 154
5.3.3 The reference points . . . 155
5.3.4 Rotation mechanism . . . 158
5.3.5 Validation of the calibration procedure on a resistor . . . 159
5.3.5.1 Measurement of the reflection coefficients of the different standards 159
5.3.5.2 Calibration of the resistor . . . 160
5.4 Sample selection . . . 162
5.4.1 Possibles candidates . . . 163
5.4.2 Superconductivity in Vanadium, probed by low frequency techniques . . . 163

5.4.2.1 Sample fabrication . . . 164
5.4.2.2 Evolution of the properties of Vanadium films with the film thickness . . . 164
5.4.2.3 Comparison with the bibliography . . . 166
5.4.2.4 RF sample . . . 169
5.5 Microwave measurement of a Vanadium film . . . 170
5.5.1 Mattis-Bardeen Predictions . . . 173
5.5.2 First calibration . . . 173
5.5.2.1 Normal state . . . 173
5.5.2.2 Evolution of the Impedance as a function of temperature and frequency . . . 176
5.5.2.3 Evolution of the conductance as a function of temperature and frequency . . . 179
5.5.3 Improvement of the calibration . . . 180
5.5.3.1 Using the normal state resistance . . . 180
5.5.3.2 Averaging on the frequency . . . 181
5.5.4 Interpretation . . . 181
5.6 Sensitivity of the calibration device . . . 184
5.7 Conclusion . . . 185

III Appendix 188

A Discussion on Zabrodskii's method 189
A.1 Possible power laws . . . 189
A.2 Dependence as a function of temperature of the prefactor in VRH . . . 191

B Over-activated insulating regime 193

C Complementary measurements to perform on NbSi films 195

D The bias-Tee 197
D.1 Dimensions . . . 197
D.2 Characterization of the bias-Tee . . . 197
D.2.1 Modelization of the bias-Tee . . . 197
D.2.2 Measurement of the bias-Tee . . . 198

E Influence of a parallel capacitance on the calibration 201

F Résumé en Français 204
F.1 Introduction . . . 204
F.2 Problématique générale . . . 205
F.2.1 Localisation dans les métaux . . . 205
F.2.1.1 Localisation par le désordre . . . 205
F.2.1.2 Localisation par les interactions . . . 205
F.2.1.3 Théorie de la localisation . . . 205
F.2.2 Supraconductivité et désordre dans les systèmes bi-dimensionnels . . . 206
F.2.2.1 Transition Supraconducteur-Isolant à 2D . . . 206
F.2.2.2 D'autre états fondamentaux à 2D ? . . . 206
F.3 Mesures basse fréquences . . . 207
F.3.1 Travaux préliminaires sur le NbSi . . . 207
F.3.1.1 Ajustement du désordre dans les films minces . . . 207
F.3.1.2 Le diagramme de phase du NbSi à 2D . . . 208
F.3.2 Résultat expérimentaux . . . 209
F.3.2.1 Les phases métalliques . . . 209
F.3.2.2 Le régime Isolant . . . 211
F.3.2.3 Continuité des lois entre les régimes M2 et isolant . . . 213
F.3.2.4 Conclusion des mesures basse fréquence . . . 216
F.4 Mesures hautes fréquences . . . 217
F.4.1 Développement d'un dispositif de calibration pour la réflectométrie micro-onde . . . 217

F.4.2 Validation du dispositif et mesure de film mince de Vanadium supraconducteur 218
F.4.3 Conductivité complexe d'un échantillon supraconducteur 219
F.4.4 Conclusion sur les développements effectués pour les mesures RF 220

Introduction

General framework

Disorder and its consequences on transport properties of electronic systems is a long-standing problem in condensed matter physics, for which the understanding is both of theoretical and practical importance. However, there is, to date, no complete theory describing entirely the experimentally observed phenomena.
In metals, as disorder is increased, a Metal-to-Insulator Transition (MIT) can occur due to Coulomb interactions and localization of the carriers. For superconducting materials, the entanglement with superconductivity complexifies this picture. Although superconductivity should not be affected by disorder according to Anderson's theorem, experimentally, the competition between the establishment of Cooper pairs, interactions and localization results in the destruction of superconductivity at high disorder. The understanding of the mechanisms at the origin of the observed transitions gave rise to a large body of literature in the last 50 to 60 years and is still, to a large extent, an open question.
In two-dimensional systems, Anderson localization should prevent the establishment of a metallic ground state. As disorder is increased in initially clean superconductors, one should therefore encounter a direct Superconductor-to-Insulator Transition (SIT). However, the increased importance of both Coulomb interactions and fluctuations in low dimensions may disrupt this long-standing paradigm. As a consequence, unpredicted new states of matter could emerge, such as 2D metallic phases in between the Superconducting and Insulating phases.

This work aimed at providing an insight on the phenomena at play in disordered thin films, especially in the vicinity of the expected disorder-tuned SIT. For this purpose, **we first studied the low frequency electronic transport properties of thin amorphous $\mathbf{Nb_xSi_{1-x}}$ films at low temperatures ($T < 1$ K)**. The goal was to understand the origin of the recently observed metallic phases in this system, as well as their destruction by disorder. To do so, we tuned disorder by modifying either the thickness, the composition or the heat treatment temperature applied to the films - this last experimental tool allowing to finely tune disorder -. **The second part of this work will be devoted to microwave reflectometry of superconductors**. AC transport measurements are a powerful probe to determine the ground state and the different excitations that coexist in a given system. However, these high frequency measurements are also extremely sensitive to the sample's environment and broadband measurements come at the price of a full set-up calibration, which is difficult to perform at low temperatures. We therefore developed and characterized a microwave reflectometry calibration device to access the absolute dynamical response of thin films. **In the long term, the comparison of both techniques (low and high frequency) could help to disentangle the various mechanisms at play, close to the expected TSI, in each phase and at the transitions**.

Outline

The first part of this work (part I) will be devoted to low frequency transport properties in 2D materials.
Chapter 1 will be dedicated to the state-of-the-art description of the MIT and of the SIT in disordered films. Chapter 2 will focus on the experimental techniques and on the knowledge acquired on a-Nb_xSi_{1-x} films from previous studies performed in the group. Finally, in chapter 3, we will present the low temperature characteristics we have performed on 2D a-Nb_xSi_{1-x} films. We will especially focus on the transition between the Insulator and the neighbouring metallic ground states. The careful analysis of the conduction laws and their evolution through the transi-

tion will bring us to propose a possible interpretation for the origin of the observed ground states.

Part II will be dedicated to microwave reflectometry measurements of superconducting thin films. The goal was the developpement and characterization of a high frequency measurement apparatus allowing us to access the absolute electrodynamic response of such systems.
In chapter 4 we will review electrodynamic measurements in thin films, and more specifically in films close to the SIT. In Chapter 5, we will detail the experimental constraints on low temperature reflectometry measurements at microwave frequencies (GHz) and provide a description of the developed apparatus. We will then qualify the device by probing the electrodynamic response of superconducting Vanadium thin films at low temperatures ($T < 4$ K).

Part I

Low Frequency transport properties of disordered films

Chapter 1

State of the Art/Theory

1.1 Introduction

In this chapter, we would like to introduce the major effects of disorder on an electronic system, be it superconducting, metallic or insulating. We will begin with an overview of current theories in this field, starting from the basic description of metals and the theory of localization. We will then examine how disorder affects quantum interferences, enhances effective Coulomb interactions and modifies electron-phonon interactions. We will derive the corresponding DC electronic transport properties as both the dimensionality and the disorder are tuned. We will end this chapter by focusing on the effects of disorder on superconductivity. We will detail theoretical and experimental points of view on the Superconductor-to-Insulator Transition in 2 dimensional systems.

1.2 Basic description of a metal

1.2.1 The Drude Model : A classical representation

In 1900, Paul Drude proposed to model the transport of electric charges in solids by the motion of free electrons. This model, inspired by the classical kinetic theory of gases, assimilates electrons to point particles with no interaction. They are driven through the material by an electric field $\vec{E}$.

in the absence of any force opposing the movement of electrons, which are subject to the electrostatic force $\vec{F} = e\vec{E}$, the average electron velocity becomes infinite, which is non-physical. To take into account the effects of the medium, and more precisely the elastic scattering of electrons by diffusive centers, this model introduces a phenomenological parameter called the **"relaxation time τ"**. Drude then infers the equation describing the movement of electrons :

$$m\frac{d\vec{v}}{dt} = e\vec{E} - \frac{m\vec{v}}{\tau} \tag{1.1}$$

where m is the mass of the electron, $\vec{v}$ its average velocity and e its charge. From this equation, one can deduce $\vec{v}$ in the stationary regime ($\frac{d\vec{v}}{dt} = 0$):

$$\vec{v} = \frac{e\tau\vec{E}}{m} \tag{1.2}$$

The associated current then is :

$$\vec{j} = ne\vec{v} = ne\frac{e\tau\vec{E}}{m} \tag{1.3}$$

Thus, one can define the conductivity σ - and the associated resistivity $\rho = \sigma^{-1}$ - by Ohm's law :

$$\vec{j} = \sigma\vec{E} \text{ with } \sigma = \frac{ne^2\tau}{m} = \frac{ne^2 l}{vm} \tag{1.4}$$

where l is the mean free path, i.e. the average distance travelled by an electron before being scattered, defined as : $l = v\tau$.

The conductivity derived by Drude therefore depends on an effective diffusion time τ. In his original work, he supposed that this quantity only depends on the collisions of electrons with atoms composing the crystal network. In reality, things are more complicated.

1.2.2 Matthiessen's rule

Contrary to Drude's expectation, electrons are barely scattered by the lattice ions. In fact, they are more sensitive to defects in the crystal periodicity. They are scattered by movements of the lattice, the so-called phonons, and by any crystal perturbation such as impurities, boundaries, defects ... One can then wonder how these scattering sources contribute to the electronic conductivity.

One answer comes from the work of Augustus Matthiessen. Indeed, a commonly used rule in condensed matter, inspired by his 1864 work [Matthiessen and Vogt, 1864] states that the total resistivity of a crystalline metallic sample is the sum of the resistivities due to the different scattering processes. This rule applies as long as the scattering sources are independent from one another. In this case, **Matthiessen's rule** can be written as :

$$\rho_{Total} = \rho_{phonons} + \rho_{impurities} + \rho_{defects} + \rho_{boundaries} + ... \tag{1.5}$$

In terms of diffusion times, and assuming Drude's law (equation 1.4) for each scattering time, Matthiensen's rule can be written as :

$$\frac{1}{\tau_{Total}} = \frac{1}{\tau_{phonons}} + \frac{1}{\tau_{impurities}} + \frac{1}{\tau_{defects}} + \frac{1}{\tau_{boundaries}} + ... \tag{1.6}$$

Scattering by phonons is usually the dominant scattering process. This contribution to transport properties is well known and, at high temperatures, is commonly described by a linear contribution to the resistivity as a function of the temperature $\rho_{ph} \propto T$. At lower temperatures, (typically for T smaller than Θ_D, the Debye temperature associated with the material), the resistivity due to phonons is given by a power law $\rho_{ph} \propto T^{\alpha}$ where α is a constant which numerical value depends on the dimensionality [1]. At low temperature, electron-electron scattering becomes important and can dominate scattering. This scattering process gives rise to $\rho_{e-e} \propto T^{1/2}$ and a crossover can occur between a electron-phonon dominated scattering and an electron-electron dominated regime. Since the other phenomena are barely dependent on T, this law, in addition to the Drude model, describes both the decrease of the resistivity in metals as a function of the temperature - when the contribution of phonons or electron-electron interactions is important - and the saturation of the resistivity at low temperature - where imperfections of the crystal structure are the dominant scattering process.

This purely classical picture provides us with a first understanding of the resistivity in metals. Furthermore, it gives an indication on the effect of disorder within this description : as disorder is increased, the contribution of defects in the crystalline structure will modify τ_{total} and the associated resistivity will increase. However this approach fails to include the properties of non metallic materials and does not capture all the effects of disorder.

1.2.3 The Fermi Gas Theory

To go beyond the classical picture provided by Drude's law and Matthiessen's rule, one should consider the **Fermi Gas Theory**. This theory, which still considers free electrons, represents an improvement of the Drude theory as it allows to understand the differences between conducting materials and insulating ones by using quantum mechanical arguments. This model, described by Sommerfeld, is the basis of Band Theory in solids.

To explain this theory, let us first consider the case of free electrons in a system of size L. In this case, Schrödinger equation for a free electron is :

$$(-\frac{\hbar^2}{2m}\nabla^2)\psi_k(r,t) = i\hbar\frac{\partial}{\partial t}\psi_k(r,t) (= \epsilon_k(r)\psi_k(r,t)) \tag{1.7}$$

By introducing a periodic boundary condition to the wave functions, reflecting the confinement of the electron inside the system, one can write that $\psi_k(x,t) = \psi_k(x+L,t)$. In this case,

1. Theoretically, for a bulk system, α should range between 3 and 4 [Rammer and Schmid, 1986] but it has been experimentally found to be between 1 and 4.

the eigenvectors are plane waves of the form $\psi_k(r,t) \propto e^{i(\vec{k}.\vec{r}-\omega t)}$. By solving equation 1.7 in this case, one finds :

$$\epsilon_{k_p} = \frac{\hbar^2 k_p^2}{2m} \tag{1.8}$$

where ϵ_{k_p} is the energy of an electron with $k_p = \frac{2p\pi}{L}$ - with p an integer - the associated wave vector.

In this picture, and for a given material, the Fermi energy $E_F = \frac{\hbar^2 k_F^2}{2m}$ (k_F being the associated Fermi wave vector) is defined as the chemical potential at zero temperature. It corresponds to the highest energy of the occupied electronic states. In the 2D free-electron case, the Fermi surface in the reciprocal space is represented figure 1.1. From E_F and k_F, one can then compute the electronic density and the corresponding conductivity for the various dimensionalities.

By considering the probability $\rho(k)$ of having an occupied state with the wave vector k , such that $\rho(k)dk$ corresponds to the number of states with a wave vector between k and $k+dk$, one can write for a sample of dimension L :

in 3D

$$\rho_{3d}(k)dk = 2\frac{4\pi k^2 dk}{(2\pi/L)^3} \tag{1.9}$$

in 2D

$$\rho_{2d}(k)dk = 2\frac{2\pi k dk}{(2\pi/L)^2} \tag{1.10}$$

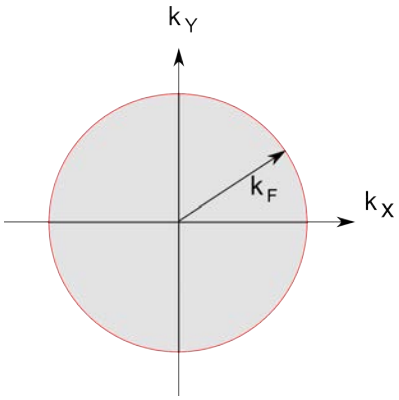

Figure 1.1: 2D Fermi surface within the Drude-Sommerfeld model.

From these equations, we can calculate the total number of electrons in 3D and 2D. This quantity is defined in d-dimensions by :

$$N = \int_0^{k_F} \rho(k)dk \tag{1.11}$$

with $N = n_{2d}S = n_{2d}L^2$ in 2D and $N = n_{3d}V = n_{3d}L^3$ in 3D, n_{2d} and n_{3d} being respectively the two dimensional and the three dimensional electronic density. By combining the above equations with equation 1.4, one obtains :

in 3D

$$\sigma_{3d} = \frac{e^2}{3\pi^2\hbar}k_F^2 l \tag{1.12}$$

in 2D

$$\sigma_{2d} = \frac{e^2}{h}k_F l \tag{1.13}$$

In the case of a quasi-2D system, the derivation is the same as the one obtained for a 3D system. Indeed, in this case, the density-of-states (DOS), i.e. the density of electrons at a given energy $\rho(E) = \rho(k)dk/dE$, is supposed to be 3D but the conductivity is given by $\sigma_{q2d} = d_\perp \sigma_{3d}$ where $d_\perp$ is the thickness of the sample. One therefore finds :

$$\sigma_{q2d} = \frac{e^2}{3\pi^2\hbar}(k_F l)(k_F d_\perp) \tag{1.14}$$

Using this theory, we are therefore able to **express the conductivity** σ - which is measurable by electronic transport experiments - **as a function of quantities which depend only on the system fermiology**. These relations have been widely used in condensed matter to estimate the microscopic parameters, knowing the conductivity of a material.
Let us note that, in this approach, a reduction of the thickness in a quasi-2D material is equivalent to diminishing the mean free path, i.e. to an enhanced effective disorder.

Let us now consider the specific case of crystals. Schrödinger equation then takes into account the crystalline potential $U(r)$:

$$(-\frac{\hbar^2}{2m}\nabla^2 + U(r))\psi_k(r,t) = i\hbar\frac{\partial}{\partial t}\psi_k(r,t) \tag{1.15}$$

The wave functions solution of this equation are periodic due to the crystalline potential, which imposes $\psi_k(r,t) = \psi_k(r+a,t)$, with a the lattice constant. In this case, the wave function is a **Bloch wave**, described by :

$$\psi(r) = e^{i(\vec{k}.\vec{r}-\omega t)}u(r) \tag{1.16}$$

with $u(r)$ a periodic function such that $u(r+a) = u(r)$. Due to the crystalline potential, the energy levels are periodically folded back into the first Brillouin zone. By a perturbative approach, one can show that energy levels at the edges of the Brillouin zone are not degenerate and that energy gaps open between successive bands. Therefore, **depending on the Fermi energy, the material can be either metallic or insulating**. It is noteworthy that, in the case of metals, the wave functions are extended along all the crystal.

The development of the Fermi gas theory (presented here in the limit of zero temperature) allows us to understand what are a metal and an insulator within band theory. A subsequent refinement is due to Laudau who developed the **Fermi liquid theory**. The main results being analogous to the Fermi gas theory, it will not be detailed here. Let us just outline the main idea behind this theory : starting from an ideal Fermi gas, interactions between particles are adiabatically introduced and increased. The evolution of the Fermi gas eigenstates is then monitored. The new eigenstates then correspond to quasiparticles states to which all particles contribute. For low enough interactions, the new quasiparticle states are similar to the Fermi gas ground states, provided that the interactions are taken into account by renormalizing the value of physical quantities, such as the effective mass and the heat capacity [Héritier, 2013].

However, the **Fermi liquid theory** (and, therefore the Fermi gas theory also) **fails when interactions are either too strong, or attractive, or when dealing with low dimensional systems**. We will now examine other theoretical models which have tried to account for these phenomena.

1.3 Localization by disorder

In the previous section, we have exposed simple models for electrical conduction. However, their application is limited when dealing with disordered materials. Indeed, they do not account for all effects that are experimentally observed in systems with strong interactions, disorder, or of low dimensionality.
In this section, we will focus on the localization of the wave function which may result from disorder effects. To describe the effects of disorder and localization on the zero temperature electrical properties of materials, we will first expose localization as described by Anderson and we will then discuss the theory of localization derived by the Gang of Four.

1.3.1 Anderson localization

In 1958 P. W. Anderson [Anderson, 1958] showed that electronic transport could be strongly altered in the presence of large disorder. For this purpose, he used a tight binding model with a periodic lattice [2]. The Hamiltonian can then be expressed as :

$$H_{Anderson} = \sum_{ij} V_{ij}c_i^\dagger c_j + \sum_i \epsilon_i n_i \tag{1.17}$$

2. In the literature, this model is sometime referred to as the "Anderson tight binding model".

where $c_i^\dagger$ is the operator representing the creation of an electron i, c_i its annihilation, $n_i = c_i^\dagger c_i$ is the occupation number operator representing the occupation of the i^{th} state and V_{ij} is the hopping element between sites i and j. Anderson assumes that the hopping matrix elements V_{ij} are equal to a constant V for nearest neighbours - zero otherwise - and disorder is taken into account by the on-site energy ϵ_i, taken to be a random variable which value varies between $-\frac{1}{2}W$ and $\frac{1}{2}W$. Let us start from a clean material ($W = 0$), where the wave functions are extended Bloch waves. As W increases, Bloch waves lose their phase coherence. Anderson showed that, for a critical value of W/V, there is a transition from extended to localized wave functions, which respectively describe a conducting and an insulating ground state. As illustrated figure 1.2, for **weak disorder**, the electrons are scattered on a characteristic lengthscale l, the mean free path, but the corresponding **wave function is still extended**. The **electronic motion is diffusive** and the material is conducting. On the other hand, for **strong disorder**, the **wave function can be localized** with an exponential decay of its amplitude on the scale of the localization length ξ_{loc} such that :

$$|\psi(\vec{r})| \propto exp(-|\vec{r} - \vec{r_0}|/\xi_{loc}) \tag{1.18}$$

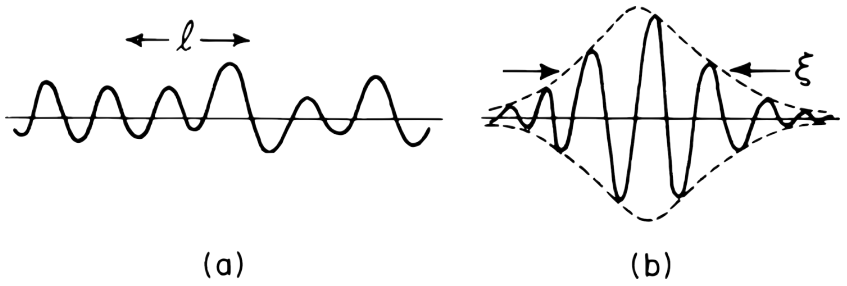

Figure 1.2: (a) For weak disorder, the one electron wave function is extended even if electrons are scattered on a characteristic distance of the order of the mean free path l. (b) In the presence of strong disorder, the wave function ψ is localized on the distance ξ_{loc} [Lee and Ramakrishnan, 1985].

As a consequence, a material which would have been a conductor in the absence of disorder can be insulating as disorder is increased. By tuning disorder, one can therefore induce a Metal-to-Insulator Transition, corresponding to a transition between non-localized and localized electronic states.

The existence of these two limits, with extended wave functions at low disorder and localized wave functions at strong disorder, let us wonder what happens for intermediate disorder. By considering this problem for semiconductors, **Ioffe and Regel** showed that if the mean free path l decreases below the inter-atomic distance a, no metallic state can exist [Ioffe and Regel, 1960]. This constraint brought them to define the **criterion $k_F l \sim 1$ for the Metal-to-Insulator Transition**.
Based on the idea of localization by disorder, **Mott** predicted that in any non-crystalline system, the states at the edges of the conduction band should be localized [Mott, 1967] [Mott, 1972]. He therefore predicted a discontinuous transition between the metallic and the insulating ground states which would occur when the Fermi energy E_F crosses a "mobility edge", as represented figure 1.3. The corresponding **minimum of conductivity** σ_{min} can be calculated by taking $k_F l \sim k_F a \sim 1$, in agreement with the Ioffe-Regel criterion. Indeed, by combining this criteria with equation 1.12, one finds in 3D :

$$\sigma_{min} = \frac{e^2}{3\pi^2\hbar}\frac{1}{a} \tag{1.19}$$

This value would, according to Mott's model, correspond to the minimum conductance achievable for the system before becoming insulating as disorder is increased.

At first, some experimental results in systems such as Si:P [Rosenbaum et al., 1980] (where the conductivity is tuned through the modification of the carrier density n, represented figure 1.4), V_2O_3 [Carter et al., 1991] (where the conductivity is changed via a modification of pressure and composition) Nb_xSi_{1-x} [Möbius et al., 1999] or $Si_{1-x}Cr_x$ [Mobius, 1985] (where the conductivity is tuned through x) seemed to be in agreement with the existence of a minimum of conductivity.

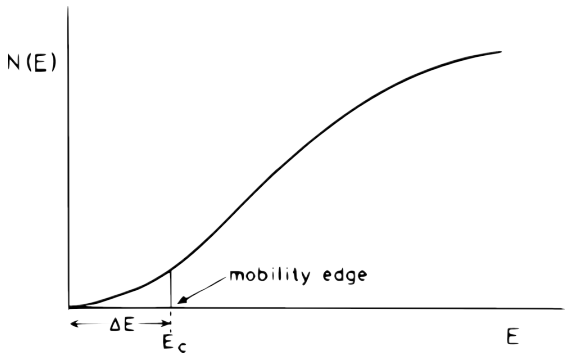

Figure 1.3: Density-of-states in the conduction band of a non-crystalline material, showing the mobility edge E_c separated by an energy ΔE from the band edge. States below E_c are localized and those above are extended [Mott, 1977].

However, subsequent works [Thomas et al., 1983] showed, through a careful analysis of the conduction properties close to the Metal-to-Insulator Transition, that the conducting ground state was continuously destroyed. Another argument against the existence of a minimum of conductivity was given by Mott himself [Mott, 1984] : he discussed the fact that no calculation had managed to compute the mobility edge for a continuous random network (which would best reproduce the situation of amorphous materials).
Nowadays, although Mott's minimum of conductivity is a founding concept, it has been shown to be inconsistent both with experiments and with subsequent theoretical developments such as the localization theory developed by Abrahams et al [Abrahams et al., 1979]. We will now expose this theory by starting by its basis : the finite size scaling theory.

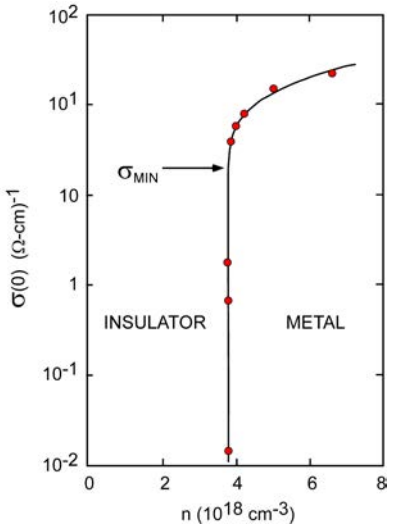

Figure 1.4: Semi-logarithmic plot of the zero temperature conductivity, $\sigma(0)$, as a function of the carrier density n for metallic samples of Si:P [Rosenbaum et al., 1980]. The abrupt decrease of $\sigma(0)$ with the carrier density can be taken to be a manifestation of Mott's minimum of conductivity : values of $\sigma(0) < \sigma_{min}$ can be interpreted as arising from inhomogeneities.

1.3.2 Finite Size Scaling Theory of Localization

After Mott's developments, a new way to calculate the properties of materials in the presence of disorder emerged, based on scaling theory. This approach for the study of the Metal-to-Insulator Transition is detailed in this section.

1.3.2.1 Thouless's approach

A qualitative scaling analysis of the localization problem for non-interacting electrons in a static disordered lattice has been proposed in 1974 by Thouless [Thouless, 1974]. The basic idea

is that extended states are sensitive to boundary effects if the dimension L of the sample is smaller than the mean free path l. By extending this idea, he defined the **Thouless energy**, such that :

$$E_T = \frac{\hbar D}{L^2} \tag{1.20}$$

where D is the diffusion constant. In this equation, the energy E_T is the characteristic energy of a diffusive electron travelling through L.

Thouless' vision was to link the macroscopic conductivity to the properties of microscopic clusters, of local dimensionless conductance g and of size L^d, by extending the system size by successive iterations. Thus the conductivity of a sample of size $(2L)^d$ is described from the properties of the L^d sample. One can therefore deduce its conductivity by scaling arguments.
Thouless showed that this dimensionless conductance g can be written as :

$$g = \frac{G}{e^2/\hbar} \propto \frac{E_T}{\delta W} \tag{1.21}$$

with G the conductance of the L^d sample, and δW the mean spacing between the energy levels of the L^d sample. Interestingly, the dimensionless conductance g is a measurable quantity which is directly related to the ratio $\frac{E_T}{\delta W}$. When this ratio between Thouless' energy and the mean spacing between the energy levels is equal to 1, one should observe a Metal-to-Insulator Transition. Indeed, as the overlap between different discrete levels of energy decreases, localized states emerge.
It is noteworthy that, due to the scaling argument, the size of the initial block should be taken to be insensitive to any microscopic structure [3].

This scaling argument by itself does not contradict Mott's idea. Indeed, in a later paper [Licciardello and Thouless, 1975] using this technique, Licciardello and Thouless found a result in agreement with Mott's minimum of conductivity. However, the gang of Four using the same scaling argument, concluded differently as we will now see.

1.3.2.2 Abrahams, Anderson, Licciardello & Ramakrishnan : the Gang of Four

Based on the ideas developed by Thouless to probe the Metal-to-Insulator Transition, a general scaling description without any microscopic model, but based on the value of **the microscopic conductance** g, has been developed by Abrahams, Anderson, Licciardello & Ramakrishnan [Abrahams et al., 1979]. By combining b^d cubes into blocks of sides bL they calculated a function β related to g as follows :

$$\beta = \frac{dln(g(L))}{dln(L)} \tag{1.22}$$

This function, giving the derivative of the (logarithmic) dimensionless conductance as a function of the (logarithmic) evolution of the system dimension, shows how the system conductance evolves as the system size is increased. In this model, the microscopic conductance g is a variable and β allows to eventually infer the corresponding ground state for a macroscopic sample.

By plotting its evolution as a function of $ln(g)$, the authors obtained the graph displayed figure 1.5. As observed, one should distinguish between two different cases when the system size is extended from L^d to infinity :

- for $\beta > 0$, the conductance increases with the size of the system. The wave functions are delocalized and the ground state of the system is metallic.
- for $\beta < 0$, the conductance decreases when the system size increases. The wave functions are localized and the ground state of the system is insulating.

Let us first focus on 3D systems. $\beta(L)$ can be positive for high enough g and is negative for $g < g_c$. Therefore, the system, depending on the microscopic conductance g, can be either metallic or insulating and g_c defines the critical point of the Metal-to-Insulator Transition in 3D. Interestingly, the transition between the two regimes is continuous. A system with a microscopic

3. This should not be a problem since the initial size L is arbitrarily chosen. Eventually, the assumption could be questionable really close to the MIT due to the divergence of the localization length.

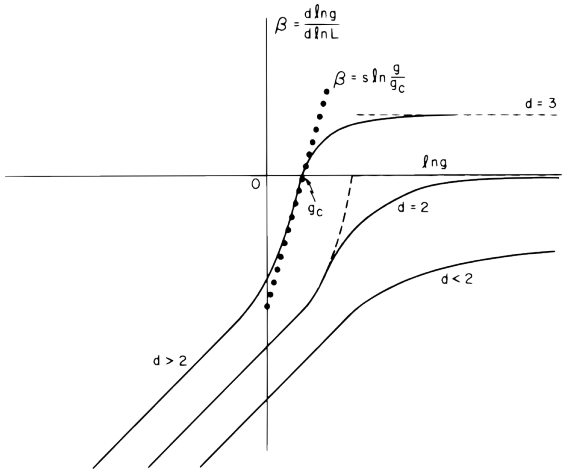

Figure 1.5: The renormalization function β as a function of the conductance g for dimensions 3, 2 and 1 [Abrahams et al., 1979].

conductance $g < g_c$ would be insulating but a system with microscopic conductance g_* close to but larger than g_c will be conducting with a conductance :

$$\sigma \propto ln(\frac{g_*}{g_c})^\nu \tag{1.23}$$

where ν is a scaling exponent. This contradicts what had been predicted by Mott : the system conductivity should not present any discontinuity at the Metal-to-Insulator Transition.

For systems of dimension d ≤ 2, $\beta(L)$ is negative whatever the initial conductance g. According to this theory, even an infinitesimal amount of disorder is, in this case, sufficient to localize the electrons as $\beta = 0$ is approached but never reached. Therefore, **no electronic system of dimension $\leq$ 2 can be metallic**.
Let us stress that this strong result for 2D systems (and systems of lower dimensions) has been calculated in the case of non-interacting fermions.

The gang of Four already noticed in their paper that, for 2D systems, depending on the value of g, a crossover from a weak localization regime (for $g >> 1$) to a strong localization regime (for $g << 1$) should occur. While the resistivity evolution in the strongly insulating regime would be exponential as L increases, the weakly localized one should have a logarithmic dependence as a function of the system size :

$$g = g_0 - \alpha ln(\frac{L}{L_0}) \tag{1.24}$$

where α and L_0 are constants. Let us now focus on this weakly localized regime.

1.3.2.3 Weak Localization

Even in the absence of Anderson localization (in the sense of what we have seen in section 1.3.1), quantum corrections to the conductance can dramatically affect the system conductivity and, in some cases, even induce an insulating ground state. In 1983, Bergmann [Bergmann, 1983] gave a microscopic interpretation of this phenomenon involving the quantum nature of electrons. As pictured figure 1.6, electrons can be scattered by diffusion centers. The different paths that can be taken by an electron are generally not coherent and do not interfere with one another since they have a random phase difference. This is the case for all paths except those which bring the electron back to the origin. Those can be run either clockwise or counter-clockwise. As these two paths **interfere constructively**, they induce an enhanced probability for the electron to come back to the origin, resulting in localization [4].

Thouless (1977) argued that inelastic scattering, with the associated inelastic scattering time τ_{in}, should limit weak localization due to a destruction of phase coherence. Indeed, electrons

4. In the presence of strong spin-orbit coupling, weak-antilocalization can occur. This case is not detailed in this thesis.

need to stay coherent along the interference pattern to interfere. Therefore, **localization can only occur on lengthscales shorter than the Thouless distance** :

$$l_{Th} \sim L_{in} = \sqrt{D\tau_{in}} \tag{1.25}$$

with $D = v_F\tau/d$ the diffusion constant, v_F the Fermi velocity and τ the elastic scattering time.

It has been discussed by Altshuler, Aronov and Khmel'nitskii [Altshuler1982] that the inelastic time is not the exact relevant quantity to take into account for l_{Th}. Indeed, it usually takes several inelastic scattering events to completely lose phase coherence. Therefore, the correct length to take into account should be l_Φ, the phase coherence length, with the associated scattering time τ_Φ. This scattering time has been calculated by Altshuler to be :

$$\tau_\Phi \sim (\frac{\tau_{in}}{\Delta E^2})^{1/3} \tag{1.26}$$

with ΔE the average energy change experienced by an electron after an inelastic collision. However τ_{in} and τ_Φ are often confused for one another as they are of the same order of magnitude.

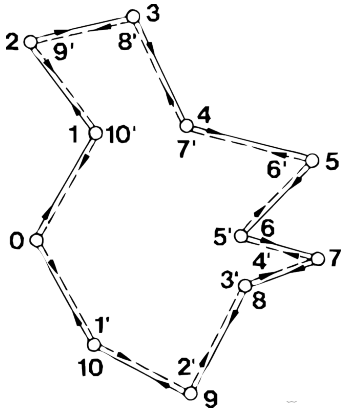

Figure 1.6: Representation of the one-electron interference pattern leading to weak localization [Bergmann, 1983].

In the weak localization regime, the correction to the conductivity takes the form :

$$\text{in 3D } \Delta\sigma = -\frac{e^2}{\hbar\pi^3}(\frac{1}{l} - \frac{1}{l_\Phi}) \tag{1.27}$$

When the thickness $d_\perp$ of the sample is shorter than the phase coherence length ($d_\perp < l_\Phi$), dimensional effects appear, affecting transport properties. The correction to the conductivity due to weak localization can then be written :

$$\text{in 2D } \Delta\sigma = -\frac{e^2}{\pi\hbar} ln(\frac{l_\Phi}{l}) \tag{1.28}$$

There are several ways to experimentally determine l_Φ based on weak localization. The most common one is to use a magnetic field. Indeed, in the presence of a magnetic field, electrons participating to weak localization acquire an additive phase which depends on the path they run along. This results in the destruction of weak localization, and therefore in a positive magnetoconductance.
As many concepts in condensed matter, the backscattering of electrons, which affect the system wavefunction, cannot be directly observed. Only its consequences on electronic transport are measurable. In cold atoms however, the displacement of particles can be directly imaged and weak localization has recently been directly evidenced in this model system. The experiment consisted in releasing non-interacting atoms with a defined momentum p from an optical trap. The released atoms travelled through an isotropic laser speckle which reproduced disordered diffusion centers. Measurement of the momentum of the atoms after times t ranging from 0 to 2.5 ms are presented figure 1.7. At the beginning of the experiment, all atoms have a momentum p.

One can observe that after 1 ms, the atoms begin to backscatter. After 2.5 ms, the distribution of momentum is isotropic at the exception of a peak of backscattering. This measurement therefore shows the increased probability of backscattering for atoms in the presence of disorder, signing weak localization.

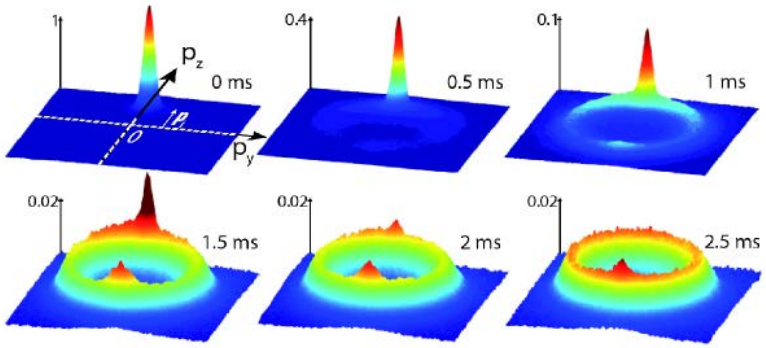

Figure 1.7: Cold atoms experiment measuring the momentum distribution after different propagation times t in the presence of disorder [Jendrzejewski et al., 2012].

We detailed here the major effects of localization in the absence of interactions and at zero temperature and showed that, even in the absence of strong localization, electronic transport can be altered by presence of disorder. However, as we will see in the following, interactions can have an important influence on the picture of localization in physical systems. Thus, in the following, we will first deal with the effects of Coulomb and electron-phonon interactions on the fundamental properties of materials. We will then discuss the conduction laws associated with localization both in the presence and absence of interactions.

1.4 Effects of interactions

The concepts presented so far in this thesis, have been developed neglecting the influence of diverse interactions. However, when those are strong, their contribution cannot be neglected. Realistically, the Hamiltonian can be written as a sum of contributions such that :

$$H_{tot} = H_{ph} + H_e + H_{ee} + H_{eph} \tag{1.29}$$

In this expression, H_{ph} represents the bare phonon contribution, H_e represents the free-electron Hamiltonian discussed in section 1.2.3, H_{ee} represents Electron-Electron Interactions and H_{eph} represents Electron-Phonon Interactions. The resolution of this Hamiltonian is however hard to achieve without making strong assumptions [5].

In this section, we will discuss the origins of these interactions and some of the resulting modifications of the fundamental properties of materials. We will, for each interaction type, discuss its modification by disorder, beginning by the Electron-Phonon interaction.

1.4.1 The Electron-Phonon Interaction

Phonons have various effects on electronic transport. We have already qualitatively described the phonon-induced scattering of electrons (see section 1.2.2). In this section, we will focus on Electron-Phonon Coupling and Electron-Phonon-induced Electron-Electron Interaction.

To grab a naive understanding of the origin of the Electron-Phonon Coupling, let us qualitatively examine it within the Jellium model. In this model, electrons are uniformly distributed in the material and move within an uniformly positive background representing the atomic nuclei. Any time a phonon is excited, it creates a charge density fluctuation in the positive background. These charge densities will then electromagnetically interact with the electron gas as the free-moving electrons will try to screen them. This gives birth to the so-called **Electron-Phonon Coupling**. In addition, these fluctuations give rise to an increased effective mass of the electrons

5. For a more extensive analysis of this Hamiltonian, see [Devreese and Alexandrov, 2009] or [Mahan, 2013].

m^*.

The study of Electron-Phonon Interactions has been principally motivated by its role in number of properties such as the thermal conductivity, the heat capacity, the conductivity of metals ... In particular, it has an **influence on superconductivity**. Indeed, as we will see later, the BCS model - which is commonly used to describe superconductivity - is based on the assumption of an attractive Electron-Electron Interaction mediated by Electron-Phonon Coupling. In this framework, McMillan calculated the dependence of the critical temperature T_c as a function of the phonon spectrum [Morel and Anderson, 1962] [McMillan, 1968]. This formula, can be written :

$$T_c = \frac{\Theta_D}{1.45} exp(\frac{1.041 + \lambda}{\lambda + \mu^*(1 + 0.62\lambda)}) \tag{1.30}$$

where Θ_D is the Debye temperature [6], μ^* is the Coulomb pseudopotential - describing the reduced Coulomb repulsion between electrons due to their retarded action and to screening effects -, and λ is the dimensionless electron-phonon coupling constant, defined as a function of the so-called **Eliashberg function** $\alpha^2(\omega)F(\omega)$ such that :

$$\lambda = 2 \int_0^\infty \alpha^2 F(\omega) \frac{d\omega}{\omega} \tag{1.31}$$

Even if $\alpha^2 F(\omega)(\equiv \alpha^2(\omega)F(\omega))$ is often identified with the phonon density-of-states, it is in fact the combination of the effective electron-phonon coupling function $\alpha(\omega)$ and of the phonon density-of-states $F(\omega)$. Let us note that λ - which is given in the BCS theory by $\lambda \sim N_0 V$ - characterises the electron mass enhancement due to electron-phonon interaction ($m^*/m = 1+\lambda$).

The question therefore arises regarding the effects of disorder on Electron-Phonon Interactions. Indeed, the phonon structure is defined by the eigenvalues of vibrations of the atoms in the crystal. Therefore, as disorder impacts the crystal structure, it should affect the phonon structure as well as the strength of Electron-Phonon Coupling. Following McMillan formula, this question has been of major interest for a long time in condensed matter physics. Indeed, the critical temperature T_c is presented as being directly proportional to the Debye temperature Θ_D which is determined by $F(\omega)$, at low energy. It was therefore suspected that disorder could greatly modify the critical temperature of superconducting materials as it should soften the phonon spectrum.

McMillan showed that Electron-Phonon Interaction can be experimentally accessible - through the measurement of the Eliashberg function $\alpha^2(\omega)F(\omega)$ - from tunnelling experiments on superconducting materials [7]. To probe the effects of disorder on Electron-Phonon Interactions, measurements of $\alpha^2(\omega)F(\omega)$ have been performed in various materials.
Let us cite an experiment performed on Pb, comparing the obtained $\alpha^2 F(\omega)$ in the case of crystalline, disordered and amorphous structures [Knorr and Barth, 1971]. As presented figure 1.8, the Eliashberg function is altered by presence of disorder. As the peaks are smeared, the value of $\alpha^2(\omega)F(\omega)$ increase at low frequency. The Debye Temperature Θ_D should therefore be increased, inducing a higher critical temperature T_c. However, Bergmann pointed that these modifications of the phonon spectrum should be mostly explained by a modification of the Electron-Phonon Coupling $\alpha(\omega)$ and that the phonon spectrum $F(\omega)$ should be almost insensitive to disorder [Bergmann, 1976], thus leaving T_c essentially unchanged.
He then modelled the modification of the Eliashberg function in the presence of disorder [8] by [Bergmann, 1971] :

$$\alpha^2(\omega)F(\omega) = \frac{\hbar n}{4\pi n_A M M_0} \frac{1}{c_{tr}^3} \frac{1}{l} \omega \tag{1.32}$$

where n is the electron density, M_0 the bare electron mass, n_A the number of atoms per volume, M the atomic mass, c_{tr} the sound velocity and l the mean free path. This expression is valid at low frequency. Thus an increase of disorder, by decreasing l, should increase the Electron-Phonon Coupling. This equation, qualitatively describing the influence of disorder on the Electron-Phonon Interactions, allows us to understand why most of disordered materials have been found to have a stronger Electron-Phonon Coupling than their crystalline counterpart [Bergmann, 1976].

6. The Debye temperature can be measured by specific heat measurements.
7. For a review about the technique and some experiments, see [Wolf, 1985].
8. In this paper, disorder has been modelled by a random displacement of the atoms.

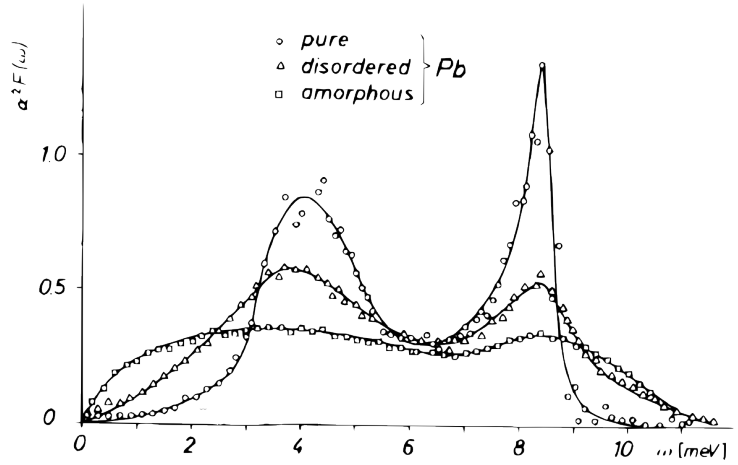

Figure 1.8: The Eliashberg function $\alpha^2(\omega)F(\omega)$ for crystalline, disordered and amorphous Pb. The symbols correspond to experimental data points. The lines are guides to the eyes. Source : [Knorr and Barth, 1971].

Even if the effects of disorder on the critical temperature T_c are lower than first expected, the electron-phonon coupling λ is increased, modifying T_c in superconducting materials. The same mechanism can explain the influence of disorder on Variable Range Hopping in the insulating regime, as we will see section 1.5.1.

1.4.2 Electron-Electron Interactions

In a pure metal, effects of Electron-Electron Interactions are small and are usually only associated with Electron-Electron collisions, giving rise, at low temperature, to corrections to the measured conductivity when the corresponding scattering time is shorter than the one associated with other processes (see section 1.2.2). In disordered materials however, the effects on conductivity of Electron-Electron Interactions are more important than the one pictured by this classical description.

Electron-Electron Interactions can give rise to a Metal-to-Insulator Transition as has been described by Mott using the so-called **Mott-Hubbard model**. Within this framework, electrons are subject to Coulomb interactions depicted by the average correlation energy U. The Hamiltonian can then be written as :

$$H_{Hubbard} = \sum_{i,j,\sigma} t_{ij}(c^{\dagger}_{i,\sigma}c_{j,\sigma} + H.C.) + U\sum_{i} n_{i,\uparrow}n_{i\downarrow} \tag{1.33}$$

where t_{ij} describes the transition probability between sites i and j (taken to be non-zero only for nearest neighbours). There is therefore a competition between the hopping conduction and the localization by Coulomb interactions. Indeed, if a site is occupied, hopping towards this site costs an additional energy U. In the limiting cases, this problem can be easily depicted :

- if $U/t << 1$, the Hubbard Hamiltonian amounts to a tight-binding Hamiltonian and band theory can apply.
- if $U/t >> 1$, Coulomb repulsion dominates and electrons are localized (one electron per site).

A representation of this transition in terms of density-of-states is provided figure 1.9. Starting from a large U/t, corresponding to an insulating state, where two separate bands correspond to the singly and doubly-occupied states, let us progressively lower the ratio U/t. Each band (of characteristic width t) progressively widens. When the two bands overlap, the Metal-to-Insulator Transition occurs and the ground state is conducting.
Let us note that, in this Hamiltonian, only short distance Coulomb interactions are treated since the intra-orbital repulsion term $U\sum_i n_{i,\uparrow}n_{i\downarrow}$ does not take into account the influence of the occupation at site i on other sites. Therefore, this reasoning should, in principle, be limited to the conducting case where Coulomb interactions are correctly screened.

The influence of disorder can be the source of such a Metal-to-Insulator Transition. Indeed, in the presence of disorder, the screening of Coulomb interactions is affected. For a metallic sample

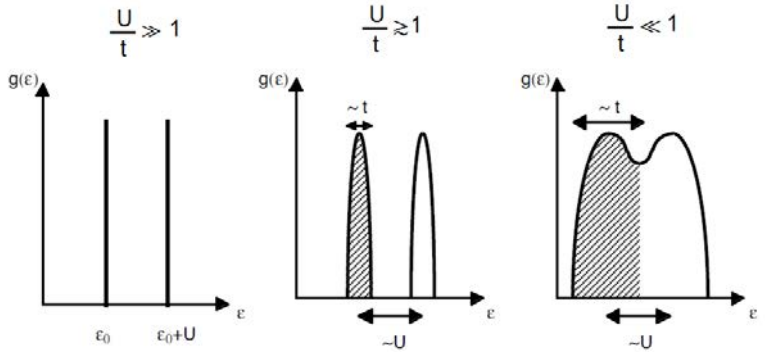

Figure 1.9: One-particle density-of-states in the Hubbard Model as a function of the ratio $\frac{U}{t}$ [Marnieros, 1998].

presenting strong Electron-Electron Interactions, these interactions have been found to give rise to singularities at the Fermi level [Pollak, 1970] : the density-of-states is slightly depleted for energies close to the Fermi energy E_F. As disorder is increased, and as screening is diminished, the strength of Coulomb interactions is increased. For strong enough interactions, this singularity, as shown by Altshuler and Aronov and represented figure 1.10 [Altshuler and Aronov, 1979], gives way to a soft Coulomb gap in the single particle density-of-states at the Fermi level. This gap has a parabolic energy dependence ($N(E) \propto E^2$) at the Fermi level, in 3D.
This gap is observable only at low enough temperature where it overcomes thermal excitation i.e. for :

$$\Delta_c = \frac{e^3 N(E_F)^{1/2}}{\kappa^{3/2}} > k_B T \tag{1.34}$$

with κ the dielectric constant of the material, and $N(E_F)$ the density-of-states at the Fermi level in the absence of interactions.

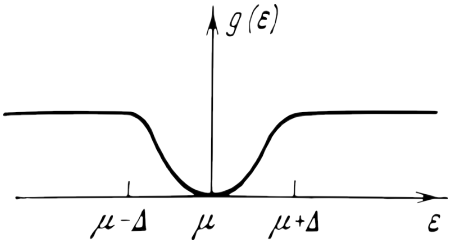

Figure 1.10: Coulomb gap in the density-of-states $g(E)$ in an amorphous semi-conductor near the Fermi level. Source : [Shklovskii and Efros, 1984].

The existence of this **Coulomb gap** has been observed using tunnel junctions in a variety of systems such as doped semiconductors [Shklovskii and Efros, 1984], $Ge_{1-x}Au_x$ [Dodson et al., 1981], Granular Al [Dynes and Garno, 1981], or Nb_xSi_{1-x} [Hertel et al., 1983].
The disorder-induced enhancement of Coulomb interactions has for instance been measured in an experiment performed by Hertel et al. [Hertel et al., 1983] (figure 1.11) on a-Nb_xSi_{1-x} films. The disorder-tuning parameter then was the Nb composition x of the films. At low Nb content, the density-of-states is finite. As disorder increases, the Altshuler-Aronov anomaly becomes more and more pronounced. At the Metal-to-Insulator Transition, the Coulomb gap opens fully, with a zero density-of-states at zero bias. However, let us note that the measurement of this gap by tunnelling experiments reflects the instantaneous density-of-states and not the thermodynamic density-of-states, accessible, for instance, through specific heat measurements.

Even in a less disordered limit ($k_F l >> 1$), it has been shown by Altshuler, Aronov and Lee that Electron-Electron many-body effects can also influence the conductivity [Altshuler et al., 1980]. This contribution to transport (which will be explicitly developed in section 1.5) has been characterized by the so-called **Hartree parameter** F which measures the screening strength. F is supposed to be of the order of unity in a perfectly screened material (short range interactions) and $F \sim 0$ in the absence of screening (long screening length).

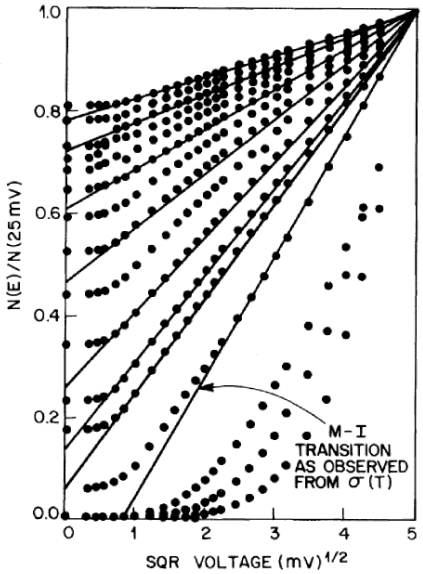

FIG. 2. $N(E)$ vs tunneling voltage.

Figure 1.11: Measurement of the density-of-states variation obtained through tunnelling experiments (renormalized by the 25mV value) across the Metal-to-Insulator Transition in a-Nb_xSi_{1-x}. Source : [Hertel et al., 1983].

The evolution of the Hartree parameter has been widely experimentally investigated, for instance in alloys[Kokanović et al., 1990] or in organic metals [Yoon et al., 1994]. By studying the weak localization regime in organic metals near the MIT, Yoon and al. showed that the contribution of Electron-Electron Interactions are of increasing importance as disorder [9] is enhanced (figure 1.12)[Yoon et al., 1994]. In this work, disorder is measured by [10] $\rho_r = \rho(1.4\text{ K})/\rho(300\text{ K})$. γF (γ is a prefactor of order unity) has been measured both by the temperature dependence of the conductivity and through its magnetic field dependence. The good agreement between the two values shows that weak localization is dominated by interaction effects.

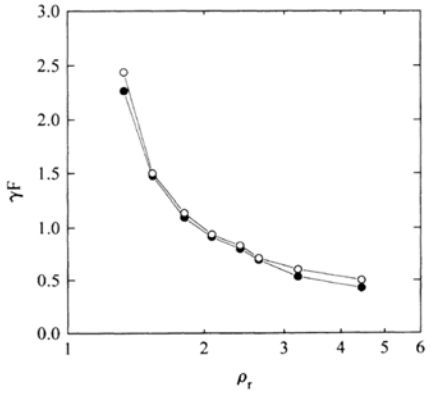

Figure 1.12: Evolution of the Hartree parameter as a function of ρ_r obtained from the conductivity dependence in temperature (full circles) and its magnetic field dependence (empty circles). Source : [Yoon et al., 1994].

Interestingly, it has been shown by Imry and Ovadyahu [Imry and Ovadyahu, 1982] that even if the system is 2D regarding the coherence length -i.e. with respect to localization- Electron-Electron Interactions can be either 2D or 3D. Indeed, as pictured figure 1.13, for films sufficiently thin (a, b, c), the tunnelling conductivity σ_T evolves logarithmically with the bias voltage V. This behaviour is typical of 2D Electron-Electron Interactions.

9. Here disorder is modified by doping and by using pressure.

10. The inverse of the usual RRR criterion : the metallic samples have small ρ_r, and the insulators have larger values of ρ_r.

For thicker films (d, e, f) σ_T is still described by a law proportional to $ln(V)$ at low bias. At high voltage however, σ_T evolves as $\sqrt{V}$, typical of a 3D system. Imry and Ovadyahu therefore showed in this experiment that there is a dimensional crossover for electron-electron interactions which is dependent on the energy E and defined by the length [Imry and Ovadyahu, 1982]:

$$l(E) = \sqrt{\hbar D/E} \tag{1.35}$$

with D the diffusion coefficient. The energy E has been provided in this experiment by the applied electric field but can be equivalently replaced by the thermal energy $k_B T$. This equation is therefore equivalent to a **temperature cross-over at the thermal length** L_T :

$$L_T = \sqrt{\hbar D/k_B T} \tag{1.36}$$

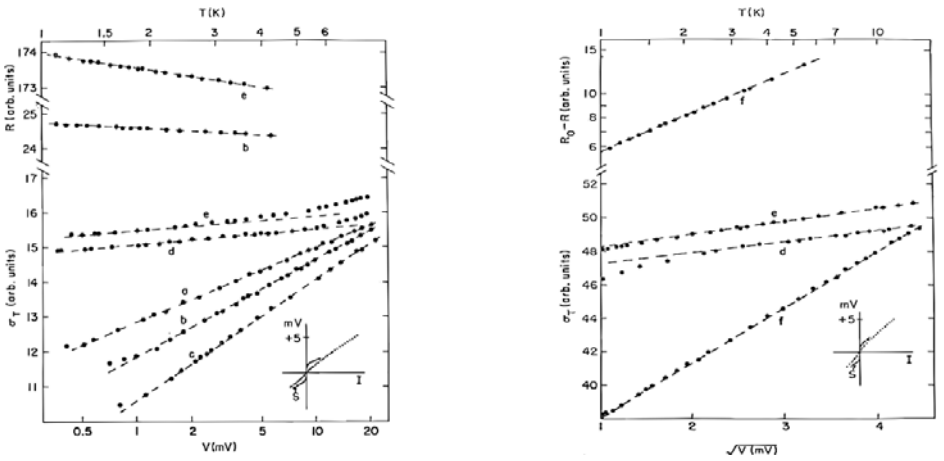

Figure 1.13: Tunnelling conductivity, σ_T, or resistance R, of InO_x films with different thicknesses, plotted as a function of the applied bias voltage [Imry and Ovadyahu, 1982]. Films a, b and c (respectively 160, 190 and 210 Å-thick) are 2D with respect to Coulomb interactions, whereas d, e and f (respectively 310, 460 and 2600 Å-thick) are 3D.

We saw that electron-electron interactions can modify the properties of a given material by different ways and can induce a Metal-to-Insulator Transition. The Metal-to-Insulator Transition is however not the only consequence of electon-electron interactions as we will now see.

1.4.3 Discussion on the effects of interactions

In section 1.3, we have seen that disorder-induces localization effects that modify transport properties and might, eventually, change the system ground state.
In two dimensions, we have seen that no metallic state could exist. As a consequence, only two different ground states should exist in this dimensionality : the system should be either superconducting or insulating.

In this section, we have outlined other effects of disorder : it increases Electron-Phonon Interactions and, most importantly, it enhances Coulomb interactions that can dramatically affect the system electrical behaviour. Alone, electron-electron interactions mainly lead to a suppression of conductivity. However, combined with disorder-induced localization, their consequence can be more complex.
Although the complete theory that treats Electron-Electron Interactions and localization on an equal footing has yet to be developed, one can already say that the "no 2D metal" dogma has been put to a challenge due, in part, to Electron-Electron Interactions.
More specifically, the evidence of metallic states in 2D electron gases measured by Kravchenko [Kravchenko et al., 1994] [11] has shaken this dogma. To measure these metallic states, Kravchenko used a Si-MOSFET of which he modified the carrier density n_s of the 2D electron gases [12] (which

11. The fist claim for a 2D electron gas was in fact reported reported in Ge-MOSFET by Zavaritskaya in [Zavaritskaya and Zavaritskaya, 1987].
12. The thickness of the gas is given by the Thomas-Fermi screening length.

form at the Si/SiO interface) by using an electric field (see figure 1.14). The Metal-to-Insulator Transition was then found to occur at $n_c = 0.96 \times 10^{-11}$ cm^{-2}, corresponding to a resistivity of $\rho_0 \sim 2h/e^2$. In these systems, Coulomb interactions are important due to the low carrier density.

At even lower dimension, 1D metallic states have been observed in Si-MOSFET under a magnetic field in the Quantum Hall regime [Klitzing et al., 1980]. In this experiment (figure 1.15), the Hall resistance has been found to have plateaus - pictured in the figure by U_H - at the value h/ie^2, i being an integer depending on the gate voltage. While U_H experiences these well-defined plateaus, the magnetoresistance, pictured by the corresponding voltage U_{pp}, drops to negligible values. These concomitant phenomena are due to 1D metallic channels running along the sample edges.

The measurement of Quantum Hall Effect and the evidence of metallic states in 2D electron gases are two instances where **Electron-Electron interactions** are thought to be sufficiently strong to **stabilize a low dimensional state of finite conductivity**.
This, in turn, has triggered a renewed interest in the work of Finkel'stein [Finkelstein, 1983][Finkel'stein, 1984] and Castellani et al [Castellani et al., 1984], who predicted such an effect.
A major issue in the theoretical approach provided by these papers is the perturbation approach used to reach this result, which has been found to be inconsistent at low temperatures. This has been recently corrected by Punnoose [Punnoose and Finkel'stein, 2005] which introduces - in the framework of the Renormalization Group Theory - a two-parameters scaling theory of quantum diffusion in disordered systems in the presence of Coulomb interactions. However, it has been pointed out that even if this theory - which does not provide a microscopic description of the phenomenon - quantitatively describes the stabilization of the metal by electron-electron interactions near the Metal-to-Insulator Transition, it cannot explain large effects far from the transition [Dobrosavljevic et al., 2012].

Therefore, to our knowledge, there is still no complete theory addressing the full interplay between localization and Coulomb interactions which would allow to fully describe the observed fermionic metallic states at 2 or lower dimensions.

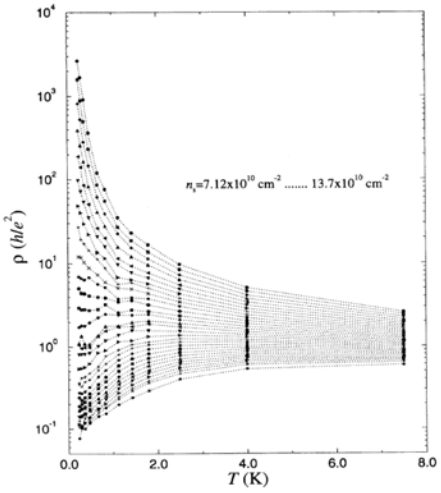

Figure 1.14: Temperature dependence of the resistivity of a Si-MOSFET for different electron densities at B=0 [Kravchenko et al., 1995]. For the highest densities, a metallic behaviour is observed at low temperature instead of the insulating one which is expected for a 2D system in the absence of Coulomb interactions.

1.5 Conduction laws linked to localization

In previous sections, we exposed different mechanisms linked to localization in the presence of disorder. In addition, we reviewed some of the microscopic phenomena which affect fundamental properties of materials. We will now focus on their influence on electronic transport.
In this section, we will first deal with conduction laws in the presence of strong disorder, as it has been first pictured by Anderson. We will then extend this approach in the presence of

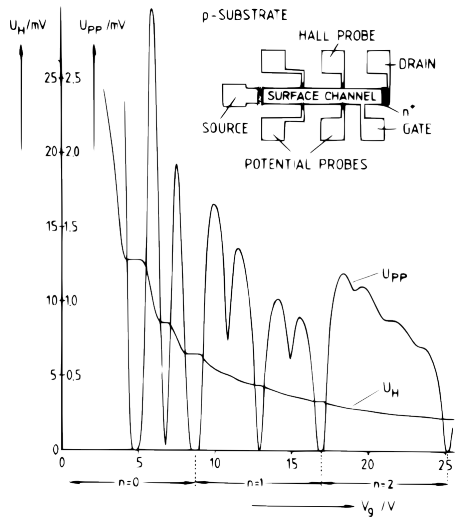

Figure 1.15: Hall voltage measurement in a Si-MOSFET as a function of the gate voltage V_g [Klitzing et al., 1980]. The Hall Resistance, pictured by U_H, have plateaus at given values of the gate voltage while the magnetoresistance, pictured by U_{pp}, goes to zero. This behaviour is a signature of 1D conduction channels running along the sample edges.

Electron-Electron Interactions. Finally, we will concentrate ourselves on detailing the conduction laws in a less disordered regime, where Weak Localization is relevant.

1.5.1 Variable Range Hopping

In the strong localization regime, we saw that the wave function exponentially decreases on a typical distance given by ξ_{loc}. At $T = 0$, there is therefore no possible conduction. However, at finite temperature, due to phonon-assisted tunnelling, the conductivity may be finite.

In 1968, Mott showed that, assuming Anderson-type localization by disorder (as seen in section 1.3.1), the hopping frequency for an electron due to phonon-assisted tunnelling is given by :

$$p = \nu_{ph} exp(-2\alpha R - \frac{W}{k_B T}) \tag{1.37}$$

where ν_{ph} is a coefficient dependent on the strength of Electron-Phonon Interactions, $\alpha = 1/\xi_{loc}$ is the decay rate of the wave function, R the distance between the two sites involved in the hopping process, and W the energy difference between the initial and final hopping sites. This formula, general for hopping conduction in disordered materials, shows that the hopping probability is dependent on Electron-Phonon Interactions, disorder [13], the localization length and the temperature T.

The major idea of equation 1.37 is that, under certain conditions, nearest neighbour hopping is not the dominant process. Indeed, as represented figure 1.16, **electrons have to find a compromise between tunnelling to nearest neighbours at the price of an energy mismatch, or to travel further where the energy difference between the two sites might be smaller. This process is known as Variable Range Hopping (VRH).**
We will now examine the different processes that then intervene, depending on the ratio $\frac{\alpha R k_B T}{W}$.

1.5.1.1 Nearest Neighbour Hopping

In the extreme case of a localization length of the order of the interatomic distance a, **hopping processes should be limited to nearest neighbour**. The area of validity of this approach depends on disorder. Indeed, as discussed by Mott [Mott, 1974], for $a\alpha << 1$ fluctuations of the potential W on available sites are too strong to permit the electrons to lower the tunnelling energy by travelling further away. One should therefore neglect the term $2\alpha R$ in the hopping

13. Disorder is pictured by W which is a random energy like in the model developed by Anderson.

frequency and expect a conductivity law of the form :

$$\sigma = \sigma_0 exp(-\frac{\alpha^3}{N(E_F)k_BT}) \tag{1.38}$$

where $N(E_F)$ is the density-of-states at the Fermi level and $\sigma_0 = \nu_{ph}(\frac{N(E_F)}{\pi\alpha k_B T})^{1/2}$.

For lower disorder, as $\xi_{loc} >> a$, different processes can occur.

1.5.1.2 Mott Variable Range Hopping

For long enough ξ_{loc}, there are number of accessible states through tunnelling. The system will therefore try to lower the cost of tunnelling and one expects a conducting law such that :

$$\sigma = \sigma_0 exp(-(\frac{T_{Mott}}{T})^{\frac{1}{1+d}}) \tag{1.39}$$

$$\text{with } T_{Mott} = \beta_d^{Mott}\alpha^d / N_d(E_F)k_B \tag{1.40}$$

d is here the dimension on which the tunnelling event occurs and $N_d(E)$ is the d-dimensional density-of-states. β_d^{Mott} is a constant dependent on the dimensionality of the hopping process. If the hopping occurs in 3D, $\beta_3^{Mott} = 22.2$. If the hopping occurs in a plane (2D), $\beta_2^{Mott} = 13.8$.

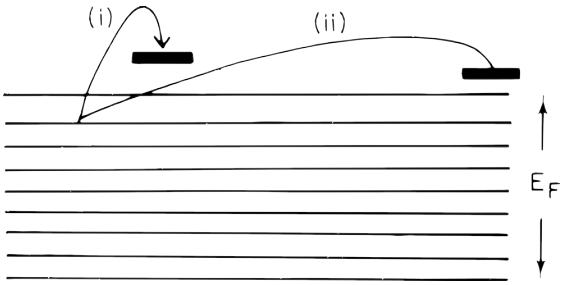

Figure 1.16: Illustration of the Variable Range Hopping process. The carriers have the possibility to travel toward a site nearby in space with an important mismatch in energy (i) or to a further site but with a lower mismatch in energy (ii). Source : [Mott, 1974].

This conduction law supposes a **constant density-of-states at the Fermi level** and neglects effects of Electron-Electron Interactions. As we will now see, the influence of these interactions can be important for the conduction law.

1.5.1.3 Efros-Shklovskii Variable Range Hopping

Due to **Coulomb repulsion**, the hopping distance and the number of accessible states for hopping are greatly reduced. Efros and Shklovskii (ES) found that in this case, even if an electron is hopping to an empty site, the system should pay the price of Coulomb interaction between the hopping electron and the remaining hole. Low energy electrons cannot tunnel and a soft gap in the density-of-states appears. The conduction law should then be given by :

$$\sigma = \sigma_0 exp(-(\frac{T_{ES}}{T})^{\frac{1}{2}}) \tag{1.41}$$

$$\text{with } T_{ES} = \frac{\beta_d^{ES}e^2}{4\pi\epsilon\epsilon_0 k_B \xi_{loc}} = \frac{\beta_d^{ES}e^2}{\kappa\xi_{loc}} \tag{1.42}$$

Contrary to the expression of Mott-VRH, this function is independent on the dimensionality of the system except for the constant β_d^{ES}. Indeed in 3D $\beta_{3D}^{ES} = 2.8$ and in 2D $\beta_{2D}^{ES} = 6.5$.

We discussed earlier the fact that the Coulomb gap appears only at low temperature, where $\Delta_C > k_BT$. For temperatures such that $\Delta_C << k_BT$, Efros-Shklovskii Variable Range Hopping is not relevant and one should consider Mott-Variable Range Hopping conducting law described earlier. As a consequence, there is a typical temperature for which a **crossover** occurs **between ES-VRH and Mott-VRH** conductivity laws. This temperature is defined as

$$T_\Delta = \frac{e^4\xi_{loc}N(E_F)}{\kappa^2} \tag{1.43}$$

1.5.2 Electronic Transport in the weak localization regime

In the presence of weaker disorder, **Weak Localization** (see section 1.3.2.3) gives rise to different correction laws to the conductivity, depending on the dominant dephasing process and the system dimensionality.

In the **absence of interactions**, the temperature dependence of the inelastic scattering time can be expressed as :

$$\tau_{in} \propto T^{-p} \tag{1.44}$$

where p **depends on the dominant scattering mechanism**. The associated coherence length L_ϕ can then be expressed as :

$$L_\phi \sim \sqrt{D\tau_{in}} = \eta T^{-p/2} \tag{1.45}$$

where η is a numerical factor and D is the diffusion constant. Thus, using this temperature dependence, equations 1.27 and 1.28 can be rewritten under the form :

$$\text{in 3D} \quad \sigma = \sigma_0 + \frac{p}{2}\frac{e^2}{\hbar\pi^3}\frac{1}{\eta}T^{p/2} \tag{1.46}$$

$$\text{in 2D} \quad \sigma = \sigma_0 + \frac{p}{2}\frac{e^2}{\hbar\pi^2} ln(\frac{T}{T_0}) \tag{1.47}$$

These equations, when quantum corrections to conductivity are relevant, reflects an enhanced localization due to enhanced electron backscattering.
In the case of interaction-free weak localization mechanism, the evolution as a function of the temperature of the conduction law depends on the dominant scattering mechanism through the parameter p, but does not depend explicitly on disorder [14]. One can therefore wonder how disorder modifies these conduction law.

The contribution from disorder comes mainly from **enhanced Coulomb interactions**. Indeed, **in the presence of Electron-Electron Interactions**, the previous equations are modified such that :

$$\text{in 3D} \quad \sigma = \sigma_0 + \frac{e^2}{2\pi^2\hbar}(\frac{p}{\pi\eta}T^{\frac{p}{2}} + \frac{1.3}{2\sqrt{2}}(\frac{4}{3} - \frac{3}{2}F)\sqrt{\frac{T}{D}}) \tag{1.48}$$

$$\text{in 2D} \quad \sigma = \sigma_0 + (\alpha p + (1 - \frac{3}{4}F))\ \frac{e^2}{2\hbar\pi^2}\ ln(\frac{T}{T_0}) \tag{1.49}$$

where F can be taken as a measure of the strength of Electron-Electron Interactions (see section 1.4.2). The influence of the Hartree factor F in these equations is to decrease the conductance further than what would be expected from the weak localization laws in the absence of interaction.

1.6 Effect of disorder on superconductivity

In the previous sections, we almost exclusively dealt with the various effects disorder could have on a metallic state and with the subsequent Metal-to-Insulator Transition. However, the ground state of all conducting systems is not metallic and it may happen that the system becomes superconducting.
Superconductivity is a macroscopic phenomenon with microscopic origins. A modification of microscopic parameters should has an impact on superconductivity as well. Under sufficient disorder, one can destroy superconductivity and a Superconductor-to-Metal Transition may be observable. In 2D, however, since metallic states should not exist, a direct Superconductor-to-Insulator Transition is expected.

Before dealing with the Superconductor-to-Insulator Transition, we would like to begin by exposing a few concepts on superconductivity in the presence of weak disorder. We will then extend the discussion to arbitrary disorder.

14. p is indeed fixed for a given dominant scattering process.

1.6.1 Superconductivity in the presence of (small) disorder

We will detail here the main ideas behind the description of superconductivity and the effects of small disorder on this phase. We will introduce a distinction between the clean limit and the dirty limit for s-wave type superconductors in the presence of non-magnetic impurities.

1.6.1.1 Superconductivity : from H.K. Onnes to the BCS theory

Superconductivity has been discovered in 1911 by Heike Kamerlingh Onnes who measured the vanishing of the resistivity of mercury at the critical temperature $T_c = 4.15$ K [Kamerlingh Onnes, 1911]. Since then, there have been numerous attempts to explain this phenomenon. In 1935, London was the first to propose a phenomenological picture of superconductivity successfully explaining the Meissner effect, in which the superconducting material expels any constant magnetic field on a lengthscale λ_L, the so-called **London penetration length**, given by :

$$\lambda_L = \sqrt{\frac{m}{\mu_0 n e^2}} \tag{1.50}$$

with m the electron mass, μ_0 the vacuum permittivity and n the total electron density.

Later, Ginzburg and Landau (1950) intuited a phenomenological microscopic wavefunction that captured the essential properties of superconductors in most conventional materials. They introduced a typical length scale over which the wavefunction varies, **the coherence length** ξ, which they found to be :

$$\xi(T) = \sqrt{\frac{\hbar^2}{2m\alpha(T)}} \tag{1.51}$$

where $\alpha(T)$ varies as $\frac{T-T_c}{T_c}$ near T_c. But this theory still missed a microscopic explanation for the mechanisms inducing superconductivity.

The microscopic description of superconductivity was subsequently proposed by Bardeen, Cooper and Schrieffer (BCS) in 1957. BCS theory emphasizes the importance of interactions of electrons with phonons, which are described as being at the origin of superconductivity, like Fröhlich (1950) and Bardeen (1951) had already pointed out. The Hamiltonian used for BCS theory is :

$$\begin{aligned} H_{BCS} &= \sum_{k,\sigma} \epsilon(k) c^\dagger_{k,\sigma} c_{k,\sigma} + \sum_{k,k'} V_{k,k'} c^\dagger_{k,\uparrow} c^\dagger_{-k,\downarrow} c_{k',\downarrow} c_{-k',\uparrow} \\ &= \sum_{k,\sigma} \epsilon(k) c^\dagger_{k,\sigma} c_{k,\sigma} + \sum_{k,k'} V_{k,k'} b^\dagger_k b_{k'} \end{aligned} \tag{1.52}$$

In this equation $c^\dagger_{k,\sigma}$ ($c_{k,\sigma}$) is the creation (annihilation) operator for the electron of wave vector k and spin $\sigma(=\uparrow,\downarrow)$. The first term of this Hamiltonian represents the kinetic energy of the electrons. The second term is the one at the origin of superconductivity : $V_{k,k'}$ ($= V$for simplicity) represents the Electron-Electron Interaction which, thanks to the mediation of Electron-Phonon Interactions, is attractive. This potential allows the condensation of electrons into bosons. These Cooper pairs consist in the binding of two electrons $b^\dagger_k = c^\dagger_{k,\uparrow} c^\dagger_{-k,\downarrow}$, having opposite spins and angular momenta $\overrightarrow{k}$.

As a consequence of BCS theory, the critical temperature T_c is given by [Bardeen et al., 1957] :

$$k_B T_c \sim \hbar < \omega > exp(-1/N(E_F)V) \tag{1.53}$$

where $< \omega >$ corresponds to a cut-off frequency such that $V_{k,k'} = 0$ for frequencies above $< \omega >$. Therefore, the critical temperature should be only dependent on $< \omega >$, the effective electron-electron interaction V and the density-of-states at the Fermi level $N(E_F)$ [15]. One of the major success of BCS theory resides in the successful prediction of the expression of a **superconducting gap** Δ in the single particle density-of-states as a simple function of the sole critical temperature T_c, given at zero temperature by [16] :

$$\Delta(T=0) = \Delta_0 = 1.76 k_B T_c \tag{1.54}$$

15. This relation - and more precisely its derivation by McMillan - as well as its modification by disorder, have been discussed in section 1.4.1.

16. This expression is valid for weak-coupling superconductors.

Following BCS, one can find an expression of the coherence length ξ as a function of the superconducting gap :

$$\xi(T=0) = \xi_0 = \frac{\hbar v_F}{\Delta_0} \tag{1.55}$$

where v_F is the Fermi velocity. This equation defines the typical size of Cooper pairs. Let us stress that, due to the existence of a superconducting gap in the single particle density-of-states, electrons are unlikely to carry an electrical current for energies lower than Δ. Cooper pairs - which exist for energies lower than the gap - then short-circuit the electrons and govern the conduction.

The above description is valid in the clean case, with no disorder. Hence one can wonder what are the effects of disorder within the BCS description of superconductivity.

1.6.1.2 The dirty limit

It seems natural to expect that disorder will affect superconductivity as it modifies the electronic wavefunction and increases electron-electron interactions. A first consideration of the effect of disorder has been proposed by Pippard who examined the effect of scattering on superconductivity. Within the limit of **weak disorder** ($k_F l >> 1$), Pippard made the distinction between two limiting cases depending on how the mean free path in the normal phase l compares with ξ_0 :

- **for** $l/\xi_0 >> 1$, there is no scattering on the distance for which Cooper pairs exist. This correspond to the **clean limit** which has been described in section 1.6.1.1.
- **for** $l/\xi_0 << 1$, scattering should affect Cooper pairs. This limit corresponds to the **dirty limit** regime.

Following this description, let us examine how superconductivity is affected in the dirty limit.

Abrikosov and Gorkov [Abrikosov and Gor'kov, 1959] and, independently, Anderson [Anderson, 1959], have shown that **the superconducting gap** Δ - and by extension the critical temperature T_c - **is insensitive to non-magnetic impurities** and should therefore not be affected by disorder. This constitutes the so-called **Anderson's theorem** [17].

Even though Δ and T_c are, within BCS theory, unaffected by disorder, impurity scattering in the dirty limit modifies the characteristic lengthscales associated with superconductivity, as pictured in the Ginzburg-Landau theory of superconductivity. Indeed, Gorkov showed in 1959 that Ginzburg-Landau equations are a limiting case of the BCS results, valid for $T \sim T_c$. One can therefore use the expressions derived by Ginzburg and Landau regarding the **coherence length** and the **penetration length in both the clean and the dirty limit near** T_c :

	Clean limit	Dirty limit
$\Delta(T)$	$\sim 1.74\Delta_0\sqrt{1-T/T_c}$	
$\xi(T)$	$0.74\xi_0\sqrt{\frac{T_c}{T_c-T}}$	$0.85\sqrt{\xi_0 l}\sqrt{\frac{T_c}{T_c-T}}$
$\lambda(T)$	$0.71\lambda_L\sqrt{\frac{T_c}{T_c-T}}$	$0.62\lambda_L\sqrt{\frac{\xi_0}{l}}\sqrt{\frac{T_c}{T_c-T}}$

According to Anderson's theorem, the expressions obtained in the dirty limit should stay true whatever the disorder. As we will see in the following developments, this constitutive theorem for superconductivity is valid only for weak disorder ($k_F l >> 1$). For strong disorder ($k_F l << 1$), the **interplay between superconductivity and disorder** cannot be neglected and further developments are needed to explain the observed experimental results.

1.6.2 Possible effects of localization on 3D superconductivity

We have shown in the previous section that Δ and T_c should not be affected by disorder for $k_F l >> 1$. However at $k_F l \sim 1$, the question of the effects of localization on superconductivity is more complex. Indeed, experiments on various materials have found a diversity of results regarding the effects of disorder on the suppression of superconductivity, as well as on the different resulting ground states. Furthermore, the problem may depend on the morphology of the

17. This is at least true in the case of an isotropic superconductor. Indeed, in the presence of an anisotropic binding, the first effect of disorder is to make it more homogeneous, which, in turn, affects superconductivity. As soon as the binding becomes isotropic, Anderson's theorem applies.

investigated material : the effect of disorder could be different if the system is granular, presents quenched disorder or is (poly-)crystalline. In all cases, however, strong disorder tends to weaken, and eventually kill, superconductivity.
In this section, we would like to non-exhaustively illustrate the fundamental question of the interplay between superconductivity and disorder by using two different examples, exposing two extreme cases [18] : the treatment of the effects of disorder for granular and amorphous superconducting materials in the 3D limit.

The effects of localization on the superconducting properties of materials have first been thought of by analogy with **granular systems**. In such systems, as described by Imry and Strongin [Imry and Strongin, 1981], **the competition between the charging energy on each grain E_c and the Josephson-tunnelling energy** E_J can be seen as the origin of the destruction of superconductivity. To model this behaviour, they used the scaling theory with elementary blocks composed of superconducting grains, with a fixed superconducting gap Δ. They therefore considered that superconductivity was well established within one grain, and neglected the effects of Coulomb interactions on the properties of individual grains or the effects of a modification of the Electron-Phonon interaction. By performing a qualitative treatment, they found different solutions depending on the studied system and the ratio between E_c and E_J :

- If the system is made out of **small grains**, a 3D system can be either superconducting, metallic or insulating. Local superconductivity is destroyed when the local conductivity g_l is below a few $\frac{e^2}{h}$.
  - **For small** E_c, the system can be metallic as the electronic transport is not blocked when superconductivity vanishes, at least when disorder is small. When the disorder is increased such that $g_l \sim g_c$, the critical conductivity of the 3D Metal-to-Insulator Transition, the system becomes overall insulating.
  - For systems such that E_c **become comparable to** E_J when disorder is increased, the system can have a direct Superconductor-to-Insulator Transition as global phase coherence is destroyed before local superconductivity.

  Thus, starting from a superconducting material and progressively increasing the disorder, one should observe successively a Superconductor-to-Metal Transition and a Metal-to-Insulator Transition, or a direct Superconductor-to-Insulator Transition.
- If the system is made out of **large enough grains**, the problem is simpler. Indeed, the charging energy E_c is way more important, and therefore electronic transport is blocked when superconductivity vanishes. The system therefore is superconducting for $E_c < E_J$ and is insulating otherwise, with a direct Superconductor-to-Insulator Transition. One can, in this case, observe two successive transitions in the R(T) characteristic corresponding to the loss of global phase coherence - giving the critical temperature of the system - and the loss of superconductivity within localized grains at higher temperature.

Therefore, in these 3D granular materials, both the ratio E_c/E_J and the local conductance determine the ground states.

Although the previous description could, in principle, apply to homogeneous materials in the sense that these can be seen as granular systems with a typical grain size of the order of the interatomic distance, Ma & Lee [Ma and Lee, 1985] and Kapitulnik & Kotliar [Kapitulnik et al., 1985, Kotliar and Kapitulnik, 1986] have shown that things were more complicated. Indeed, they considered the possibility of having a **superconducting ground states starting from localized single particle states**. Both papers showed that superconductivity can exist as long as the superconducting gap is larger than the inter-level spacing of the density-of-states in the insulator. This remarkable result is schematically explicited figure 1.17 : the average values of the superconducting gap Δ and of the superfluid density n_s do not go to zero at the Metal-to-Insulator Transition (point C) and bear finite values well within the normal insulating regime. Δ and n_s are even unaffected until point D which marks the limit of validity of Anderson's theorem. Point D corresponds to the criterion $\Delta N(E_F)L^3 \sim 1$. For larger disorder levels, global coherence weakens and Δ and n_s fluctuate in space. They eventually vanish and superconductivity is destroyed.

18. The question of the interplay between localization and disorder will be exposed more exhaustively in the following sections, in the case of thin films.

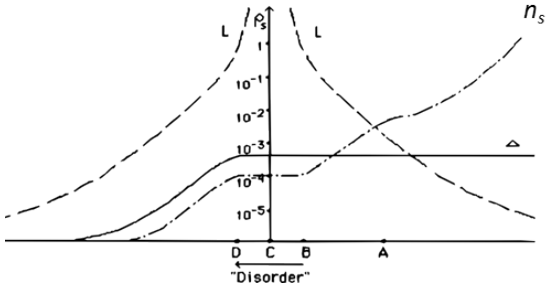

Figure 1.17: Evolution of some relevant quantities for a amorphous superconducting material in the presence of disorder. Point C corresponds to the Metal-to-Insulator Transition. The dashed line corresponds to the evolution of L, the correlation length on the metallic side and the localization length on the insulating side, as a function of disorder. The spatial average of the superconducting gap Δ and of the superfluid density n_s are also shown [Ma and Lee, 1985].

1.6.3 Effects of a thickness reduction depending on the morphology

As seen above, material morphology is of primary importance when dealing with the effects of disorder on superconductivity. By changing the thickness of a sample, one can modify the normal state conductivity of a film. Therefore, by taking $k_F l$ as a measure of the disorder and through the Drude model, it is of common belief that changing the thickness of a film also modifies its effective disorder. In this section, we will get a first look on the dramatic effects that a thickness modification can have on electrical properties of materials, depending on their morphology.

The behaviour of the resistivity near the thickness-tuned Superconductor-to-Insulator Transition for granular and amorphous Pb is illustrated figure 1.18 [Gantmakher and Dolgopolov, 2010]. To compare the two morphologies, the authors have evaporated Pb with or without adding an amorphous sub-layer of Ge. In the absence of this amorphous layer, and due to interfacial tensions, the evaporated material will not wet the substrate and islands form, giving rise to granularity.

In the case of **granular films** (illustrated figure 1.18b for Pb), superconductivity first appears locally, within each grain, at a temperature T_{c0}, the critical temperature of the bulk material. As the temperature is further lowered, the grains couple to each other until macroscopic coherence is achieved. The film then becomes superconducting. As the thickness is lowered, the first appearance of **local superconductivity still occurs at** $T = T_{c0}$ since the critical temperature within each grain is essentially unchanged. However, the competition between the charging energy E_c and the Josephson coupling energy between the grains E_J evolves, similarly to the description provided by Imry and Strongin (section 1.6.2), such that the **superconducting transition broadens**. As disorder is further increased, the ground state becomes insulating [19].

In amorphous or, more generally, **homogeneously disordered films**, the superconducting transition temperature is also affected by disorder. As the film thickness is reduced, the superconducting critical temperature T_c is reduced but, contrary to granular films, **the superconducting transition remains sharp** as can be seen figure 1.18a, in the case of a-Pb films. Furthermore, since superconductivity is affected in the entire film, one should not observe a re-entrant behaviour of the resistivity at low temperatures.

In these systems, the origin of the destruction of superconductivity and the nature of the insulating phase is a subject of intense debate in the community. In the following section, we will present a brief review of the state-of-the-art of the subject.

1.7 Dimensional Effects on Superconductivity

Dimensional effects begin to affect superconductivity when the superconducting coherence length ξ is of the same order of magnitude than the film thickness $d_\perp$. However, the exact

19. In some cases, re-entrant behaviours are observed in the transport properties as the grains become locally superconducting but the ground state still is insulating due to the lack of long-range ordering of the phase of the superconducting order parameter.

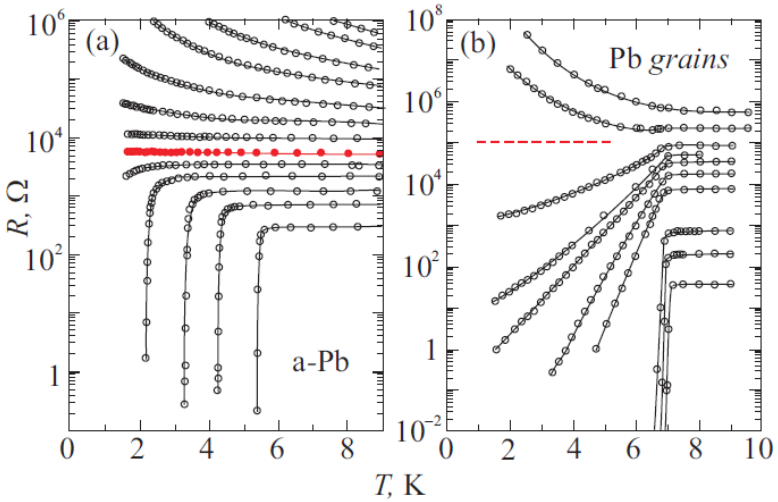

Figure 1.18: Comparaison of the resistance as a function of the temperature for Pb films of different thicknesses in the granular (a) and amorphous (b) cases. Adapted from : [Gantmakher and Dolgopolov, 2010].

description of a thickness reduction on superconductivity is still an object of debate within the condensed matter community. In this part, we will detail different models that have been proposed to describe this issue. To do so, we will first detail the effects of surface scattering on the properties of thin films. We will then present a mechanism through which phase fluctuations can affect superconductivity in 2D : the Berezinskii-Kosterlitz-Thouless (BKT) transition. Surface effects and BKT transition play an important role in 2D superconductivity but do not account for the SIT observed in disordered thin films. We will therefore expose current theories explaining this phenomenon along with experimental evidence which will be discussed in light of the different models.

1.7.1 Surface effects

In this paragraph, we will outline a few theoretical ideas underlying the specific role of the film thickness on thin films properties. To do so, we will expose different models taking into account effects due to the surface, both for metallic and superconducting materials.

One of the first models to describe size effects on **metals** has been derived by **Fuchs** [Fuchs, 1938] and Sondheimer [Sondheimer, 1952]. The idea behind this model is that the film resistivity should be influenced by **specular reflections** of the electrons on the sample surfaces. Following this description, Sondheimer calculated the correction to resistivity, depending on the mean free path l and the thickness of the film $d_\perp$:

$$\text{for} \quad l << d_\perp \qquad \rho = \rho_0(1 + \frac{3}{8}\frac{l}{d_\perp}(1-p)) \tag{1.56}$$

$$\text{for} \quad l >> d_\perp \qquad \rho = \rho_0(\frac{4}{3}\ \frac{1-p}{1+p}\ \frac{l}{d\ ln(l/d)}) \tag{1.57}$$

where ρ_0 corresponds to the conductivity of the bulk material in the presence of exactly the same amount of disorder as the considered film and p is a parameter representing the probability of specular reflection.

In the case of superconductivity, De Gennes pointed out that boundary conditions should affect the description of superconductivity given by Ginzburg-Landau equations [De Gennes, 1999]. This idea of an influence of surfaces has been used by Simonin who, to depict the modification of the boundary conditions due to a thickness modification, introduced **a surface energy term in the Ginzburg-Landau free energy**. Assuming that the material has a thickness-independent density-of-states, he found the thickness $d_\perp$ to influence the evolution of the critical temperature

T_c such that :

$$T_c = T_{c0}[1 - 2C\xi_0^2/d_\perp] \quad = T_{c0}[1 - d_m/d_\perp] \tag{1.58}$$

where T_{c0} is the bulk value of the superconducting critical temperature, ξ_0 is the zero temperature superconducting coherence length and d_m is the critical thickness at which superconductivity disappears. The constant $C \sim a/N(E_F)V\xi_0^2$ is material-dependent, with a the Thomas-Fermi screening length and V the effective Electron-Electron Interaction that intervenes in the BCS theory.

Simonin's model, predicting the behaviour of the critical temperature reduction as a function of the thickness is rarely mentioned. It has, however, been experimentally verified in numerous systems, as can be seen figure 1.19 [20]. It is true that this model does not predict the state (metallic or insulating) into which the system transits as the critical thickness is crossed, or the underlying transition mechanism (bosonic or fermionic). However, it takes into account surface effects which are neglected in other models and which, in our opinion, should contribute to the destruction of superconductivity in thin films. Moreover, to the best of our knowledge, there has not been any theoretical arguments put forward against this description.

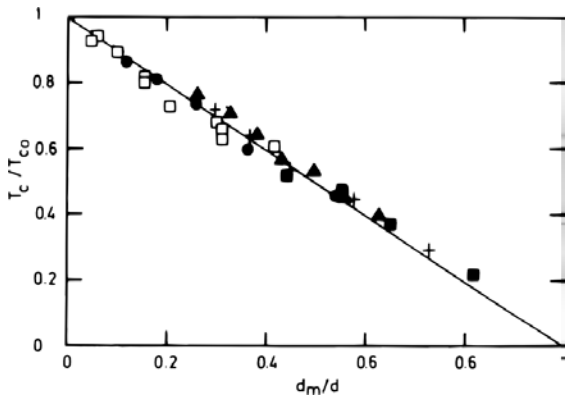

Figure 1.19: Superconducting properties of films of Nb, Pb and Bi plotted as a function of the inverse of their thickness. Adapted from [Simonin, 1986].

1.7.2 The Berezinskii-Kosterlitz-Thouless Transition

As dimensionality is reduced, new phenomena can occur in solids. One of these effects is the **Berezinskii-Kosterlitz-Thouless (BKT) transition** which is observable only at low dimension. In 2D, thermally activated vortices spontaneously form. For $T < T_{BKT}$, the BKT temperature, vortices condense under the form of vortex-antivortex pairs. The corresponding state is superconducting. For $T_{BKT} < T < T_c$, with T_c the mean field superconducting critical temperature, the pairs size increases and they acquire sufficient energy to start dissociating. Their motion then induces a dissipative state.

Effects of the Berezinskii-Kosterlitz-Thouless transition can be observed by low-frequency transport measurements. Halperin & Nelson showed that the evolution of the resistivity below T_{BKT} is then given by [Halperin and Nelson, 1979]:

$$\rho \sim \rho_0 exp(-\frac{b}{\sqrt{T - T_{BKT}}}) \tag{1.59}$$

where ρ_0 and b are material-dependent constants. For $T < T_{BKT}$, the transition is therefore characterized by a linear dependence of the logarithmic resistivity as a function of temperature. This has been experimentaly observed - for example - in InO_x thin films, as shown figure 1.20. BKT mechanism only affects the last few % of the resistive transition, but the existence of this transition is crucial for theoretical models of the Superconductor-to-Insulator transition, such as the Dirty Boson Model.

20. This description has been found to adequately account for experimental results in other materials such as Al [Chubov et al., 1969], La [Löptien et al., 2014] or Nb_xSi_{1-x} [Crauste et al., 2014].

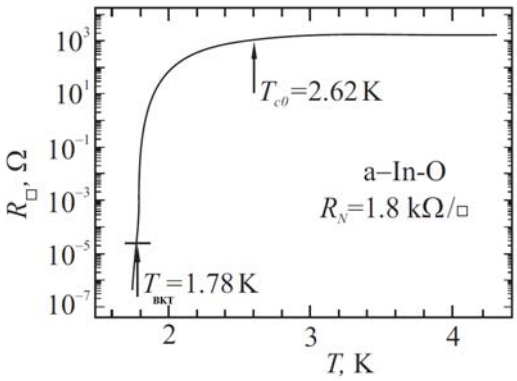

Figure 1.20: Resistance of a 100 Å-thick InO_x film with T_{c0} the critical temperature of the bulk system and T_{BKT} the temperature of the BKT transition [Fiory et al., 1983].

1.7.3 The Superconductor-to-Insulator Transition

A pioneering work for the study of the ground state (defined at $T = 0$) in superconducting thin films has been provided by Haviland et al [Haviland et al., 1989] who quench-condensed a-Bi films at low temperature onto an a-Ge layer (figure 1.21) and studied their transport properties as a function of their thickness, modified by successive evaporations from 4.36 Å to 74.27 Å. By doing so, they observed a direct transition between the superconducting and the insulating ground states. This transition occurred at a thickness smaller than 7 Å, well below the value of the superconducting coherence length.
We saw in section 1.2.3 that it is possible to link the resistivity of the film to the fermiologic quantity $k_F l$. This Superconductor-to-Insulator Transition has therefore been interpreted as a change in the system ground state due to a modification of the effective disorder, measured through the Ioffe Regel parameter $k_F l$. The question of the physical origin of this Superconductor-to-Insulator Transition (SIT) has given rise to numerous experiments and theories in the following decades which tried to characterise and explain the microscopic machinery behind this phenomenon.

In the following, we will try to expose the major theoretical models which aim at explaining this transition. These models are usually divided into two different categories, depending on the microscopic nature of the resulting insulating phase : Fermionic or Bosonic. The discussion of these models will be illustrated by experiments.

1.7.3.1 Fermionic models of the SIT

1.7.3.1.a Maekawa & Fukuyama first order calculation

Maekawa and Fukuyama [Maekawa and Fukuyama, 1982] & Takagi and Kuroda [Takagi and Kuroda, 1982] studied the effects of Coulomb interactions on the properties of superconductors. They found that, in the case of a thickness $d_\perp < l$ the mean free path, as disorder increases, the increasing electron-electron repulsion in the material suppresses the superconducting order parameter Δ, violating Anderson's Theorem. Thus, they quantified the effects of Coulomb interactions on the critical temperature and found that T_c is lowered as :

$$ln\frac{T_c}{T_{c0}} = -\frac{e^2}{6\pi^2\hbar}g_1 R_\square (ln\frac{\hbar}{k_B T_c \tau})^3 \tag{1.60}$$

where τ is the time associated with the mean free path, g_1 [21] is a constant related to electron-electron interaction, and T_{c0} is the transition temperature for the bulk superconductor presenting the same microscopic structure. This relation has been found to correctly fit the experimental data when the corrections to T_{c0} are small. However this expression fails in the case of highly disordered films. Indeed, the calculation has been made by treating disorder, and thus the thickness reduction, as a first order perturbation. For high enough disorder, this approach therefore had to be extended.

21. $g_1 = 1/2$ for screened Coulomb interactions.

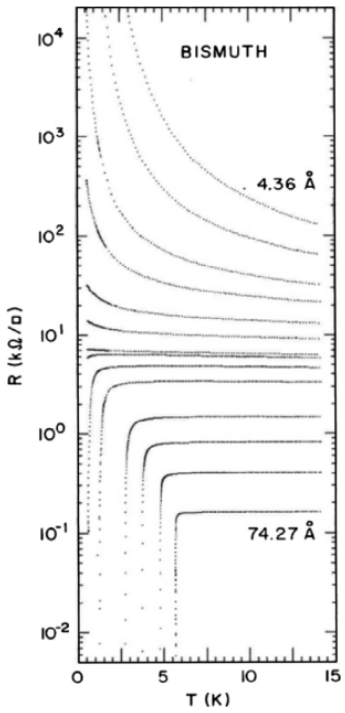

Figure 1.21: Evolution of the sheet resistance as a function of the temperature of amorphous-Bi thin films depending of the evaporated thickness [Haviland et al., 1989].

1.7.3.1.b Finkel'stein's theory

In 1984, Finkel'stein [Finkelstein, 1983] extended Maekawa & Fukuyama's theory for more disordered films using the renomalization group. This theory assumed uniformly disordered films, with no electronic or morphological structure and it therefore principally applies to morphologically homogeneous systems.

Finkel'stein's theory is sometime considered as an extension of the BCS mean field theory [Skvortsov, 2015] which, in addition, takes into account the repulsive effects of electron-electron interactions, which give rise to the **vanishing amplitude of the superconducting gap** Δ. Indeed, in this theory and due to diffusion in the presence of disorder, **screening properties are modified**. Thus, repulsive interactions between electrons are enhanced resulting in a negative correction to the BCS pairing.

By developing this theory, Finkel'stein found that the critical temperature in the presence of Coulomb interactions in disordered materials should be corrected along :

$$\frac{T_c}{T_{c0}} = exp(-\frac{1}{\gamma})[(1+\frac{\sqrt{t/2}}{\gamma - t/4})(1-\frac{\sqrt{t/2}}{\gamma - t/4})^{-1}]^{1/\sqrt{2t}} \tag{1.61}$$

with $\gamma = 1/ln(k_B T_{c0}\tau/\hbar)$ and the renormalized sheet resistance $t = R_\square e^2/(2\pi^2\hbar)$. For small disorder, this equation is equivalent to equation 1.60.

Fits of the evolution of the critical temperature using equation 1.61 following Finkels'tein's theory have been performed in various materials like in MoGe (figure 1.22) and have been found to be in good agreement with experimental data. The calculation of the critical temperature evolution provided by Finkels'tein is convenient for analyzing real experiments since the only free parameter is the mean free path time τ.

According to equation 1.61, the Superconductor-Insulator Transition occurs when the modification of the sheet resistance $R_\square$ leads to a critical temperature $T_c = 0$. This argument leads to the critical conductance :

$$g_c = \frac{1}{8\pi} ln(\frac{\hbar}{k_B T_{c0}\tau}) \tag{1.62}$$

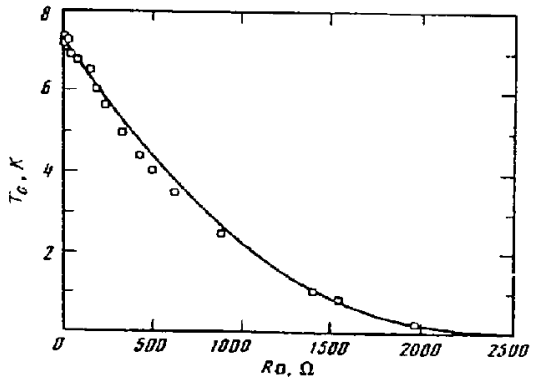

Figure 1.22: Reduction of the superconducting critical temperature T_c as a function of the sheet resistance $R_\square$ in MoGe thin films and fit according to Finkelstein's theory [Graybeal and Beasley, 1984] [Finkelstein, 1983].

This value, due to the presence of τ and T_{c0}, is dependent on the considered material and is not universal. An important point regarding the development of Finkel'stein's theory is that it has been developed in a mean field approximation and, due to this approximation, is valid for $5<1/\gamma<9$. Outside this range, even though the destruction of superconductivity may still be described by Coulomb interactions, Finkel'stein's theory should not be quantitatively true.
Let us moreover stress that, in this fermionic picture, **superconductivity is destroyed through its pairing amplitude** to give rise to a, a priori, **fermionic state**. Since, in 2D, the scaling theory of localization prevents any metallic state to exist, the ground state arising from the destruction of superconductivity is an **insulator**.

1.7.3.1.c Experiments pointing to a fermionic scenario in some materials

Non-universal critical resistance R_c
As we will see later, some bosonic models support the idea of a universal value of the critical resistance at the Superconducting-Insulating transition. On the other hand, as can be seen from equation 1.62, such expectation does not exist for fermionic models of the SIT. Experimentally, the critical resistance in most materials has been found to be highly dependent on the considered system. It has been even showed by A. Yazdani and A. Kapitulnik that a-MoGe films of different thicknesses and compositions have critical values of the resistance R_c ranging from 651 to 2026 Ohms and that two films of the same composition but with different thicknesses can have different R_c in a magnetic field-tuned SIT [Yazdani and Kapitulnik, 1995]. This has also been observed in other systems like Nb_xSi_{1-x} [Marrache-Kikuchi et al., 2008].

Tunnelling measurements of the superconducting gap
Electron tunnelling directly measures the quasiparticle density-of-states and is therefore a powerful tool to measure the superconducting gap. The appearance (or not) of a superconducting gap in the density-of-states in the insulating state just above the transition will be a direct indication of the bosonic (or fermionic) nature of the transition.
Different experiments in pure materials usually tend to show that the result is highly dependent on the morphology of the films. Indeed, in amorphous Bi [Valles et al., 1992] (figure 1.23), the measurement of the tunnelling conductance shows that the superconducting gap is vanishing near the Superconductor-to-Insulator Transition, in agreement with what is expected in a fermionic scenario. On the other hand, in quench-condensed granular Pb [Barber et al., 1994], measurements of the tunnelling conductance on both sides of the transition show that, even when the film is found to be insulating by electronic transport measurements, the superconducting gap remains and keeps almost the same value as in the bulk.

To gain a more precise view on this issue, one can wonder how the local superconducting gap evolves. Indeed, using macroscopic tunnelling junctions averages the measurement on macroscopic sizes, potentially hiding spatial inhomogeneities of the gap. Therefore, if one site is superconducting and the next metallic, one can measure a non-zero density-of-states using a macroscopic tunnel junction. By using a more local probe, STM measurements circumvent this averaging effect. Such STM measurements performed in MoC by Szabò et al. [Szabó et al., 2016]

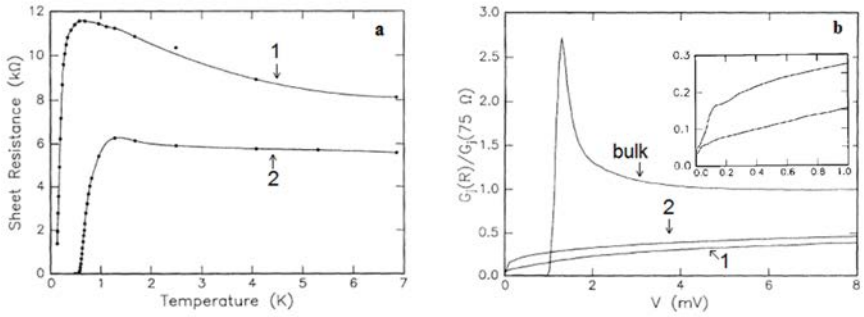

Figure 1.23: (a) Sheet resistance of two a-Bi superconducting films close to the Superconductor-to-Insulator Transition. (b) Tunnelling conductance of the two films presented in (a) compared with the tunneling conductance of a bulk sample [Valles et al., 1992].

are plotted figure 1.24.b . They show that, in this system, as T_c is lowered by modifying the thickness of the sample (figure 1.24.a.), both T_c and Δ decrease as the Superconductor-to-Insulator Transition is crossed, with a ratio Δ/k_BT_c almost constant and independent on the tip position (figure 1.24.c). This constancy of the ratio Δ/k_BT_c has been also found by Noat et al. in NbN for films with thicknesses ranging from 2.16 to 15 nm where no inhomogeneity of the order parameter has been found in the absence of a magnetic field [Noat et al., 2013]. These experimental results therefore favor a fermionic scenario for the destruction of superconductivity in these materials. We will later see that similar STM measurement conclude otherwise for other materials (see section 1.7.3.2.d).

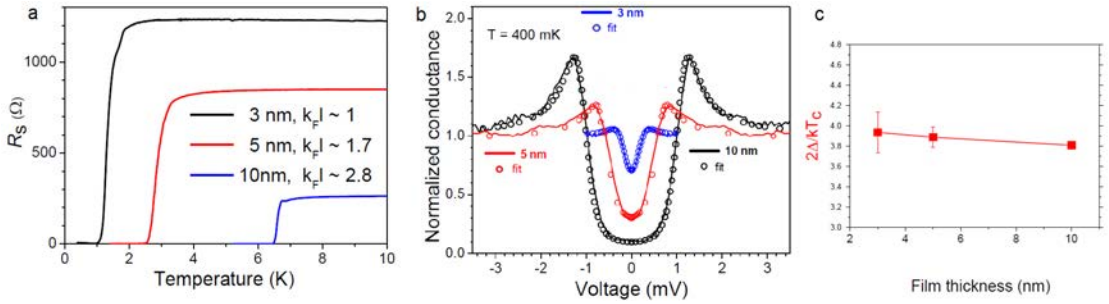

Figure 1.24: (a) Sheet resistance of different MoC samples measured by electronic transport measurements. (b) Tunneling spectra obtained by STM for the same MoC samples. (c) Evolution of the ratio $2\Delta/k_BT_c$ extracted from the fitting of tunneling spectra as a function of the film thickness. Source : [Szabó et al., 2016].

1.7.3.2 Bosonic models of the transition

All Superconductor-to-Insulator Transitions may not occur following a fermionic model. Indeed, as we saw in the 3D case, superconductivity may locally survive to single electron localization. Based on an analogy with granular models, different theoretical works have been developed throughout the years in which the mechanism at the origin of the transition is not the disappearance of the superconducting order parameter but fluctuations of its phase between different grains. Some of these scenarii are presented below.

1.7.3.2.a The "Dirty Boson Model"

In the early 90's, M.P.A. Fisher proposed a theory for the 2D Superconductor-Insulator Transition tuned either by disorder or by a magnetic field [Fisher, 1990]. This description of the Superconductor-Insulator Transition is summarized figure 1.25. To develop this model, he started from the existence of the BKT transition and makes use of the existing duality between Cooper pairs and vortices :

– In the superconducting phase, the system presents localized vortices and condensed Cooper pairs.

– In the insulating phase, Cooper pairs are localized and the vortices are condensed.

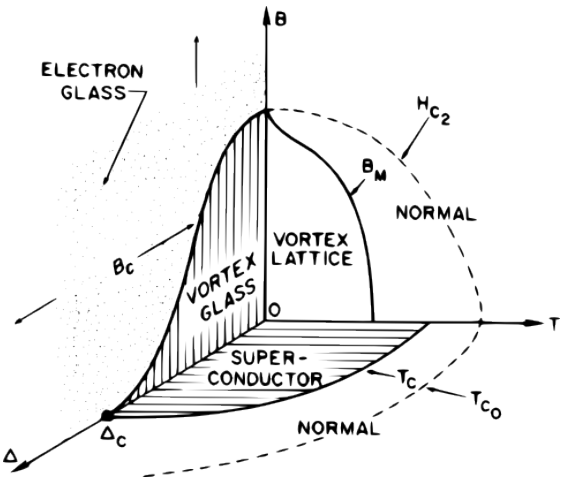

Figure 1.25: Schematic phase diagram for the Superconductor-Insulator Transition in the presence of disorder Δ and magnetic field B [Fisher, 1990].

Fisher starts by pointing out that a zero-disorder superconducting film in zero magnetic field has a critical temperature T_c, given by BKT theory, lower than the bulk value T_{c0}. Thus, for $T > T_{c0}$, thermal fluctuations destroy the amplitude of the order parameter. For $T_{c0} > T > T_c$, the amplitude of the order parameter is non zero, but its phase fluctuates, due to the motion of vortices - which occurs at zero energy -, preventing the establishment of a long-ranged coherent superconducting state. The Superconductor-to-Insulator Transition is then due to phase fluctuations and the superconducting order parameter is non-zero in the corresponding insulating state. The SIT is bosonic in the sense that Cooper pairs survive at the transition, giving rise to a Bose glass.

This "Dirty Boson Model", has been studied using the scaling description of quantum phase transitions. Close to the phase transition, the scale of phase fluctuations is given by the correlation length :

$$\xi = |K - K_c|^{-\nu} \tag{1.63}$$

where K is the tuning parameter, K_c its critical value and ν is the critical exponent associated with the coherence length. This scaling law depicts the typical length over which Cooper pairs in the superconductor and of vortices in the insulator are correlated.

The associated scaling law for resistivity, valid in the quantum critical regime, is :

$$\frac{R}{R_c} = \frac{h}{4e^2} F(\delta/T^{-\frac{1}{\nu z}}, \delta/E^{1/(\nu(z+1))}) \tag{1.64}$$

where F is a scaling function, $\delta = \frac{K-K_c}{K_c}$ is the distance to the transition and z is the dynamical critical exponent. Such a scaling law is presented figure 1.26 on which we can observe that all curves obtained from resistance measurements of a-Bi samples of different thicknesses collapse onto the same universal curve (one for the superconducting state and one for insulating state) for the scaling variable $t|d_\perp - d_{\perp c}|$, t being here $\mathrm{T}^{-\nu z}$ and $d_\perp$ ($d_{\perp c}$) the sample (critical) thickness. In this scaling treatment, the authors found a critical exponent product of $\nu z \sim 1.2$.

If a strict duality between Cooper pairs and vortices is assumed, M.P.A. Fisher found that :

$$\sigma_{bosons} = \rho_{vortex} (\frac{4e^2}{h})^2 \tag{1.65}$$

As the transition should occur when the resistivity of bosons and vortices are similar, this relation is equivalent to saying that the transition should occur at a universal value $R_Q = \frac{h}{4e^2} \sim 6450\,\Omega$, the quantum of resistance for Cooper pairs.

The values of the critical exponents depend on the nature of the transition. It has been showed by Markovic et al [Markovic et al., 1998] (figure 1.27) and by Marrache-Kikuchi et al

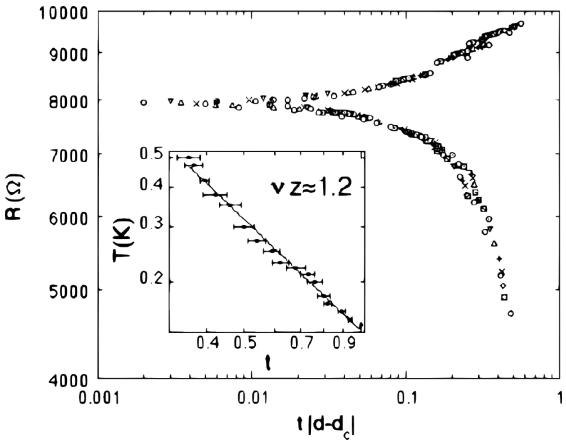

Figure 1.26: Sheet resistance as a function of the scaling parameter $t|d_\perp - d_{\perp c}|$ for temperatures ranging from 0.14 to 0.5 K. Different symbols correspond to different temperatures [Markovic et al., 1998].

[Marrache-Kikuchi, 2006][Marrache-Kikuchi et al., 2008] that, depending on the tuning parameter of the transition, the mechanism underlying the transition may differ, giving different critical exponents. Markovic indeed found that, depending on whether the tuning parameter was the thickness of the film or the magnetic field, νz have different values ranging from 1.4 (in the case of the thickness-tuned transition) down to 0.7 (in the case of the magnetic field-tuned transition).

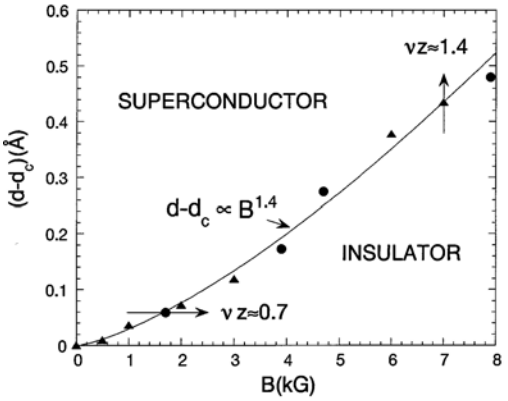

Figure 1.27: Phase diagram in the $d_\perp - B$ plane in the T=0 limit. The points correspond to experimental data obtained from thickness (disorder)-driven transitions (triangles) and magnetic field-driven transition (circles). The critical exponents product is equal to 0.7 for a magnetic field-tuned transition and to 1.4 for a disorder-tuned transition [Markovic et al., 1998].

We discussed the scaling procedure in the framework of the Dirty Boson Model. However it seems important to us to stress that the scaling procedure should work whatever the nature of the transition (bosonic of fermionic). Indeed, this process is inherent to the existence of a Quantum Phase Transition. The mechanisms at the origin of the destruction of superconductivity in the bosonic and the fermionic scenarii should however differ, giving rise to different critical exponents and different scaling functions.

1.7.3.2.b Layered 2D superconductor

Dubi et al. [?] proposed a different model based on the BKT transition to explain the Superconductor-to-Insulator Transition observed at finite temperature. They proposed to consider the system as a multilayer of true 2D layers, presenting BKT transitions at $T_c \sim T_{KBT} = \frac{\pi}{2}K$. Here K is the phase stiffness. They computed that disorder modifies the phase stiffness of the superconductor such that $K(d_\perp) \sim \frac{1}{3}K_0 d_\perp/a$ where a is the distance between layers. The system then exhibits a Superconductor-to-Insulator Transition of bosonic type. The particularity of their approach is that they found that in this quasi-2D BKT transition, T_{BKT} can be written

as :

$$T_{BKT} \sim T_{c0}(1 - \frac{6T_{c0}}{\pi K_0}\frac{a}{d_\perp}) \tag{1.66}$$

where T_{c0} is the mean field critical temperature and $K_0 = \hbar^2 n_s/m$ with n_s the superfluid density and m the electron mass.

This result is quite interesting since it gives a description of the evolution of T_c (or T_{BKT}), in agreement with what Simonin [Simonin, 1986] has found, but by assuming this time a bosonic model of the SIT [22].

1.7.3.2.c Numerical studies of the SIT

The models described below have been developed in the group of Nandini Trivedi by using numerical calculations in order to give an insight on the nature of the transition. Ghosal et al proposed to solve this problem in the framework of the BCS theory by solving an attractive Hubbard model described by the Hamiltonian :

$$H = -t \sum_{<ij>,\sigma} (c_{i,\sigma}c^\dagger_{j,\sigma} + c^\dagger_{j,\sigma}c_{i,\sigma}) + \sum_{i,\sigma}(V_i - \mu)n_{i,\sigma} - |U| \sum_i n^\dagger_{i,\uparrow}n_{i,\downarrow} \tag{1.67}$$

with $\sigma = (\uparrow, \downarrow)$, i (j) the electronic sites, $c_{i,\sigma}(c^\dagger_{i,\sigma})$ the operator creation (annihilation) of an electron of spin σ on site i, $n_{i,\sigma} = c^\dagger_{i,\sigma}c_{i,\sigma}$ the operator number for a Cooper pair on site i, and V_i the disorder potential associated with site i. The first term describes the kinetic energy, the second one is the one-particle free energy in the presence of disorder and the last one describes the pairing of Cooper pairs in the presence of the coupling potential $|U|$.

By numerically solving this Hamiltonian with a self-consistent Bogoliubov-de Gennes approach, Ghosal et al. [Ghosal et al., 1998][Ghosal et al., 2001] showed that - at zero temperature and in a 2D material - the spatial distribution of the superconducting pairing amplitude becomes inhomogeneous in the presence of disorder. Interestingly, the superconducting gap remains a hard gap when disorder is increased and, due to inhomogeneities, superconducting puddles appears. Starting from this numerical result, the authors used a quantum XY model with which they further showed that, due to phase fluctuations, an insulating state can emerge even in the presence of local superconductivity. The authors therefore predict localized Cooper pairs in the insulator even if the disorder only affects the fermionic part of the Hamiltonian. The destruction of superconductivity however has been treated by assuming the initial existence of Cooper pairs and by using a quantum XY model.

Further investigations by Bouadim et al. and using the same Hamiltonian, but treating it with Quantum Monte Carlo techniques, confirmed this result [Bouadim et al., 2011]. However, contrary to what had been done by Ghosal, quantum fluctuations were already included in the treatment of the model and the authors did not need the addition of the quantum XY model to explain the transition. Figure 1.28 summarizes the main results of the paper. As phase fluctuations increase by adding disorder (represented here by V), the superconducting critical temperature T_c vanishes and eventually goes to zero while the superconducting gap, depicted by the gap in the one particle density-of-states ω_{DOS}, remains finite and almost constant. To explain the origin of the insulating phase, the authors calculated the pair susceptibility $P(\omega)$, which amplitude corresponds to the energy necessary for inserting a pair at a energy ω. They showed that, in the insulator, this pair susceptibility presents a gap $2\omega_{pair}$ representing the distance on which pair transport is coherent (this distance is proportional to ω^{-1}_{pair}). Starting from the insulating side of the transition, ω^{-1}_{pair} is finite. As disorder increases, ω^{-1}_{pair} increases as the size of the superconducting islands. As disorder decreases further, ω^{-1}_{pair} eventually diverges at the Superconductor-Insulator Transition : the superconducting ground state is coherent over macroscopic distances.

These models gave rise to the concept of **"emergent granularity"**, even in the absence of any structural inhomogeneities. Due to many-body interactions, the position and size of the appearing superconducting puddles are uncorrelated with the initial disorder distribution in the

22. However, let us note that, in our system, the application of this theory has been found to give irrealistic parameters by [Crauste, 2010].

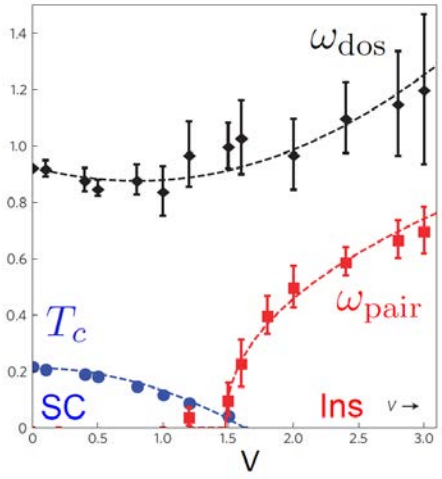

Figure 1.28: Evolution of the critical temperature T_c, the gap of the one particule density-of-states ω_{DOS}, and the two-particles energy scale ω_{pair} as a function of the disorder depicted by the parameter V [Bouadim et al., 2011].

sample. Therefore, even in a homogeneously disordered superconductor, one could in principle use the same arguments as for the destruction of global phase coherence in granular materials.

One of the predictions of these numerical models is a pseudogap superconducting phase which should appear at temperatures such that $T > T_c$ and in which $\omega_{DOS} \neq 0$, i.e. where Copper pairing survives above T_c.
Experimentally, local measurements of the tunnelling characteristics of thin films by Scanning Tunnelling Microscopy, which gives the superconducting gap with a spatial resolution usually less than 10 nm, tested the results of these numerical calculations. In several binary alloys, the superconducting gap has been found to be highly inhomogeneous in space (see figure 1.29). These experimental facts have been reported in several materials (InO_x [Sacépé et al., 2011], TiN [Sacépé et al., 2008]) and agree qualitatively with the results obtained by Trivedi's group. The pseudogap phase also has been observed in these materials. In this phase, it has been found that disorder can alter the measured tunnelling characteristics of the superconducting phase by suppressing the superconducting coherence peaks. This feature has been interpreted as the signature for the loss of global phase coherence in the system.

1.7.3.2.d Some experiment supporting the Bosonic picture

Transport Measurements
In a purely fermionic scenario, as superconductivity is destroyed, the insulator should be fermionic (with localized electrons). The first indication of a different behaviour has been measured by D. Shahar and Z. Ovadyahu in 2000 Å-thick a-InO_x films [Shahar and Ovadyahu, 1992]. To modify the film disorder, the authors used a thermal annealing procedure which modifies the oxygen content within the film. By measuring the resistivity of the films after several annealings, they found a direct Superconductor-to-Insulator Transition with nearest-neighbour hopping properties in the insulating state, close to the transition, i.e. with a resistivity given by $\rho(T) \propto exp(T_0/T)$. By extracting the critical temperature in the superconducting regime T_c and the activation energy T_0 in the insulating regime, they obtained the plot displayed figure 1.30. T_c does not reach zero when the insulating regime arises, which is an indication that superconductivity could survive within the insulator.

Magneto-Transport Measurements Using magneto-resistance measurements, it has been shown by Gantmakher [Gantmakher and Golubkov, 1996][Gantmakher et al., 2000] that a-InO_x exhibits a giant magnetoresistance in the insulating regime as shown figure 1.31. This phenomenon has been observed not only a-InO_x, but also in polycrystalline disordered materials like TiN [Baturina et al., 2007].
A mechanism which could explain this giant negative magnetoresistance has been exposed by Dubi et al. [Dubi et al., 2006]. They assume that the system is made out of superconducting islands of charging energy E_c placed in a normal fermionic matrix which resistance is only weakly

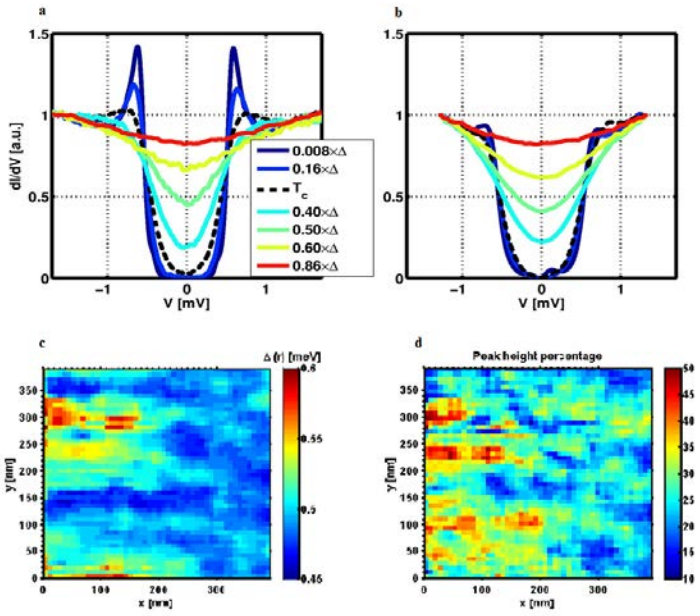

Figure 1.29: Evolution of the tunnelling gap for a low-disorder InO_x sample (a) and a more disordered sample (b) taken at different temperatures. For the low-disordered film, maps of the superconducting gap (c) and of the height of coherence peaks (d) taken in a 400 nm square with a spatial resolution around 8nm. [Sacépé et al., 2011][Sacépé, 2011].

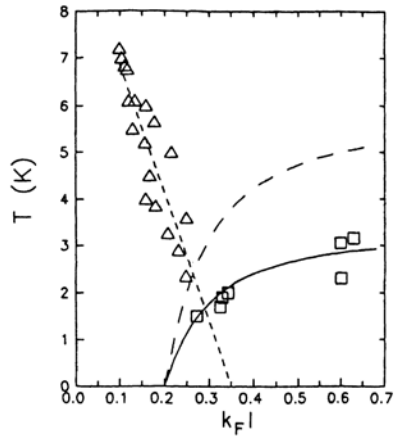

Figure 1.30: Dependence of the critical temperature T_c (squares) and of the activation energy T_0 (triangles) as a function of $k_F l$. Source : [Shahar and Ovadyahu, 1992].

affected by magnetic field. At zero magnetic field, the island density is such that they percolate through the sample and the system is superconducting. At small magnetic field, the density of superconducting islands decreases and above the critical field for the SIT, B_c, the percolation threshold is not attained and the system ground state becomes insulating. Then, an increase in B localizes Cooper pairs in smaller and smaller islands, thus increasing the overall resistance. At the field corresponding to the maximum of the magnetoresistance B_{max}, the density of superconducting islands and their increased charging energy are such that transport through the normal matrix is favored. In other words, Cooper pairs start to unbind and participate to the electric conduction. The resistance then progressively decreases. For fields such that $B_c < B < B_{max}$, Cooper pairs exist within the insulating phase. For fields such that $B > B_{max}$, the insulator is mostly fermionic.

These measurements have been taken as a proof in favor of a bosonic mechanism for the destruction of superconductivity.

An interesting experiment performed in the team of J. Valles on Bi films quench-condensed onto a patterned substrate, thus forcing the formation of superconducting puddles coupled by weak links, shows the same magnetoresistance behavior, enforcing the argument that this phenomenon

is a signature of a bosonic insulator [Stewart et al., 2007].

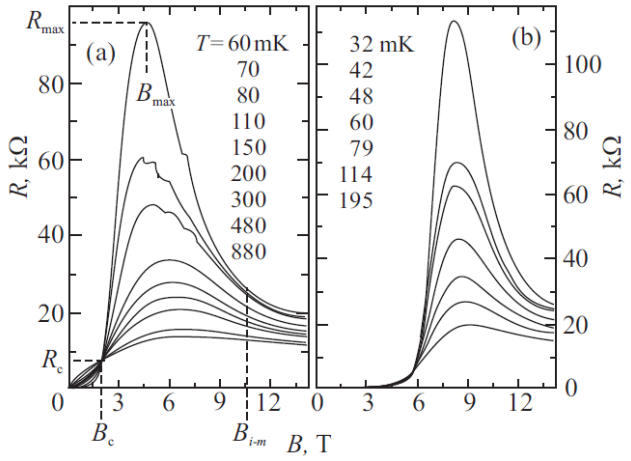

Figure 1.31: Measurement of the sheet resistance of a 200 Å InO_x film at different temperatures and as a function of the applied magnetic field (a) perpendicular (b) parallel to the film [Gantmakher et al., 2000].

1.7.3.3 A link between the bosonic and fermionic pictures ?

Until now, we have detailed different models for the SIT dependent either on a bosonic or on a fermionic mechanism for the destruction of superconductivity. The bosonic mechanism usually describes systems which are inhomogeneous or present granularity (at least electronically), and for which superconducting grains exist and are connected through weak links. Fermionic scenarii have been developed in the specific case of a system homogeneous at all scales where superconductivity is uniformly destroyed. However, a description detailed by Skvortsov et al. shows that the limit between these two descriptions is not as well defined as it seems to be.

Indeed, in 2005, Skvortsov discussed the fact that Finkel'stein's fermionic model may give rise to a bosonic-like scenario near the transition [Skvortsov and Feigel'man, 2005]. The system then is fermionic at low disorder and becomes bosonic as the system is driven close to the SIT due to mesoscopic fluctuations of the order parameter.

What is the origin of these fluctuations ? We have already discussed the fact that, due to electron scattering by impurities, weak localization can occur. Weak localization in a metal, as discussed in by Altshuler [Altshuler, 1985], gives rise to macroscopic fluctuations of the electronic wave function. Spivak pointed out that in the case of Cooper pairs, a similar mechanism should occur. These fluctuations should give rise to a spatial distribution of the superconducting gap $\Delta(r)$, engendering droplets of superconductor in the material, nucleating above T_c. Said differently, due to quantum phenomena, the system can be locally superconducting without the macroscopic establishment of superconductivity and **a Fermionic model** like Finkelstein's will **give rise to a granular-like system**, at least on the superconducting side of the transition, when the system is sufficiently disordered.

In a clean metal, the amplitude of this phenomenon is small since there are few scattering centers. As disorder in increased, it becomes more and more relevant and gives rise to a broadening of the superconducting transition. Skvortsov showed that the concentration of these superconducting droplets varies as :

$$P \sim exp(-\frac{1}{\delta_d}\frac{T-T_c}{T_c}) \tag{1.68}$$

When P increases, the droplets eventually percolate and the system become truly superconducting. In this equation δ_d correspond to the width of the superconducting transition due to mesoscopic fluctuations. It is given by :

$$\delta_d = \frac{0.4}{g(g-g_c)} \tag{1.69}$$

where g is the dimensionless conductance and g_c is the critical conductance at the transition. As one approaches the transition δ_d becomes increasingly important . Therefore, there is a crossover between a transition dominated by classical superconducting fluctuations and one dominated by quantum fluctuations as pictured figure 1.32.

One can wonder if, really close to the transition, δ_d truly diverges. Indeed, close to the SIT, $g \sim g_c$ leads to $\delta_d \to \infty$ and therefore to a finite resistance for $T = 0$, describing a quantum metallic state driven by mesoscopic fluctuations so that the SIT never effectively takes place. However, the described mechanism has been developed in a perturbative way and should stand only for $\delta_d < 1$. Otherwise, fluctuations become too strong and another theory should be developed [Skvortsov, 2015].

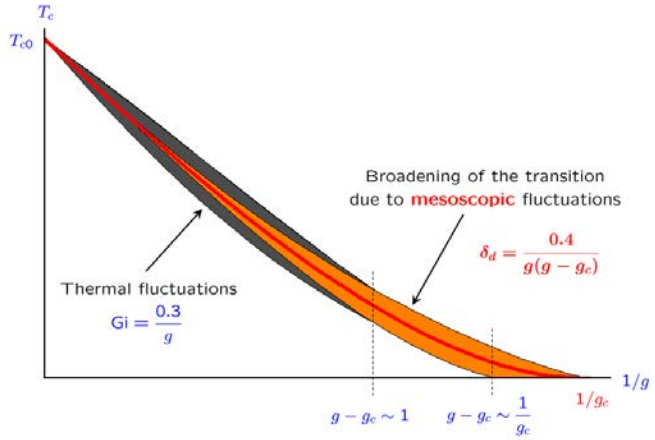

Figure 1.32: Broadening of the superconducting transition due to thermal fluctuations (grey) and mesoscopic fluctuations (orange). A crossover between a thermally activated broadening and a broadening due to mesoscopic fluctuations occurs when the dimensionless quantity $g - g_c \sim 1$. The red line corresponds to Finkelstein's evolution of the destruction of superconductivity by Coulomb interactions as disorder is increased [Skvortsov, 2008].

1.7.3.4 Possible metallic states

As we have seen, the study of the Superconductor-to-Insulator Transition is mainly standing on the paradigm that a 2D metal should not exist. However, some experimental evidences, supported by recent theories, are pointing toward a more complex scenario.

1.7.3.4.a Experimental evidence

As early as 1986, early studies have, from the outset, shown unexpected "metallic" behaviours in 2D films, with states having a saturation of the resistivity at low temperature [Jaeger et al., 1986]. These seemed to appear on both sides of the transition as can be observe figure 1.33 and have been found in various ultra-thin granular films such Ga, In, Pb and Al in the absence of any external magnetic field.

Due to the theoretical "ban" on 2D metals, these measurements have been for a long time considered as artefacts and thus discarded. It seems that it is only since the measurement of metallic states in 2D semiconductor heterostructures (see discussion in section 1.4.3) that theoretical and experimental efforts to measure and test the properties of such metals have found some support.

Under a magnetic field, the existence of such states has been found in MoGe by Mason and Kapitulnik in 1999 (see figure 1.34). At non-zero magnetic field, the authors indeed found that the metallic ground state does not only exist as a single point in the phase diagram - as expected from the Dirty Boson Model for instance - but corresponds to a completely distinct phase [Mason and Kapitulnik, 1999, A. Kapitulnik and Chakravarty, 2001], calling for a theoretical model to explain this discrepancy to existing theories of the Superconductor-to-Insulator

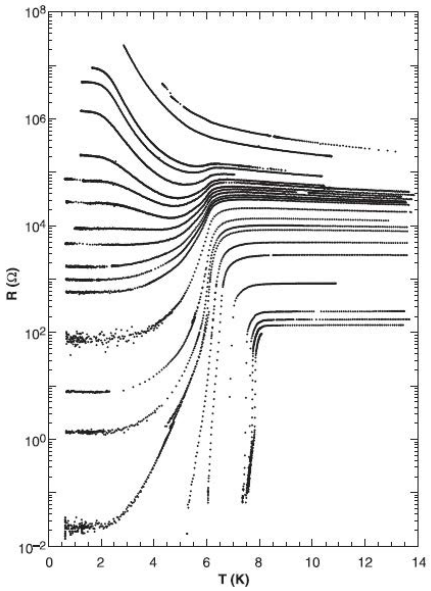

Figure 1.33: Evolution of the resistance of a series of Ga films of different thicknesses ranging from 12.75 to 26.67 Å by increments of 0.05 Å [Christiansen et al., 2002].

Transition.

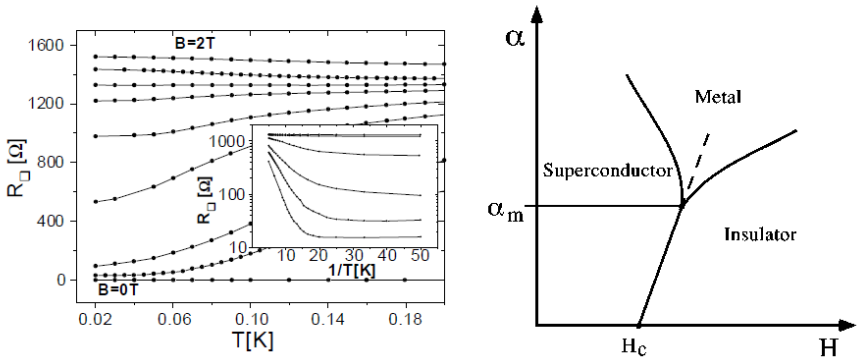

Figure 1.34: a. Resistance versus temperature characteristics of a 30 Å-thick $Mo_{0.43}Ge_{0.57}$ film at different magnetic fields, with $B = 0 - 2T$. The inset represents Log(R) versus 1/T. b. Proposition of a phase diagram for the field-tuned SIT at finite disorder. α represents the dissipation strength. From [Mason and Kapitulnik, 1999, A. Kapitulnik and Chakravarty, 2001].

One of the early pictures dealing with the existence of such metals, is to imagine that there are superconducting puddles coupled with each other through metallic weak links, made out of the normal state material itself. This hypothesis, represented figure 1.35, has been first used by Feigelman and Larkin [Feigel'man and Larkin, 1998] to explain the existence of a 2D bosonic metal. It has been re-visited by Spivak [Spivak et al., 2001] who imagined a network of superconducting islands of radius $R < \xi$, ξ being the coherence length which, due to diffusion is given by :

$$\xi(T = 0) = min[v_F/\Delta_0; (D/\Delta_0)^{1/2}] \tag{1.70}$$

where Δ_0 is the zero-temperature value of the gap in the bulk superconductor. By considering that the system is 2D ($d_\perp << \xi(T = 0)$), the author demonstrated that there is a zero temperature quantum Superconductor-to-Normal metal phase transition, the apparition of the metal being driven by fluctuations of the superconducting gap Δ. The origin of these fluctuations could be mesoscopic fluctuations of the order parameter (as discussed in section 1.7.3.3).

This result has been reproduced experimentally by different teams either by using a patterned network of superconducting islands onto a metallic layer [Eley et al., 2012], or by using graphene as a substrate for superconducting islands [Han et al., 2014]. In the second experiment

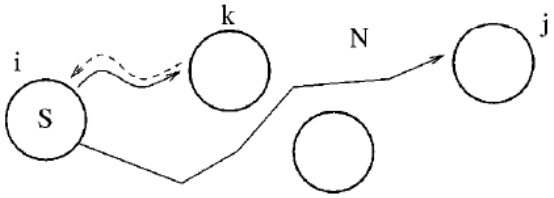

Figure 1.35: Superconducting grains embedded into a normal metal. Source : [Spivak et al., 2001].

(see figure 1.36), the coupling between the islands is controlled by tuning the conductivity of the substrate. For a conducting substrate, the system is superconducting. In the case of a less conducting substrate, the system becomes metallic.

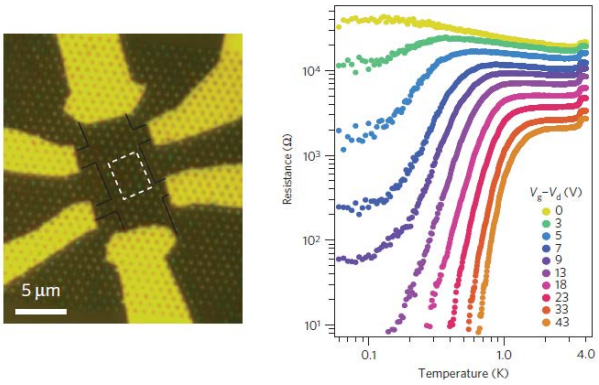

Figure 1.36: (On the left) Optical micrograph of the sample. The substrate in made of graphene with tin islands patterned on top of it. (On the right) Sheet resistance of the system as a function of the gate voltage. Source : [Han et al., 2014].

1.7.3.4.b Fermionic theories of 2D metals

As we have seen in section 1.4.3, 2D metallic states can arise from the competition between disorder and Coulomb interactions and could well serve as a basis for explaining the dissipative states observed in the vicinity of the SIT. These would then be fermionic.
In addition to those theoretical developments, let us mention that mesoscopic fluctuations could also engender a 2D metal. As we have seen section 1.7.3.3, mesoscopic fluctuations could well be important when superconductivity is destroyed. In this framework, Feigel'man and Skvortsov have calculated the density-of-states, starting from the superconducting phase. They have found that the BCS peak in the density-of-states is progressively smeared as the transition is approached, with possible appearance of subgap tail states [Feigel'man and Skvortsov, 2012] (figure 1.37). The energy width of these states, characterized by Γ_{tail}, widens near the transition. Mesoscopic fluctuations could therefore induce a metallic state which would then be fermionic.

1.7.3.4.c Bosonic theories of 2D metals

Other theoretical models have predicted the existence of a homogeneous Bose metal. This is the case, for instance, of the model developed by Das and Doniach [Das and Doniach, 1999]. In their 1999 paper, the two authors consider the Superconductor-to-Insulator Transition as bosonic. From this starting point, they point out that the superconducting phase presents a phase ordering whereas the insulating phase presents a charge ordering. These two order parameters have, a priori, no reason to change simultaneously. The SIT could then be composed of two distinct quantum phase transitions : the Superconductor-to-Metal Transition would correspond to the loss of phase ordering and the Metal-to-Insulator Transition would correspond to the emergence of charge ordering. In this scenario, the metallic phase would then be a homogeneous phase where uncondensed vortices, which would also be unbound into vortex-antivortex pairs, would be free

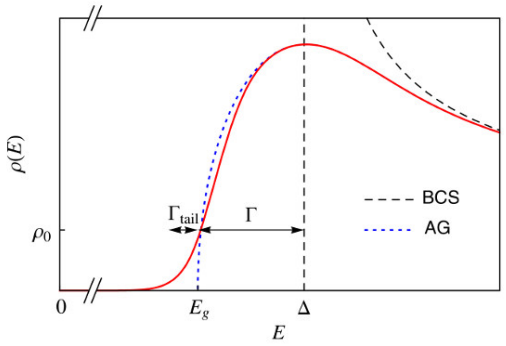

Figure 1.37: Schematic representation of the density-of-states in a disordered superconductor [Feigel'man and Skvortsov, 2012].

to move and create dissipation, even at zero magnetic field, and hence form a metallic phase. This ground state, which persists even at T=0, is then characterized by a zero-temperature sheet resistance $R_\square$ varying as:

$$R_\square \sim R_Q \left(\frac{R_n}{R_c} - 1 \right)^{2\nu} \tag{1.71}$$

where R_n is the normal state resistance, $R_Q = \frac{h}{4e^2}$ the quantum of resistance for Cooper pairs, R_c is the critical resistance at the Superconductor-to-Metal Transition, and ν is the critical exponent for the correlation length predicted to be of the order of 2/3. This model yields reasonable agreement with some experimental data [Das and Doniach, 1999, Marrache-Kikuchi, 2006], as shown figure 1.38.

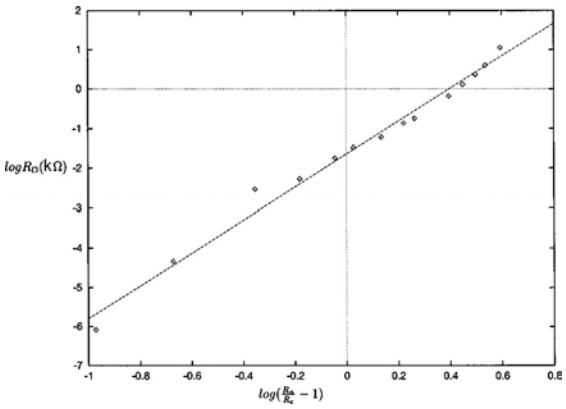

Figure 1.38: Zero-temperature resistance as a function of the normal state resistance in Ga thin films [Jaeger et al., 1986, Das and Doniach, 1999].

Another model based on bosonic phases has been developed by Phillips and Dalidovich [Phillips and Dalidovich, 2003, Dalidovich and Phillips, 2002]. They considered an array of superconducting islands with fixed on-site energies but random Josephson coupling, both positive and negative to take into account exchange effects arising from the hopping of a Cooper pair through a localized impurity [Spivak and Kivelson, 1991]. They showed that the randomness in the Josephson coupling combined with quantum fluctuations gave rise to a phase glass, in which the phase of the superconducting order parameter has a glassy behavior. The dissipation is then self-generated by the glassy environment and the corresponding phase is metallic. The predicted behavior for the thickness-tuned transition then is :

$$R_\square \propto R_c \left(d_\perp - d_{\perp,c} \right)^{2\nu z} \tag{1.72}$$

where R_c is the critical resistance at the Superconductor-to-Metal Transition, $d_{\perp,c}$ is the critical thickness, ν is the critical exponent for the correlation length and z the dynamical critical exponent. The theoretical predictions have been tested in the case of a-Nb_xSi_{1-x} films but fail to explain the experimental results [Marrache-Kikuchi, 2006].

1.8 Conclusion

In this chapter, we have introduced the disorder-induced Metal-to-Insulator (MIT) and Superconductor-to-Insulator (SIT) Transitions. We have shown how these Quantum Phase Transitions could emerge from the competition between disorder-induced localization, Coulomb interactions and superconductivity. In 3D, we have seen that both transitions are possible, whereas 2D metallic phases are prohibited by standard theories, so that the SIT is believed to be a direct transition.

However, the recent observations of theoretically unpredicted 2D metallic states challenge this conventional picture of the SIT and have encouraged a more thorough investigation of the phenomena at play, from both a theoretical and an experimental point of view.

In the following chapters, we will present how we have tried to contribute to this effort by investigating precisely these new metallic states, their emergence and destruction, in a model disordered system.

Chapter 2

Low frequency transport properties of Nb_xSi_{1-x}

2.1 Introduction

In this chapter, we will concentrate ourselves on the low frequency transport properties of amorphous Nb_xSi_{1-x} films (a-Nb_xSi_{1-x}). This alloy, studied in our group for several years, is a model system to study the effects of disorder on thin films - and especially the Superconductor-to-Insulator Transition - thanks to the different experimentally accessible control parameters : the thickness $d_\perp$, the composition x, and the heat treatment temperature θ which, as we will see, allows to finely tune the disorder without modifying the morphology of the film.

In section 2.2, we will detail the measurement apparatus and how our films are grown. We will then, in section 2.3, sum up the results obtained in our group on a-Nb_xSi_{1-x} films. We will especially detail how disorder can be modified and the effects of the different tuning parameters. For films in the 2D limit, we will review results on the emergence two different unconventional metallic ground states (M1 and M2) which have been recently found in this system.

2.2 Sample fabrication and measurements

2.2.1 Sample fabrication

Different techniques are available to grow samples. In the framework of this thesis, all samples have been synthesized in the laboratory by conventional evaporation techniques. This section will detail how they have been grown as well as their design.

2.2.1.1 Evaporators

2.2.1.1.a Principle of evaporation techniques

The basis of the deposition technique is that all materials can be evaporated if they are heated up at high enough temperature. This process, coupled with high vacuum techniques, permits to create a gas of atoms travelling without collision towards a substrate on which they will condense. The key ingredient is to heat the material at the evaporation temperature while preventing, via pumping and careful design and operation, any degassing which automatically occurs as the deposition chamber is heated and might contaminate the sample during its growth.

Two different deposition methods are used in the laboratory, depending on the material to evaporate.
The first method is using **Joule effect** : a high intensity current flows through a resistor, or the crucible itself, to heat up the material positioned inside. We will refer to this technique as Joule effect evaporation.
Another method is to bombard the target with highly energetic electrons. These electrons, extracted from a tungsten wire by an intense electric field, are guided and collimated onto a small spot of the material. The heating is obtained by the kinetic energy released by the electrons when they arrive in contact with the material. We will refer to this technique as **e-beam deposition**. This last technique has the advantage of heating the material locally which permits to reach a

higher power and hence to evaporate the material while limiting its degassing. In addition, only part of the surface of the pellet melts while the bulk remains solid. This reduces the contamination that might come from the crucible itself.

For our films, all materials are grown by e-beam deposition except for SiO, which is grown by Joule effect evaporation.

2.2.1.1.b Co-deposition process for a-Nb_xSi_{1-x}

In order to finely tune the composition x of Nb_xSi_{1-x}, we are using a co-deposition process. It consists in the simultaneous evaporation of Niobium and Silicon onto the substrate as represented figure 2.1.

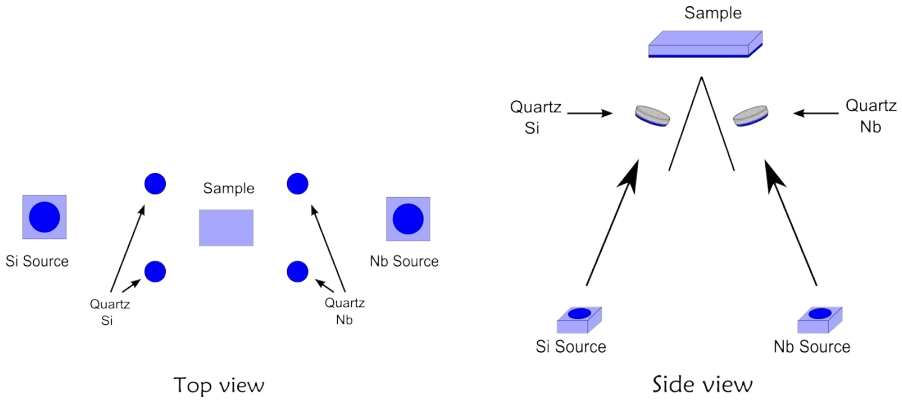

Figure 2.1: Schematic representation of the co-deposition process.

Dedicated pairs of quartz - one pair for each source - allow the control of the proportion of each compound evaporated. These pairs are separated by a blanker to avoid mixing the readouts of evaporation rates from each source. Furthermore, the evaporation is never totally isotropic and using two quartz for a single element permits to correct the anisotropic effect and to monitor more precisely the deposition rate. The composition x is determined by the relative evaporation rate of the Nb and Si sources, whereas the sample thickness d is given by the deposition time at steady rate of deposition.

Note that it would have been more complicated to have reproducible results by evaporating an ingot of Nb_xSi_{1-x} of a given composition because of distillation effect. In comparison, co-deposition enables a high reproducibility and a greater control of the composition.

A question can arise on the rate at which impurities from the residual gas can contaminate the sample. One can show that this rate, in molecules/s, is equal to $\phi = \chi SP\sqrt{\frac{1}{2\pi m k_B T}}$ where χ is the probability for an incoming molecule to stay attached to the sample, S is the surface of the sample, P is the pressure inside the evaporator, m is the mass of the incoming molecule and T is the sample temperature. Taking the maximum value χ=1, a vacuum level of 10^{-7} mbar and the characteristics of O_2, this formula gives a rate of incoming impurities equivalent to 0.03 monolayer/s. This hypothetical value is highly overestimated since it supposes that all the incoming impurities would stick on the sample. It has to be compared to the evaporation rate which is of the order of 1.5 Å/s, corresponding to $\sim$ 0.3 monolayer/s. It gives us a maximum - and improbable - impurity content of 10% in thickness. Taking more reasonable values of the sticking coefficient of Oxygen of $\chi_{Nb} = 0.75$ on Nb [Dawson and Tam, 1979] and $\chi_{Si} = 3.10^{-4}$ on Si [Kim et al., 1998], this value drops to $\sim$ 1% in thickness for a $Nb_{13.5}Si_{86.5}$ film by supposing that the residual gas is composed only of Oxygen. Since previous studies on a-NbSi films have shown no correlation between the deposition pressure and the film electrical behaviour, we believe that the impurities deposited within the film are scarce and anyhow do not have a major effect on the transport properties which we are studying.

A drawback of the co-deposition process is linked to **shadow effect** : since the sources are not at the same point in space, the deposition area defined by the shadow mask is not exactly the

same for each source. This can engender edge effects : a superconducting path can be created on the edge of the sample and bypass the measurement of the sample. A specific shape for the sample has been developed in order to prevent these effects as we will see later.

Another drawback of this deposition method is the intrinsic **gradient in composition** that exists along the axis of the sources. We have previously estimated this gradient to be of less than 0.2% in composition [Marrache-Kikuchi, 2006]. It can be corrected by a rotation of the substrate during the evaporation but its effect on transport properties is negligible, as we will see. We will therefore consider the composition of Nb_xSi_{1-x} to be homogeneous along the sample.

2.2.1.2 Sample fabrication

The samples are made thanks to two different evaporators. One is dedicated to the contact pads and the other one to the co-deposition of Nb_xSi_{1-x}. Each evaporator contains a mask changer in order to be able to deposit through various mechanical shadow mask patterns without breaking the vaccum and contaminating the sample. All depositions are performed under ultra-high vacuum (P $\sim 10^{-8}$ mbar). During the evaporation process, the pressure in the deposition chamber is usually of a few 10^{-7} mbar due to degassing. We have seen in the previous paragraph that this pressure is compatible with an acceptable impurity concentration and therefore is not prejudicial for the measured electrical properties.

The schematic representation of the overall sample is given figure 2.2. The sawtooth shape of the sample has been designed to prevent edge effects. Indeed, if one edge is superconducting due to shadow effect, the superconducting path is necessarily interrupted by the neighbouring insulating edge. Moreover the 6 electrodes enable us to measure different film geometries to cross-check their size dependence.

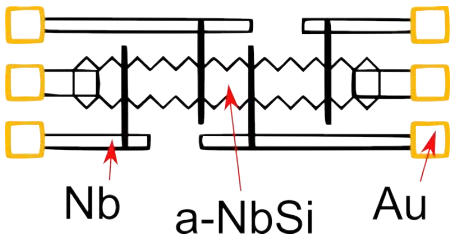

Figure 2.2: Sample design. The film is made of a-Nb_xSi_{1-x} and contacted with Nb electrodes. The wiring to the measurement apparatus is made by bonding on the Au pads.

The first step is to deposit a 12 nm-thick amorphous layer of **SiO** onto a 20x30 mm^2 sapphire substrate by a Joule effect evaporation. This **under-layer** enables to smooth all substrate defects.
We evaporate the electrodes in three steps :

1. deposition of **Gold** ($\sim$ 200 nm thick) with a $\sim$ 2 nm Chromium under-layer with a first shadow mask to delimit the **pads used for wire bonding**. The under-layer is used to increase the adherence of Gold onto the substrate. Gold is used to facilitate the wire bonding. However, due to the easy migration of this element within Nb_xSi_{1-x}, it cannot be put in direct contact with the film. We therefore have to use Nb electrodes to connect the gold bonding pads to the film.
2. deposition of $\sim$ 50 nm of **Niobium** with a second mask to delimit the **electrodes** which will contact the sample.
3. deposition of $\sim$ 2 nm of Iridium on top of the Niobium to protect the electrodes from oxidation.

The corresponding masks are presented figure 2.3 (a. and b. for step 2., c. for step 3).

The substrate is then removed from the first evaporator and inserted in the co-deposition chamber of the evaporator dedicated to NbSi. We co-deposit the $\mathbf{Nb_xSi_{1-x}}$ by e-beam deposition at the rate of $\sim$ 1.5 Å/s through the mask presented figure 2.3 (c). The composition is computer-monitored in order to ensure the composition reliability during the evaporation.
Finally the film is **capped** by $\sim$ 12 nm of **SiO** deposited by Joule effect evaporation to protect

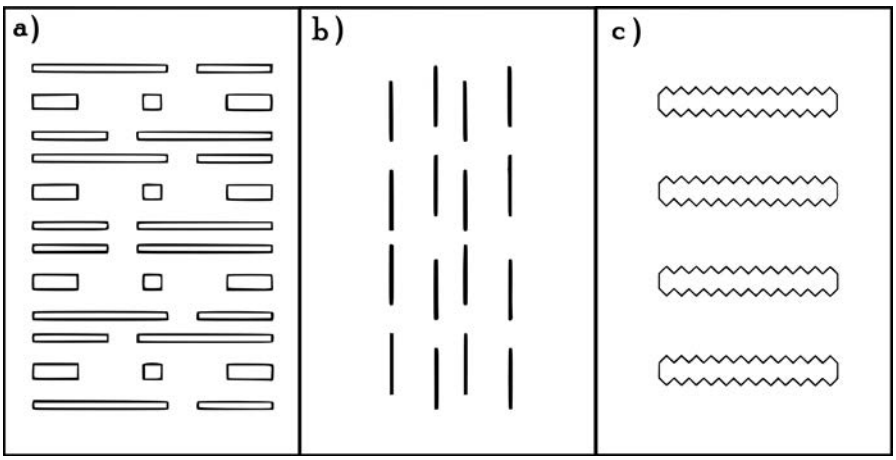

Figure 2.3: Design of the evaporation masks for : (a) and (b) the Niobium contacts (c) the film of interest. The gold pads are not represented. The assembled pattern is seen figure 2.2. The masks are designed for a 20x30 mm^2 substrate onto which 4 different samples are deposited.

the film against oxidation. Taking this care is especially important in the case of very thin films. Indeed, the native oxide layer forming at the surface of a-Nb_xSi_{1-x} films can be estimated to be of a few nm. Since this is the typical thickness of our samples, we must prevent this oxide layer from forming.

2.2.1.3 Heat Treatment Procedure

One of the specificities of the present work is the use of a **heat treatment** to finely tune the disorder level within a single sample of Nb_xSi_{1-x}. The physical mechanisms behind this phenomenon will be detailed in section 2.3.2.2. This procedure is the same for all our samples dedicated to electronic transport measurements.

To do so, we use a dedicated oven which heats the sample under a steady N_2 flow. This is an additional protection against any spurious oxidation during the process, although the sample is already protected by a SiO overlayer.

This procedure is divided into different steps as follows :

1. The temperature is progressively increased from room temperature to the heat treatment temperature θ during 1 hour.
2. The temperature is maintained at the heat treatment temperature θ for 1 hour.
3. The temperature is set to decrease down to room temperature during 1 hour.

These durations have been chosen to be long enough in order to permit the stabilization of the electronic modification. Indeed, previous work [Lesueur et al., 1985] on a similar amorphous system has shown that, during heat treatment, the change in the sample resistivity was negligible after few minutes.

2.2.2 Cryogenics

In this section, we will detail the cryogenic apparatus used for performing our measurements.

2.2.2.1 Dilution refrigerator

The a-Nb_xSi_{1-x} samples measured during this thesis have all been measured in the cryostat presented figure 2.4. This dilution refrigerator allows to continuously measure samples down to 7 mK.

In order to reach these temperatures, one uses the dilution properties of a mixture of $^3He/^4He$ in a close cycle. The working principle of a dilution unit is schematically presented figure 2.5. It

Figure 2.4: Picture of the dilution refrigerator used in this work.

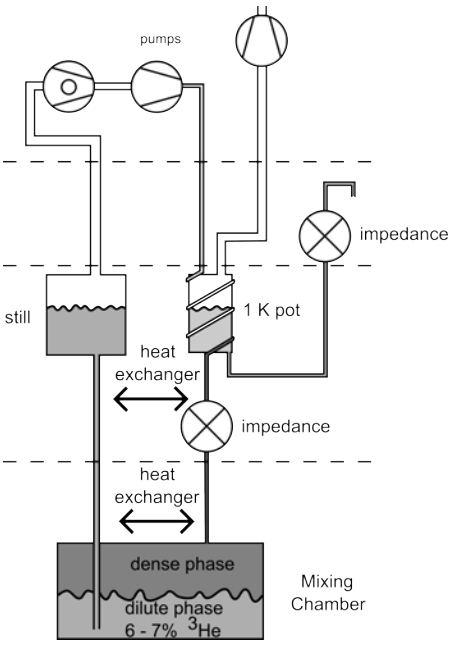

Figure 2.5: Schematic representation of the working principle of the dilution refrigerator.

can be described as follows : a first cooling of the mixture is achieved thanks to a 1 K pot and a Joule-Thomson cooler. A dissociation of the mixture into a phase rich in ^{4}He and a phase rich in ^{3}He occurs in the mixing chamber at temperatures lower than 800 mK. As we pump on the ^{4}He-rich phase through the still, ^{3}He evaporates first since its vapour pressure is lower than the one of ^{4}He. The ^{4}He-rich phase is therefore depleted of its ^{3}He. In order to stay at thermodynamic equilibrium, ^{3}He atoms migrate at the interface between the two phases, resulting in an enthalpy absorption in the mixing chamber. During all these processes, the cooling power from the evaporated ^{3}He is recycled using heat exchangers. The closed circuitry permits to re-use the mixture indefinitely.

An extension of the lower temperature part of the cryostat - i.e. the mixing chamber - has been fabricated in order to lodge the sample holder. Both the sample holder and the mixing chamber extensions are made out of oxygen-free copper and all the different parts are tightly screwed to one another in order to minimize the thermal gradient between the mixing chamber and the sample.

The sample is fixed onto the sample holder by mechanical springs and vacuum grease for good thermal anchoring as seen figure 2.6. The sample gold contact pads are then wire-bonded to the sample holder contact pads.

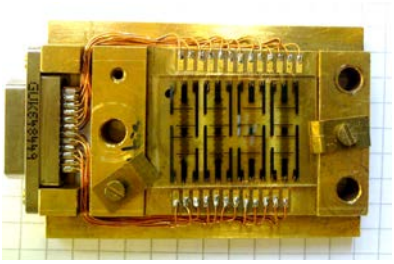

Figure 2.6: Sample attached and electrically connected on the sample holder via gold bonding wires.

2.2.2.2 Thermometry

This work on the measurement of electronic transport properties to study Quantum Phase Transitions is highly dependent on the precision of the temperature readout. This is why **special care has been taken regarding the precision of the thermometry**.

To measure the temperature of the sample, two thermometers are located near the sample holder :
- a RuO_2 thermometer, measuring from 300 K down to 50 mK.
- a Carbon Glass (CG) thermometer, measuring from 100 mK down to 7 mK.

Each of them is encapsulated into a copper shield and is carefully thermally anchored to the mixing chamber.

These thermometers have repeatedly been calibrated by four different means depending on the temperature range :
- down to 4 K, they have been compared to a calibrated commercial Cernox thermometer.
- down to 20 mK, they have been compared to a known RuO_2 thermometer.
- for temperatures from 1.2 K and down to 15 mK, they have been calibrated via the SRD-1000 calibration set [1], which uses transition temperatures of known superconductors.
- for temperatures lower than 20 mK, nuclear orientation measurements have been performed. It consists in the measurement of the anisotropy of the γ radiation of a ^{60}Co source. The degree of anisotropy gives a primary measurement of the temperature.

All calibrations coincided within experimental uncertainty and no evolution in time has been found in the CG and RuO_2 thermometer characteristics.

2.2.3 Measurement Techniques

We describe here how the low-frequency electronic transport measurements have been carried out. Depending on the impedance of the sample, different measurement set-ups have been used.

2.2.3.1 Low-frequency AC technique

To measure samples with **resistances lower than 1 MΩ**, we use a dedicated **low noise TRMC2© resistor bridge**. This device has been specially developed at the Néel Institute (Grenoble) for low temperature and low power measurements. It provides a square wave signal at 25 Hz and is capable - in theory - of measuring resistances up to a few MΩ at 10 mK. This is possible thanks to a low-noise pre-amplifier stage positioned directly at the head of the cryostat. This stage, thanks to an electro-mechanical switch, permits to scan alternatively four different samples in a single cool-down while performing four-probes measurements.

For **impedances lower than a few hundred Ohms**, it is possible to verify the obtained value of resistances with **conventional lock-in techniques**.

1. http://hdleiden.home.xs4all.nl/srd1000/ for more information on this calibration device.

However, both techniques, TRMC2 or lock-in, cannot access the higher impedance range. Indeed, at very low temperature, the maximum electrical power that is acceptable for measuring the sample without heating it up is of the order of $P_{elec} = RI^2 = \frac{V^2}{R} \sim 10^{-17}W$ due to electron-phonon coupling. The minimum current the TRMC2 is able to provide is 10 pA, thus giving $P_{elec} \sim RI^2 = 10^{-17}W$ for 1 MΩ. Moreover the lock-in amplifiers we are using have a noise level of 10^{-14} A/$\sqrt{Hz}$ at 100 Hz and 10^{-13} A/$\sqrt{Hz}$ at 1 kHz [2]. By taking the lowest value on a 10 MΩ resistor (corresponding to the input impedance) and by using a bandwidth of 1 MHz, it corresponds to an electrical power of $P_{elec} \sim 10^{-15}$ W. For high impedance resistances another measurement setup has therefore been used.

2.2.3.2 DC technique

For the more insulating samples, a setup using a battery as voltage source allows us to measure in the resistance range from 300 kΩ to several GΩ, limited by the input-impedance of the instruments. The use of a battery allows us to reduce the noise due to the electrical source. The setup is presented figure 2.7. The voltage across the sample is first roughly set by R_p and finely tuned with the ten turn potentiometer R_{pot}. The voltage across the sample is first amplified with a low noise SR560 pre-amplifier and then measured with a Keithley K2000 multimeter. The current flowing through the sample is measured with a Keithley K617 ammeter. Since $R_{pot} + R_p << R_{sample} + R_1$, R_1 being a resistor in series with the sample which can be used to increase the impedance of the circuit if needed, the **voltage across the sample is almost constant**. This is convenient for the measurement of highly resistive samples at low temperatures.

Rigorously, this setup is a two probes measurement so that the impedance of the lines and polarisation resistance should be taken into account. However, the resistance of the cables, of the order of few tens of kΩ, is negligible in this range of sample resistance.

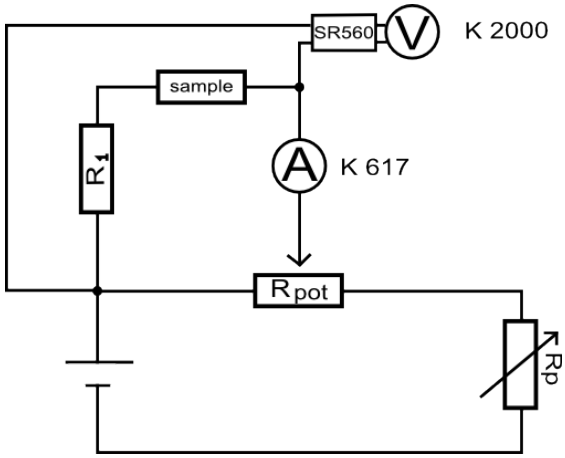

Figure 2.7: Fixed DC voltage measurement technique.

2.2.3.3 Protection against parasitic power

Parasitic power at low temperature can distort the measurements. Indeed, any spurious power source (IR radiation, electrical noise, mechanical vibrations, ..) can heat up the incoming electrons which flow through the sample during the measurements. If the corresponding power is large enough, it can induce an uncontrolled thermal decoupling between the electrons and the sample lattice, thus affecting the measurement. This part explains the measures taken to avoid such problems.

1. **Thermal coupling**
   In order to avoid spurious heating, incoming electric wires are tightly thermally anchored at 4 K, 100 mK and 10 mK. Thus, the electrons injected in the sample for measurement are correctly thermalized.

2. Value for the sr830 lock-in amplifier.

2. **Protection against IR radiation**
   The electric cable duct is a possible wave guides for photons. By breaking the continuity of the insulator, thermal anchoring allows to break these wave guides which may contribute to the introduction of IR photons at low temperature. In addition, the inside of the 1 K shield is covered with anti-IR Nextel paint in order to absorb any remaining photon that might enter this volume.

3. **Filtering of the lines**
   The cabling of the cryostat, via the anchoring points, creates a natural RC filter distributed all along the cables. One can demonstrate that the capacitance of a coaxial cable is $C = \frac{56\epsilon_d}{Ln_{10}(D/d)} = \frac{3326\sqrt{\epsilon_d}}{Z_c}$ in pF/m with ϵ_d the relative permittivity of the dielectric (2.1 for PTFE) and Z_c the characteristic impedance of the cable (here 50 Ω). Therefore, the capacitance is of the order of 200 pF for 2 meters of coaxial cables. Taking into account the resistivity of the cable of the order of 100 Ω, one find a natural RC filter with a cut-off frequency of 10 MHz. In addition to this natural filtering, passive low-pass filters are introduced on all electric lines:
   – All lines dedicated to thermometry are filtered with Pi-filters.
   – All lines dedicated to the sample measurement are filtered at room temperature. However the kind of filtering varies depending on the use of the AC or DC techniques mentioned above. Indeed, for AC measurements, lines are filtered by the 2^{nd} order low-pass filter presented figure 2.8. This filter has a cut-off frequency around 1 MHz, high enough to let the square-wave signal provided by the TRMC2 unaltered. For DC measurements, a 1^{st} order RC filter with a cut-off frequency of 1 Hz has been used. The use of DC allows us to use a very low cut-off frequency, providing a more efficient filtering.

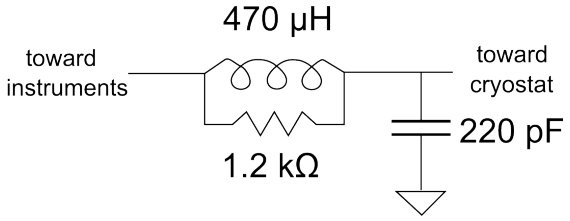

Figure 2.8: Filter used for low-frequency AC measurements.

4. **Vibrations**
   Vibrations can generate a parasitic power through tribo-electric effect or mechanical energy dissipation. To limit these sources of noise, the cryostat is sustained by springs to suppress vibrations. At the same time, a bellows hose links the cryostat to the pumps, so that the vibrations of the pumps are cut-off.

As we will see in section 3, we are therefore confident that our results cannot be explained by experimental artefacts, and in particular by a spurious heating of the electrons.

2.2.4 Sample homogeneity and morphological structure

As seen in the theoretical introduction to this work, sample morphology is an important characteristic which may determine the physical phenomena at play. a-Nb_xSi_{1-x} has previously been morphologically characterized [Crauste, 2010] by Atomic Force Microscopy (AFM), Transmission Electron Microscopy (TEM) and and Energy Filtered Transmission Electron Microscopy (EFTEM) techniques. The findings of the study will be summarized in this section.

In this work, we have also performed systematic measurements of the composition and thickness of the samples by **Rutherford Backscattering Spectrometry (RBS)**, which we will detail here.

2.2.4.1 Rutherford Backscattering Spectrometry

As previously mentioned, the composition and thickness of the films are controlled in situ by sets of piezoelectric quartz. To verify ex situ these important sample parameters, we have

performed Rutherford Backscattering Spectrometry (RBS) experiments at the CSNSM JANNuS-Orsay facility.

2.2.4.1.a Principle

RBS consists in accelerating light ions - commonly He^+ - by means of an accelerator and to send them onto the sample. As the ions encounter the sample atoms, they will be retro-diffused with an energy depending on the mass and atomic number of the encountered atom as well as on the ions incident energy. The retro-diffused ions energy is then measured by means of a Silicon PN junction. The obtained spectrum is an histogram of the number of out-coming ions with a specific energy.

Several informations can be extracted from the obtained spectrum :

- The peaks positions depend on both the depth and the mass of the atoms on which retro-diffusion occurs. The closer to the surface and the heavier the atoms on which retro diffusion occurs, the higher the energy of the out-coming ion.
- The peak area is proportional to the diffusion cross-section ($\propto Z^4$) and to the incident flux of ions and therefore gives information on the number of encountered atoms. Knowing the material density, it gives information on the deposited thickness.
- Information about the thickness can also be obtained from the peaks extension in energy. Indeed, the thicker the layer, the larger the peak width, as incident He ions will lose energy by penetrating into the sample.

The setup is calibrated :

i. in energy using known references : in our case Au, Al and Co films.

ii. in number of atoms using a sample of known density : in our case a Bi implanted target.

The calibration then allows us to identify the sample atoms, by giving the channel/energy correspondence, as well as the density of atoms encountered.

2.2.4.1.b Experiment

During each Nb_xSi_{1-x} deposition, a control sample is made for each film on a LiF or an a-C substrate. The samples are later measured ex-situ by RBS. These samples are not protected by a SiO over-layer since it would induce an excess of Silicon and complicate the interpretation of the obtained spectra.
The choice of the substrate, with atomic masses far from the ones of interest, enables a good resolution of the peaks of interest. This is why ^{6}C, ^{3}Li and ^{9}F are good candidates as substrates to measure ^{14}Si and ^{41}Nb by RBS.

A typical spectrum on a LiF substrate is presented figure 2.9 for a relatively thick (650 Å) a-$Nb_{13.5}Si_{86.5}$ sample [Crauste, 2010]. As can be seen, the Nb and Si peaks are well defined. The position of the peaks in energy allows us to identify the atoms present in the sample while the comparison of the area of the different peaks permits to determine the composition. The total area of the peaks permits to determine the sample thickness.

However, for films of smaller thicknesses, the spectra are slightly more difficult to interpret as can be seen figure 2.10 where the spectrum of a 45 Å-thick $Nb_{13.5}Si_{86.5}$ sample is presented. On this spectrum, we can see both the contribution of the substrate and of the Nb_xSi_{1-x} film. We can note that the substrate contribution is large compared to that of the film. This is mainly due to the small sample thickness. However, by performing an integration on the peaks, one can find the sample relative composition in Nb and Si as well as its thickness.

We have also checked the composition of the sample by simulating the spectrum with the software SIMNRA©. This has been performed as shown figure 2.11. The simulation parameters are in agreement with the values obtained through the integration method.

For all our films, the composition and thickness measured by RBS were, within experimental uncertainty ($\Delta x \sim \pm 0.2\%$ in composition and $\Delta d_\perp \sim \pm 10$ Å in thickness), consistent with their nominal values measured in situ by the quartz.

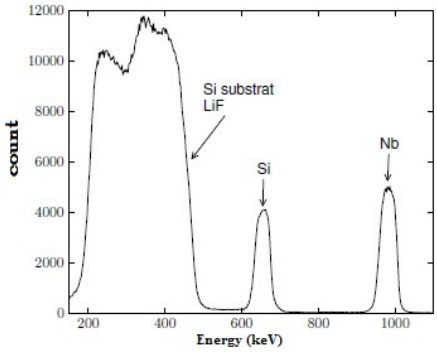

Figure 2.9: Example of a RBS spectrum for a thick a-$Nb_{13.5}Si_{86.5}$ sample. We can clearly see the contribution the LiF substrate in addition to those of the Nb and Si [Crauste, 2010].

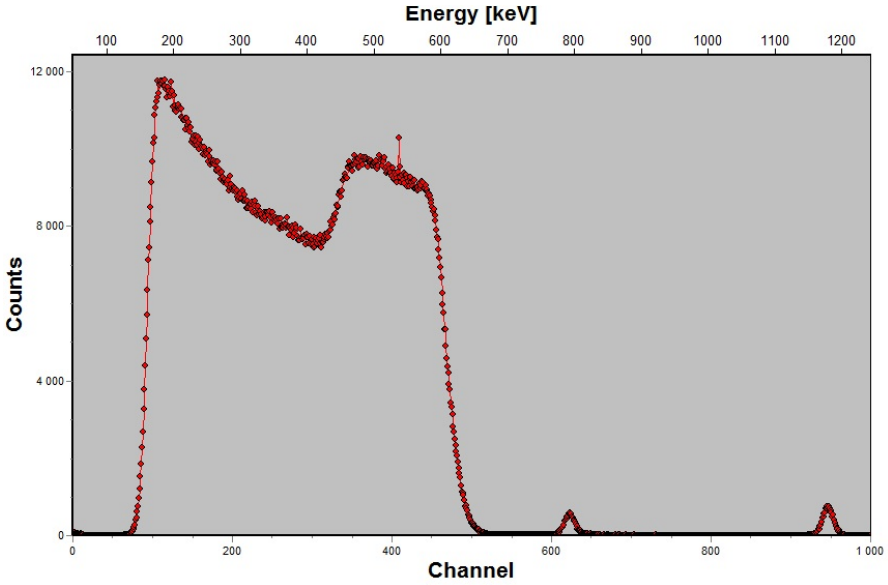

Figure 2.10: RBS spectrum of a 45 Å-thick $Nb_{13.5}Si_{86.5}$ sample. Red dots and lines are experimental data.

As mentioned before, one cannot rule out a contamination during the deposition process due to degassing or residual gases present in the deposition chamber. In particular, the Oxygen contamination is the most probable and the most problematic in our case since silicon oxides and niobium oxides are generally insulating.
The amount of Oxygen present in our film cannot be exactly determined by RBS spectra obtained from films deposited onto a LiF substrate, since its mass is very close to the mass of Fluor. In samples deposited onto an a-C substrate, it is easier to distinguish an Oxygen peak as one can see figure 2.12. Due to the small sample thickness, it is difficult to determine from the peak width whether this Oxygen comes from the native oxide layer of both the a-C substrate and the sample, or is distributed all along the film thickness. However, if the contamination in Oxygen was uniform throughout the film thickness, the simulated spectrum would fit the experimental data for an Oxygen content of 7.5% (in green figure 2.12). This would, in return, result in a discrepancy in the film thickness of 10% compared to the nominal value given by the quartz during the deposition process. This is highly unlikely, especially since the simulation with a pure Nb_xSi_{1-x} film of nominal thickness with a native oxide layer also well fits the experimental RBS spectrum. Moreover, no oxygen peak has been measured in the RBS spectra of bulk samples. We are therefore confident in the fact that the observed Oxygen contamination most predominantly occurs at the surface through a native layer for the RBS samples [3].

3. These RBS samples have not been capped by a SiO layer. The films used for transport measurement are all protected by an SiO overlayer and are therefore less likely to present an Oxygen contamination.

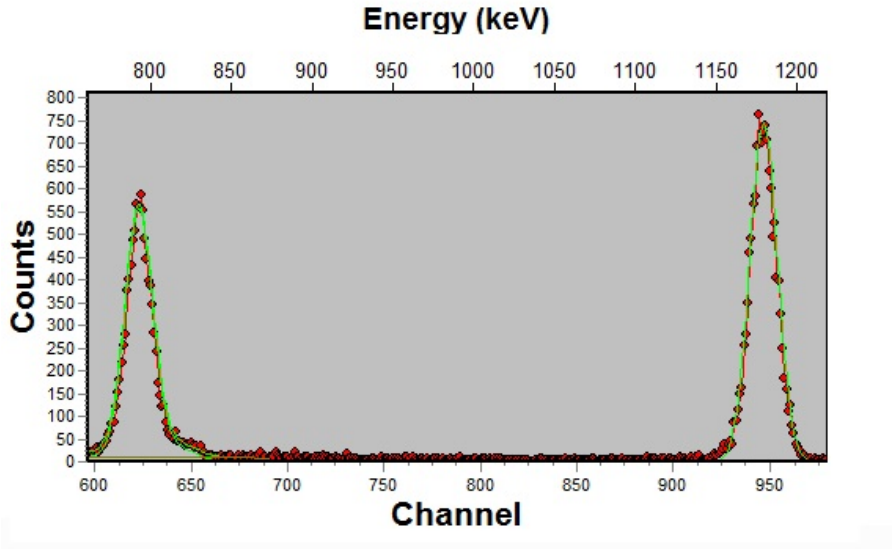

Figure 2.11: (Red lines and dots) Close-up of the RBS spectrum on the Nb and Si peaks, for a 50 Å-thick $Nb_{13.5}Si_{86.5}$ sample (nominal values). The simulated spectrum (green line) corresponds to a 44.6 Å-thick $Nb_{13.4}Si_{86.6}$ sample. The parameters of the simulated spectrum are in good agreement (within $\pm$ 0.1% for the composition x and $\pm$ 5 Å for the thickness $d_\perp$) with the nominal values.

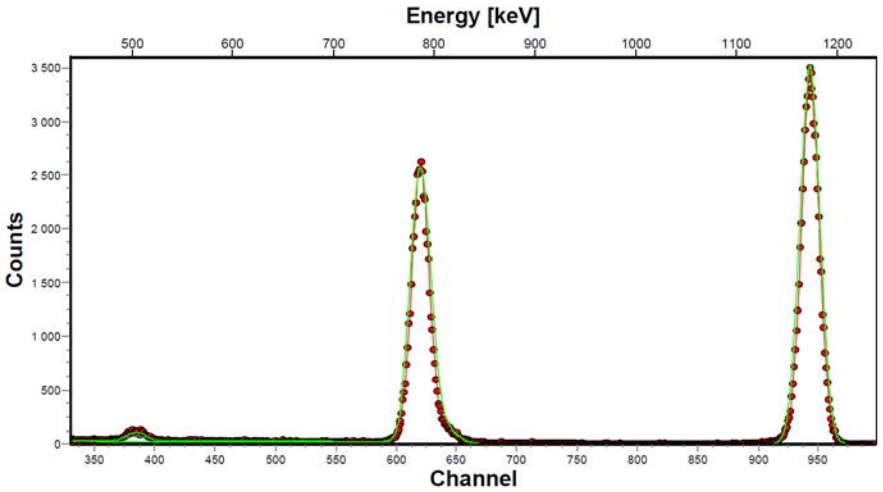

Figure 2.12: Close-up of the RBS spectrum on the O, Si and Nb peaks for a 230 Å-thick $Nb_{13.5}Si_{86.5}$ sample (nominal values). The simulation for a 254 Å-thick $Nb_{10}Si_{80.5}O_{7.5}$ sample is represented by the green line. The same fit is obtained by simulating a 230Å-thick $Nb_{13.5}Si_{86.5}$ with a naturally oxidized overlayer.

2.2.4.2 Determination of the morphology

a-Nb_xSi_{1-x} properties have been sudied for a few years in the group. Morphological characterisation have been carried out by AFM, TEM and EFTEM. In this section, we will describe those as well as the effects of a heat treatment on the structural features of this material.

2.2.4.2.a Structural characterisation techniques

In order to check the continuity of the films and the morphological structure of disorder, Atomic Force Microscopy (AFM) and Transmission Electron Microscopy (TEM) measurements have been performed on samples similar to the ones measured in this thesis [Crauste et al., 2013]. Electronic diffraction has been performed at the same time. The measurement of the diffraction pattern is a valuable side-product.

AFM is a technique of surface characterisation. It uses the interaction between the atoms of a tip, scanning the sample, and the atoms of the sample surface. It measures the surface topology of a sample on a typical size of several μm^2.

TEM is a microscopy technique where one measures the electrons passing through a thin sample. To do so, electrons are accelerated by an intense electric field [4]. The transmission of these incoming electrons through the sample depends on their interactions with the material. Thus scanning the sample enables to draw a picture of these interactions. This technique is sensitive both to the electronic structure of the analysed material and to its thickness.
By filtering the energy on a single atomic emission ray, one can isolate the measurement of a single element from the sample. We will then refer to Energy Filtered Transmission Electronic Microscopy (EFTEM).

The use of all these techniques is complementary since it gives us access to different information :
- AFM gives information on the continuity of the sample and surface roughness.
- TEM permits to access the composition homogeneity of the film and to its morphological structure.
- Electronic diffraction gives information about the crystallographic properties of the sample.

2.2.4.2.b Observation of as-deposited a-Nb_XSi_{1-x} thin films

For AFM, the samples have been measured at the Centre Technique Universitaire IEF-Minerve (Orsay) by Youri Dolgorouky [Crauste, 2010].
a-Nb_xSi_{1-x} films have been deposited onto a Si substrate without any SiO underlayer. This is compensated by the presence of native oxidation of the substrate. The films have been grown without a SiO protection layer to be able to access the surface morphology. A typical result, corresponding to a 25 Å-thick $Nb_{18}Si_{82}$ sample, is given figure 2.13.

These measurements showed that the films are continuous at least down to 25 Å and have a good thickness homogeneity since the roughness of the film is lower than 1 Å on the probed surface.

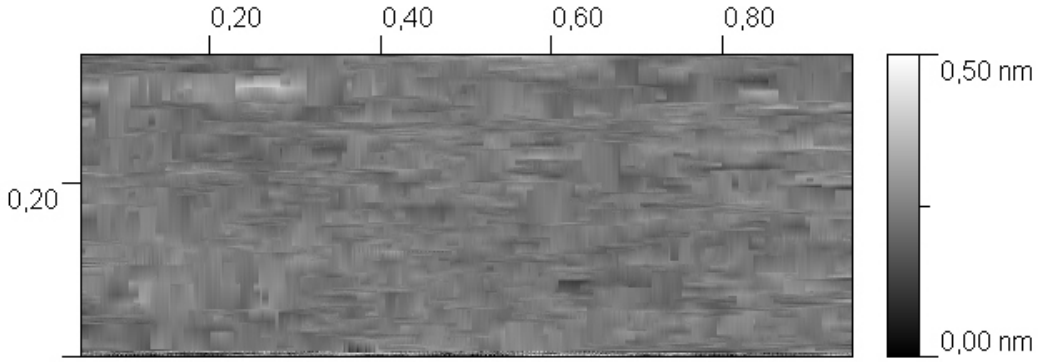

Figure 2.13: AFM measurement of the surface of a 25 Å-thick $Nb_{18}Si_{82}$ sample [Crauste, 2010]. The measured area is 0.5x1 μm^2.

For TEM measurements, samples have been measured by a Tecnai G^2-20 twin FEI operating at 200 keV at the CSNSM. The experiments have been carried out by Aurélie Gentils [Crauste, 2010].
Dedicated samples of 25 and 100 Å of $Nb_{18}Si_{82}$ have been grown onto a 25 nm thick SiO_2 membrane, thin enough to provide a good transmission. These films have not been protected by a SiO overlayer to facilitate both the measurement and analysis. Figure 2.14 shows the measurement of the plain substrate (a), of the 25 Å-thick sample (b) and of the 100 Å-thick sample. The

4. Typically of a few hundreds keV.

electronic diffraction pictures obtained, performed on the same samples, are given in the insets.

On the TEM pictures, we observe no morphological modification as a function of the thickness. In addition, electronic diffraction pictures show diffusive halos, characteristic of a lack of atomic order. Our films can thus be considered to be amorphous.

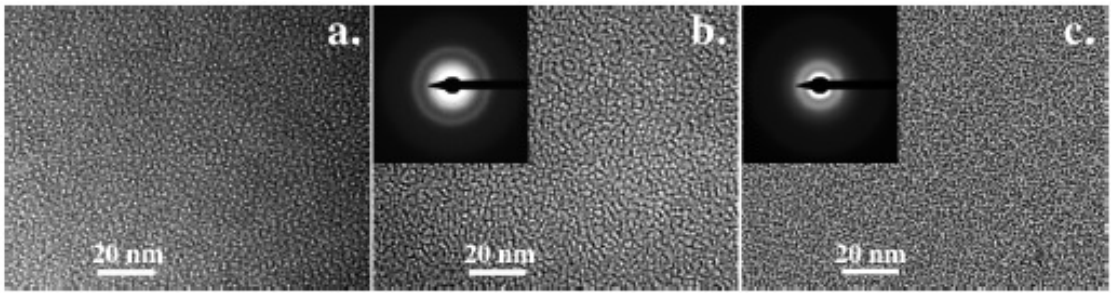

Figure 2.14: TEM pictures of (a) a plain SiO_2 substrate, (b) a 25 Å-thick a-$Nb_{18}Si_{82}$ sample and (c) a 100 Å-thick a-$Nb_{18}Si_{82}$ film with their electronic diffraction patterns (insets). [Crauste et al., 2013].

The absence of clustering can be seen on the EFTEM picture presented figure 2.15 for a 25 Å-thick $Nb_{18}Si_{82}$ sample, on which one can observe the spatial distribution of Nb (figure b) and Si (figure c). Our films can therefore be considered to have a homogeneous distribution of Nb and Si throughout the sample.

In conclusion, **our Nb_xSi_{1-x} samples are continuous down to the lowest thickness (25 Å), amorphous and homogeneous both in composition and thickness**.

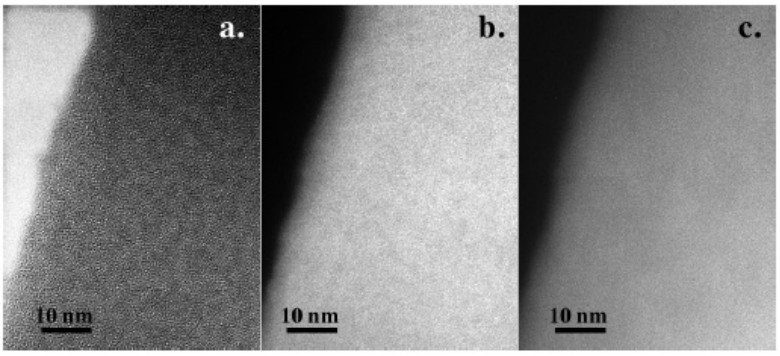

Figure 2.15: (a) TEM pictures of 25 Å-thick a-$Nb_{18}Si_{82}$ film, (b) picture of the Nb atoms repartition along the sample, (c) picture of the Si atoms repartition along the sample. [Crauste et al., 2013].

2.2.4.2.c Effect of heat treatment on the sample morphology

As we will see in section 2.3.2.2, heat treatments have an effect on the effective disorder of the sample. To ensure that the changes in the electronic transport measurements, which will be detailed in the following sections, were not associated to any morphological change and truly linked to an intrinsic disorder modification, TEM and electronic diffraction measurements have also been performed after different heat treatments.
To do so, a sample of 25 Å-thick $Nb_{18}Si_{82}$ with a 100 Å-thick SiO top layer has been grown. This top layer has been added, compared to previous TEM measurements, so that the TEM sample and those for transport measurements have the closest possible structure.

Heat treatments up to 700 ℃ have been performed in the transmission microscope. On figure 2.16 are presented the observed TEM and electronic diffraction diffraction pictures for a selection of heat treatment temperatures.

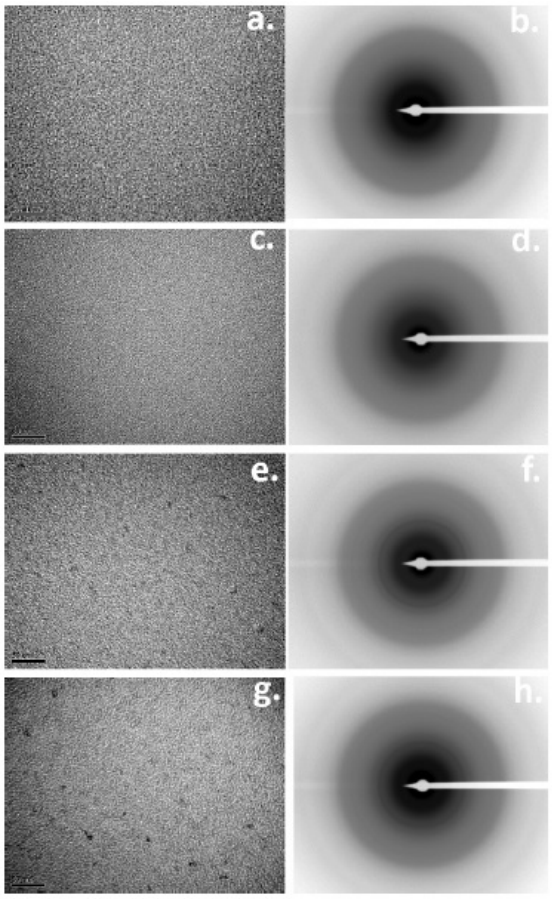

Figure 2.16: TEM and electronic diffraction pictures obtained without heat treatment (figures (a) and (b)) and after a heat treatment at 200 ℃ (figures (c) and (d)), at 500 ℃ (figures (e) and (f)), and at 700 ℃ (figures (g) and (h)) [Crauste et al., 2013].

For heat treatment temperatures lower than 200 ℃ (figures (a) to (d)), TEM pictures are similar to figure 2.14. There is no obvious clustering of size larger than 2 nm in the TEM pictures [5] and the electronic diffraction images present diffusive halos, characteristic of amorphousness. As the temperature is increased further (figures (e) to (f)), we eventually observe a clustering of the electronic density on TEM measurements. At the same time, well defined circles appear in diffraction measurements [6]. This is even more obvious as we reach the highest achievable heat treatment temperature [7] (figures (g) and (h)) where crystalline clusters of few nm are clearly observable in the TEM picture.

This is a first element showing that, **for moderate heating of the sample, we do not change the film morphology**. From 500 ℃, we do observe a change in the morphological properties of the sample which may, in turn, affect the electric properties of the samples. However, all the samples studied in this thesis have sustained a heat treatment of $\theta \leq 250$ ℃. Clustering as a result of heat treatment can therefore be excluded in the case of our transport samples.

2.3 Characteristics of a-NbSi

As we have seen in chapter 1, a Quantum Phase Transition (QPT), such as the SIT or MIT, is a transition occurring at zero temperature and tuned by an external parameter. In a-Nb_xSi_{1-x}, previous studies [Marnieros, 1998][Marrache-Kikuchi, 2006][Crauste, 2010][Couëdo, 2014] have shown that QPTs can be achieved by tuning the system disorder through the variation of different experimental knobs. Indeed, the sample composition x, the thickness $d_\perp$ or the heat treatment

5. This limit is given by the microscope resolution.
6. These have been attributed to nanometric Nb_3Si crystallites forming for $\theta \geq 500$℃.
7. For this experimental apparatus : 700 ℃.

temperature θ changes the electrical properties of the films as well as their ground state.

In this section, we will first review the effects of disorder on three-dimensional (3D) films, before examining how a variation in the sample thickness, i.e. a change in the effective dimensionality of the films, affects their electronic properties.

But let us first define the "disorder" in our films.

2.3.1 Estimation of the Disorder

In the previous chapter, we have seen that $k_F l$ has commonly been taken as a measure of disorder (with k_F the Fermi wave vector and l the mean free path) since $k_F l > 1$ characterizes a conducting state, whereas $k_F l < 1$ signs an insulating state.

As seen in section 1.2.3, the relation between the Ioffe-Regel parameter $k_F l$ and experimentally measurable quantities, such as the conductivity σ [8] or the sheet resistance $R_\square = \frac{1}{\sigma d_\perp}$, depends on the dimensionality of the sample.

In this work, our films are generally either in the 2D or in the quasi-2D limit where $R_\square$ is directly proportional to $\frac{1}{k_F l}$ (see section 1.2.3). In order to compare our samples with one another, we will therefore use the **sheet resistance $R_\square$ as an indication of the disorder level in our samples**. However, an *absolute measurement* of $k_F l$ by transport experiments is challenging since the above-mentioned expressions of the Ioffe-Regel parameter have been developed in the framework of a free-electron model, i.e. in the absence of any localization or interaction. The discussion of the meaning of the absolute value of $R_\square$ with respect to disorder at a given temperature is beyond the scope of this thesis, but it is important to emphasize that its evolution is monotonic with disorder.

Usually, disorder is estimated by taking the value of $R_\square$ either at 4 K or at room temperature. At room temperature, the measured resistance is supposedly closer to Drude's value for disordered materials, whereas, at low temperatures, other phenomena - such as localization for instance - have to be taken into account. In our case, for sufficiently conducting samples, including samples that have an insulating ground state but are close to the insulating threshold, taking $R_\square$(4K) or $R_\square$(300K) has an influence on the extracted value of $k_F l$ but has scarcely any effect on the observed trends, as the evolution of $R_\square$ is monotonic with disorder. In other words, not subtracting localization effects by evaluating $k_F l$ through $R_\square$(4K) does not modify the properties described in this manuscript. For samples far in the insulating region, the evaluation of $k_F l$ is problematic as deviations from Drude's model are then important, even at 300 K. Therefore, estimating $k_F l$ by taking $R_\square$(4K) or $R_\square$(300K) are almost equally questionable choices. We therefore arbitrarily chose to take **$R_\square$(4K) to estimate the disorder level** in all our samples.

In previous studies carried out in the group, $k_F l$ has been estimated by $R_\square$ taken either at 4 K [Crauste, 2010] or 500 mK[Couëdo, 2014]. We saw section 2.2.1.2 that during the fabrication of our samples, the films are connected to superconducting electrodes for electronic transport measurements. Their superconductivity, at $T_{c,\,electrodes}$ can induce a drop of the measured film resistance of $\sim 100\,\Omega$ which should be corrected as it does not reflect the film properties and can induces an inaccuracy in the evaluation of disorder [9]. In the present studies, whenever relevant, all samples from previous studies have been reanalysed to take the modification of the film resistance below $T_{c,\,electrodes}$ into account.

2.3.2 External disorder-tuning parameters for 3D Nb_xSi_{1-x}

Let us now examine how disorder affects the ground states (defined at $T = 0$) in the case of 3D a-Nb_xSi_{1-x} films.

8. σ is here defined as the 3D conductivity.

9. These resistance drops have not been seen in the samples grown for this thesis. In previous studies, to cope with this experimental issue, the sheet resistance has been corrected by applying the adequate correction in geometry for $T_{c,\,electrodes}$ in [Crauste, 2010] or by taking the sheet resistance at $T \ll T_{c,\,electrodes}$ in [Couëdo, 2014]. These corrections are, rigorously, necessary in order to compare different films with one another. However, let us note that taking into account these corrections or not modifies the evaluation of $k_F l$ by $\sim 10\%$ and does not change the observed trends.

2.3.2.1 Effects of a modification of the composition

For thick samples, a modification of the relative composition x of a-Nb_xSi_{1-x} permits to cross several transitions, from superconductor to insulator as illustrated figure 2.17. When x diminishes, the 4 K conductivity σ_{4K} decreases and the critical temperature T_c, when it is defined, simultaneously vanishes. This is in agreement with expectations for an increasing disorder as seen in section 1.6.2.

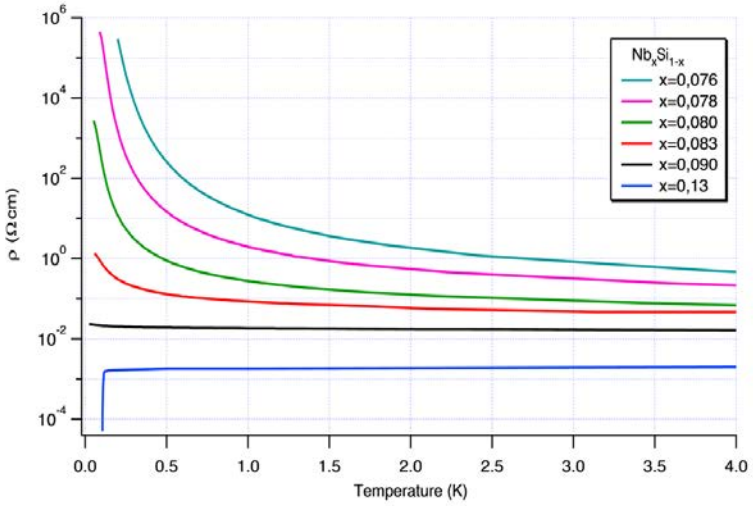

Figure 2.17: Evolution of the resistivity of bulk a-Nb_xSi_{1-x} films for samples of different compositions x [Marnieros, 1998].

The evolution of σ_{4K} and T_c with Niobium content is linear and given figure 2.18. The compositions at which each of these characteristics go to zero define changes in the system ground state as follows :

- The system is superconducting for $x \gtrsim 12\%$.
- The system is metallic for $12\% \gtrsim x \gtrsim 9\%$.
- The system is insulating for $x \lesssim 9\%$.

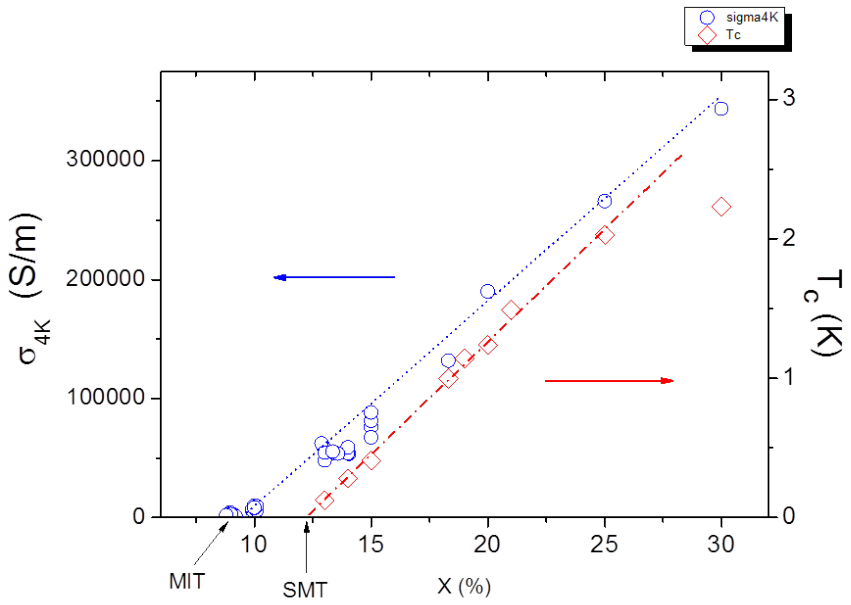

Figure 2.18: Evolution of σ_{4K} and T_c for Nb_xSi_{1-x} samples of thicknesses larger than 150 Å from [Marrache-Kikuchi, 2006][Crauste, 2010][Couëdo, 2014] and [Diener, 2013]. The intersections of $T_c(x)$ and $\sigma_{4K}(x)$ curves with the x-axis define the Superconductor-to-Metal-Transition (SMT) and the Metal-to-Insulator-Transition (MIT) respectively.

As we have seen in the previous section, a decrease in the 4 K conductance, σ_{4K}, corresponds to an increase in the sample disorder : $k_F l$, extracted from σ_{4K}, diminishes. In amorphous systems, l is of the order of the inter-atomic distance a. The large variations in $k_F l$ that have been measured can then only be explained by a change in k_F since $\sigma \sim (k_F l)^2 \sim (k_F a)^2$.
Therefore, our interpretation is that the main effect of a **change in x is to modify the density-of-states** (and therefore k_F) in the material.
However, varying the sample composition is not the only way to tune the transitions in bulk samples.

2.3.2.2 Heat treatment : fine-tuning of the disorder

By using the heat treatment procedure described section 2.2.1.3, it is possible to irreversibly change the electrical properties of our films, as shown figure 2.19. Indeed, a heat treatment at a fixed temperature θ increases the sheet resistance $R_\square$ and, when relevant, decreases the superconducting critical temperature of the film T_c. Therefore, a heat treatment procedure is equivalent to an increase in disorder.

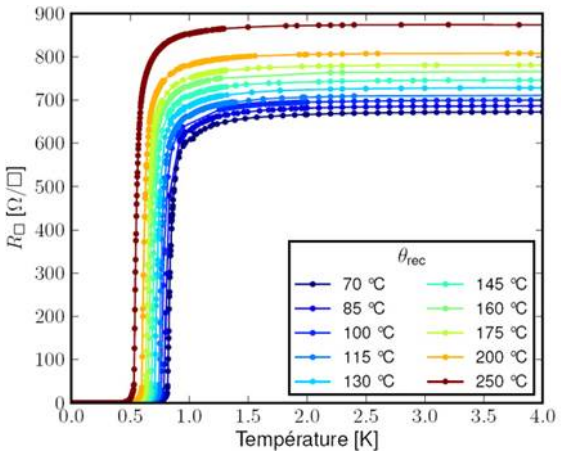

Figure 2.19: Evolution of the low temperature sheet resistance for a 125 Å-thick a-$Nb_{18}Si_{82}$ film submitted to different heat treatment temperatures.

The evolutions of the observable parameters T_c and σ_{4K}, for different films as a function of the heat treatment temperature, are given figures 2.20 and 2.21. σ_{4K} and T_c are decreasing linearly with θ. Eventually, as observed in figure 2.21, a change of behaviour occurs at a certain heat treatment temperature θ_{lim} for films of thicknesses lower than 50 Å : after an initial decrease of σ_{4K} with θ, corresponding to an increase in the disorder level, $\sigma_{4K}(\theta > \theta_{lim})$ increases with θ. We interpret this as the early signs of a change in morphology, probably due to some initial stages of chemical segregation. θ_{lim} depends on the thickness of the film : for thinner films, the change in behaviour is observed at lower θ_{lim}.
One can remark that θ_{lim} is lower than the crystallization temperature found by TEM and X-ray measurements (section 2.2.4.2.b). This may be due to the limitation in spatial resolution (a few nm) of the morphological characterization experiments which have been performed. These results therefore show that transport measurements are extremely sensitive to any morphological change. For the purpose of our work, we will only analyse samples for $\theta < \theta_{lim}$ to avoid spurious effects on electronic transport measurements due to a modification in the system's morphology.

This modification of the disorder as a function of the sustained heat treatment temperature is counter-intuitive since, for most materials, annealing decreases disorder.
We can therefore wonder what are the microscopic phenomena at play here. As one can observe figure 2.22, Hall measurements performed on quench-condensed a-$Nb_{26.3}Si_{73.7}$ films show a constant density-of-states [10] as a function of the heat treatment [Nava et al., 1986]. Therefore, since $\sigma \propto (k_F l)^2$, the mean free path l is the only parameter which should be modified by heat treatments. This idea is supported by a paper in which the authors [Béal and Friedel, 1964] demonstrated that, for binary alloys, a heat treatment will induce subatomic changes in the

10. Represented here by the Hall resistance.

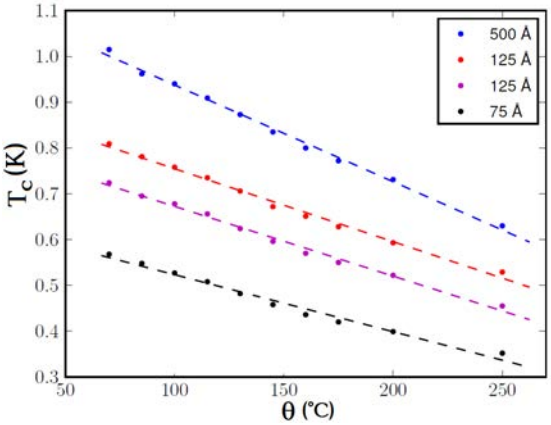

Figure 2.20: Evolution of the superconducting critical temperature with the heat treatment temperature θ for $Nb_{18}Si_{82}$ thin films of different thicknesses [Crauste, 2010] .

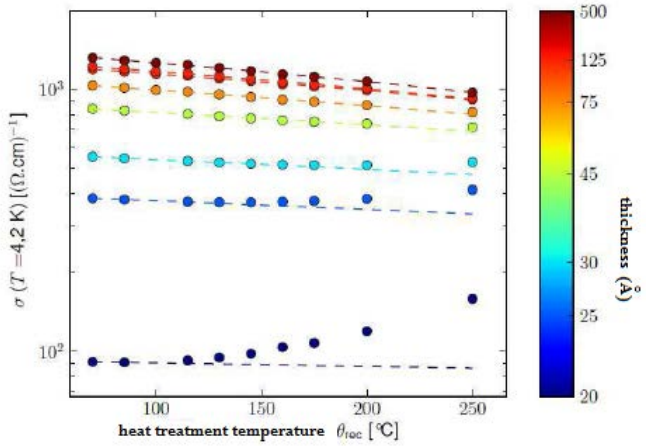

Figure 2.21: Evolution of σ_{4K} as a function of the annealing temperature for several films of $Nb_{18}Si_{82}$ [Crauste, 2010].

position of the atoms, thanks to the relaxation of structural stress. They showed that these relaxations lead to a modification of the interference patterns of the electrons which always induces a decrease in the local conductance.

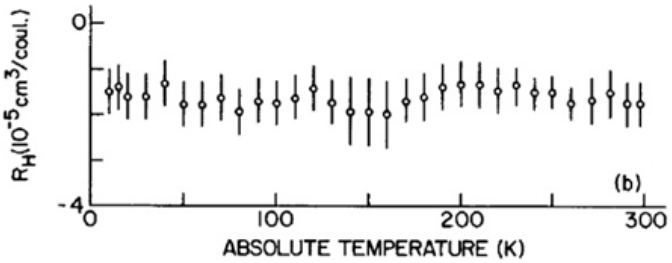

Figure 2.22: Variation of the Hall resistance as a function of the heat treatment temperature for a-Nb_xSi_{1-x} alloys (here $x = 26.3$ %). The evolution of the Hall resistance, if any, is lower than the error bars [Nava et al., 1986].

Heat treatment is a convenient tool to study the effects of disorder in amorphous thin films since it allows to induce slight changes in disorder within a single sample. This can be used for a variety of materials such as NbSi, AlGe [Lesueur et al., 1985] or InO_x[Ovadyahu and Imry, 1983] for instance. One should however be careful about the interpretation of such effects since mechanisms at the origin of the disorder modification may differ from system to system. Indeed, in the

case of InO_x, the mechanism at the origin the modification of disorder is different from the one encountered in NbSi or AlGe. In this particular case, heat treatment induces a modification of both the composition and the thickness of the sample [Ovadyahu and Imry, 1983][Gantmakher, 1998].

In the present work, **we have used θ to fine-tune the disorder level** in our samples. In particular, for films close to a QPT, this parameter allowed us to cross the transition very small steps by very small steps in a single sample.

2.3.3 Approaching the 2 dimensional limit

We saw that one can modify disorder in our system by tuning either the composition x or by submitting the sample to a heat treatment procedure at the temperature θ. Another way to do so is to reduce the dimensionality of the sample by tuning its thickness $d_\perp$. In this section, we will detail the effects of a thickness modification. For this purpose, we will define the dimensionality of the samples by comparing their thickness with different relevant lengths. We will then detail the effect of a thickness modification on the sample resistivity and compare it with the influence of the tuning parameters that we have seen before. Finally, I will present the phase diagram for Nb_xSi_{1-x} obtained in previous studies, and which will be the starting point of this thesis.

2.3.3.1 Characteristic length-scales and dimensions

As seen section 1.7, the effects of dimensionality reduction are observable when the relevant sample dimension is smaller than the characteristic length scale of the considered phenomenon. The different relevant length scales then define criteria for the cross-over between a 2D and 3D behaviour.

1. **Coulomb interactions**

   As mentioned section 1.4.2, the effects of electron-electron interactions can be important in thin films since their screening is lowered when the transversal dimension is reduced. The crossover in dimensionality is then governed by the thermal length $L_T = \sqrt{\frac{\hbar D}{k_B T}}$[Imry and Ovadyahu, 1982]. By taking $D = 0.6\ \mathrm{cm}^2/\mathrm{s}$ [Marrache-Kikuchi et al., 2008] and $T = 10$ mK, we find that $L_T \sim 210$ nm. All the considered samples in this study will therefore be considered **2D regarding Coulomb interactions** at the lowest temperatures.

2. **For a metal**

   As we have seen in section 1.3.2.3, the sample dimensionality for metals - when dealing with localization - is given by the ratio $L_{Th}/d_\perp$, where $d_\perp$ is the thickness of the sample and L_{Th} is the Thouless length. A dimensional cross-over from 3D to 2D happens when the ratio is ~ 1, corresponding to the value for which the electrons sense the sample edges. We can estimate the Thouless length :
   - By using $L_{Th} = \sqrt{l l_\Phi}$ where l_Φ is the coherence length. For our films, by taking the value of l_Φ for crystalline Si at low temperature ($\sim 5.10^{-7}$m) [Ferry et al., 2009] - as the films are mainly made out of Si - and a mean free path of the order of the inter-atomic distance (~ 5 Å), one finds $L_{Th} = 50$ nm, which corresponds to a very crude estimation as the mean free path has been taken to be minimum and the value of the coherence length corresponds to non-disordered Si.
   - By studying the magnetoresistance of a 1000 Å-thick a-$Nb_{12}Si_{88}$ film, Juillard et al. showed that $L_{Th} \sim L_{in} = 16$ nm at 4 K [Juillard, 1996].
   - This value can also be experimentally obtained thanks to the cross-over between 3D and 2D localization laws in conduction. For our samples, we will derive a direct measurement of L_{Th} by this mean in section 3.4.

   We would like to stress that the obtained values of L_{Th} are all larger or of the order of the thickness of the samples grown for the upcoming study. We therefore considered that our samples are **2D from the point of view of the Thouless length**.

3. **For an insulator**

For Anderson insulators, dimensionality is determined by comparing $d_\perp$ to the extent of the wavefunction in space, which is given by the localization length ξ_{loc}. ξ_{loc}, in turns, depends on the dominant conduction mechanism.

Mott insulator
In the case of a Mott insulator, in 2D, $\xi_{loc}^2 = \frac{\beta_2^{Mott}}{N(E_F)d_\perp k_B T_{Mott}}$. By taking $N(E_F) \sim 1.10^{41}$ states/J/cm^3 [Crauste, 2010], a sample of thickness $d_\perp = 10$ nm and a characteristic temperature of the order of 1 K, we found in 2D ($\beta_2^{Mott} = 13.8$) that $\xi_{loc} \sim 30$ nm, well above the size of our insulating samples. Moreover, ξ_{loc} increases as $d_\perp$ decreases, so that all samples exhibiting this regime at low temperature can be considered to be 2D, as confirmed by the measured conduction law $R_\square \propto e^{(\frac{T_0}{T})^{1/3}}$, specific to two-dimensionality.

Efros-Shklovskii insulator
Regarding ES VRH, in the presence of 2D interactions, $\xi_{loc} = \frac{\beta_2^{ES} e^2}{k_B T_{ES} \kappa}$ with $\beta_2^{ES} = 6.5$ and $\kappa = 4\pi\epsilon\epsilon_0$. Thus, taking a characteristic temperature of 1 K and $\epsilon \sim 10$ (which is the order of magnitude of ϵ in Si), $\xi_{loc} \sim 1.10^{-5}$ m, way larger than our sample thicknesses.

All our **insulating films** can therefore be considered **2D from the point of view of VRH at the lowest temperatures**.

4. **For a superconductor**
The criterion for bi-dimensionality of superconducting films is the ratio between superconducting the coherence length ξ and $d_\perp$; when $d_\perp \leq \xi$ the film is considered to be 2D. As we have seen section 1.6.1.2, $\xi = 0.85\sqrt{\frac{\hbar v_F l}{\Delta_0}}$ in the dirty limit. For a critical temperature $T_c = 200$ mK, taking $v_F = 4.10^5$ m/s [Marrache-Kikuchi et al., 2008] and $l = 5$ Å of the order of the inter-atomic distance, $\xi = 56$ nm. This length is underestimated for most films presented in this manuscript as their mean field T_c is usually lower.
All our superconducting films can therefore be considered **2D with respect to the superconducting coherence length**.

Regarding all the estimated lengths, we will therefore consider ourselves as being 2D whatever the considered ground state.

2.3.3.2 Effects of the modification of the thickness

For samples in the 3D limit, we saw that a modification of the proportion of Nb inside the film (x), or a heat treatment procedure at the temperature θ, can change the electrical properties of an a-Nb_xSi_{1-x} film due to the modification of either the Fermi wave length k_F, or the mean free path l. In both cases, within this limit, the resistivity as a function of the thickness stays constant.

However, as the thickness of the sample is reduced below 100 Å typically, the electrical properties dramatically change. To illustrate this point, we have plotted the evolution of the 4 K resistivity of a-$Nb_{18}Si_{82}$ figure 2.23. The resistivity is almost constant for thicknesses larger than 100 Å and begins to increase steeply for lower values.

The thickness evolution has a direct influence on the ground state of the films as one can observe on figure 2.25 for a-$Nb_{18}Si_{82}$ films. Indeed, for thick films, the ground state is superconducting with a critical temperature T_c around 1 K. As the thickness is reduced, the sheet resistance $R_\square$ increases and T_c, plotted figure 2.24, vanishes. By reducing the sample thickness further, the film eventually becomes insulating.
The observed linear evolution of T_c as a function of $1/d_\perp$, discussed in section 1.7.1, allows us to define a critical thickness d_c, characteristic of a phase transition, at which superconductivity disappears for a given alloy composition x.

Let us emphasize that, even for the thinnest films presented here, we do not observe any reentrance behaviour, which would be characteristic of granular films as we have seen section 1.6.3. This is a further indication, in addition to the ones detailed section 2.2.4.2.b, of the homogeneity of our films.

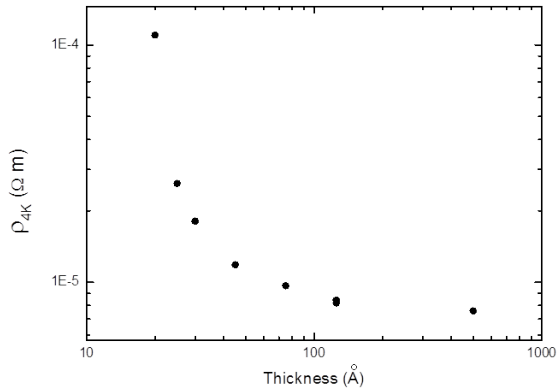

Figure 2.23: Evolution of the 4 K resistivity of a-$Nb_{18}Si_{82}$ films as a function of their thickness.

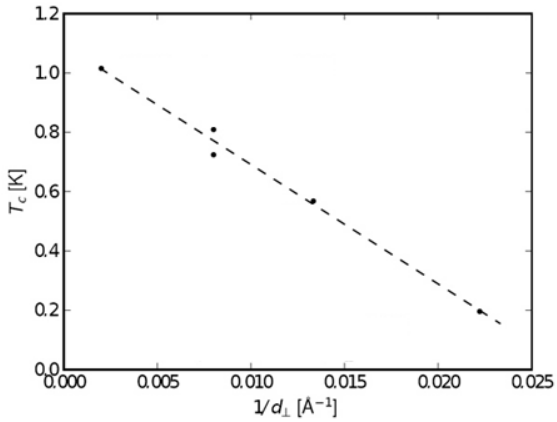

Figure 2.24: Evolution of the superconducting critical temperature of a-$Nb_{18}Si_{82}$ films as a function of the film thickness $d_\perp$. Adapted from [Crauste, 2010].

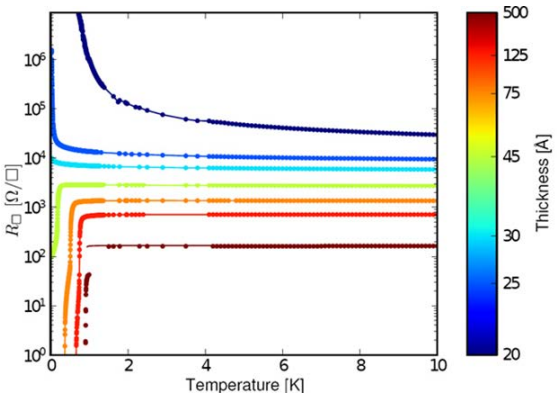

Figure 2.25: Superconductor-to-Insulator Transition in $Nb_{18}Si_{82}$ films obtained by a modification of the thickness [Crauste, 2010].

A change in sample thickness can therefore induce a phase transition towards an insulating state, very much like what has been described in the previous section for a modification of x or θ. Let us now compare the effects of these three different disorder-tuning parameters on the electrical properties of a-Nb_xSi_{1-x} thin films.

2.3.3.3 Comparison with other tuning parameters

In this section, we present the comparison between the effects of the different tuning parameters : x, θ and $d_\perp$. We will first compare the effects of the Nb composition x and the heat

treatment temperature θ. We will then include the comparison with the effects of the thickness modification $d_\perp$. These results are summarised in [Crauste et al., 2013].

To compare the effects of disorder tuned by a modification of x and θ, let us start from a single superconducting film and see how a change in Niobium composition or a change in θ affects its properties. On figure 2.26, we can see that, starting from a 125 Å-thick $Nb_{18}Si_{82}$ film thermally treated at 70 ℃, a change of 1 % in composition or a heat treatment at 200 ℃ increases the disorder in the film. Both parameters modify the film properties in the same manner : effects on the normal sheet resistance and the superconducting critical temperature T_c are similar.

Another way to see this is to plot the evolution of the T_c as a function of the sheet resistance taken at 4 K (figure 2.28 (a)). For different compositions and annealing temperatures, the evolution of the superconducting critical temperature with $R_\square$ is continuous. In other words, T_c is completely determined by the disorder level, measured by $R_\square$, whatever the disorder-tuning parameter, x or θ. Furthermore, it has been demonstrated [Crauste et al., 2013] that this result is in qualitative agreement with Finkelstein's theory for the evolution of the critical temperature with disorder.

We saw that the effects of a modification of x and θ affect the disorder in a similar manner in our films. But what about the effects of $d_\perp$ on the disorder ?As seen figure 2.27, starting from the same $Nb_{18}Si_{82}$ 125 Å-thick film which has been thermally treated at $\theta = 70$ ℃, we can reach the same T_c reduction either through a change in x or $d_\perp$, but the corresponding determination of the disorder level, obtained from $R_\square$, is different. In figure 2.28 (b), this discordance is clearly visible since there is no visible continuity of the critical temperature as a function of the disorder. In other words, T_c is no longer unequivocally determined by $R_\square$.

This discrepancy is not due to the choice of $R_\square$ as the relevant disorder parameter [11]. Extending the analysis to the quasi-2D or 3D limit yields the same result.

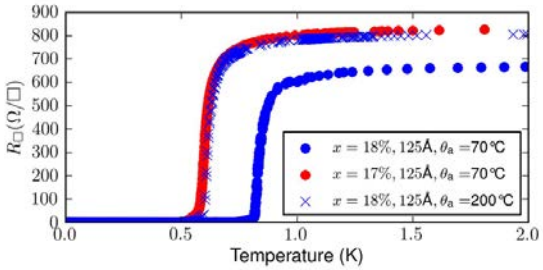

Figure 2.26: Comparison of the effects of composition and heat treatment on 125 Å-thick Nb_xSi_{1-x} film. From [Crauste et al., 2013].

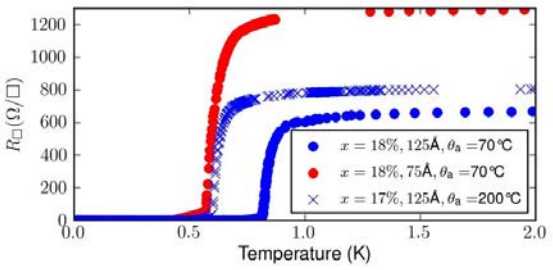

Figure 2.27: Comparison of the effects of thickness and composition on 125 Å and 75 Å-thick Nb_xSi_{1-x} films. From [Crauste et al., 2013].

Thus, **a modification of x or θ has the same effects on the disorder in our films**. A contrario, $d_\perp$ **changes T_c and $R_\square$ - hence the disorder - in a non-identical manner**. We do not have a clear explanation regarding the nature of this role but we believe that this dimensional effect should be taken into account for the study of the transition, at least for superconducting films.

11. Which implies that the films are in the 2D limit : $d < \xi$ for superconductivity.

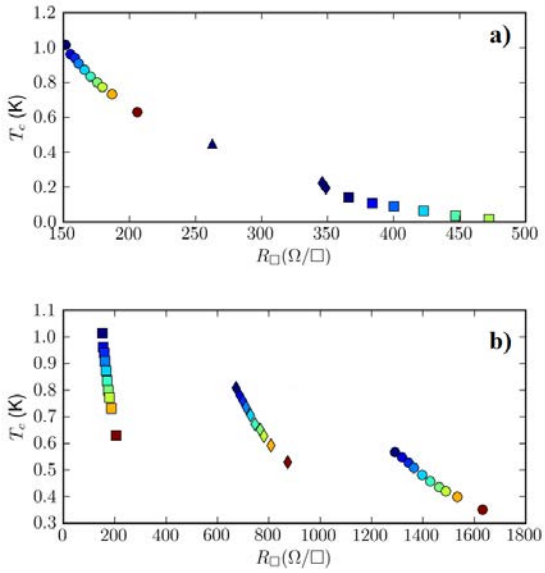

Figure 2.28: Evolution of the critical temperature T_c as a function of disorder, evaluated by the sheet resistance $R_\square$ for (a) films of Nb_xSi_{1-x} of 50 nm with different compositions and heat treatments (b) films of $Nb_{18}Si_{82}$ of different thicknesses and heat treatments. From [Crauste et al., 2013].

2.3.3.4 Different ground states

As seen in section 1.7, for the thickness-tuned transition, one can define a critical thickness d_c below which the films become insulating. For binary alloys and since the films are 2D from the point of view of superconductivity, this critical thickness depends on the composition of the sample and delimits an apparent Superconductor-to-Insulator-Transition. By plotting the dependence of this critical thickness as a function of the composition x, one can draw the phase diagram presented figure 2.29, and obtained by O. Crauste in his PhD thesis [Crauste, 2010].

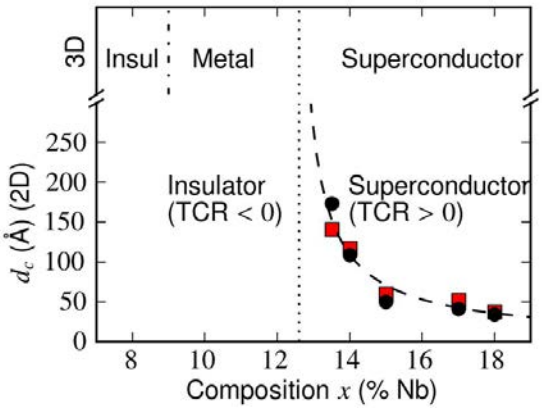

Figure 2.29: Phase diagram defining the thickness-induced apparent SIT observed for different compositions x of Nb_xSi_{1-x}. The dashed line is a guide to the eye. The straight lines correspond to the observed 3D phase transitions [Crauste et al., 2014].

One can then wonder what really happens in the vicinity of this transition and if it is possible to refine this diagram. To do so, subsequent work has focused on the systematic study of a-$Nb_{13.5}Si_{86.5}$ films of different thicknesses and heat treatment temperatures θ, close to d_c in order to finely study the system behaviour close to the observed disorder-induced transition.
By doing so, two additional regimes have been identified in addition to the superconducting and insulating ones, as one can see figure 2.30 [Couëdo, 2014]. These two new regimes are separated by a dashed line for clarity.
One can therefore categorize the different regimes as follows :

- **a superconducting phase**, with a complete superconducting transition. At the lowest measured temperature, $R_\square = 0$ for these samples.
- **a first metallic-like phase**, to which we will refer as **M1**, for which a sharp decrease in the resistivity is observable, but for which the resistance of the film saturates at a finite value at the lowest temperatures.
- **a second metallic-like phase**, to which we will refer as **M2**. For this phase, the Temperature Coefficient of Resistance (TCR) $\frac{dR}{dT}$ is $\leqslant 0$ at all temperatures, but the resistivity saturates at a finite value at the lowest temperatures.
- **an insulating phase**, with infinite resistance at zero temperature.

Thus one can sum up the different phases appearing at low temperature in the table below, taking into account the lowest temperature behaviour of the different phases :

	zero temperature resistance	superconducting transition	TCR sign
Superconductor	0	yes	+
M1	finite value	partial transition	+
M2	finite value	no	-
Insulator	∞	no	-

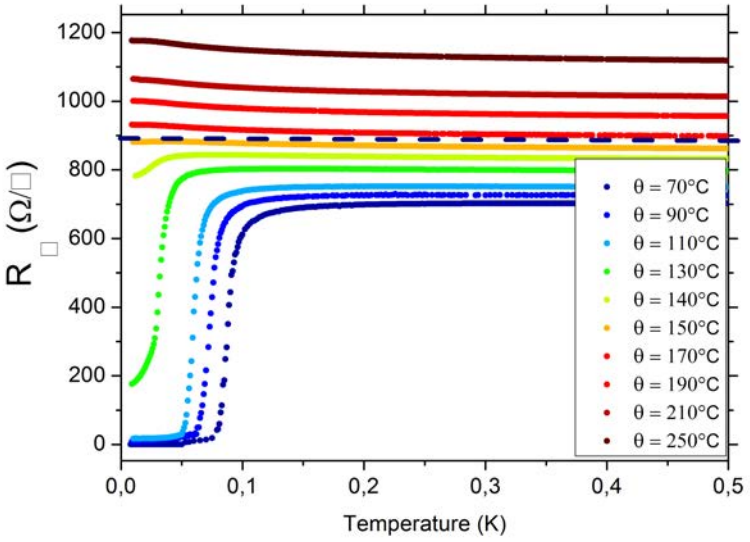

Figure 2.30: Sheet resistance $R_\square$ as a function of the temperature for a 23 nm-thick a-$Nb_{13.5}Si_{86.5}$ film where the disorder is varied via different heat treatment temperatures. The dashed line corresponds to the separation between the M1 and M2 regimes.

For all measured samples, we can therefore use the above mentioned criteria to define the cross-over between the different regimes. For convenience, we will define here the characteristic temperature T_{c0} as the temperature for which the sign of the second derivative of the resistance as a function of the temperature, $\frac{d^2R}{dT^2}$, changes at low temperature. For a superconducting film, this is a good estimation of the mean field superconducting critical temperature T_c. For films in the M1 regime, T_{c0} corresponds to the temperature at which the resistance abruptly drops. T_{c0} therefore allows us to define a characteristic energy for both superconducting films and films in the M1 regime.

For a single film measured for different heat treatment temperatures θ, T_{c0} and the residual sheet resistance R_{min}, obtained at the lowest measured temperature, present two different changes in regimes as disorder (measured via $\sigma_{4K} = 1/R_\square(4K)$ [12]) is increased. These changes are notified figure 2.31 by blue lines. The first one, as σ_{4K} is lowered, corresponds to the appearance of a finite resistance R_{min} while T_{c0} is still finite. This characterizes the appearance of the M1 phase and allows us to define the Superconducting-to-M1 Transition.
A second change occurs at the vanishing point of T_{c0}. Concomitantly, the evolution of R_{min} with

12. σ_{4K} here is a 2D conductivity, contrary to σ which is a 3D quantity.

$k_F l$ (or σ_{4K}) slows down, and the low temperature TCR changes sign. These three criteria allow us to define the M1-to-M2 Transition.
Figure 2.32 shows the evolution of T_{c0}, R_{min} and of the TCR for films of different thicknesses. The simultaneity of the three above-mentioned criteria is observed in all cases. The critical sheet conductance $\sigma_{c,4K}$ at which this transition occurs is however shifted toward higher values as the film thickness is increased.

To characterize the M2-to-Insulator-Transition, we plotted figure 2.33 the evolution of $\sigma_{min} = 1/R_{min}$ for all our films in the M2 regime. It is remarkable that the residual sheet conductance in this metallic regime all collapse on a single universal curve, whatever the film composition, thickness, or heat treatment temperature. Moreover, σ_{min} vanishes near $k_F l$=1, signing the transition between M2 and the insulating regime at a value close to the Ioffe-Regel criterion for the usual Metal-to-Insulator Transition.

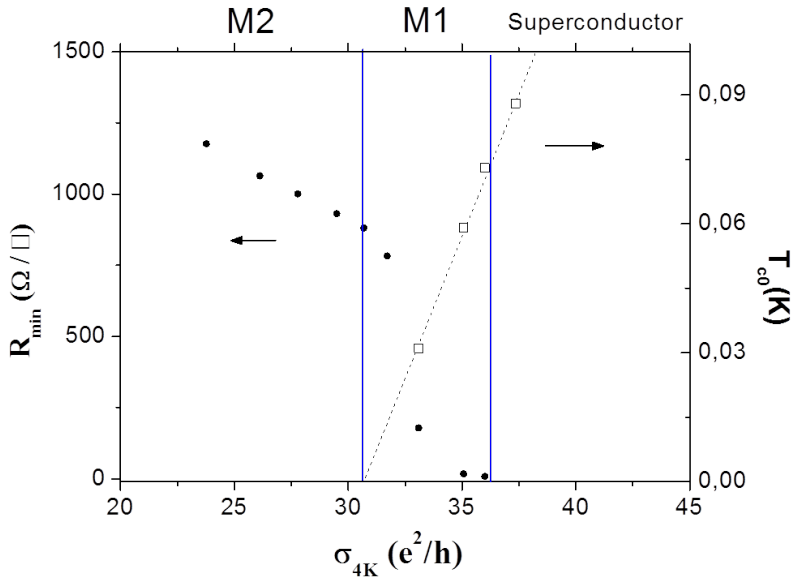

Figure 2.31: Evolution of the residual resistance R_{min} and of the characteristic temperature T_{c0} as a function of disorder for a 23 nm-thick a-$Nb_{13.5}Si_{86.5}$ film. Blue lines correspond to limits between the different regimes.

On the insulating side of the transition, a first analysis has been performed by identifying the evolution of the resistance as a function of the temperature with a thermally-activated Arrhenius law $R = R_0 e^{\frac{T_0}{T}}$ (as seen in section 1.5.1.1). By extracting the characteristic temperature T_0, one obtains figure 2.34. T_0 is vanishing at about the same value than the one found in figure 2.33, confirming the value of $k_F l$ at which the M2-to-Insulator-Transition occurs.

2.3.4 Conclusion

In conclusion, let us comment on the phase diagram as it had been established when we started this work : figure 2.35 [Couëdo, 2014] exhibits the possible ground states of a-Nb_xSi_{1-x} thin films depending on their thickness and disorder level (as measured by σ_{4K}).

As seen section 2.3.2.1, 3D samples ($d_\perp \gtrsim 50$ nm) can either be superconducting, metallic or insulating. The system ground state then is exclusively determined by $k_F l$.

In 2D ($d_\perp \lesssim 50$ nm), standard theories for the destruction of superconductivity predict a direct Superconductor-to-Insulator Transition, mainly driven by the disorder level. However, for a-Nb_xSi_{1-x}, the experimental situation is more complex. Not only can the ground state also be metallic, but it is determined both by disorder and the film thickness.
For a given thickness, films are superconducting at low enough disorder.
As σ_{4K} is lowered, a first metallic ground state, M1, emerges. This phase seems to retain fea-

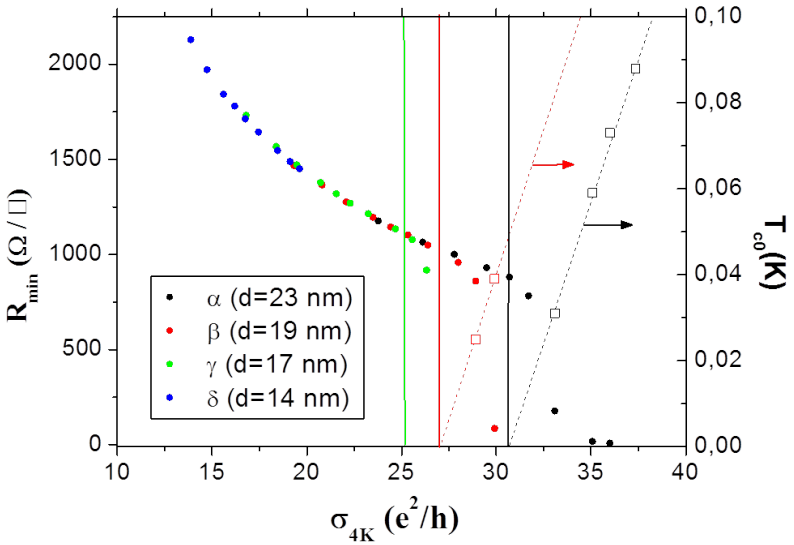

Figure 2.32: Evolution of the residual resistance R_{min} and of the characteristic temperature T_{c0} as a function of disorder for a-$Nb_{13.5}Si_{86.5}$ films of different thicknesses. The lines are guides to the eye corresponding to the M1-to-M2 Transition for the different films.

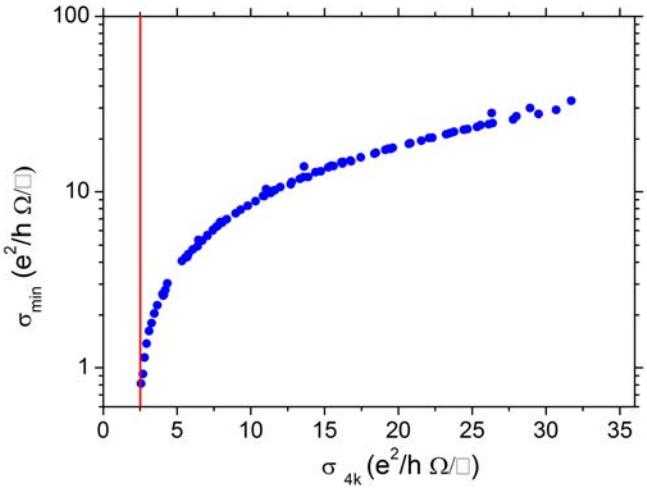

Figure 2.33: σ_{min} as a function of disorder for a-Nb_xSi_{1-x} films of different thicknesses $d_\perp$, composition x, and heat treatment temperature θ. The considered films are all in the M2 phase.

tures of Cooper pairing [13]. The phase coherence is nonetheless absent, causing dissipation at very low temperature. Although our Nb_xSi_{1-x} films are amorphous, this behavior recalls the experimental results obtained in model granular systems [Eley et al., 2012, Han et al., 2014] (see section 1.7.3.4.a), where each individual grain is superconducting but phase fluctuations are too important for Cooper pairs to condense in a single wave function. This intuitive analogy remains however to be confirmed.

As disorder is further increased, a second metallic phase, M2, arises. This ground state is neighbouring the 3D metallic state, but the proximity to the M1 phase indicates it may be more complex than a standard fermionic phase. Finally, below $\sigma_{4K} \sim \frac{e^2}{h}$, the system is insulating.

In [Couëdo, 2014], the different phases have been characterized, but there is to date no clear picture of their nature [14] (fermionic or bosonic) nor of the mechanism leading to these phase transitions. Moreover, the specific role of the thickness $d_\perp$ compared with other tuning parame-

13. A signature of this can be seen, for example, in the abrupt drop in resistance at T_{c0}.
14. Except, of course, for the superconducting phase.

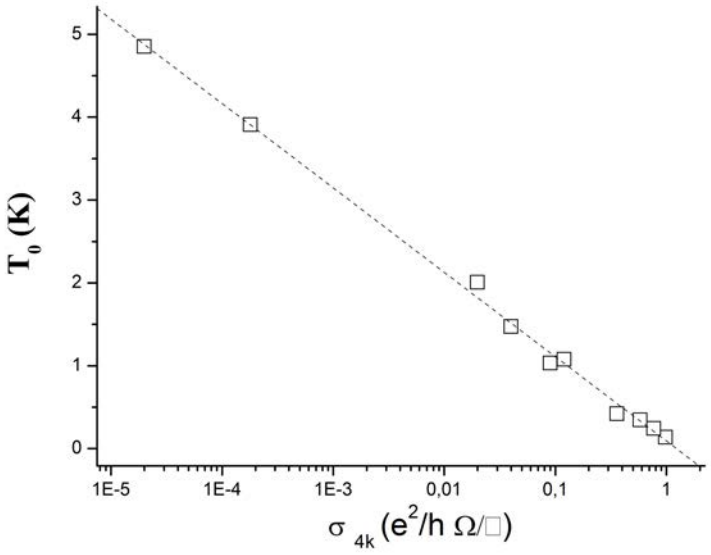

Figure 2.34: T_0 extracted from Arrhenius fits of the low temperature behaviours of the resistance for samples of the CK6 (β and γ), CK8 (β and γ), CK9 (β and γ), and CK10 (γ) batches [Marrache-Kikuchi, 2006].

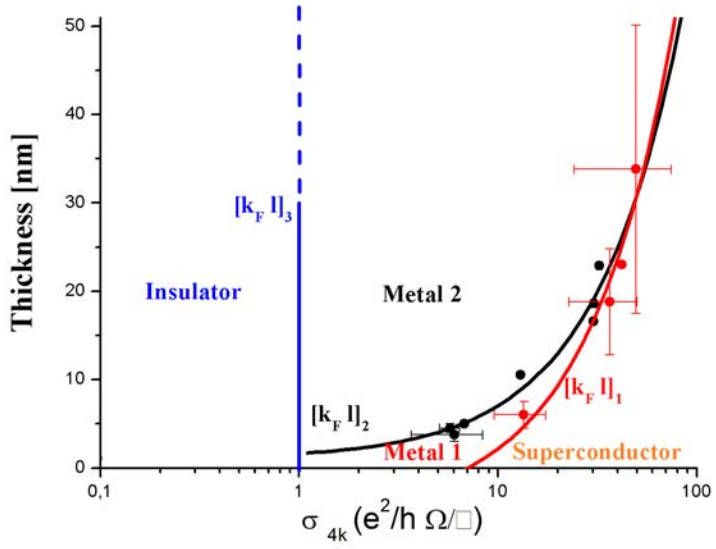

Figure 2.35: Disorder-Thickness phase diagram of a-Nb_xSi_{1-x} thin films. The lines are guides to the eye. The blue line corresponds to the Ioffe-Regel value of the 3D Metal-to-Insulator Transition.

ters (θ and x), at least in the 3 conducting states [15], has to be explicited.

Let us end this section by emphasizing the interest of low dimensional systems : the M1 phase only appears at low $d_\perp$ for instance. New unconventional ground states thus can emerge due to reduced dimensionality.

15. The insulator, by contrast, seems to appear at a definite value of σ_{4K}, no matter what the sample thickness is.

Chapter 3

Experimental results

In the previous sections, I have outlined the state-of-the art understanding of the a-NbSi phase diagram at the beginning of my PhD. By separately tuning the different accessible experimental knobs, unpredicted metallic phases - the M1 and M2 phases - had been evidenced and the destruction of superconductivity in this system had been characterized. The corresponding phase diagram has been drawn figure 2.35 and it will serve as the starting point of this work.

However, the nature of the metallic phases, as well as the evolution from the M2 phase toward an insulating one, were still open questions. As can be seen figure 2.35, the M2 phase seems to arise from a fermionic 3D metal as the thickness is reduced. However the proximity of this phase with the M1 regime where superconducting fluctuations are expected to play an important role may suggest that the M2 phase is actually more complicated than a simple fermionic metal.

Most of the previous work had focused on the study of the transitions using criteria at the lowest temperatures. One of the challenges of the present work was to **determine if we could access some information on the mechanisms leading to the observed ground states by characterizing the features appearing at higher temperature**. This has been the subject of my work which will more particularly **focus on the M2 and insulating phases**.

More specifically, amongst the questions that motivated this study were :
- Is the M1-to-M2 Transition a real phase transition or a crossover between, for instance, a regime dominated by superconducting fluctuations and a regime where the fermionic component dominates?
- Is the M2 phase fermionic or bosonic? Is it a 3D or a 2D phase? What are the relevant properties that define the dimensionality of such a phase? In other words, what are the dominant mechanisms at play ?
- How can we describe the $R(T)$ characteristics in the M2 phase? Could its evolution be explained by a pure weak localization behaviour before the resistance saturation sets in?
- How does the M2 phase behave close to the transition?
- The insulating regime had not yet been studied close to the M2-to-Insulator transition. How does the insulating phase emerge from a saturating resistance at low temperature when the transition is crossed ? Is the evolution continuous or abrupt ?
- 3D insulating a-Nb_xSi_{1-x} samples have previously been found to be Anderson insulators. Is this still the case in 2D? If so, how can the simply activated conductivity law be explained?
- Is the insulator fermionic or bosonic?

To perform this study, we fabricated - in addition to the pre-existing batches of samples - 6 films (batches CKSAS43 and CKSAS61) of a-$Nb_{13.5}Si_{86.5}$ with thicknesses ranging from 20 to 50 Å. Their composition and thicknesses have been specifically chosen in order to probe both sides of the M2-to-Insulator Transition. Heat treatment also enabled us to drive the M2 samples very progressively across the transition.

In the following, we will first present the low frequency transport characteristics of these new films at very low temperature (section 3.2) and verify that their properties are in agreement with previously measured a-Nb_xSi_{1-x} samples. We will then analyze the features of the insulating phase (section 3.3) before examining the M2 samples (section 3.4). In these sections, samples of previous batches will also be included in the analysis. Section 3.5 will particularly focus on

the M2-to-Insulator Transition. We will end this chapter by proposing a possible interpretation of the observed phenomena (section 3.6). But let us first justify our choice for the disorder parameter used throughout this chapter.

3.1 Relevant disorder parameter for transport measurement

In the following, we chose to expose our results by taking the films' **sheet resistance as the relevant quantity for transport measurements**, as is usual for thin films. This choice is consistent with the fact that our films are two-dimensional from the points of view of Coulomb interactions, localization, Variable-Range-Hopping and superconductivity, at least at temperatures lower than a few hundred mK (see discussion of the relevant length scales section 2.3.3.1). In addition, since we will mainly focus on the M2-to-Insulator Transition, both the coherence and localization lengths diverge at the transition, meaning that all samples are two-dimensional close enough to the transition. Moreover, as mentioned section 2.3.3.3, a previous work has shown that, for superconducting thin films of constant thickness, the 4 K sheet resistance R_{4K} drives the destruction of superconductivity [Crauste et al., 2013], thus emphasizing the 2D character of the transition.

In the same way, in the M2 regime, the relevant parameter is the normal sheet resistance R_{4K} (or equivalently $\sigma_{4K} = \frac{1}{R_{4K}}$). This assertion can be tested by qualitatively comparing the behaviour of films with similar R_{4K} or similar $\rho(4\text{ K})$. We have done so on figures 3.1 and 3.2 for films in the M2 regime. Two films with similar R_{4K} have similar evolutions in temperature and the value of the metallic saturation resistance is almost identical (with a 20% difference on the value of $R_\square$ at 10 mK for a 2.5 % difference in R_{4K}). On the other hand, two films with similar $\rho(4\text{ K})$ do not behave similarly a low temperature. Indeed, the resistivity of the thinner film is lower at high temperature. Eventually, the resistivities measured at 10 mK differ by ~ 100 % for a 1.2% difference in $\rho(4\text{ K})$. Moreover, analysis shows that these 2 samples follow different conduction laws as we will later see. Taking $R_\square(300\text{ K})$ or $\rho(300\text{ K})$ as references for comparing different samples yields the same result : the sheet resistance, and not the resistivity, seems to determine unequivocally the low temperature behaviour and the ground state of the system. Therefore, the 2D quantity - namely R_{4K} - seems more appropriate to describe the disorder in our films.

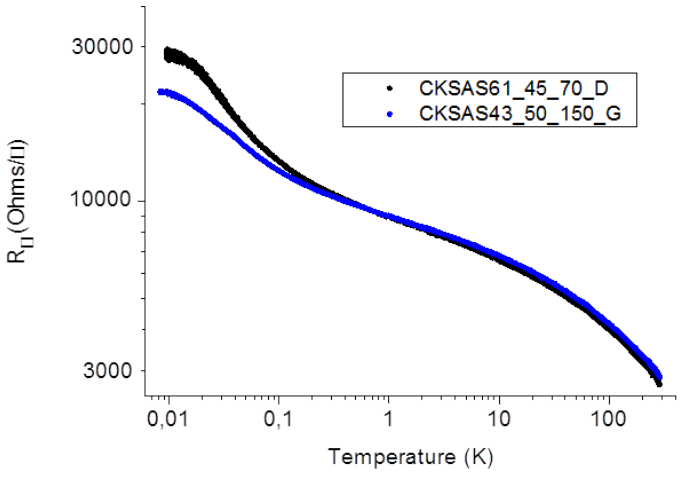

Figure 3.1: Comparison of the $R_\square$(T) characteristics of two a-$Nb_{13.5}Si_{86.5}$ films of similar R_{4K} (an as-deposited 45 Å-thick film of the CKSAS61 batch is displayed in black and 50 Å-thick film of the CKSAS61 batch, having sustained a heat treatment at 150 ℃, is displayed in blue).

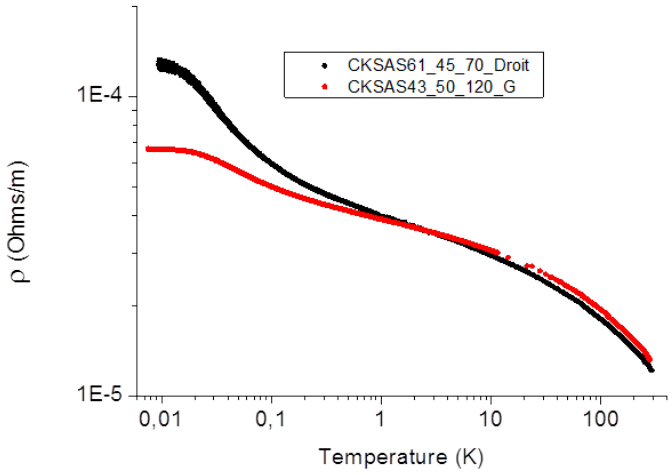

Figure 3.2: Comparison of the ρ(T) characteristics of two a-$Nb_{13.5}Si_{86.5}$ films of similar ρ(4 K) (an as-deposited 45 Å-thick film of the CKSAS61 batch is displayed in black and 50 Å-thick film of the CKSAS61 batch, having sustained a heat treatment at 120 ℃, is displayed in red).

3.2 Thickness evolution of the properties of the samples

As seen in section 2.3.3.2, the electrical properties of thin a-Nb_xSi_{1-x} films at a given composition depend on the thickness of the film. By varying the thickness, one can therefore tune both the electrical properties and the ground state of as-deposited films at a given x.

In this section, we will first present the evolution of the resistance of our samples as a function of temperature. Then, by comparing the 4 K electrical properties of the samples with those obtained from previous sets, we will define the extension of disorder explored in this work. Finally, we will detail the effects of heat treatment, used to finely modify the level of disorder within each sample and, in some cases, to cross the M2-to-Insulator Transition.

3.2.1 As-deposited films

We will here focus on the ground state - as well as its evolution as a function of the film thickness - for the as-deposited films grown in the framework of this thesis. Measurements of the sheet resistance for two different parts of each sample (parts a and c shown figure 3.3) are presented figure 3.4. Depending on the probed sample area, we observe small variations of the $R_{\square}(T)$ characteristics. These can be explained by a gradient in composition x along the sample [1], and are sufficiently small to be neglected ($\sim$ 5 % on the sheet resistance at all temperature for the as-deposited metallic samples presented and more generally less than 3 % on R_{4K}). This is yet another evidence that the films are homogeneous in thickness and composition.

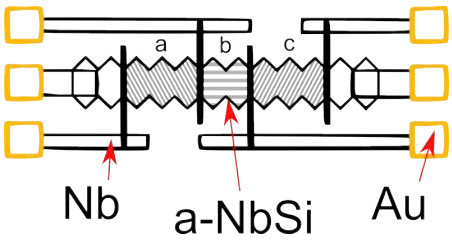

Figure 3.3: Sample design. a, b and c refer to different parts of the sample which can be separately measured in a 4 probes configuration.

1. These variations cannot be avoided during co-deposition. As mentioned section 2.2.1.1.b, they have a maximum value of 0.2 % between the two sides (a and c) of a single film.

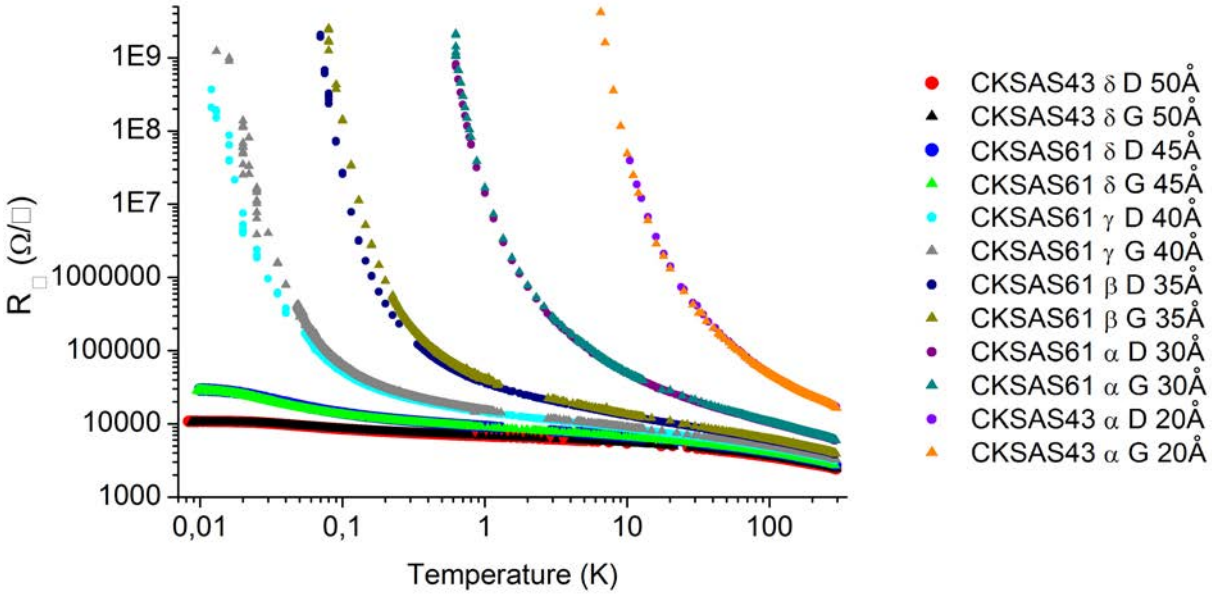

Figure 3.4: Resistance as a function of temperature for the as-deposited films grown in the framework of this thesis The "D" films correspond to part c of the film, whereas "G" films correspond to part a of the film.

For the thinnest films, R_{4K} is large (a few tens of kΩ), and the corresponding ground state is insulating. The thickest films (50 Å and 45 Å-thick a-$Nb_{13.5}Si_{86.5}$ films presented figure 3.5) have a resistance that first increases as the temperature is lowered and then saturates at very low temperature. They have been identified to be in the M2 regime described section 2.3.3.4 [2]. We would like to emphasize that, as shown figure 3.5, these saturations mark an abrupt change in the behaviour of the resistance compared to that encountered at higher temperatures.

Let us remark that the 45 Å-thick film on the metallic side of the transition and the 40 Å-thick film on the insulating side are really close to the transition. **The transition between the M2 and insulating states is therefore extremely abrupt**, as it occurs within a change in thickness smaller than 5 Å. It is therefore convenient to use a tuning parameter other than the thickness in order to progressively cross the transition. In this thesis, this parameter is provided by the heat treatment. However, as the saturations in resistance occur at very low temperatures, we should first verify that the observed results are intrinsic to the sample and not linked to experimental artefacts.

3.2.2 Experimental artefacts

For this study, it is particularly important, especially in the M2 regime where we do observe saturations of the resistivity at the lowest temperatures, to be sure that the observed phases are intrinsic to the samples and are not the result of experimental artefacts. In addition to the precautions taken in the design of the setup - which have been detailed section 2.2.3.3 - different experimental facts allow us to state that these phases are not linked to spurious effects.

As one can observe figure 3.4, we were able to measure insulating samples down to 13 mK. For instance, for the film CKSAS61 γ D 40Å (also shown figure 3.6a.), the resistivity has been found to follow a thermally activated law $R = R_0 e^{\frac{T_0}{T}}$ at low temperatures. By plotting the logarithmic resistance as a function of $1/T$ (figure 3.6 (b)), one can observe that there is no deviation from the activation law down to the lowest measurable temperatures. As **we are able to measure insulating samples**, we are sure that the electrons of the films are well thermalised at temperatures down to 13 mK.

2. Let us note that, according to the Dirty Boson Model, these films should be insulating, as they have a negative TCR at all temperatures.

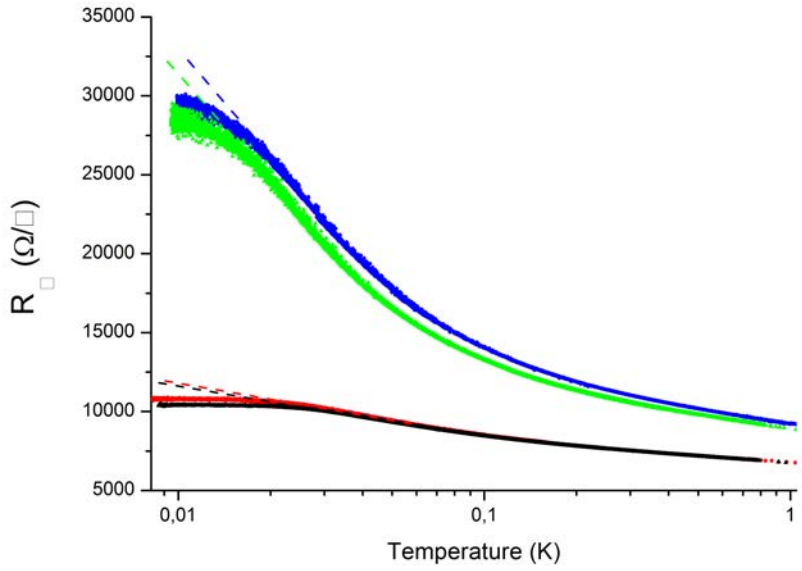

Figure 3.5: Resistance as a function of temperature for as-deposited 50 Å (red and black points for the corresponding "D" and "G" films) and 45 Å-thick (green and blue points for the corresponding "D" and "G" films) a-$Nb_{13.5}Si_{86.5}$ films. These exhibit saturations of the resistance at the lowest temperatures. The dashed lines correspond to guides to the eye obtained by the linear extrapolation of data before the saturations.

To measure this insulating behaviour, the maximum electrical power that could be injected before heating the film with the DC apparatus presented in section 2.2.3.2 was $P_{max} \sim 2.10^{-17}$ W at 13 mK. For thicker films, as the electron-phonon coupling is proportional to the volume of the film, the electrical power that could be used without heating the sample is larger. For the as-deposited films in the M2 regime, **the maximum power used for measuring the sample is of the order of $\sim 10^{-17}$ W, lower than P_{max}**. Furthermore, **films were measured at different excitations** to ensure that the resistance was measured in the Ohmic regime.

Finally, to ensure that the existence of the M2 regime was not linked to any electrical noise or parasitic power [3] which could induce a flattening of the measured resistance at low temperature, some samples in the M2 regime have been measured using **cold electronics** and **different**

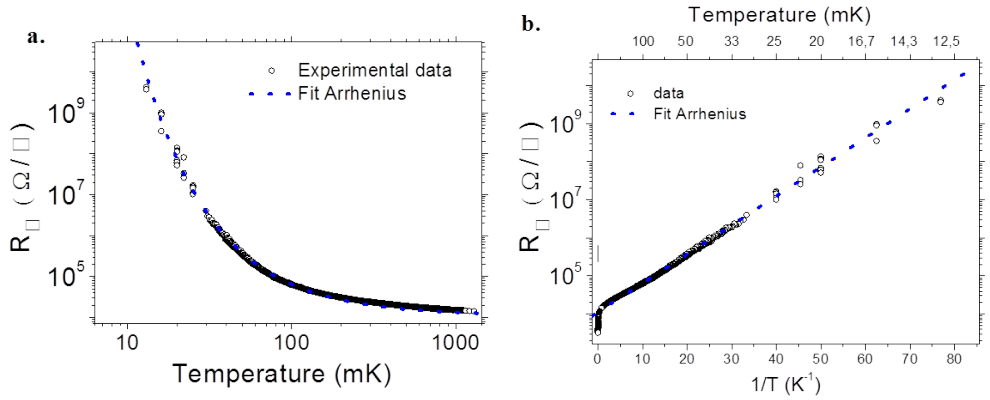

Figure 3.6: (a) Sheet resistance of the as-deposited 40 Å-thick a-$Nb_{13.5}Si_{86.5}$ film grown in the framework of this thesis. (b) Close-up of the sheet resistance of the film at low temperature. The dashed blue line corresponds to an activated law $R = R_0 e^{\frac{T_0}{T}}$.

3. Including infrared radiation, current noise and voltage noise.

cryostats[4] [Marrache-Kikuchi, 2006] with the same results.

In all cases, the existence of these metallic phases has been found to be **independent of the surface of the sample, of its volume, of its resistance or conductance, of the parasitic infra-red environment, of the electronic noise and of the measurement power** (when measured in the Ohmic regime). Therefore, we believe **the observed phases are intrinsic to our samples**.

3.2.3 Inclusion in other sets of data

Continuity in the measured electrical characteristics of the films between different batches is crucial. Indeed, it ensures the auto-coherence of the measurements and permits to exclude pathological samples.

The effects of a modification of the thickness or of the composition of the sample on the 4 K sheet resistance are presented figure 3.7. In the case of a-$Nb_{13.5}Si_{86.5}$, corresponding to the as-deposited samples, the new batch is in the continuity of the previously obtained ones. Furthermore, the evolution of the 4 K sheet resistance is compatible with those of films of different compositions x grown in previous studies.
To ensure continuity between the old batches and the new ones, we can in particular compare the characteristics of 50 Å-thick samples obtained during separate depositions (samples of batches OC5 and CKSAS43). The two experimental points obtained are superimposed on the plot given figure 3.7 and are reported in table 3.1, witnessing the **good reproducibility of the evaporation** conditions between the different batches.

Let us note that the sheet resistance increases with decreasing thickness $d_\perp$, faster than $\frac{1}{d_\perp}$. As remarked in previous work [Crauste, 2010] [Couëdo, 2014], this evolution cannot be explained by a simple model. Indeed, at low thickness (typically $d_\perp < 100$ Å), it is steeper than what is expected from Fuchs law[5].

The values of the sheet resistance, as well as the corresponding conductivity and ground state, are summarised for as-deposited a-$Nb_{13.5}Si_{86.5}$ films in the table 3.1. The 20 Å-thick sample is not displayed as its 4 K resistance is higher than the measurement capability of our apparatus (typically 10 GΩ).

3.2.4 Evolution as a function of heat treatment

Starting from the as-deposited films presented figure 3.4, we used the heat treatment procedure described section 2.2.1.3 to finely tune the disorder. Its effect on the measured sheet resistance of the film, is presented figures 3.9 to 3.14 for all samples grown in the framework of this thesis. When increasing the heat treatment temperature, the sheet resistance of the films is increased : the sample's disorder becomes larger.

As can be seen figure 3.8, σ_{4K} decreases linearly as the heat treatment temperature θ increases. This behavior is a sign that there is no major morphological modification in these films [Crauste, 2010] [Crauste et al., 2013] and characterizes the effect of the sole disorder on electrical properties of our samples. Films of different batches, with same thickness and composition confirms the reproducibility of the heat treatment effects (shown here on 50 Å-thick samples).
The advantage of a-Nb_xSi_{1-x} films is here apparent : by varying the different tuning parameters for this system ($d_\perp$, θ and x), **we are able to probe a very large spectrum of disorder levels**. Even if only considering as-deposited samples of $x = 13.5\%$, σ_{4K} ranges from 0.16 to 70.7 $\frac{e^2}{h}$ if one includes all batches, both new and previously grown.

At lower temperatures, one can see the effects of heat treatment on both sides of the M2-to-Insulator Transition : films which were already in the insulating phase become even more insulating (figures 3.9, 3.10, 3.11 & 3.12), whereas films initially in the M2 regime come closer

4. i.e. different electromagnetic environments.
5. The Fuchs law explains an increase in the resistivity ρ as $d_\perp$ is decreased through surface scattering effects (see section 1.7.1).

Sample	Thickness $d_\perp$(Å)	R_{4K} (Ω)	σ_{4K} ($\frac{e^2}{h}$)	Ground state
OC5	350	366	70.7	Superconductor
OC5	300	600	43	Superconductor
CKSAS33	230	691	37.4	Superconductor
OC5	250	739	34.9	M1
CKSAS33	185	863	29.9	M1
OC5	200	929	27.8	M1
CKSAS33	165	990	26.1	M1
CKSAS33	140	1315	19.6	M2
OC5	150	1390	18.6	M2
OC5	100	2170	11.9	M2
CK11	130	2390	10.8	M2
OC5	75	3170	8.1	M2
CKSAS43	50	6049	4.3	M2
OC5	50	6420	4	M2
CKSAS61	45	7600	3.4	M2
CKSAS61	40	10800	2.4	Insulator
CKSAS61	35	18800	1.4	Insulator
CKSAS61	30	162000	0.16	Insulator

Table 3.1: List of as-deposited a-$Nb_{13.5}Si_{86.5}$ samples. These include pre-existing (from [Marrache-Kikuchi, 2006] [Crauste, 2010] & [Couëdo, 2014]) and new batches. The 4 K sheet resistance (R_{4K}) and the conductivity (σ_{4K}) as well as the corresponding ground state are mentioned.

to the transition (figure 3.14) or even cross the transition (figure 3.13).

In the following, we will study in more details the quantitative features of these evolutions, but let us already note that, in the M2 regime, the insulating-like behavior observed between 40 mK and 1 K is all the more pronounced as θ increases. Moreover, the maximum resistance - which corresponds to the value at saturation - increases strongly with θ, gaining more than 1 order of magnitude in the case of the 45 Å-thick films between $\theta = 70$ ℃ and $\theta = 100$ ℃. At the same time, the temperature below which the saturation in the M2 samples appears tends to decrease until it vanishes.

For both the insulating and the metallic films grown for this thesis, increasing the disorder via either a modification of the thickness or a heat treatment procedure therefore sharpens the increase of resistance as a function of temperature, due to enhanced localization effects. To go beyond this qualitative approach, we will here try to characterize this evolution, first in the insulating samples and later in the metallic ones, by including - in addition to our samples - batches from [Marrache-Kikuchi, 2006] [Crauste, 2010] and [Couëdo, 2014]. We will also propose and discuss a way to analyze our samples characteristics near the M2-to-Insulator Transition.

3.3 Analysis of the insulating phase

To analyze our insulating samples, we will restrict ourselves in this section to the study of the activated resistivity [6] which is expected at low temperature for disordered insulating samples (see section 1.5.1). As we will see later, different conduction processes, mainly due to weak localization, become dominant at higher temperature. These will be briefly discussed in section 3.4.2.

A first approach to characterize insulating samples has been performed in [Couëdo, 2014] where the conduction mechanism had been analyzed as a unique simply activated law (of Arrhenius-type). As we will see in the following, this description is valid at very low temperatures but fails at higher temperatures. In the following, we will describe the transport characteristics of insulating samples at all temperature scales (from 10 to 100K) and we will analyze the different

6. Variable Range Hopping or simply activated conduction.

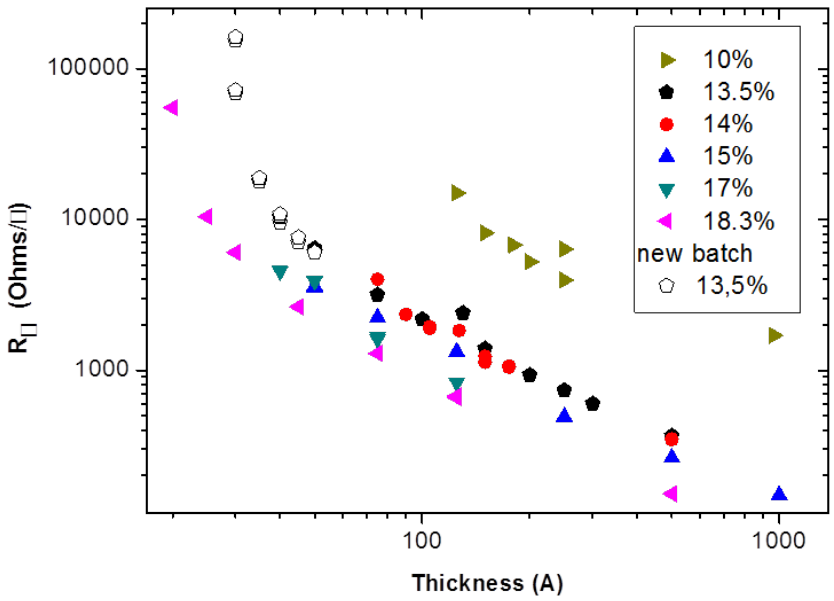

Figure 3.7: 4 K sheet resistance of films of different compositions as a function of the thickness. The set of samples grown for this thesis is represented by open symbols.

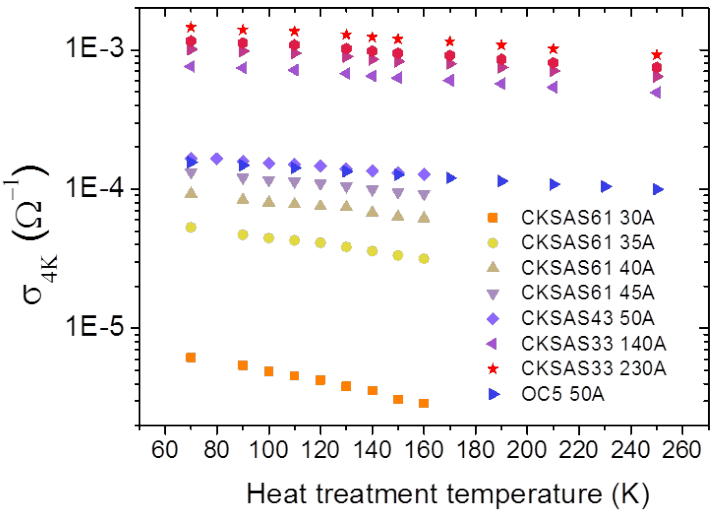

Figure 3.8: Evolution of the conductance as a function of the heat treatment temperature for samples of table 3.1.

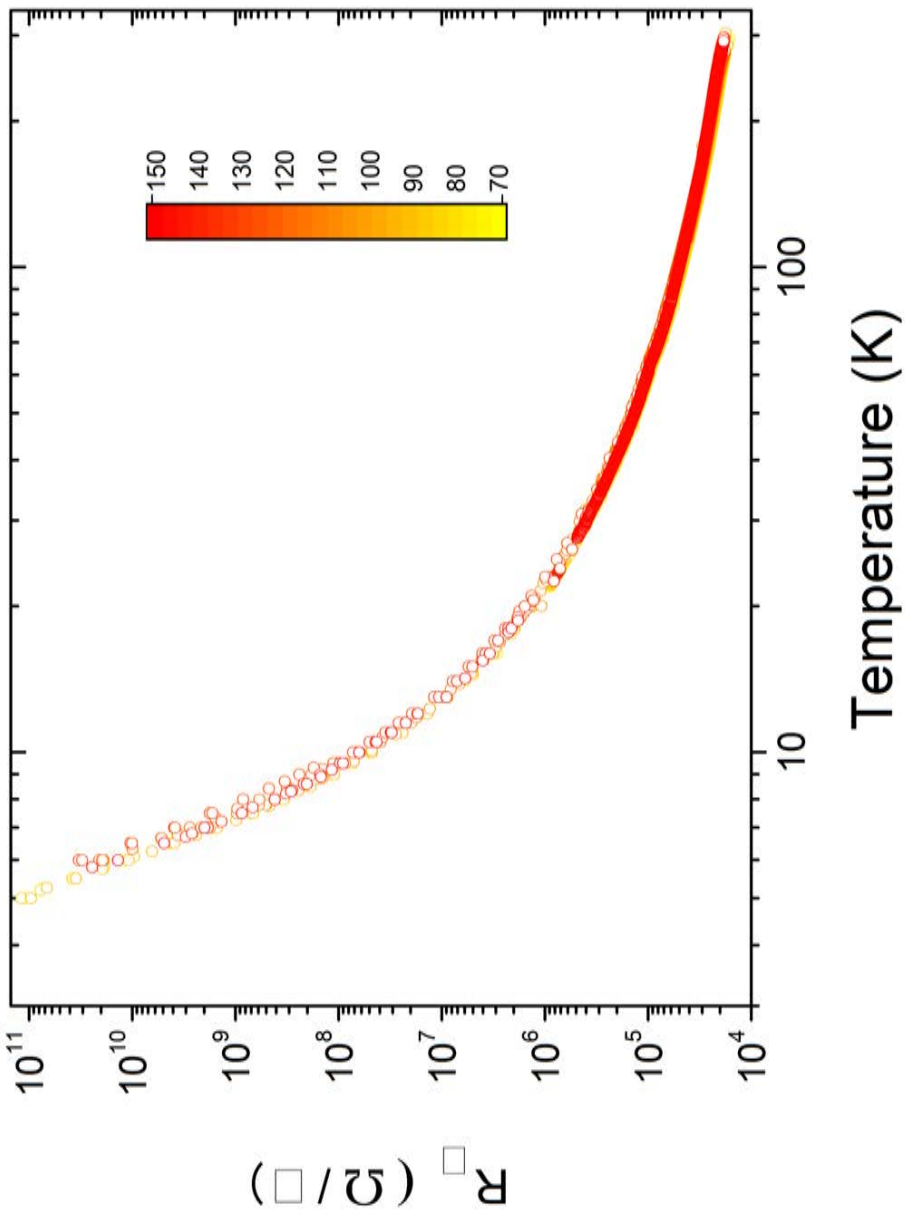

Figure 3.9: Evolution of the sheet resistance $R_{\square}$ as a function of temperature for different heat treatment temperatures for sample CKSAS43 α (20 Å).

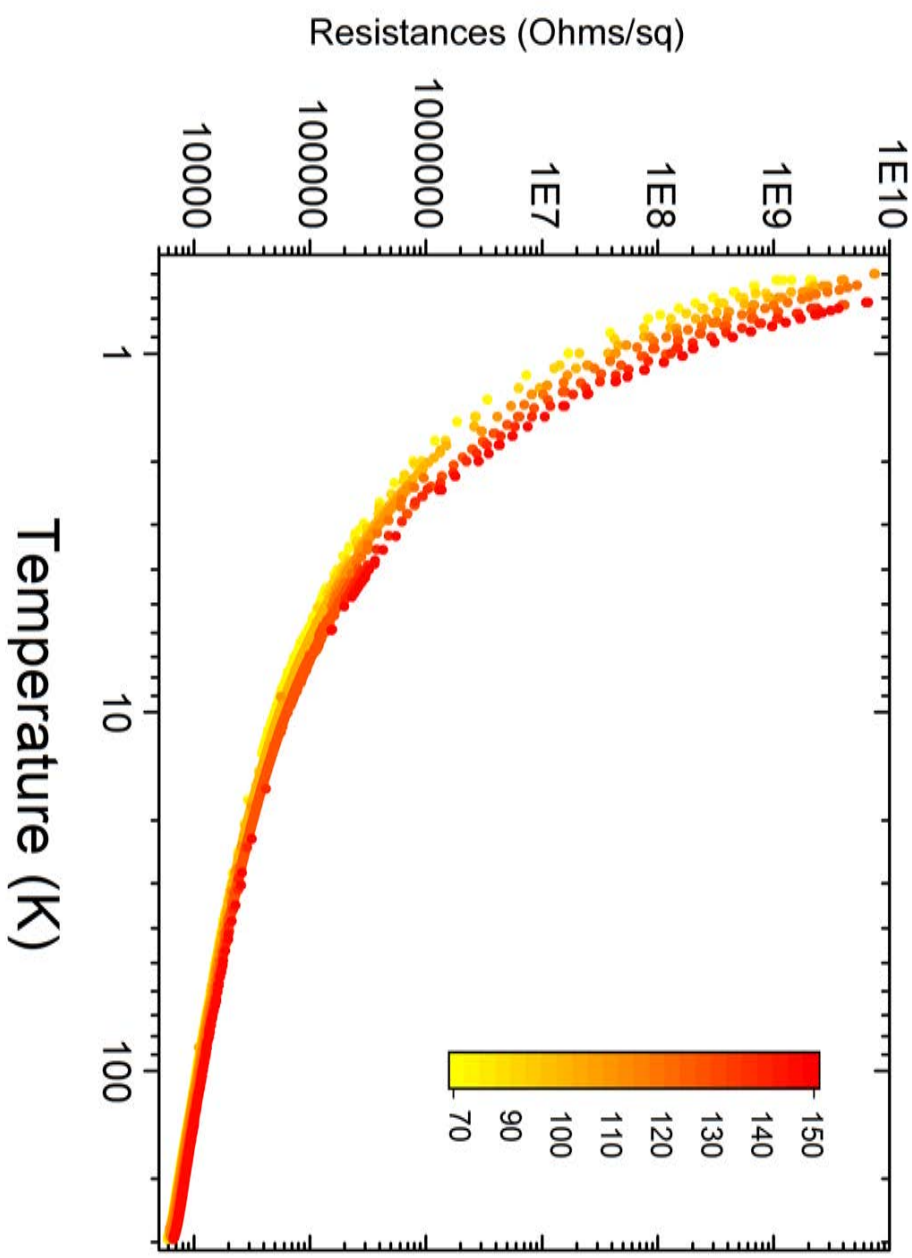

Figure 3.10: Evolution of the sheet resistance $R_{\square}$ as a function of temperature for different heat treatment temperatures for sample CKSAS61 α (30 Å).

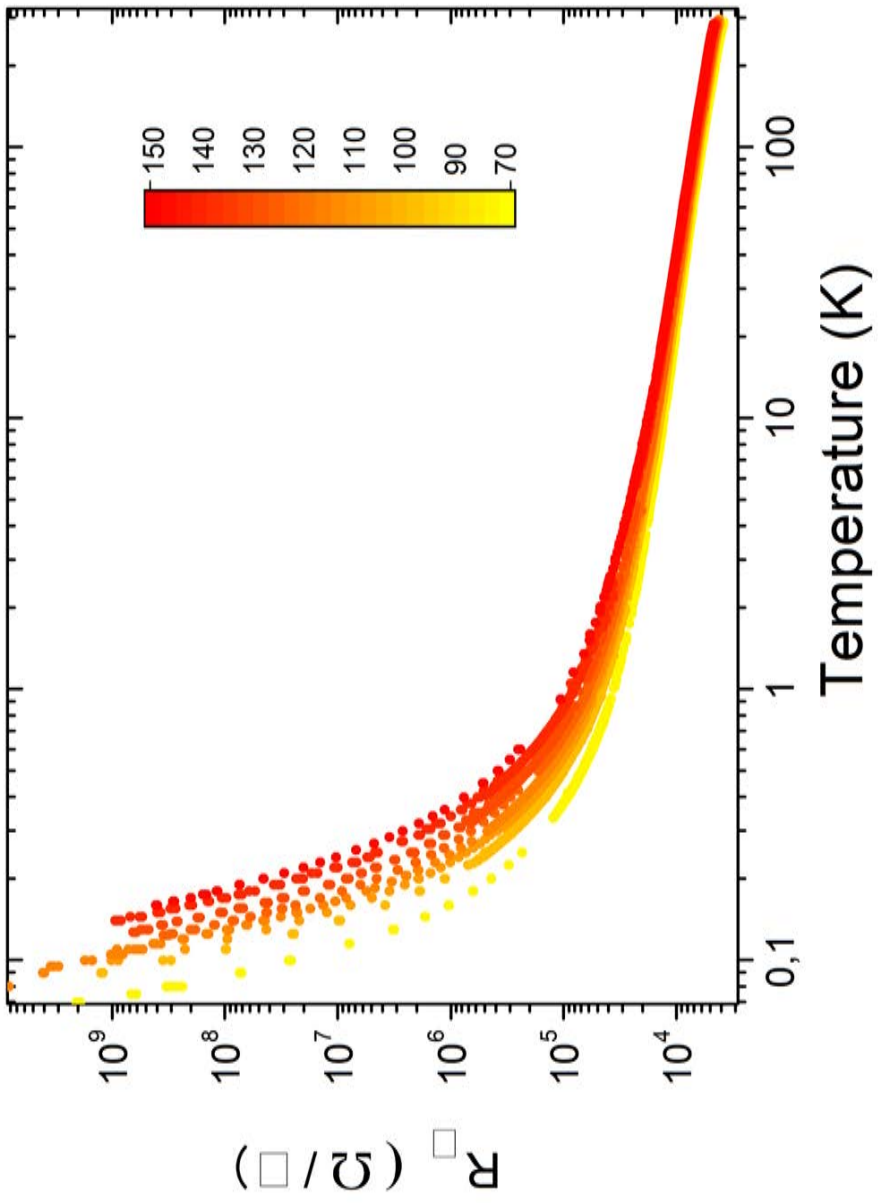

Figure 3.11: Evolution of the sheet resistance $R_\square$ as a function of temperature for different heat treatment temperatures for sample CKSAS61 β (35 Å).

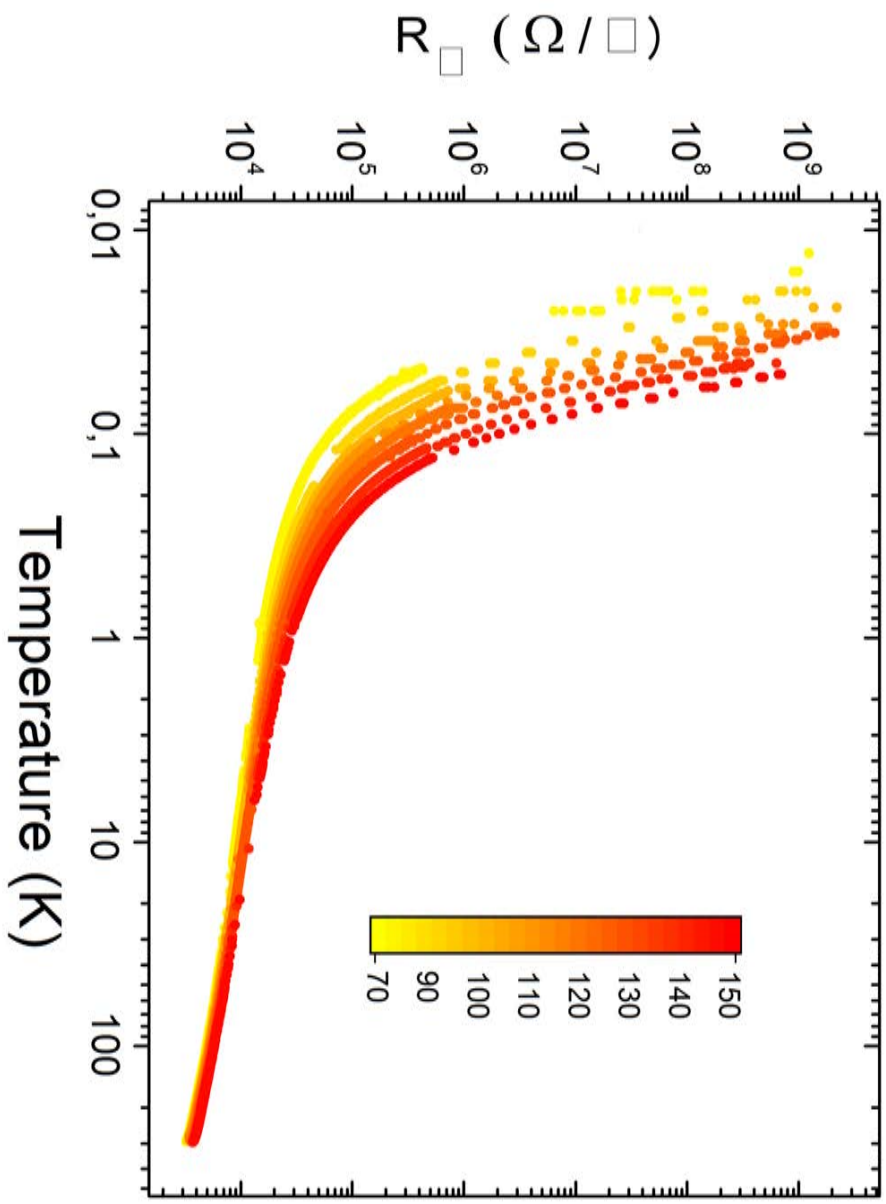

Figure 3.12: Evolution of the sheet resistance $R_{\square}$ as a function of temperature for different heat treatment temperatures for sample CKSAS61 γ (40 Å).

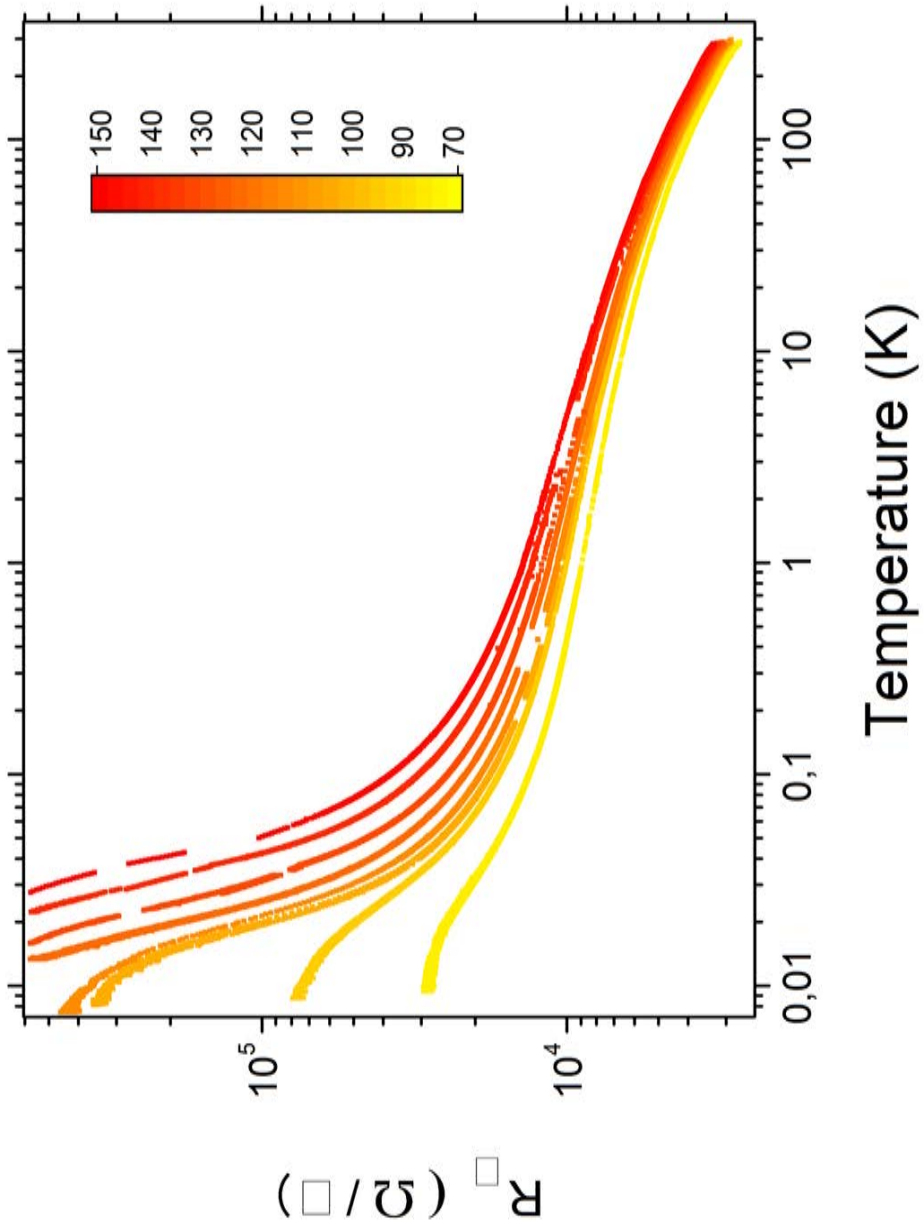

Figure 3.13: Evolution of the sheet resistance $R_\square$ [a] as a function of temperature for different heat treatment temperatures for sample CKSAS61 δ (45 Å).

a. Let us note that, in the case of this sample, the low temperature values of the sheet resistance is of the order of a few 100 kΩ. This range in resistance is particularly tricky to measure properly at very low temperatures : the DC apparatus does not give sufficient resolution in this range and the low-frequency TRMC2 apparatus has a minimum current of 10 pA thus inducing a typical measurement power of $\sim 3.10^{-17}$ W for a 100 kΩ sheet resistance. Although we have taken all the precautions listed in section 3.2.2, the measured resistance could have an increased uncertainty for temperatures lower than 13 mK for heat treatments such that $120 \geq \theta \geq 100$ °C. The effective M2-to-Insulator Transition will be identified in section 3.5.1 by taking this caveat into account.

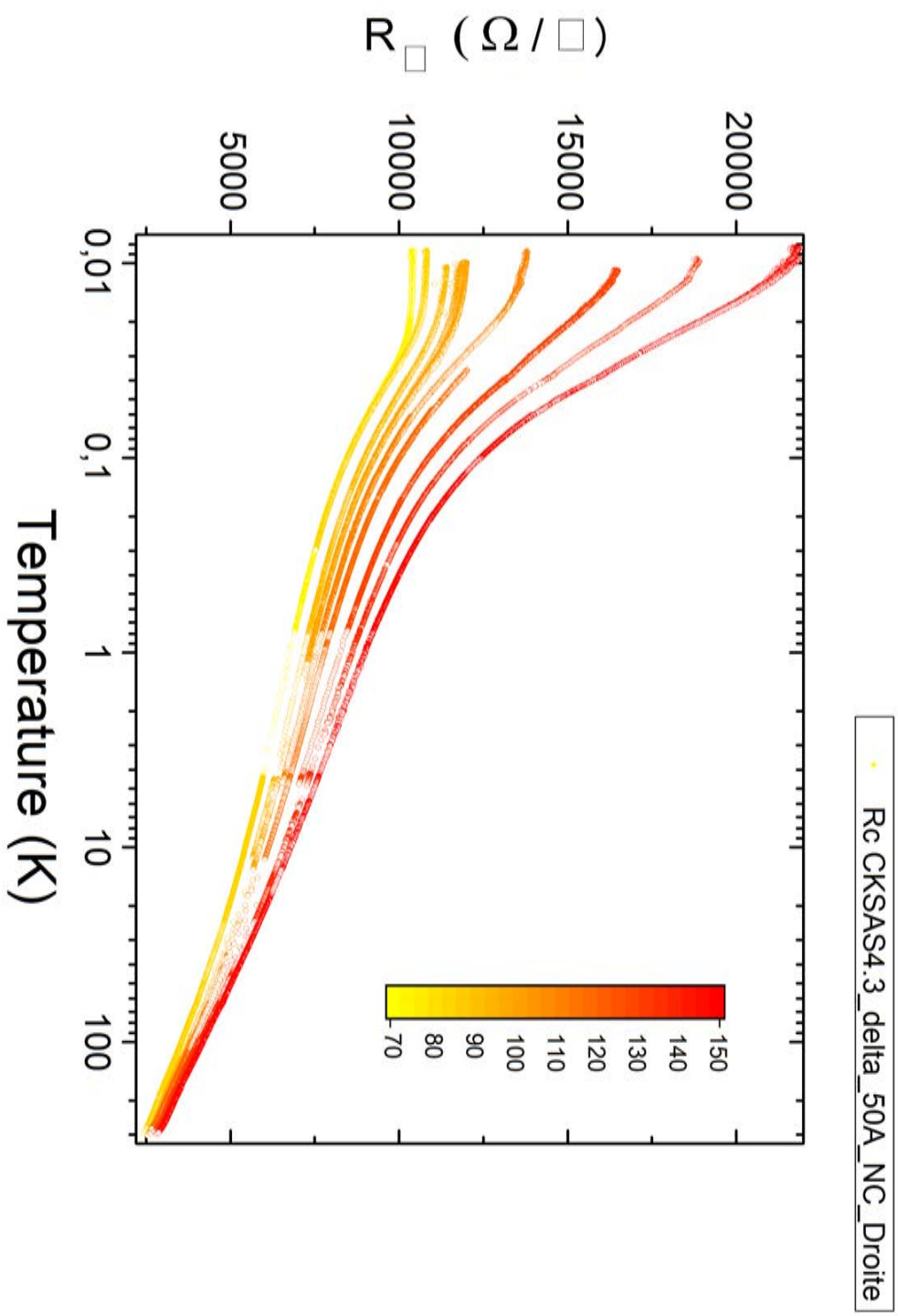

Figure 3.14: Evolution of the sheet resistance $R_{\square}$ as a function of temperature for different heat treatment temperatures for sample CKSAS43 δ (50 Å).

regimes and corresponding crossovers.

3.3.1 Brief overview of our results

Before beginning the analysis, we would like to briefly overview our approach in the study of insulating samples. This section will serve as a guideline for the following paragraphs.

Let us recall that for activated conduction, the resistance takes the form (section 1.5.1):

$$R = R_0 e^{(\frac{T_0}{T})^n} \tag{3.1}$$

where R_0, T_0 and n are constants characteristic of the conduction mechanism at play. Depending on the relevant conduction process and the dimensionality d (2 or 3) regarding the hopping mechanism, one can obtain different parameters n ranging from $n = 1/4$ to 1, such that :

- $n = 1$ for an simply activated or Arrhenius law, characteristic of either Nearest-Neighbour-Hopping conduction or a hard gap.
- $n = \frac{1}{2}$ for Efros-Shklovskii (ES) Variable Range Hopping (VRH), characteristic of the existence of a Coulomb gap.
- $n = \frac{1}{d+1}$ for Mott Variable Range Hopping, characteristic of hopping while having a constant density-of-states.

We will use the so-called Zabrodskii's method described in section 3.3.2.1 to obtain the value of the parameter n. We will characterise how conduction evolves as a function of the temperature and observe successive insulating regimes. At the lowest temperatures a conduction law with $n \sim 1$ will systematically be observed, giving way to VRH laws at higher temperature. Depending on disorder, we will observe different behaviours which are represented figure 3.15. In addition with $n \sim 1$ at the lowest temperature, we will observe :

- for the most disordered films (typically $\sigma_{4K} \lesssim 0.05\ \frac{e^2}{h}$), a crossover to an ES-VRH regime (figure 3.15a).
- for less disordered films (typically $0.05 \lesssim \sigma_{4K} \lesssim 2\ \frac{e^2}{h}$), successive crossovers to $n = 1/2$ and $n = 1/3$ regimes (figure 3.15b), $n = 1/3$ corresponding to a 2D Mott VRH law.
- For films closer to the MIT, the Mott regime will scarcely be visible as its range in temperature shrinks. We will describe our data in the activated regime with $n \sim 1$ at the lowest temperatures and $n = 1/2$ at intermediates temperature, before weak localization sets in (see section 3.4.2).

A first overview of our insulating samples and of their conduction behaviours below 1 K is given in figure 3.16 for selected samples with $2.5 > \sigma_{4K} > 1.1\ \frac{e^2}{h}$.

In the following, we will call :

- T_{c1} **the highest temperature at which a $n \sim 1$ regime is observed.**
- T_{c2} **the highest temperature at which the ES VRH regime is observed.**
- T_{c3} **the highest temperature at which the 2D Mott VRH regime is observed.**

The identification and the consistency of the different activated laws encountered in the insulator will be tested by extracting physical quantities for the different laws as well as through their evolution with disorder. The corresponding analysis will allow us to express hypotheses on the various regimes.

3.3.2 Identification of the different laws in the insulator

3.3.2.1 Identification of the different parameters

In a paper studying the Metal-to-Insulator Transition in compensated semiconductors, **Zabrodskii** described a way to unequivocally find n for samples having a conduction law of the form :

$$R = A\,T^{-m}\,e^{(\frac{T_0}{T})^n} \tag{3.2}$$

We will see in appendix A.2 that - in our samples - m is negligible so that $A\,T^{-m}$ is equatable to a constant R_0 for all our samples. Under the condition of $m \ll 1$, Zabrodskii calculated that [Zabrodskii and Zinoveva, 1984] :

$$ln(-\frac{dln(R)}{dln(T)}) = ln(n\,T_0^n) - n\,ln(T) \tag{3.3}$$

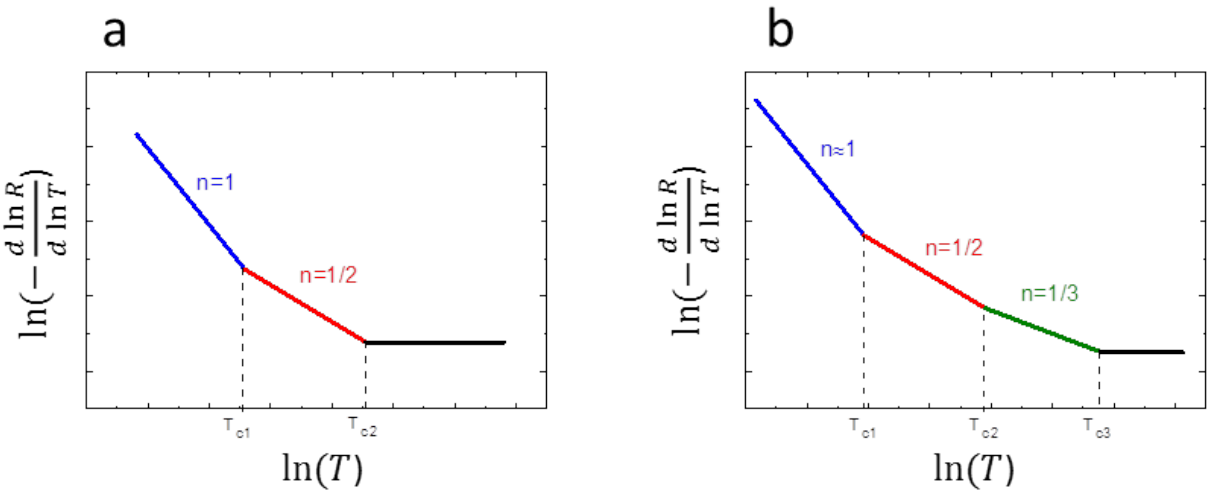

Figure 3.15: Schematic representation of the different observed regimes as a function of the temperature in the insulating phase. We observe (a) a unique transition from $n \sim 1$ to $n = \frac{1}{2}$ or (b) two successive crossovers $n \sim 1$, $n = \frac{1}{2}$ and $n = \frac{1}{3}$.

	Temperature	CKSAS61 45A G	CKSAS61 40A G	CKSAS61 40A G	CKSAS61 40A G	CKSAS61 40A G	CKSAS61 35A G	CKSAS61 35A G
Thickness (A)		45	40	40	40	40	35	35
Heat treatment temperature		150	70	100	130	150	70	110
composition		13,5	13,5	13,5	13,5	13,5	13,5	13,5
σ_{4K} (e^2/h)	-	2,44903	2,34236	2,07165	1,84246	1,63787	1,35146	1,10453
	0,01	Arr	Arr	no data	no data	no data	no data	no data
	0,02	Arr	Arr	Arr	no data	no data	no data	no data
	0,03	Arr	Arr	Arr	Arr	no data	no data	no data
	0,04	Arr	Arr	Arr	Arr	no data	no data	no data
	0,05	Arr	Arr	Arr	Arr	Arr	no data	no data
	0,06	Arr	Arr	Arr	Arr	Arr	no data	no data
	0,07	Arr	Arr	Arr	Arr	Arr	no data	no data
	0,08	Arr	Arr	Arr	Arr	Arr	Arr	no data
	0,09	Arr	Arr	Arr	Arr	Arr	Arr	no data
	0,1	Arr	ES	ES	Arr	Arr	Arr	Arr
	0,2	ES	ES	ES	Arr	Arr	Arr	Arr
	0,3	ES	ES	ES	Arr	Arr	Arr	Arr
	0,4	ES	ES	ES	ES	Arr	Arr	Arr
	0,5	ES	ES	ES	ES	Arr	Arr	Arr
	0,6	ES	ES	ES	ES	ES	Arr	Arr
	0,7	ES	ES	ES	ES	ES	Arr	Arr
	0,8	ES	ES	ES	ES	ES	Arr	Arr
	0,9	ES	ES	ES	ES	ES	ES	Arr
	1	ES	ES	ES	ES	ES	ES	Arr

Figure 3.16: Illustration of the different regimes observed near the M2-to-Insulator Transition at low temperature ($T < 1$ K) for a selection of samples. The $n \sim 1$ activated regime is represented in grey. ES VRH regime is represented in green. Black cells correspond to $R \gtrsim 10^{10}\,\Omega$ (too large to be measured). The Mott regime, not pictured here, is observed at higher temperature for samples with $\sigma_{4K} < 2\ \frac{e^2}{h}$.

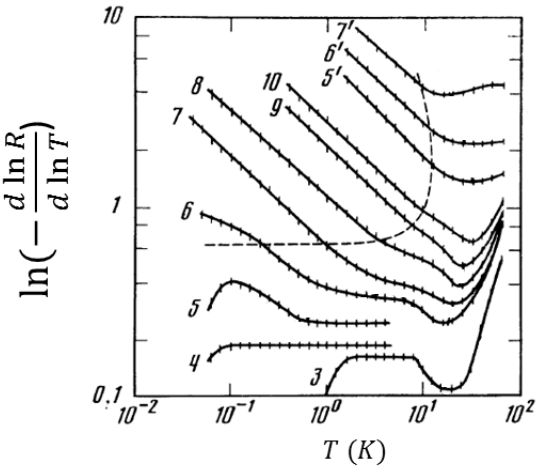

Figure 3.17: $log(-\frac{dln(R)}{dln(T)})$ plotted as a function of $log(T)$ for compensated Ge samples, with different degrees of compensation. Samples 3, 4 and 5 have a metallic ground state. The other films are insulating. The dashed curve corresponds to the limit in temperature where $log(-\frac{dln(R)}{dln(T)})$ has a linear dependence as a function of $log(T)$ for each sample. Adapted from [Zabrodskii and Zinoveva, 1984].

By plotting $ln(-\frac{dln(R)}{dln(T)})$ as a function of the logarithmic temperature $ln(T)$, we can therefore extract the parameter n from the slope of the obtained affine function. As pictured figure 3.17, there is a clear transition between the Variable Range Hopping regime, which gives rise to a linear dependence, and other regimes with a non-exponential evolution of $R(T)$. In particular, metallic samples (samples 3, 4 and 5 in this study) appear, in this representation, with a positive derivative when $T \to 0$, unlike insulating samples.

At this point, let us mention that, in the case of our samples, for each insulator, n has been extracted both :
- by setting n to values predicted by standard theories ($n = \frac{1}{3}$, $n = \frac{1}{2}$ or $n = 1$).
- and by letting n be a free parameter, obtained by Zabrodskii's method.

Except otherwise mentioned, both methods yield the same results within error bars.

By using the extracted value of the parameter n, we can obtain parameters R_0 and T_0 through :

$$ln(R) = ln(R_0) + (\frac{T_0}{T})^n \tag{3.4}$$

Thus, by plotting $ln\, R$ as a function of $(\frac{1}{T})^n$, all parameters are obtained by making no other assumption than the exponential variation of the resistance as a function of temperature.
We will now examine the evolution of the different relevant parameters in our films both in temperature and with disorder.

3.3.2.2 Application to our films

At first, let us apply this method to our thinnest - most disordered - as-deposited sample (figure 3.18). Depending on the temperature range, we obtain different values of n. At the lowest temperatures, $n = 1$. We would like to stress that finding a simply activated regime at the lowest temperatures is unusual in the literature of disordered films. We will come back on this point later in section 3.6.
As the temperature is increased, a crossover occurs between 25 and 35 K to an ES-type VRH regime, which adequately describes the data almost until room temperature.

The value of n obtained by Zabrodskii's method can then be checked by plotting $ln(R)$ as a function of the corresponding power of the temperature ($\frac{1}{T}$ for $n = 1$ is given figure 3.19, $\frac{1}{\sqrt{T}}$ for $n = \frac{1}{2}$ is given figure 3.20 for the 20Å-thick film presented above). The temperature range of each regime - i.e. the part where the curves are linear in $\frac{1}{T^n}$ - are in agreement with what is found figure 3.18. The fit of the linear part allows us to directly extract R_0 and T_0 for each identified regime. Let us note that for this highly disordered sample, both regimes are clearly

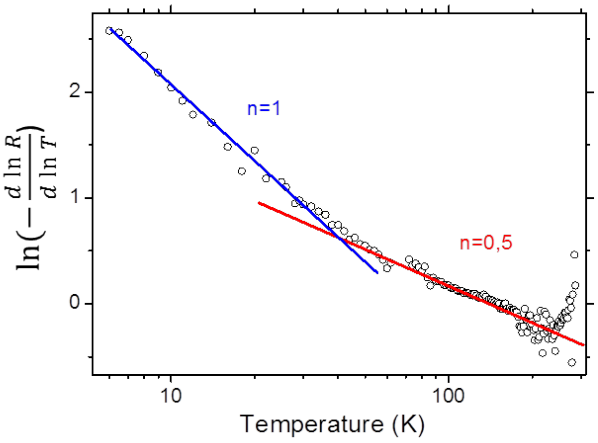

Figure 3.18: Extraction of the parameter n as a function of temperature for an as-deposited 20 Å-thick a-$Nb_{13.5}Si_{86.5}$ sample using Zabrodskii's technique. The extracted parameter n is equal to 1 at the lowest temperature and $\frac{1}{2}$ otherwise, almost until room temperature.

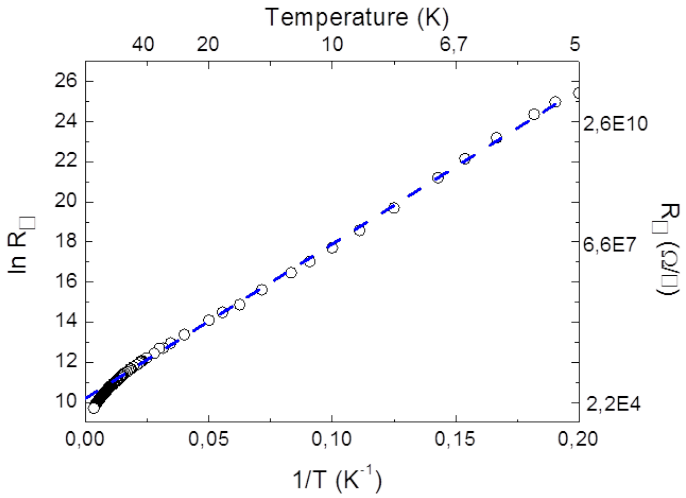

Figure 3.19: Sheet resistance $R_\square$ as a function of the inverse temperature for an as-deposited 20 Å-thick sample of a-$Nb_{13.5}Si_{86.5}$. The dashed line is a fit of the linear part of the plot. From this plot, we can extract $T_0 = 77 \pm 4$ K and $R_0 = 27 \pm 5$ $k\Omega$.

defined on about a decade both in temperature and in resistance as pictured figure 3.21. The good agreement between the law obtained from the extracted values of R_0, T_0 and n and the experimental data confirms the validity of the method.

For slightly less disordered films, we observe the same trend : Zabrodskii's method reveals a transition between a regime with $n = 1$ at the lowest temperatures and a VRH-type law at intermediate temperatures (figure 3.22). However, the identification of the exact regime at intermediate temperatures is less clear than in the previous example. The obtained plot for an as-deposited 30 Å-thick a-$Nb_{13.5}Si_{86.5}$ sample may indeed be compatible with a $n \sim 1$ regime at low temperatures having transitions either to :

- a sole ES VRH.
- successively an ES VRH and a 2D Mott VRH regime.
- a sole 2D Mott VRH.

We will later see that due to continuity of physical parameters as disorder evolves, the last scenario is unlikely.

In order to choose between the different cases which are still possible (i.e. cases a and b of figure 3.22), we have conducted numerous tests to examine the consistency of the evolution of the different regimes, especially with disorder and thickness, as well as the realism of the derived

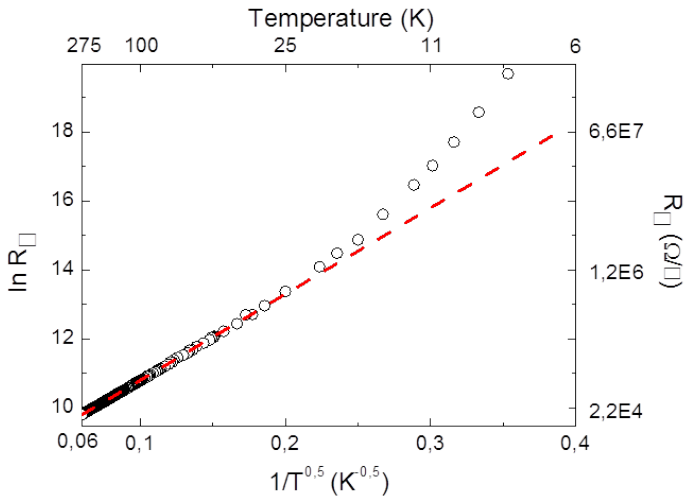

Figure 3.20: Sheet resistance $R_\square$ as a function of $\frac{1}{T^{0.5}}$ for an as-deposited 20 Å-thick sample of a-$Nb_{13.5}Si_{86.5}$. The dashed line is a fit of the linear part of the plot. From this plot, we can extract $T_{ES} = 625 \pm 25$ K and $R_{ES} = 3950 \pm 150$ Ω.

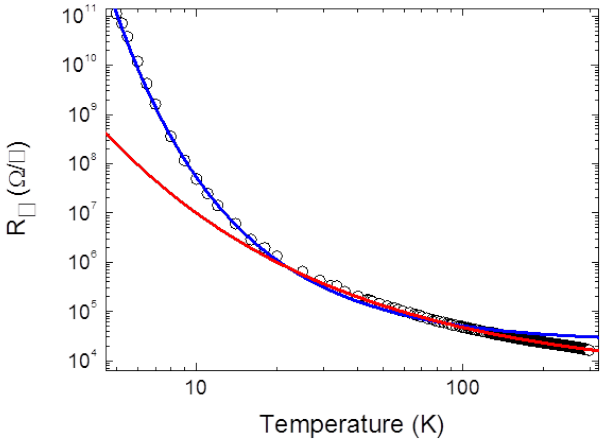

Figure 3.21: Sheet resistance $R_\square$(T) for an as-deposited 20 Å-thick sample of a-$Nb_{13.5}Si_{86.5}$. The blue line corresponds to the fit of the simply activated regime ($n = 1$) and the red line to the fit of the ES VRH regime ($n = \frac{1}{2}$).

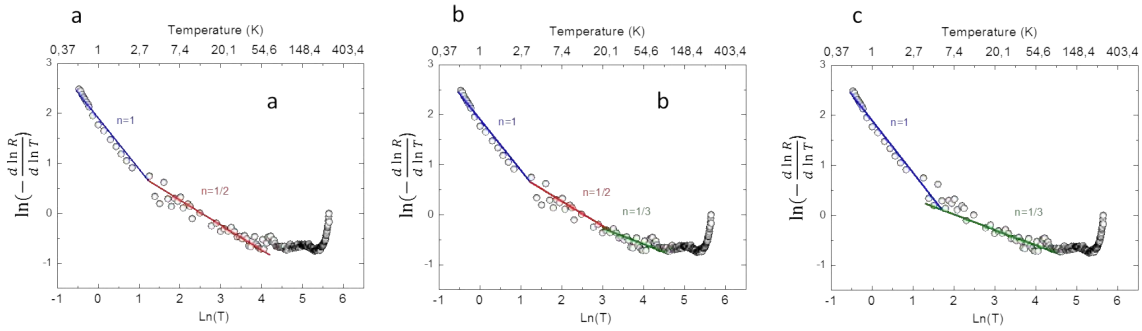

Figure 3.22: Extraction of the parameter n as a function of temperature for an as-deposited 30 Å-thick a-$Nb_{13.5}Si_{86.5}$ sample using Zabrodskii's technique. We observe successive crossovers between an activated regime and VRH regimes, compatible with different scenarii giving $n = 1/3$ or $n = 1/2$ for different temperatures (refer to text).

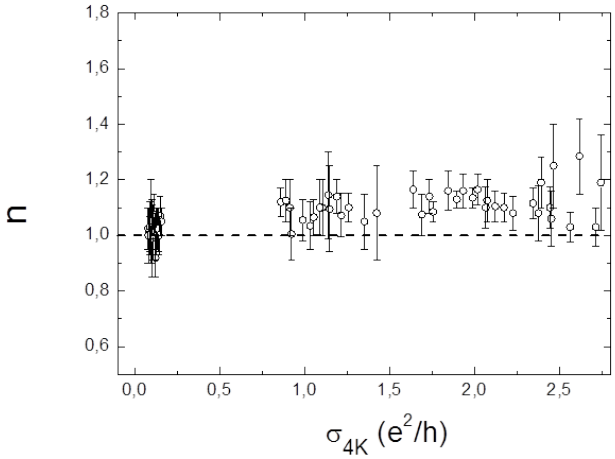

Figure 3.23: Parameter n extracted from Zabrodskii's method in the low temperature regime for the insulating samples grown for this thesis as a function of σ_{4K}.

characteristic parameters. We will here mainly expose the tests and the hypotheses that proved to be the most realistic and consistent.

3.3.2.3 Extraction of the parameters in the different regimes

The simply activated regime

We will here focus on the regime identified at the lowest temperature in our insulating films. Figure 3.23 shows the evolution of n, determined by Zabrodskii's method letting n be a free parameter, as a function of σ_{4K}. It is in good agreement with $n = 1$, with a $\sim 10\%$ discrepancy for $\sigma_{4K} < 1.5\,\frac{e^2}{h}$, which is within the error bars for these samples.
Close to the M2-to-Insulator Transition, we found $n > 1$ for some samples. This "super-activated" behavior cannot be attributed to uncertainties ($n - \Delta n > 1$). We will come back on a possible explanation for this unusual behaviour later (see appendix B). For now, let us stress that these samples cannot be described by a single law with $n = 1$ at the lowest temperatures, as shown figure 3.24. The corresponding samples could however be compatible with two $n = 1$ regimes, with different R_0 and T_0 (red and blue dashed lines on figure 3.24(a)), or with a more insulating law (green dashed line on figure 3.24(b)), $n = 1.25$ in the case of the 45 Å-thick a-$Nb_{13.5}Si_{86.5}$ sample which sustained a heat treatment at $\theta = 140$ ℃. These laws have been fitted on a resistance range larger than one decade.

For simplicity, and for coherence with the analysis performed close to the M2-to-Insulator

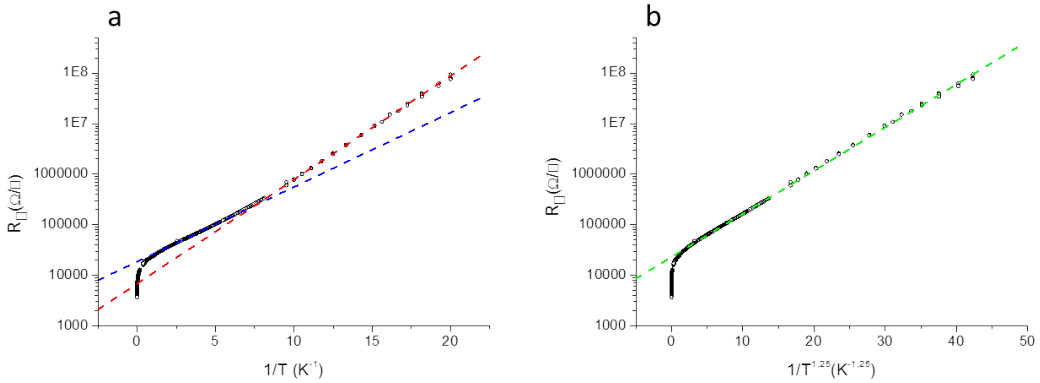

Figure 3.24: Sheet resistance of a 45 Å-thick a-$Nb_{13.5}Si_{86.5}$ insulating sample which sustained a heat treatment at 140 ℃. This sample is close to the M2-to-Insulator transition. It has been plotted as a function of the inverse temperature 1/T (a) and as a function of $1/T^{1.25}$ (b). The plot (a) is not consistent with a simple $n = 1$ regime at the lowest temperatures and may be described with 2 different $n = 1$ regimes or with a more insulating law (b) (n=1.25 in this case).

Transition, we have chosen to present parameters (R_0 ; T_0) obtained using the value of n extracted from Zabrodskii's method where n is set as a free parameter. We have verified that this treatment does not have a strong influence on the extracted parameters. It induces an uncertainty on the extracted T_0 and R_0 of a factor 2 at most compared to what we would obtain by setting $n = 1$. It does not modify the observed trends.

The evolution of parameters R_0 and T_0 with σ_{4K} is presented figure 3.25. The prefactor R_0 first decreases by a factor about 2 for highly disordered films ($\sigma_{4K} < 1.5\,\frac{e^2}{h}$) and tends to saturate as we get closer to the M2-to-Insulator Transition, with $R_0 \sim (13 \pm 3)$ kΩ/□ ($\sim \frac{e^2}{2h}$) for $\sigma_{4K} \to 3\,\frac{e^2}{h}$. Simultaneously, T_0 decreases continuously over about 3 orders in magnitude. Thus, both R_0 and T_0 seems to be independent of the thickness. Indeed, the evolution trend is similar whatever the thickness of the sample.

As the temperature is increased, we already mentioned that we observe a transition toward an ES-VRH regime. The extracted crossover temperature T_{c1} (presented figure 3.26) increases continuously as disorder is increased, independently of the thickness. This crossover is therefore determined by the sole sheet conductance.

To summarize our findings on the simply activated regime :
- All insulating samples present **a simply activated conduction regime ($n \sim 1$) at the lowest temperatures**.
- As could be expected, its **extension in temperature is larger as disorder is increased.**
- The **characteristic resistance R_0 and temperature T_0 both increase as disorder is increased.** Again this could be expected.
- **None of the characteristic parameters seems to be thickness-dependent.**

We will now characterise the VRH regimes which appear at temperatures higher than this crossover.

The VRH regimes

As seen in section 3.3.2.2, at intermediate temperature and depending on disorder, we identified two different VRH behaviours, with either a unique ES VRH regime or with a transition between ES and 2D Mott VRH. We will see in this paragraph in particular that :
- for $\sigma_{4K} < 0.05\,\frac{e^2}{h}$, the transport properties of the film can be described **by a unique ES VRH regime** practically until room temperature.
- for $0.05\,\frac{e^2}{h} < \sigma_{4K} < 2\,\frac{e^2}{h}$ we observed **both an ES VRH and a 2D Mott VRH** regimes depending on the temperature range.
- For $\sigma_{4K} > 2\,\frac{e^2}{h}$, as we will see, we can describe our data with **a unique ES VRH** regime

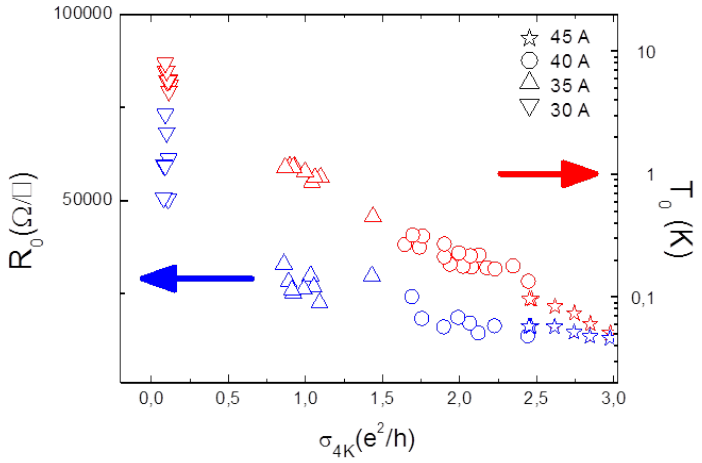

Figure 3.25: Extracted values of the pre-factor R_0 and the characteristic temperature T_0 for insulating films as a function of the 4 K sheet conductance.

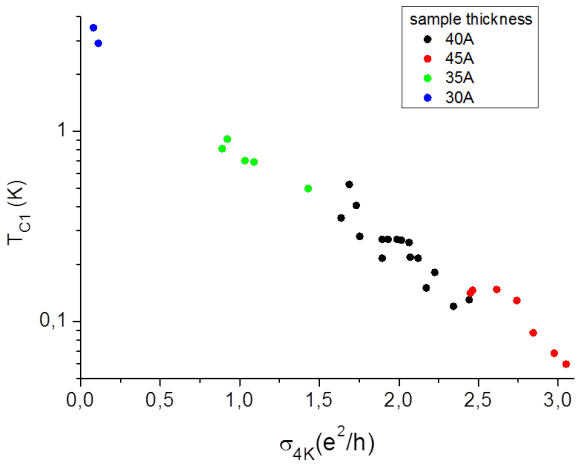

Figure 3.26: Measured crossover temperature T_{c1} between the $n \sim 1$ regime and the ES VRH regime. Samples of different thicknesses are of different colors.

before it gives way to a non-activated conduction regime. **The Mott VRH regime** is not observable, probably because the corresponding range in temperature is too small to be experimentally observed.

Before proceeding, let us recall that the characteristic energies for Mott and ES VRH regimes are respectively given in 2D by $T_{Mott} = \frac{\beta_2^{Mott}}{N(E_F)d_\perp k_B \xi_{loc}^2}$ and $T_{ES} = \frac{\beta_2^{ES} e^2}{\kappa \xi_{loc}}$, (see section 1.5.1 for the definition of the different quantities). Moreover, the resistance pre-factor in each regime should vary as a positive power law of ξ_{loc} [Pollak and Shklovskii, 1991]. The extracted characteristic parameters in the Mott and ES VRH regimes are presented figures 3.27 and 3.28 [7].
The characteristic energies of both the Mott and ES VRH decrease exponentially as a function of σ_{4K}. This is expected as both energies should vanish at the MIT.
Simultaneously, the prefactor R_{Mott} is increasing in the Mott VRH regime. So does R_{ES} for $\sigma_{4K} < 0.5\,\frac{e^2}{h}$ in the ES VRH regime. The increase of the prefactor in both regimes is theoretically predicted as it varies as a power law of the localization length ξ_{loc}, and ξ_{loc} diverges as we get closer to the MIT [Pollak and Shklovskii, 1991].
However, it seems that R_{ES} saturates at a value (9000 ± 1000) Ω/□ ($\sim \frac{e^2}{3h}$) for $\sigma_{4K} > 0.5\,\frac{e^2}{h}$. This saturation of R_{ES} has been observed in some 2D materials like 2D gases [Mason et al., 1995] [Shlimak et al., 1999] [Khondaker et al., 1999] and may indicate a phononless mechanism of hopping -i.e. a hopping mechanism which is not assisted by electron-phonon interaction-. We will come back on this point in section 3.6.

One may wonder if there is a thickness effect in these regimes, especially in the 2D Mott regime for which one expects $T_{Mott} \propto 1/d_\perp$. Although, we do not have samples in this regime with a sufficiently large range in $d_\perp$ (here 30 Å $\leqslant d_\perp \leqslant$ 45 Å) to conclude firmly on this point, the trends in both evolutions of R_{Mott} (resp. R_{ES}) and T_{Mott} (resp. T_{ES}) are continuous, so that, in our case, **the effects of disorder dominate over thickness effects** (if any).

To picture the evolution of the different regimes as a function of disorder and temperature, we can plot the different crossover temperatures between the different regimes (i.e. simply activated, ES VRH, 2D Mott VRH and weak localization) as a function of disorder (figure 3.29). As could be expected, as disorder is reduced, the characteristic temperatures at which each regime appears decrease. The explored disorder range allowed us to monitor the continuous evolution of T_{c1}, T_{c2} and T_{c3} on two orders of magnitude. Moreover, as can be seen, the temperature ranges on which the simply activated and the Mott regimes are observable shrink considerably close to $\sigma_{4K} = 3\,\frac{e^2}{h}$. Eventually, for $2\,\frac{e^2}{h} < \sigma_{4K} < 2.5\,\frac{e^2}{h}$, Mott and ES regimes are scarcely distinguishable. This leads to difficulty in separating the two regimes in the analysis. This uncertainty vanishes for $\sigma_{4K} > 2.5\,\frac{e^2}{h}$ as the ES regime begins to be better defined again near the MIT as we can observe figure 3.30 for a sample with $\sigma_{4K} = 2.6\,\frac{e^2}{h}$. Although the 2D Mott VRH regime either could exist on a limited range in temperature, or vanishes at $\sigma_{4K} \sim 2-2.5\frac{e^2}{h}$.

3.3.2.4 Parameters extracted from the crossover temperatures

In this paragraph, we would like to use the crossover temperature between the different regimes to access some relevant parameters. This will also allow us to validate the hypotheses underlying the different conduction regimes.

To do so, we can extract the ratios $\frac{T_0}{T_{c1}}$, $\frac{T_{ES}}{T_{c2}}$, and $\frac{T_{Mott}}{T_{c3}}$ for a selection of insulating films -spanning the insulating region and for which we were able to identify an activated regime, and both ES and Mott VRH regimes -. The results are presented in table 3.2. These quantities will allow us to check one important condition for each of the regimes to exist. Indeed, **the $n \sim 1$, as well as the ES and Mott VRH regimes, can theoretically exist only if the temperatures at which they are observed are smaller than the characteristic energy**. In other words, one must theoretically have $\{\frac{T_0}{T_{c1}}, \frac{T_{ES}}{T_{c2}}, \frac{T_{Mott}}{T_{c3}}\} > 1$.
For all samples, these conditions are met, except for the sample closest to the transition(CKSAS61 D 40 Å-thick sample which sustained a heat treatment at 150 ℃). However, this discrepancy is

7. The uncertainties on T_0 and T_{ES} are lower than ± 5 % for the presented samples. For T_{Mott}, uncertainties range from less than ± 5 % for the more insulating films to ± 20 % for $\sigma_{4K} \sim 2\,\frac{e^2}{h}$.

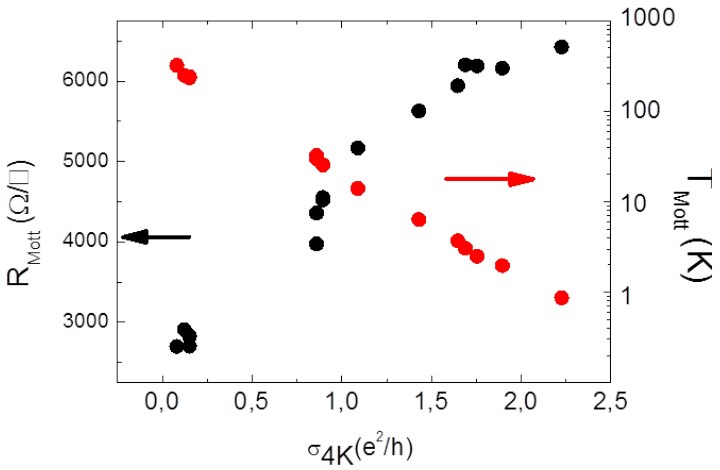

Figure 3.27: Extracted values of the pre-factor R_{Mott} and of the characteristic temperature T_{Mott} for insulating films in the 2D-Mott VRH regime as a function of the 4 K sheet conductance.

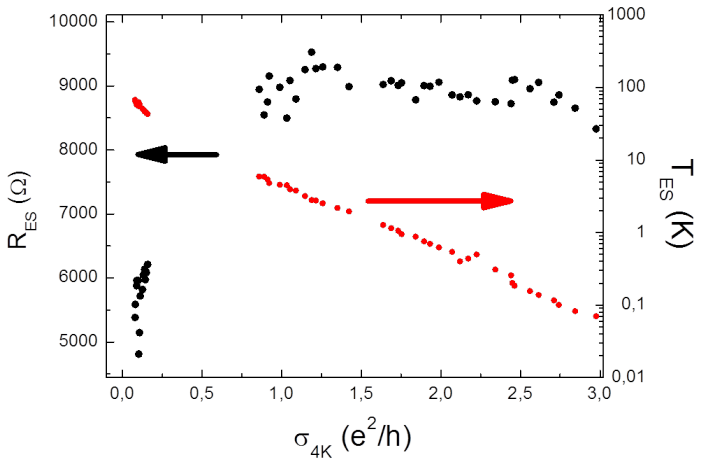

Figure 3.28: Extracted values of the prefactor R_{ES} and of the characteristic temperature T_{ES} for insulating films in the ES VRH regime as a function of the 4 K sheet conductance.

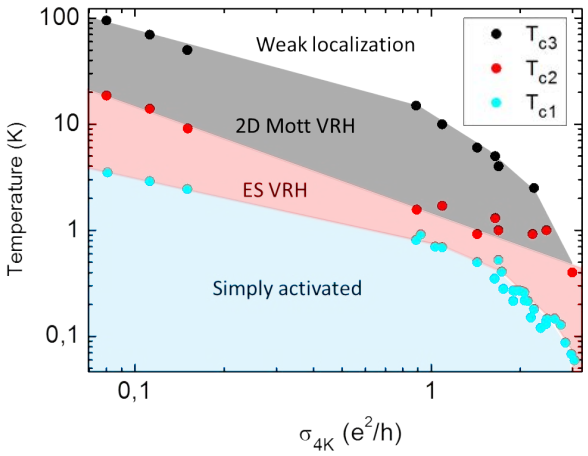

Figure 3.29: Crossover temperatures T_{c1} (blue dots), T_{c2} (red dots) and T_{c3} (black dots) as a function of σ_{4K} for insulating films.

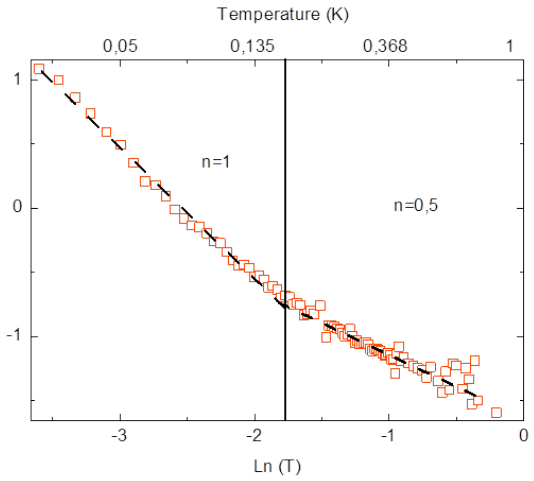

Figure 3.30: Extraction of the parameter n as a function of temperature for a 45 Å-thick a-$Nb_{13.5}Si_{86.5}$ sample which sustained a heat treatment at 140 ℃ ($\sigma_{4K} \sim 2.6\ \frac{e^2}{h}$), obtained by using Zabrodskii's technique. We observe a crossover between an activated and an ES VRH regime.

small and could be explained by our uncertainty in the determination of T_0, T_{ES} and T_{Mott} or on the crossover temperatures [8].

Sample & heat treatment temperature θ	$\sigma_{4K}(\frac{e^2}{h})$	T_{Mott} (K)	T_{ES} (K)	T_0 (K)	$\frac{T_{Mott}}{T_{c3}}$	$\frac{T_{ES}}{T_{c2}}$	$\frac{T_0}{T_{c1}}$
CKSAS61 G 30 Å 150 ℃	0.08	321	64	8	3.4	3.4	2.3
CKSAS61 G 30 Å 70 ℃	0.15	242	43	7.6	4.9	4.7	3.2
CKSAS61 D 35 Å 150 ℃	0.9	25.7	6.5	1.15	2.6	4.2	1.45
CKSAS61 D 35 Å 70 ℃	1.43	6.3	2.55	0.62	1	2.8	1.25
CKSAS61 D 40 Å 150 ℃	1.69	3.05	1.1	0.32	0.8	1.1	0.8

Table 3.2: Values of the ratios $\frac{T_{Mott}}{T_{c3}}$, $\frac{T_{ES}}{T_{c2}}$, and $\frac{T_0}{T_{c1}}$, for a selection of samples.

Theoretically, the transition between the two VRH regimes (Mott and ES) occurs at :

$$T \sim T_{CG} \tag{3.5}$$

This condition is linked to the filling of the Coulomb gap due to thermal excitations at temperatures above T_{CG}, so that the effective DOS is no longer depleted by Coulomb interactions and becomes eventually constant (which is the condition for a Mott-type VRH).

For 3D films, where the Coulomb gap is usually described by a parabolic dependence of the density-of-states with the energy, the crossover between Mott and Efros-Schlovskii VRH regimes should occur at [Rosenbaum, 1991] [Pollak and Shklovskii, 1991] :

$$T_{ME} = 16\frac{T_{ES}^2}{T_{Mott}} = 2\frac{\Delta_3^{CG}}{k_B} = 2\frac{e^3 N(E_F)^{1/2}}{\kappa^{3/2}} \tag{3.6}$$

where $N(E_F)$ is the non perturbed density-of-states at the Fermi level and $\kappa = 4\pi\epsilon\epsilon_0$, with ϵ_0 the vacuum permittivity and ϵ the relative permittivity of the material.

In 3D a-$Nb_{8.3}Si_{91.7}$ films (1000 Å-thick), a crossover between the two VRH regimes - 3D Mott and ES - has been found at 1 K (figure 3.31). In this case, the experimentally extracted parameters (given in the figure caption) are in good agreement with the theoretical value obtained from equation 3.6.

8. If we take the error bars into account, one obtains for CKSAS61 D 40 Å, $\frac{T_{Mott}}{T_{c3}} = 0.8 \pm 0.35$ and $\frac{T_0}{T_{c1}} = 0.8 \pm 0.1$.

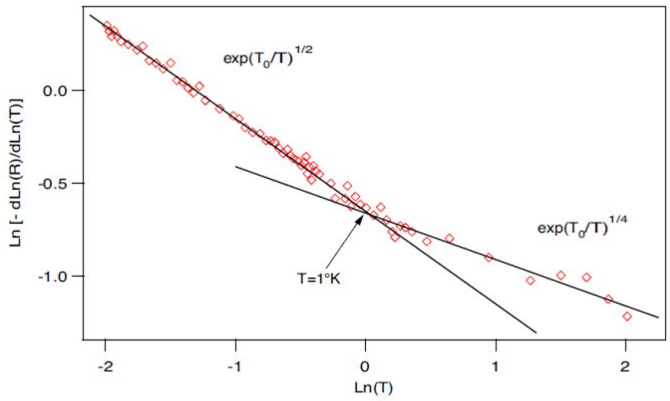

Figure 3.31: Zabrodskii fit of a 3D (1000 Å) a-$Nb_{8.3}Si_{91.7}$ sample. The straight lines correspond to the 3D Mott ($n = 1/4$) and Efros-Shklovskii ($n = 1/2$) VRH regimes fits. The analysis allowed to extract T_M =18.2 K and T_{ES} =1.08 K with a crossover between the two insulating regimes at $T = 1$ K. This is in agreement with the theoretical value ($T_{ME} = 1.15K$) obtained from equation 3.6 [Marnieros, 1998].

In lower dimension, the form and the width of the Coulomb gap are altered by the dimensionality. Indeed, the gap is described in 2D by a linear dependence of the density-of-states on the energy, and its width is given by :

$$\Delta_2^{CG} = \frac{e^4\, N(E_F)}{\kappa^2} \tag{3.7}$$

Using the definitions of T_{Mott} and T_{ES} (see section 1.5.1), one can show that equation 3.7 becomes :

$$\Delta_2^{CG} = \frac{k_B\, T_{ES}^2\, \beta_2^{Mott}}{(\beta_2^{ES})^2\, T_{Mott}} \tag{3.8}$$

where $\beta_2^{ES} = 6.5$ and β_2^{Mott} has been found to vary between 13.8 and 18 depending on the authors([Mott, 1967], [Tsigankov and Efros, 2002] and [Shafarman et al., 1989]). Therefore, we should observe a crossover between the two regimes at a temperature :

$$T_{c2} \sim 2\,\frac{\Delta_2^{CG}}{k_B} \tag{3.9}$$

Sample & θ	$\sigma_{4K}(\frac{e^2}{h})$	measured T_{c2} (K)	theoretical T_{c2} (K)	$R_\square(T_{c3})$ ($\Omega/\square$)
CKSAS61 G 30 Å 150 ℃	0.08	18.6	8.5	12250
CKSAS61 G 30 Å 70 ℃	0.15	9.1	5.1	15000
CKSAS61 D 35 Å 150 ℃	0.9	1.55	1.1	14500
CKSAS61 D 35 Å 70 ℃	1.43	0.9	0.7	15500
CKSAS61 D 40 Å 150 ℃	1.69	1	0.3	15300

Table 3.3: Measured and theoretical values of T_{c2} obtained using equations 3.9 and 3.8, with β_2^{Mott}=13.8 and β_2^{ES}=6.5. The sheet resistance at $T = T_{c3}$ is also given.

The experimentally measured crossover temperatures are presented in table 3.3, along with the theoretical values obtained from equations 3.9 and 3.8. The comparison between the experimental and theoretical value is presented figure 3.32 for clarity.
We find a good qualitative agreement between the theoretical and experimental values. Quantitatively, they differ by a factor of about 2. This small discrepancy could well be explained by experimental uncertainties on the found temperatures and by theoretical uncertainty on β_2^{Mott} : in addition to the dispersion found in the literature (13.8 to 18), β_2^{Mott} may be modified by correlated hopping effects which are not taken into account in the original theory [van Keuls et al., 1997]. Moreover let us emphasize that this value assumes a completely flat DOS in the Mott regime which may not be totally realistic in our case.

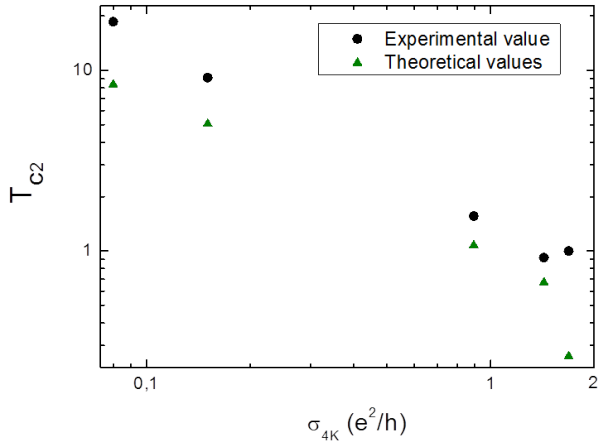

Figure 3.32: Measured and theoretical values of T_{c2} for the selection of films presented table 3.3.

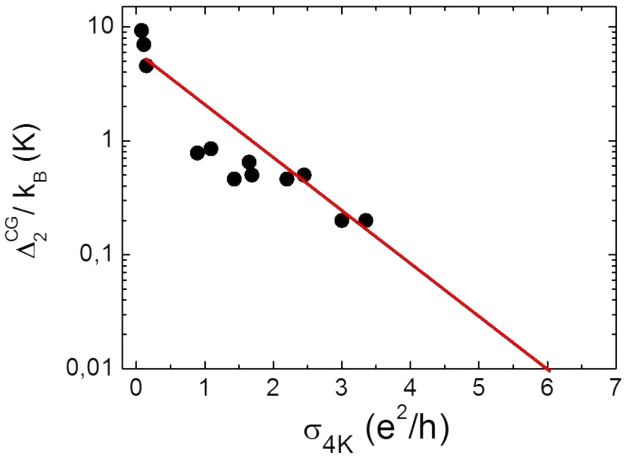

Figure 3.33: Evolution of the Coulomb gap as a function of σ_{4K}. A linear fit gives $\frac{\Delta_2^{CG}}{k_B} \sim 10$ mK, our base temperature, for $\sigma_{4K} \sim$ 4-7 $\frac{e^2}{h}$. The red line is a guide to the eye.

We therefore believe that **there is a fair agreement between theoretical and experimental values regarding the crossover temperature between Mott and ES VRH regimes**. This is another indication that the two observed regimes are indeed distinct and consistent.
Moreover, T_{c2} is a direct measurement of Δ_2^{CG}. As expected, the Coulomb gap decreases in size when nearing the MIT. Its evolution with disorder is given figure 3.33. As can be seen, Δ_2^{CG} evolves exponentially with σ_{4K}. Moreover, $\frac{\Delta_2^{CG}}{k_B} \sim 10$ mK, our base temperature, for $\sigma_{4K} \sim$ 4-7 $\frac{e^2}{h}$. This means that, even at our lowest available temperature, Δ_2^{CG} would be filled with thermal excitations for samples with $\sigma_{4K} >$ 4-7 $\frac{e^2}{h}$. Moreover, it is noteworthy that, according to this preliminary extrapolation of $\Delta_2^{CG}(\sigma_{4K})$, Δ_2^{CG} does not vanish at the MIT which, as we will see, occurs at $\sigma_{4K} = 3\ \frac{e^2}{h}$. We will come back on a possible interpretation for this in section 3.6.

Going back to the hypothesis formulated in the analysis of figure 3.22, we believe we can now discard the third scenario for insulating samples. For films with $\sigma_{4K} < 2\,\frac{e^2}{h}$, we observe two crossovers, from a simply activated law to an ES and then to 2D Mott VRH regimes.
However the observation of Mott VRH becomes more complicated for films really close to the transition, as its range in temperature shrinks. For samples close to the MIT, the conductivity will therefore be described as a simply activated regime evolving into an ES regime.

3.3.2.5 Extracted parameters from Mott VRH

We have seen that we have good reasons to believe in a scenario with 2 distinct VRH regimes. Another way to make sure that the identified regimes are relevant and realistic is to analyze the evolution of characteristic lengthscales that can be extracted in this way. For instance, the Mott characteristic temperature gives an estimate of the localization length ξ_{loc}, provided the DOS is known, via the equation :

$$\xi_{loc} = \sqrt{\frac{\beta_2^{Mott}}{T_{Mott} N(E_F) d_\perp k_B}} \tag{3.10}$$

In a-Nb_xSi_{1-x}, the density-of-states has been measured by several authors by specific heat measurements [Marnieros, 1998][Marnieros et al., 2000], Hall measurements [Nava et al., 1986], by using the combined properties of Variable Range Hopping and scaling [Marnieros, 1998], and by measuring the critical field in the superconducting state [Aubin et al., 2006]. It varies between 0.3 and 1.8×10^{41} states.J^{-1}.cm^{-3} depending on the measurement, uncorrelated with the value of x for $x \in [0.07; 0.15]$. In the following, we will take it to be 1.10^{41} states/J/cm^3.
For the films listed table 3.3, the obtained values of the localisation length ξ_{loc} have been transcribed in table 3.4. As expected, this distance diverges when we approach the Metal(M2)-to-Insulator Transition (figure 3.34). In theory, ξ_{loc} should diverge as :

$$\xi_{loc} \propto |x - x_c|^{-\nu} \tag{3.11}$$

where x is the composition driving the MIT, x_c its critical value, and ν the critical exponent for the localization length. Since σ_{4K} is proportional to x (see figure 2.18), we can determine ν by fitting a power law onto the dependence $\xi_{loc} \propto |\sigma_{4K} - \sigma_{4K,c}|^{-\nu}$. Figure 3.34 shows several equally possible fits : ν then ranges from 1.2 to 4.4 whereas $\sigma_{4K,c}$ varies from 2.5-5$\frac{e^2}{h}$. Due to experimental uncertainties and to the limited range in ξ_{loc}, **it is therefore difficult to conclude further than to say that the localization length is compatible with a power law evolution as a function of disorder and that it diverges close to** $\sigma_{4K,c} = 3\frac{e^2}{h}$.

From the localization length, one can calculate the most probable hopping distance. In 2D, this distance is given by [Pollak and Shklovskii, 1991] :

$$r_m \sim \left(\frac{2\xi_{loc}}{\pi N(E_F) d_\perp k_B T}\right)^{1/3} \tag{3.12}$$

In table 3.4, we estimated both the highest and lowest values of r_m, such that $r_m(T_{c3}) < r_m < r_m(T_{c2})$. **The hopping distance is of the same order or greater than the thickness of the sample, consistent with the idea of a 2D Mott regime** [Shahar and Ovadyahu, 1990]. Furthermore, r_m is of the order of a few nm to a few tens of nm, as expected in VRH.

In the conventional theory, one condition for the Mott VRH regime to be valid is that $r_m > (\xi_{loc}, a)$ where a is the nearest neighbour distance (in our case ~ 4.5 Å). This is the case only for $T \sim T_{c2}$. On the temperature range on which Mott regime is observed, $r_m \sim \frac{1}{3} - \frac{1}{2}\xi_{loc}$. The **validity criterion** is thus not strictly obeyed. However, there may be several reasons to explain this small discrepancy :

- the effective value of r_m depends on the estimation of $N(E_F)$ which may have been underestimated.
- ξ_{loc} depends on β_2^{Mott} which values varies with authors ($\beta_2^{Mott} \sim 13.8 - 18$), on $N(E_F)$, and on experimentally determined parameters (T_{Mott} mainly), giving a typical overall uncertainty of $\sim 50\%$ on its value.
- such discrepancy has already been observed in other systems and has been explained by corrections to the VRH theory which should be added near the MIT [9] [Shafarman et al., 1989].

We therefore believe the validity criterion is reasonably well obeyed.

Finally, we can measure **the resistance at the crossover between this regime and the weak localization regime** at higher temperatures. In the insulating phase, we found

9. Mott VRH assumes a totally flat density-of-states (which is not necessarily the case), multi-hopping is not taken into account in conventional VRH theories and the hopping probability calculated in VRH theory has been derived in a dilute limit (i.e. hopping takes place only between a pair of sites and each pair is independent of other pairs due to low contributing site densities, which is not necessarily valid near the MIT) [Shafarman et al., 1989].

it to occur at an almost constant value of $R_{\square}(T_{c3}) \sim (14 \pm 2)$ kΩ/□ $\sim \frac{h}{2e^2}$ (see table 3.3). Theoretically, a crossover from weak to strong localization is expected at $R_{\square} = \frac{2\pi^2\hbar}{e^2} \simeq 81$ kΩ/□ [Larkin and Khmel'nitskii, 1982, Hsu and Valles, 1995]. However, this value was obtained by developing quantum corrections in the first order in $k_F l$. When higher order corrections are taken into account, as recent developments have [Minkov et al., 2004], the crossover is expected to occur at a constant resistance $\frac{h}{5e^2} < R_{\square} < \frac{h}{e^2}$, i.e. for 5.17 kΩ $< R_{\square} <$25.85 kΩ. Our measured value for $R_{\square}(T_{c3})$ is consistent with this range. This is yet another argument for the existence of the Mott-VRH regime.

3.3.2.6 Extracted parameters from ES regime

One can also evaluate the hopping distance in the ES VRH regime. In this regime, the hopping distance is given by :

$$r_{ES} \sim \frac{1}{4}\xi_{loc}\sqrt{\frac{T_{ES}}{T}} \tag{3.13}$$

Using the previously determined value of ξ_{loc}, we calculated $r_{ES}(T_{c2})$ and $r_{ES}(T_{c1})$ (presented table 3.4), corresponding to the theoretical maximum and minimum values of r_{ES}(T). Far in the insulating phase, $r_{ES}(T_{c2}) < \xi_{loc} < r_{ES}(T_{c1})$. Therefore, the validity criterion for ES VRH ($\xi < r_{ES}$) works on a restricted temperature range. However, as the transition towards the metallic state is approached, this condition is no longer fulfilled by a factor 2-3. There may be several reasons for this :

1. Here again, the different approximations (on $N(E_F)$ or error on the experimental quantities for instance) may induce some uncertainties explaining these small deviations.
2. The ES VRH theory has been developed for a strongly insulating regime. Nearing the MIT may modify the expression of T_{ES} and r_{ES} [Lee et al., 1999]. Other authors have found that, near the MIT, although the validity criterion is not strictly observed, the data may nonetheless be described by a ES-type conduction law [10] [Rodríguez et al., 2007].
3. Larkin et al. have extended the calculation for conducting samples of large ξ_{loc} and have found that the activation energy could have a logarithmic temperature dependence, which may affect the expression of T_{ES} and r_{ES} [Larkin and Khmel'nitskii, 1982].

sample & θ	ξ_{loc} (m)	$r_m(T_{c3})$ (m)	$r_m(T_{c2})$ (m)	$r_{ES}(T_{c2})$ (m)	$r_{ES}(T_{c1})$ (m)
CKSAS61 G 30 Å 150 ℃	$3.25\,10^{-9}$	$1.8\,10^{-9}$	$3\,10^{-9}$	$1.5\,10^{-9}$	$3.5\,10^{-9}$
CKSAS61 G 30 Å 70 ℃	$3.7\,10^{-9}$	$2.3\,10^{-9}$	$4\,10^{-9}$	$2\,10^{-9}$	$3.9\,10^{-9}$
CKSAS61 D 35 Å 150 ℃	$1\,10^{-8}$	$5.2\,10^{-9}$	$9.7\,10^{-9}$	$5.1\,10^{-9}$	$7\,10^{-9}$
CKSAS61 D 35 Å 70 ℃	$2.1\,10^{-8}$	$7.6\,10^{-9}$	$1.5\,10^{-8}$	$8.8\,10^{-9}$	$1.2\,10^{-8}$
CKSAS61 D 40 Å 150 ℃	$2.9\,10^{-8}$	$9\,10^{-9}$	$1.5\,10^{-8}$	$7.6\,10^{-9}$	$1\,10^{-8}$

Table 3.4: Calculated values of the localization length ξ_{loc} as well as the hopping distance r_m extracted from Mott VRH and the hopping distance r_{ES} extracted from ES VRH evaluated at the crossover temperatures. The hopping distances have been calculated using with β_2^{Mott}=13.8 and β_2^{ES}=6.5.

D**espite these small inconsistencies** regarding for the parameters extracted from the ES VRH regime, **we have good reason to believe that this mechanism describes correctly the conduction in our samples**, even for samples close to the transition. We indeed saw that, far into the insulating regime, the characteristic parameters extracted are coherent and that the crossover between the observed Mott and ES VRH regimes (when we are able to measure it) is in good agreement with what is expected. In addition, the capacity of Zabrodskii's method to discriminate non activated regime - which will be discussed in section A.2 - as well as the evolution of the parameters on the metallic side of the transition - as we will see in section 3.4.3.3 - tend to strengthen our arguments.

To conclude this section, let us summarize our findings on the insulating regime :

10. This approach has been justified by the fact that, close to the MIT, the conventional expression of ES VRH has to be corrected due to : (i) $x \sim x_c$, so that $T_{ES} \sim (1 - \frac{x}{x_c})$ can be small. (ii) the wave function has a larger spatial distribution to take into account short-range structural defects or longer-range defects.

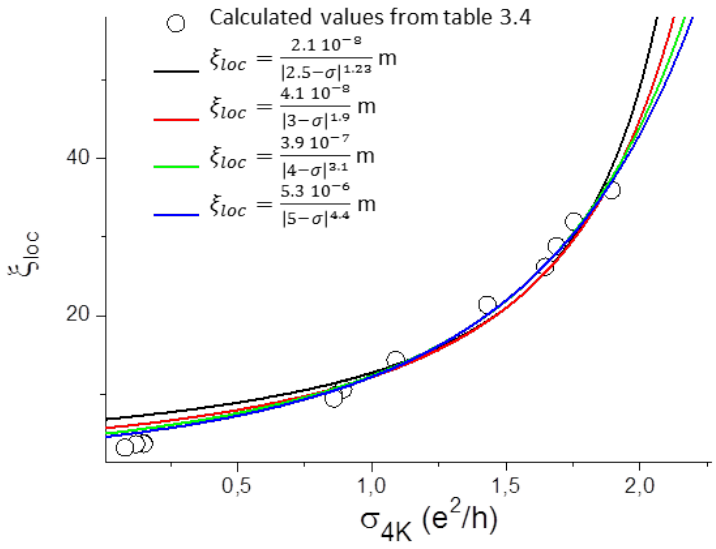

Figure 3.34: For the samples listed table 3.4, estimation of the localization length ξ_{loc} (see text) and fit attempts using equation 3.11.

- All insulating samples present **a simply activated conduction regime at the lowest temperatures** which gives way to a VRH-type conduction regime (either a single ES or two successive ES and 2D Mott regimes).
- **The characteristic energies continuously increase when disorder is increased**.
- Close to the MIT, Mott VRH is no-longer observable.
- It is interesting to note that **ES-type VRH is always observable**. As we will discuss in the section devoted to the interpretation of our results, this signals the importance of Coulomb interactions in these films.
- Moreover, the extrapolation of the evolution of the Coulomb gap with disorder tends to indicate that it does not vanish at the M2IT.
- The **different validation criteria** ($T < T_{charac}$, $r_{hop} > \xi_{loc}$, $T_{c2} \sim 2\frac{\Delta_2 CG}{k_B}$) **have been reasonably well verified**.

3.4 Analysis of metallic samples

In this section, we would like to review the different conduction mechanisms encountered in M2 samples. As previously mentioned, when the temperature decreases, the sample first presents a weakly localizing behaviour, from which it sometimes moves away, before the resistance saturates at very low temperatures. We will first focus on the weak localization regime and the deviation from it, before examining the saturation regime.
To do so, we will mainly detail analyzes performed on films in the M2 phase, but, whenever we consider it relevant, we will also mention films in the M1 phase. The main aim is to achieve a comprehensive picture of the M2 phase and its existence in between the M1 and the insulating states.

3.4.1 Brief overview of the results regarding metallic samples

In metallic samples, we will encounter three types of evolutions of the sheet resistance as a function of the temperature :

- **In the M1 phase**, conductivity will be described by weak localization laws until superconducting fluctuations dominate the conduction (figure 3.35.a).
- **In the M2**,
  - **near the M1-to-M2 transition, in the M2 phase**, conductivity will be described by weak localization, until the sheet resistance saturates at the lowest temperatures (figure 3.35.b).

– **near the M2-to-Insulator transition, in the M2 phase**, the situation will be more complex. We will encounter a conduction law that is more strongly insulating than weak localization at the lowest temperatures (typically $T \lesssim 300$ mK) before observing the resistance saturations (observed typically for $T \lesssim 30$ mK). We will therefore describe conductivity successively with a saturation of resistivity, an activated law and a weak localization law, as pictured figure 3.35.c.

In this section, we will :
– Identify and study the different localization laws observed in the metallic phases (M1 and M2), outside superconducting fluctuations.
– Follow the evolution of the localization laws as a function of disorder and sample thickness, as they approach the M2-to-Insulator transition.
– This analysis will lead to a discussion on the transition toward the insulating phase, where the resistance saturation vanishes.

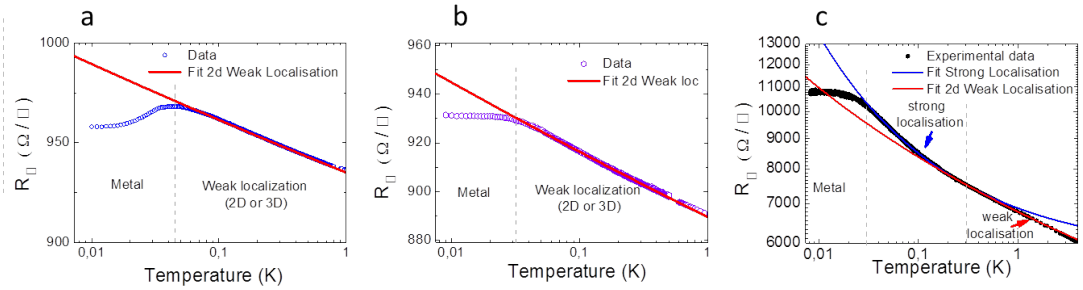

Figure 3.35: The different regimes observed in metallic sample : (a) the M1 phase. (b) the least disordered M2 sample. (c) the most disordered M2 sample.

3.4.2 Weak localization in metallic samples

We will here identify and characterize the weak localization mechanisms in our samples, as well as their evolution as a function of disorder. Indeed, in our metallic films, conductivity at high temperature (typically higher than a few K) can be associated with a 3D weak localization mechanism, giving rise to a conductance of the form :

$$\sigma(T) = \sigma_0 + \beta T^{p/2} \tag{3.14}$$

with σ_0 being the Drude conductance, β a constant and p a constant ranging from 1 to 3 for dimension $d \geq 2$, depending on the conduction process and dimensionality (see section 1.5.2).

In films in the M1 phase with a characteristic energy [11] T_{c0} lower than 80 mK, or in the M2 regime, we found a crossover between 3D and 2D weak localization at typically 500 mK $\lesssim T \lesssim$ 2 K [12]. In this case, the conductance is given at low temperatures by 2D weak localization laws of the form :

$$\sigma = \sigma_0 + \alpha_{wl}\, ln(T) \tag{3.15}$$

where σ_0 is the Drude conductance and α_{wl} is a constant taking into account the strength of Coulomb interactions which, in turn, depend on disorder [13] (see section 1.5.2 and 1.4.2 for details).

11. See section 2.3.3.4 or [Couëdo, 2014] for the definition of T_{c0}.
12. This crossover is not visible in M1 films with higher T_{c0} due to superconducting fluctuations.
13. We will here limit ourselves to the analysis of weak localization in our metallic samples. However, the high temperature behaviour of insulators - beyond the ES or the 2D Mott VRH regime discussed in the previous section - is the same : a 2D weak localization regime gives way to a 3D localization regime at even higher temperatures, at least for films having $\sigma_{4K} > 2.5\,\frac{e^2}{h}$.

3.4.2.1 3D weak localization

For metallic a-$Nb_{13.5}Si_{86.5}$ films analyzed during this thesis, $p = 3/2$ is usually found in a large range of temperatures (typically from room temperature to 1 K) as seen figure 3.36 for a M1 sample near the M1-to-M2 transition. A weak localization mechanism with $\sigma \propto T^{3/4}$ is consistent with our data for this 228 Å-thick film, from, at least, 200 K to 1 K. In this sample, eventually, weak localization is counterbalanced by superconducting fluctuations at the lowest temperatures.
$p = 3/2$ is consistent with a **3D weak localization** regime dominated by **3D electron-electron inelastic scattering**, i.e. $(L_\phi, L_T) \leq d_\perp$, where $L_T = \sqrt{\hbar D/k_B T}$ is the thermal length (see section 1.4.2).
For the thinnest films ($d_\perp \leq 50$ Å, $\sigma_{4K} \lesssim 4.5 \frac{e^2}{h}$)- which are closer to the M2-to-Insulator transition - a parameter $p = 1$ is found, consistent with a **3D weak localization** regime dominated by **2D electron-electron inelastic scattering**, i.e. $L_\phi \leq d_\perp \leq L_T$.
The transition between the 2 regimes (2D or 3D electron-electron scattering) occurs typically when $d_\perp \sim L_T$. In both cases however, the localization is 3D ($d_\perp \geq L_\phi$).

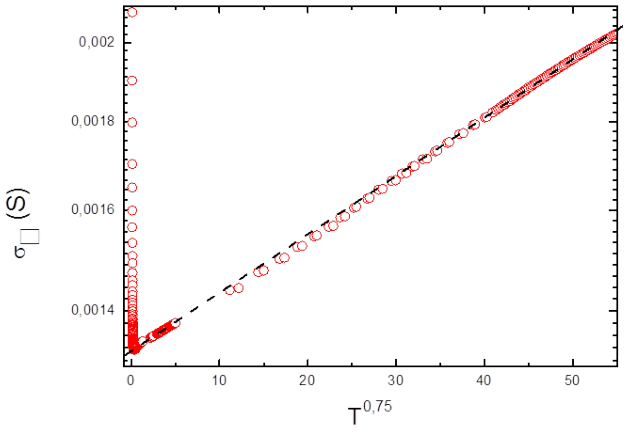

Figure 3.36: Conductance as a function of $T^{3/4}$ for a 228 Å-thick sample which sustained a 110 ℃ heat treatment (sample of CKSAS33 set from [Couëdo, 2014]). The sample is in the M1 phase, near the M1-to-M2 transition. The dashed line is a fit for 3D localization with $p = \frac{3}{2}$.

3.4.2.2 Dimensional crossover for weak localization

Eventually, a dimensional crossover occurs for the weak localization mechanism, as illustrated figure 3.37 for a sample in the M2 phase. 3D weak localization is encountered from room temperature to $T \sim 1$ K (figure 3.37.a). At lower temperature, this law is replaced by a more insulating law, consistent with 2D weak localization (figure 3.37.b) until the metallic regime induces a saturation of the resistivity.

For non-interacting electrons, this crossover between 2D and 3D weak localization is expected when the thickness $d_\perp$ of the sample is such that [Berggren, 1982] :

$$d_\perp \sim L_{in}(T_{crossover})(\sim L_\phi(T_{crossover})) \tag{3.16}$$

Hence, for $T > T_{crossover}$, the film is 3D from the weak localization point of view, with $\sigma \propto T^{p/2}$. For $T < T_{crossover}$, the film is 2D regarding weak localization and $\sigma \propto ln(T)$ (see section 1.5.2). The coherence length is such that $L_\phi \sim \sqrt{D\tau_{in}}$ and evolves as $L_\phi \sim \sqrt{T^p}$. Therefore, using the value of p extracted from 3D weak localization and the crossover temperature, we can obtain both $L_\phi(T_{crossover})$ and its evolution as a function of the temperature.

For some representative samples, corresponding to samples near the M1-to-M2 transition (CKSAS33 228 Å with a heat treatment of 250 ℃), deep in the M2 phase (OC5 75 Å with a heat treatment of 70 ℃) and close to the M2-to-Insulator transition (CKSAS61 50 Å with a

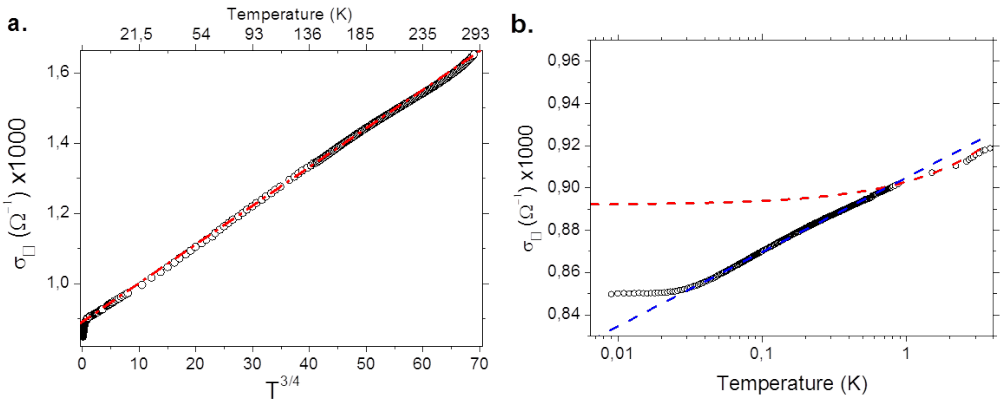

Figure 3.37: (a) Observation and fit (in red) for 1 K $< T <$ 300 K of a 3D weakly insulating regime in a 228 Å-thick $Nb_{13.5}Si_{86.5}$ sample after a heat treatment at 250 ℃ (sample of the CKSAS33 set from [Couëdo, 2014]), which has a M2 ground state. The exponent 3/4 is characteristic of a weak localization mechanism dominated by 3D electron-electron inelastic scattering.(b) Observation and fit (in blue) of the 2D weakly insulating regime in the same sample at lower temperatures (30 mK $< T <$ 1 K). A crossover occurs between 3D weak localization (red dashed curve) and 2D weak localization (blue dashed curve) at $T \sim 1$ K.

heat treatment of 70 ℃), the estimated $L_\phi(T)$ are presented figure 3.38, as well as the thermal length L_T estimated with parameters from [Marrache-Kikuchi et al., 2006] [14]. **These samples are 2D regarding both the coherence length and the thermal length at $T = 10$ mK**, with $L_\Phi \gtrsim 80$ nm and $L_T \sim 200$ nm, well above the thickness of the thickest sample analyzed in this thesis, ($d_\perp \sim 250$ Å). At low temperatures, **all our samples can therefore be deemed two-dimensional both for weak localization and Coulomb interactions**.

We will now concentrate ourselves on the description of the evolution of the 2D weak localization law observed at low temperature, as a function of disorder.

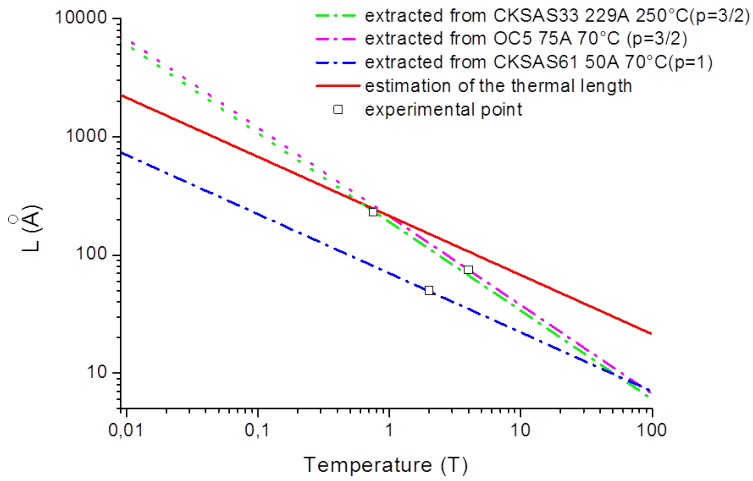

Figure 3.38: Evaluation of the coherence length for different samples, compared with the evolution of the thermal length. The samples have been chosen to be at various distances (regarding disorder) to the M2-to-Insulator transition on the M2 side. The dashed lines are extrapolated values obtained by using the theoretical evolution of the coherence length as a function of temperature and the parameter p extracted from 3D weak localization. L_T has been evaluated by taking D= 0.6 $cm^2.s^{-1}$.

14. D= 0.6 $cm^2.s^{-1}$, estimated from measurements of the critical field in the superconducting phase of $Nb_{15}Si_{85}$.

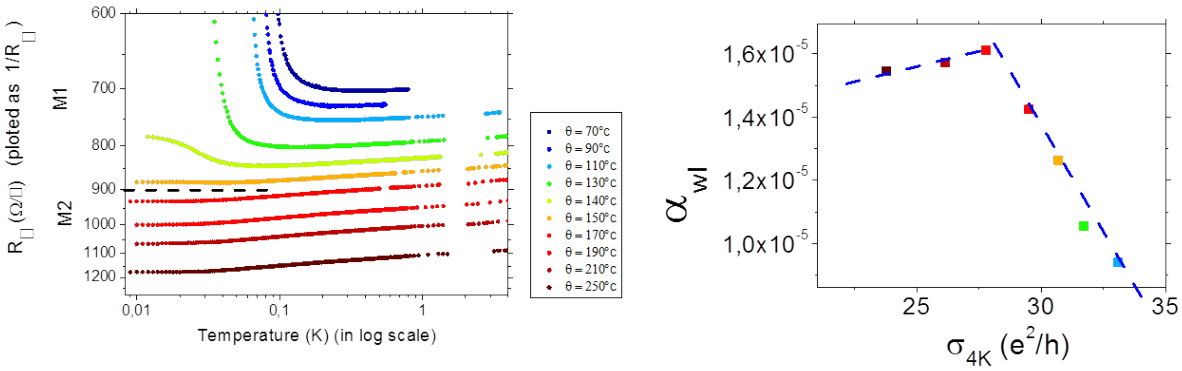

Figure 3.39: (left) Conductivity of a 228 Å-thick sample for different heat treatment temperatures. The dashed line corresponds to the M1-to-M2 transition as identified in [Couëdo, 2014].(right) Evolution of parameter α_{wl} as a function of σ_{4K} for the same samples. The blue dashed lines are guides to the eye to highlight the modification of α_{wl} across the M1-to-M2 transition.

3.4.2.3 Evolution of the 2D weak localization law as a function of disorder

Near and across the M1-to-M2 Transition

Once the 2D weak localization regime is identified, we can extract $\alpha_{wl} = (1 - \frac{3}{4}F)) \frac{e^2}{2\hbar\pi^2}$. This parameter, which depends on the Hartree parameter F, should give us an insight on the strength of Coulomb interactions as a function of disorder.
By doing so for a 228 Å-thick sample of a-$Nb_{13.5}Si_{86.5}$ at different heat treatment temperatures (presented figure 3.39), we found that α_{wl} increases linearly as a function of disorder by a factor of about 2 for a change of σ_{4K} of $\sim$ 15 %. This increase is expected for enhanced electron-electron interactions due to impaired screening in less conducting samples. However, as we cross the M1-to-M2 phase transition, this trend reverses and α_{wl} evolves counter-intuitively, decreasing as disorder increases. We will come back on this in the section devoted to the interpretation (section 3.6).

For samples of different thicknesses, each one crossing the M1-to-M2 transition through heat treatment, the same trend is observed (figure 3.40) : α_{wl} grows with disorder until the M1-to-M2 transition, after which it decreases. **The change in the evolution of α_{wl} can therefore be used as yet another marker for the M1-to-M2 transition.** We recover, as identified in [Couëdo, 2014], the thickness dependence of the M1-to-M2 transition : this transition occurs at lower values of σ_{4K} for thinner samples.
By comparing the $\sigma_{4K,c}$ at the transition obtained by using either the change in the evolution of α_{wl} or the low temperature criteria (see section 2.3.3.4), represented respectively by arrows and by vertical lines on figure 3.40, we find a systematic difference between the two evaluation methods : the critical value found using α_{wl} corresponds to one heat treatment hotter.
This small shift could be due the combined uncertainties of both methods, as the transition has been identified at ± one heat treatment temperature in [Couëdo, 2014].

Near the M2-to-Insulator Transition

In samples exhibiting a M2 ground state, α_{wl} continues at first to decrease with increasing disorder. As presented figure 3.41, a second change in the evolution of α_{wl} with disorder occurs for $\sigma_{4K} = (4.7 \pm 0.7) \frac{e^2}{h}$, after which α_{wl} increases with increasing disorder. After the M2-to-Insulator Transition, which occurs at $\sigma_{4K} \sim 3 \frac{e^2}{h}$ as we will see in section 3.5, α_{wl} continues to increase until 2D weak localization is not observable anymore and is replaced by a more insulating law. As we will see in the interpretation section, the **second change in the trend followed by** α_{wl} (at $\sigma_{4K} \sim 4.7 \frac{e^2}{h}$), although it does not correspond to the M2-to-Insulator Transition, **can be viewed as a precursor to the insulating phase**.

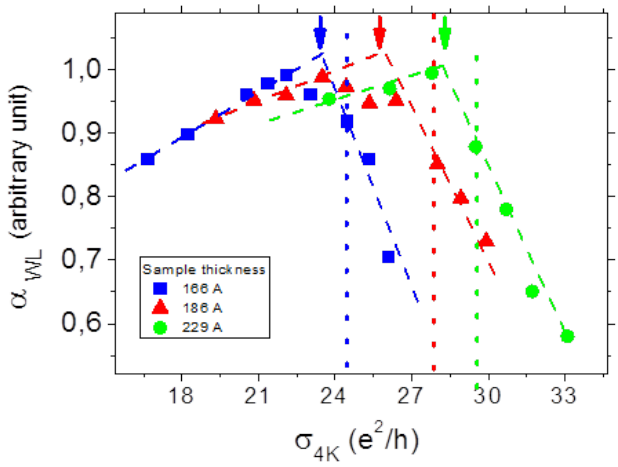

Figure 3.40: α_{wl} as a function of σ_{4K} for samples crossing the M1-to-M2 transition with heat treatment. Each color corresponds to one sample. The dashed lines are guides to the eye. The dotted line corresponds to the first M2 sample as identified in [Couëdo, 2014]. Arrows point on the change in evolution of α_{wl} with disorder.

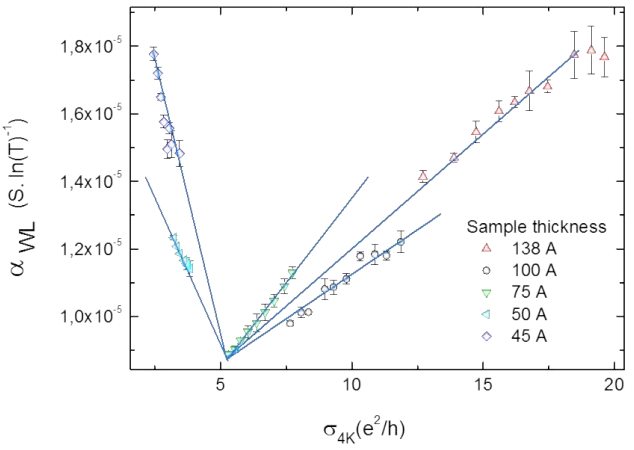

Figure 3.41: Evolution of α_{wl} as a function of σ_{4K} for samples of a-$Nb_{13.5}Si_{86.5}$ of different thicknesses and heat treatment temperatures. The blue lines are guides to the eye extrapolating the evolution of $\alpha_{wl}(\sigma_{4K})$. They cross at $\sigma_{4K} \sim 5\,\frac{e^2}{h}$.

Let us now examine the absolute value of α_{wl}. The theoretical value of α_{wl} is of the order of $\frac{e^2}{2\pi^2\hbar} \sim 1.25\,10^{-5}\,S.(ln(\mathrm{K})^{-1})$ for non-interacting weak localizing electrons. In the presence of interactions, this value should be modified due to a modification of the screening by disorder. In our samples, we found values of α_{wl} ranging between $1.9\,10^{-5}$ and $0.9\,10^{-5}\,S(ln(\mathrm{K})^{-1})$, close to the value for non-interacting electrons. The measured order of magnitude for α_{wl} is therefore consistent with theory.

As shown figure 3.41, α_{wl} seems to be sample-dependent, or, at least, thickness-dependent. However, a systematic evolution as a function of disorder is clearly visible and it is particularly striking that $\alpha_{wl}(\sigma_{4K})$ for the different sample thicknesses all cross close to $\sigma_{4K} \sim 5\,\frac{e^2}{h}$. This value of disorder is close to $\sigma_{4K} \sim 4\,\frac{e^2}{h}$, where the SIT is predicted within the bosonic scenario (see section 1.7.3.2). We do not currently have an explanation for this and the concidence of both values could well be fortuitous. A possible interpretation for the general trend of $\alpha_{wl}(\sigma_{4K})$ will however be given in section 3.6.

3.4.2.4 Toward a more localizing law

We have described how α_{wl} evolves with disorder. We would now like to look into more details to the low temperature dependence of the resistance near the M2-to-Insulator Transition. More specifically, in this paragraph, we will focus on the deviations from weak localization laws that are observed as the M2-to-Insulator Transition is neared. To do so, let us examine the evolution in $R(T)$ for a 75 Å-thick a-$Nb_{13.5}Si_{86.5}$ sample with the heat treatment temperature.

By monitoring the evolution of the R(T) characteristics of this film (presented figure 3.42), several points can be noticed as disorder is increased :

- A first observable effect is an decrease of the overall conductance with θ, in line with what has been described section 2.3.2.2 : the effective mean free path is decreased as θ increases.
- The value of the conductance at saturation, σ_{min}, is lower for more disordered films [15].
- At the same time, the temperature at which the plateau in resistance appears is lowered as disorder is increased. Indeed, a variation of 1 % in the resistance compared to $1/\sigma_{min}$ occurs at $\sim$ 45 mK for θ=90 ℃ and $\sim$ 30 mK for θ = 250 ℃.
- For the more disordered samples, a deviation from weak localisation seems to appear at very low temperature.

To go beyond this last remark, we plotted figure 3.43 the deviation of the measured conductance of the films (plotted as $1/R_{\square}$) from the best 2D weak localization fits. 2D weak localization is consistent with the measured conduction between 1 K and 200 mK for all θ. However, at low temperature, there is an observable deviation from this law, of small magnitude ($\lesssim$ 0.5 % for θ=90 ℃ for instance).
As disorder is increased :

- The magnitude of this deviation increases by a factor of about 5 between θ = 90 ℃ and θ =250 ℃ [16].
- The maximum deviation (represented by the dotted line on figure 3.43) occurs at higher temperatures as σ_{4K} increases, ranging for this sample from 35 to 55 mK [17].

The observable deviation from weak localisation is small in this sample. However, its importance increases as disorder is further increased. To illustrate this point, we plotted figure 3.44 the resistivity of a 50 Å-thick sample of a-$Nb_{13.5}Si_{86.5}$. The deviation from weak localization, in this sample, is larger than 10% at low temperature. Deviation from weak localization then cannot not be neglected and it is likely that a different conduction process comes into play.
Since the low temperature behaviour of M2 samples, in particular close to the M2-to-Insulator Transition, cannot be accounted for by weak localization only, we will try to understand in the following paragraph what conduction mechanism could be involved.

3.4.3 Strong localization in the metallic samples

3.4.3.1 Identification of the observed localization law

Since, close to the M2-to-Insulator transition, samples show a behaviour more resistive than weak localization, at least before the resistance saturates, one can wonder what mechanism could describe our data. Considering that all activation energies does not go to zero at the M2-to-Insulator Transition (see section 3.3.2.3), one can also wonder if signs or heralds of the insulating phase could not be found on the metallic side of the transition.
To answer this question, we have applied Zabrodskii's method to samples on the metallic side, close to the transition. Although we acknowledge that this represent an unusual approach for metallic samples, Zabrodskii's method gives an indication on possible conduction mechanism [18].

By performing such treatment on samples similar to the one presented figure 3.44, we found that, close to the M2-to-Insulator Transition, the conductivity can be described at low temperature (typically $T < 300$ mK) by an exponential law of the form :

$$R_{\square} = R_M e^{(T_M/T)^n} \tag{3.17}$$

15. We will come back on this point in section 3.4.4.2.
16. We would like to note that, as the temperatures at which these deviations appear are similar, this effect cannot be explained by a problem of thermometer calibration. Indeed, such renormalized curves would, in this case, give a constant deviation at the lowest temperatures.
17. This maximum does not correspond to the onset of the saturating regime.
18. As will be discussed in section A, we will also be able to rule out a power law evolution of the conductivity with temperature.

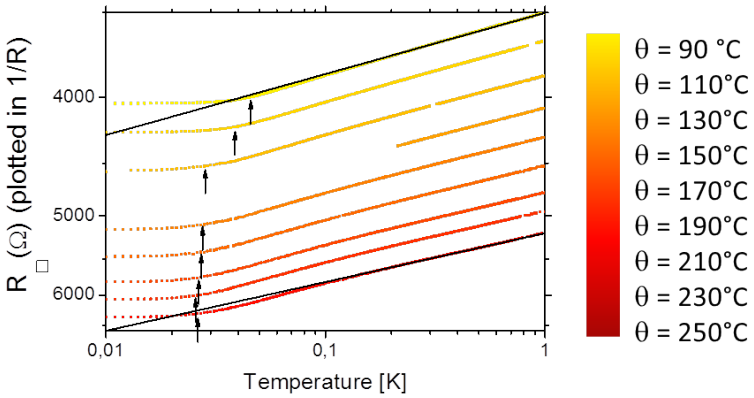

Figure 3.42: $R_{\square}(T)$ for a 75 Å-thick a-$Nb_{13.5}Si_{86.5}$ film for different heat treatment temperatures θ. The straight lines correspond to fits of 2D weak localization for the two extreme values of θ. For $\theta = 250$ ℃, a quantifiable deviation from this law appears at low temperatures before the saturation of the resistance. The arrows correspond to the temperatures at which $R_{\square}(T) = \frac{0.99}{\sigma_{min}}$.(Sample of the OC5 set, from [Crauste, 2010]).

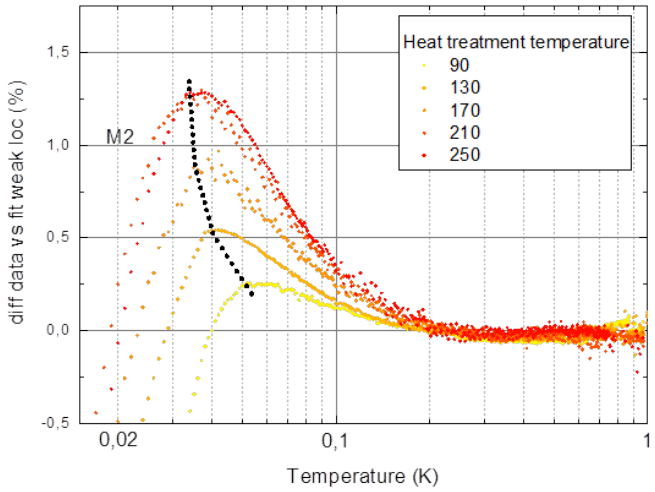

Figure 3.43: Difference in sheet resistance between best 2D weak localization fits and data measured on a 75 Å-thick a-$Nb_{13.5}Si_{86.5}$ film (OC5 set) for different heat treatment temperatures. The dashed line is a guide to the eye showing the maximum deviation from weak localization in temperature.

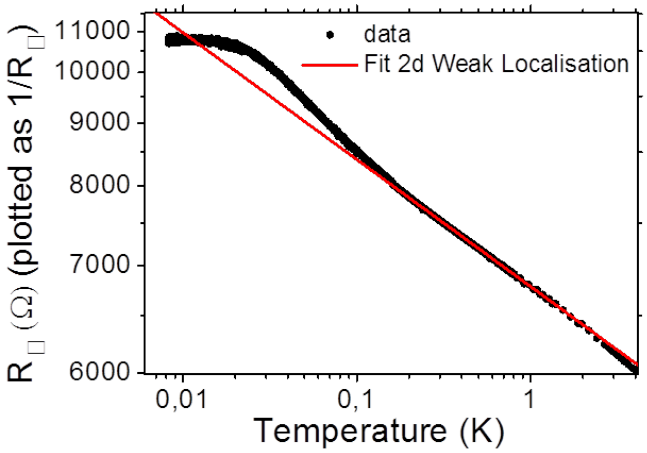

Figure 3.44: Resistance of an as-deposited 50 Å-thick a-$Nb_{13.5}Si_{86.5}$ film as a function of temperature. The red curve is a fit of the 2D weak localization regime (CKSAS43 set).

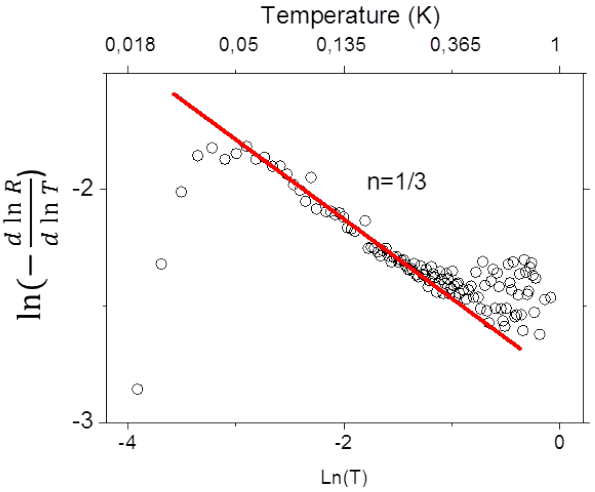

Figure 3.45: Application of Zabrodskii's method on the sample presented figure 3.44. We found a constant slope on about one decade in temperature with a linear coefficient $-\frac{1}{3}$ (represented by a red line), possibly corresponding to a 2D Mott regime. The deviation from the red line reflects the resistance saturation observed at very low temperature.

with $n = \frac{1}{3}$. This law adequately describe experimental data on about one order of magnitude in temperature (see figure 3.45). This regime has been observed for several samples ($3.75 \leqslant \sigma_{4K} \leqslant 6\,\frac{e^2}{h}$). As we have already seen in insulators, $n = \frac{1}{3}$ corresponds to a **2D Mott VRH regime**. We will moreover later see that the characteristic parameters of this evolution (T_M and R_M) are evolving continuously from this regime to the insulating phase.

3.4.3.2 Dependence as a function of the thickness and disorder

By using the same procedure as for insulating films, we extracted R_M and T_M for the samples in the M2 phase with an identified $n = \frac{1}{3}$ regime (figure 3.46). In this figure, σ_{4K} is tuned by both thickness and disorder. R_M is found to evolve continuously as a function of disorder. R_M seems to be mainly controlled by the value of σ_{4K} : samples of similar σ_{4K} having different thicknesses or compositions have R_M that differ by less than 10 %. However, the evolution of R_M with σ_{4K} is opposite to what has been observed in the Mott and ES VRH regimes for insulating samples. At the same time, T_M is also increasing as samples grow closer to the M2-to-Insulator Transition. T_M is moreover thickness-dependent : for the same disorder level at $\sigma_{4K} \sim 4.25\,\frac{e^2}{h}$, the as-deposited 125 Å-thick a-$Nb_{11.3}Si_{88.7}$ sample has a characteristic energy of $T_M = 2.3$ mK whereas the as-deposited 50 Å thick a-$Nb_{13.5}Si_{86.5}$ sample has $T_M = 5.8$ mK.

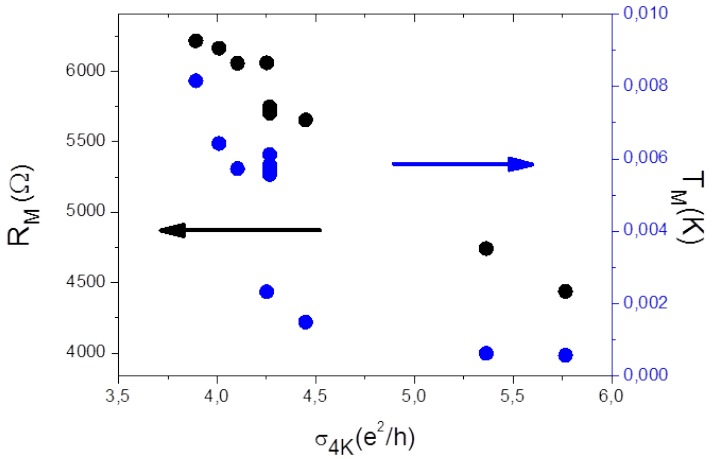

Figure 3.46: Extracted parameters R_M and T_M for metallic samples for which a $n = \frac{1}{3}$ activated regime has been identified. This figure includes samples from batches CKSAS43, CK11, CK13 and CK15 (from [Marrache-Kikuchi, 2006]), of thicknesses ranging from 5 to 25 nm and x ranging from 10 to 13.5 %.

If the identified regime indeed corresponds to a 2D Mott regime, one could expect an effect of the thickness on the characteristic energy since $T_{Mott} \propto \frac{1}{N(E_F)d_\perp}$. One should therefore obtain that $T_M\, d_\perp$ is a constant for a given $N(E_F)$. $T_M\, d_\perp$ has been plotted figure 3.47. As can be seen, $T_M d_\perp$ presents a continuous evolution as a function of disorder and no longer seems to depend on the thickness $d_\perp$ as T_M was. This thickness dependence is a strong argument to support that the observed regime indeed corresponds to a 2D Mott-type VRH regime.

The hopping distance r_m calculated from the extracted parameters in this regime is of the order of 0.15 μm for the as-deposited 50 Å-thick a-$Nb_{13.5}Si_{86.5}$ sample, which is quite long for a hopping process. In addition, T_M is of the order of 0.1 mK. Considering the validity criteria for observing a Mott-type VRH regime (section 3.3.2), this value is way too low regarding Mott's theory. These unusual values are in line with those obtained on the insulating side of the M2-to-Insulator transition (see section 3.3.2.5) : T_{Mott} decreased rapidly as disorder diminished close to the M2-to-Insulator transition, whereas the average hopping distance r_M increased.
Since we are confident in our identification of the insulating behavior ($n = \frac{1}{3}$), we believe that the intermediate temperature regime in these M2 films can be explained by a 2D Mott-type VRH with values of the characteristic temperature T_M which remain to be understood [19].

3.4.3.3 Evolution of the insulating law close to the M2-to-Insulator transition

By increasing disorder further than what has been presented in our metallic state so far, we expect to eventually cross the M2-to-Insulator Transition. We can wonder what would happen to the observed Mott regime in this case, as on the other side of the transition we systematically found an activation law with $n \sim 1$ at the lowest temperatures (see 3.3).

For this, let us start from a M2 sample where a 2D Mott regime has been identified at intermediate temperatures (namely the as-deposited 50 Å-thick a-$Nb_{13.5}Si_{86.5}$ sample). We will use Zabrodskii's method to follow the evolution of n as the sample moves closer to the M2-to-Insulator transition with the heat treatment θ. n then is set as a free parameter for Zabrodskii's method. The corresponding Zabrodskii's plots are shown figure 3.48. n is barely modified until $\theta > 100$ ℃. Then, as disorder is further increased, n progressively evolves from $n = \frac{1}{3}$ until it reaches $n = \frac{1}{2}$ for $\theta = 160$ ℃. For this heat treatment temperature, the resistance still saturates at very low temperature. The sample is therefore still in the M2 regime. However, in the intermediate temperature range, the evolution of conductivity cannot be explained by a Mott-type VRH regime.

19. As mentioned in section 3.3.2.5, these values could well be acceptable when taking into account corrections to the VRH theory close to the MIT [Shafarman et al., 1989].

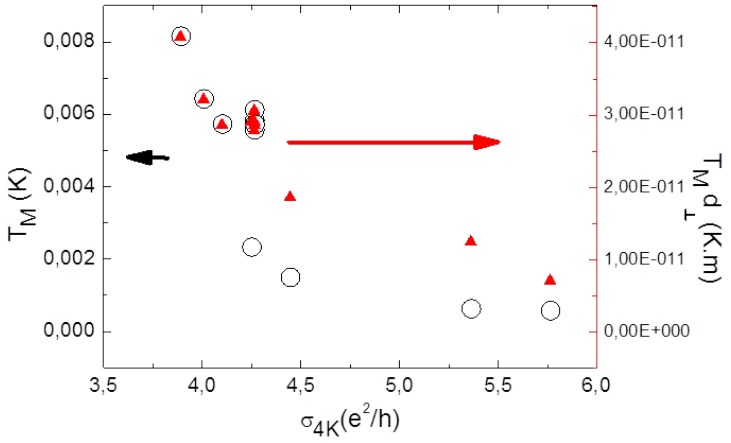

Figure 3.47: Effect of thickness and disorder on the extracted characteristic energy. This figure includes samples of a-Nb_xSi_{1-x} from batches CKSAS43, CK11, CK13 and CK15 (from [Marrache-Kikuchi, 2006], of thicknesses $d_\perp$ ranging from 5 to 25 nm and x ranging from 10 to 13.5 % .

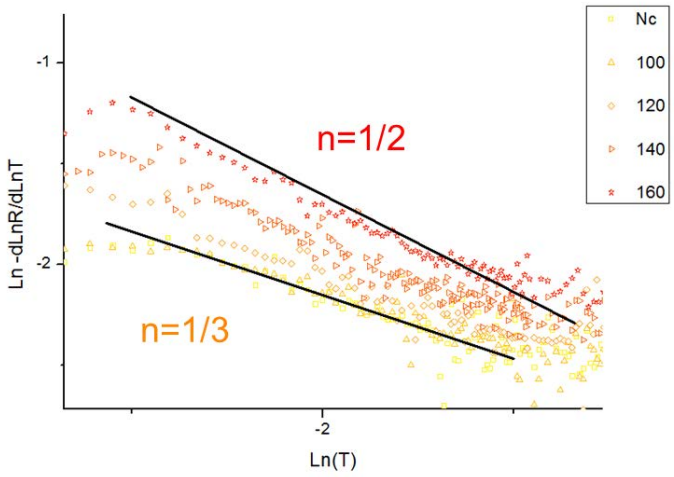

Figure 3.48: Zabrodskii's technique used on a 50 Å-thick sample of a-$Nb_{13.5}Si_{86.5}$ for different heat treatment temperatures θ (in ℃). Only a selection of θ is shown for clarity.

The evolution of n is represented figure 3.49 for a 45Å and a 50 Å-thick a-$Nb_{13.5}Si_{86.5}$ samples of different θ. As can be seen, for both thicknesses, n is constant and signs a 2D Mott regime for $4 \leq \sigma_{4K} \leq 6\frac{e^2}{h}$. When disorder is further increased ($\sigma_{4K} \leq 4.0 \pm 0.2\frac{e^2}{h}$), n increases until it reaches almost $n = 1$ close to the M2-to-Insulator transition (which will be properly defined in section 3.5).

Using the value of n determined in this manner, we extracted the parameters R_n and T_n defined in this continuously evolving regime by $R_\square = R_n e\left(\frac{T_n}{T}\right)^n$. Under the assumption that T_n is a characteristic energy for the system, we can examine how T_n and R_n evolve with disorder. The corresponding plots are given figure 3.50. Both quantities evolve continuously with σ_{4K}. As could be expected, T_n continues to decrease as disorder lessens. However, R_n concomitantly decreases, in line with what has been observed for R_M in the previous paragraph, but contrary to what happens for the VRH laws in the insulating regime.
As can be seen figure 3.51, T_n continuously evolves from the energies found in the previously identified regime. Thickness dependence in this evolving regime is illustrated figure 3.52, where the $R_\square(T)$ characteristics have been plotted for samples of similar $\sigma_{4K} \simeq 3.2\,\frac{e^2}{h}$ but different thicknesses (45 Å, 50 Å and 150 Å). Although these samples all present an intermediate regime with $n = \frac{1}{2}$, the corresponding characteristic temperatures T_n vary with the film thickness. T_n

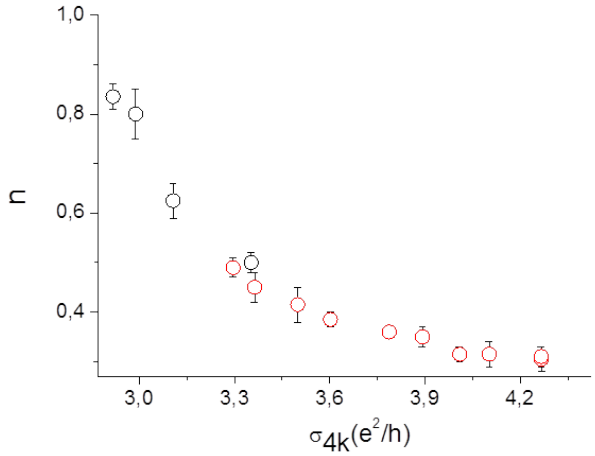

Figure 3.49: Evolution of the parameter n as a function of disorder for 45 Å (in black) and 50 Å-thick (in red) a-$Nb_{13.5}Si_{86.5}$ samples of different θ (θ ranging from 70 to 160 ℃ for the 50 Å-thick sample and ranging from 70 to 110 ℃ for the 45 Å-thick sample).

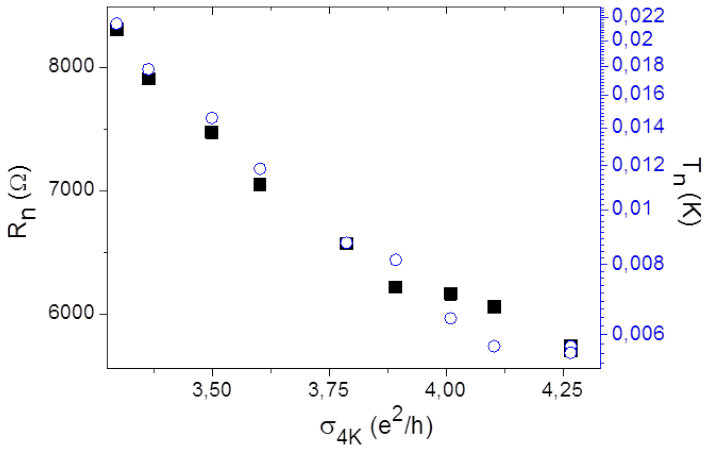

Figure 3.50: 50 Å-thick sample of a-$Nb_{13.5}Si_{86.5}$: evolution of the parameters T_n and R_n as a function of heat treatment.

therefore is thickness-dependent, similarly to a Mott-type characteristic energy, even though, for these samples, the activation law resembles more an ES-type VRH. We will come back on a possible interpretation of this effect in a later section.

3.4.4 The saturations

Until now, we have studied the intermediate temperature behaviour of our metallic samples. Let us now turn to the very low temperature behaviour of the resistance, namely the "resistance saturations".

In sections 2.3.3.4, 3.4.1 and 3.4.2.4, we mentioned that previously studied M2 samples presented a well-defined plateau in resistance at very low temperature, which value $R_{min} = R_{\square}$(10 mK) increased as disorder increased. The temperature at which the saturation sets in, T_{sat} also decreases with σ_{4K}. In the present work, low-disordered M2 samples present the same kind of behaviour as shown figures 3.13 and 3.14. However, for more disordered M2 samples, such a plateau is not measurable at 10 mK, although there is a clear deviation from the higher temperature conduction law.
The question then is : how can we separate the M2 regime from the insulating one?

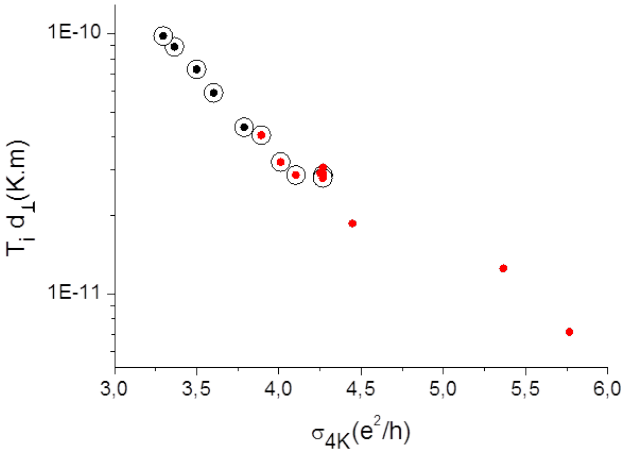

Figure 3.51: (Empty circles) $T_i d_\perp$ $(i = M, n)$ of a single 50 Å-thick sample of a-$Nb_{13.5}Si_{86.5}$ at heat treatment temperatures ranging from 70 to 160 ℃, and samples from the batches CK11, CK13 and CK15 (from [Marrache-Kikuchi, 2006]) identified in the $n = \frac{1}{3}$ regime (shown figure 3.49). (Red dots) $T_M d_\perp$ for samples which have been identified with a 2D Mott regime for M2 samples in which a 2D Mott regime has been identified. (Black dots) samples with $n > 1/3$ as seen in 3.49.

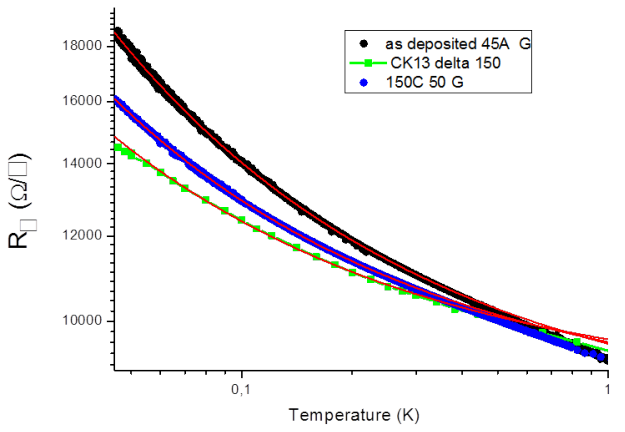

Figure 3.52: Close-up on the $R_\square(T)$ characteristic between 0.5 and 1 K of samples of a-$Nb_{13.5}Si_{86.5}$ (50 Å-thick which sustained a heat treatment at 150 ℃ in black, as-deposited 45 Å-thick in blue) and a-$Nb_{10}Si_{90}$ (as-deposited 150 Å-thick, in green). Fits of the resistivity with $n = \frac{1}{2}$ activated laws are presented in red.

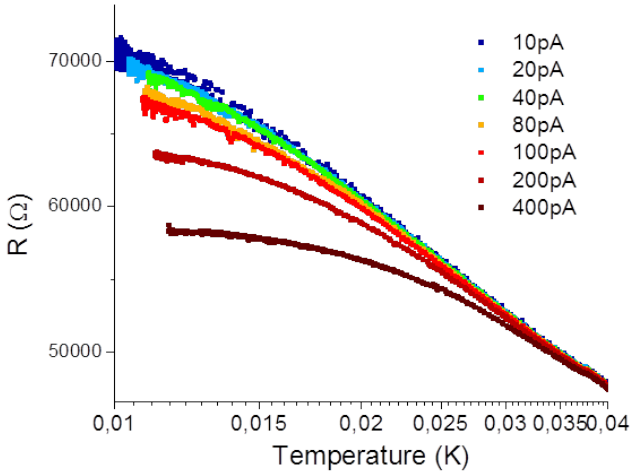

Figure 3.53: Measurement of the $R(T)$ characteristics at different bias currents, for a 50 Å-thick a-$Nb_{13.5}Si_{86.5}$ sample which sustained a heat treatment at 160 ℃. This plot allows us to ensure that we are in the Ohmic regime.

In order to answer this question, one ought to carefully take into account electron-phonon decoupling, since the corresponding samples have resistances of the order of a few tens of kΩ for which measurement at 10 mK is not easy. Indeed, our high impedance set-up gives a large uncertainty at these values of resistance, and the TRMC2 cannot send excitations lower than 10 pA (see section 2.2.3). In this range of resistance, the measurements are therefore subject to possible electron heating effects which have to be considered.

Let us emphasize that this problem is limited to a small number of samples (the 45 Å-thick $Nb_{13.5}Si_{86.5}$ sample with heat treatments of 100 and 110 ℃). For most of our samples, several measurements at different biases have been made, ensuring that we indeed were in the ohmic regime. For instance, figure 3.53 shows measurements made at biases ranging from 10 to 400 pA for the 50 Å-thick $Nb_{13.5}Si_{86.5}$ sample with heat treatments of 160 ℃ : if electron-heating effects can be seen at high currents, the three smaller biases give the same value of the resistance.

In this section, we will check that our observed metals cannot be explained by electron-phonon decoupling linked to an external source of noise or to a limitation of the measurement apparatus. We will also monitor the evolution of the resistance observed at the lowest measured temperature, close to the MIT.

3.4.4.1 Electron-phonon decoupling

Measurement of the Electron-Phonon coupling constant

When electrons are subjected to a power source (under the effects of an increased polarisation or of a spurious electromagnetic power for instance), inelastic scattering with phonons may not be sufficient to thermalize them at low temperature. In this case, the electrons have a temperature T_e which differ from the temperature of the thermal bath, which we will assume to be equal to the phonon temperature T_{ph}. This phenomena is described by the following equation :

$$\frac{P}{V} = g_{e-ph}(T_e^{\beta} - T_{ph}^{\beta}) \tag{3.18}$$

where P is, in our case, the Joule heating power, V is the volume of the film, β is a constant related to the electron-phonon relaxation time [20] and g_{e-ph} is the electron-phonon coupling coefficient. If g_{e-ph} is too low - or equivalently P is too high - we may observe a saturation of the resistance due to electron heating.

20. $\beta = 5$ has been found in 100 nm-thick a-$Nb_{8.3}Si_{91.7}$ [Marnieros et al., 2000]. This value is consistent with a two dimensions electron-phonon interaction in the dirty case [Liu and Giordano, 1991].

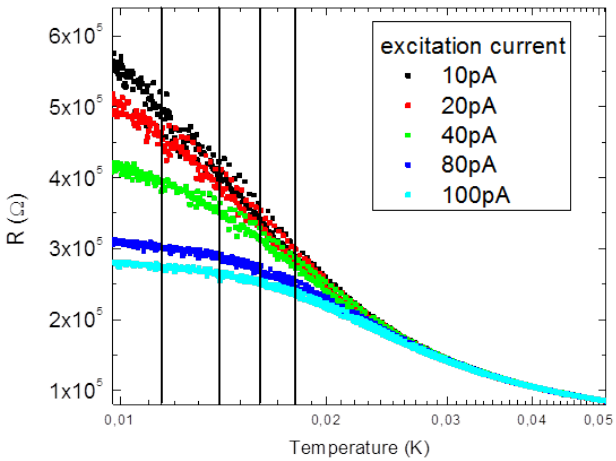

Figure 3.54: Measurement of the $R(T)$ characteristics at different bias currents, for a 45 Å-thick a-$Nb_{13.5}Si_{86.5}$ sample which sustained heat treatment at 110 ℃.

g_{e-ph} can be experimentally determined by measuring the considered film at different polarizations. Indeed, taking the lowest bias as the reference [21] - i.e. the one for which electronic and phononic temperatures are equal -, and acknowledging that the resistance is dependent on the electron temperature (and not the phonon one), at each (phononic) temperature the resistance measured at bias I allows to determine the electronic temperature. Then, $P(T_e^\beta - T_{ph}^\beta)$ should be linear with a coefficient g_{e-ph} [Marnieros et al., 2000].
For the 45 Å-thick $Nb_{13.5}Si_{86.5}$ sample which has sustained a heat treatment at 110 ℃ [22], such bias current effect can be seen figure 3.54. In particular : the 10 pA and 20 pA biases gave identical values (within the measurement noise) of R down to 11 mK. This is the region where the 10 pA measurement was considered trustworthy. However, there is a 10% difference in the resistance measured below 12 mK at 10 pA and at 20 pA. The measurement at 10 pA can therefore not be completely trusted to be in the ohmic regime at these temperatures.

By performing the electron-phonon analysis, shown figure 3.55, we extracted $g_{e-ph} = (1 \pm 0.25) \times 10^8$ W.K^{-5}.m^{-3} in the [11,20 mK] range. This value is consistent with other measurements of the electron-phonon coupling constant that have been performed throughout the years in the group : for a thick (1000 Å) a-$Nb_{8.3}Si_{91.7}$ sample, $g_{e-ph} = (1.3 \pm 0.3) \times 10^8$ W.K^{-5}.m^{-3} was obtained between 30 and 600 mK.

For samples close to the M2-to-Insulator Transition

Having determined the electron-phonon coupling constant, and assuming that it is temperature independent (in the [8 mK, 30 mK] range), we can simulate the effect of Joule heating in our samples as a function of the applied current. In particular, we are able to check if deviations occurring at low temperature are linked to electron-phonon decoupling.
We then start from the assumption that the "real" conduction law, corresponding to non-heated electrons, is the continuation of the law followed at intermediate temperatures. Then, using the value of g_{e-ph} for the considered film, we simulate the sample response for a given bias.
Figure 3.56 shows the result of this modelization for a sample which exhibits a strong localization-type of law at intermediate temperatures (see section 3.4.3). First, the intermediate temperature (here $17 < T < 200$ mK) law is determined. In the present case, it is of activated type, with n=0.83, and corresponds to the green line figure 3.4.3. Then, knowing the electron-phonon coupling constant (here $g_{e-ph} = 1 \times 10^8$ W.K^{-5}.m^{-3}), we model the effect of a 10 pA bias current. The corresponding curve is shown in orange. As can be seen, **the simulated curve cannot explain the observed resistance saturation**. In particular, the value measured at 10 mK is two times smaller than the simulated value.

21. This is reasonable as long as the two lowest biases yield the same resistance value.
22. This sample is on the verge of the M2-to-Insulator Transition.

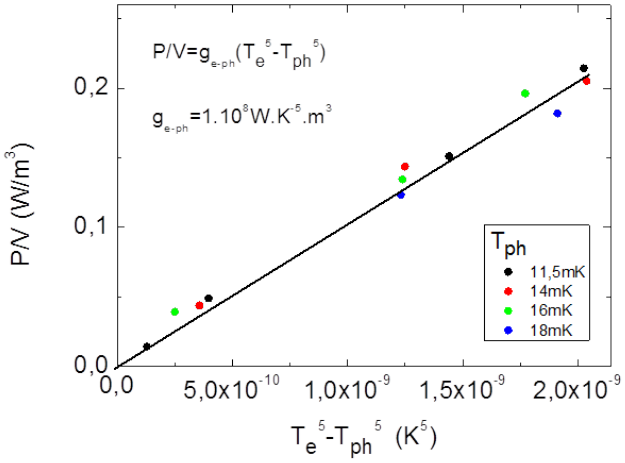

Figure 3.55: P/V as a function of $T_e^5 - T_{ph}^5$ for the measurements presented figure 3.54. From the linear fit (solid line), we obtain $g_{e-ph} = (1 \pm 0.25)\, 10^8$ W.K^{-5}.m^{-3}.

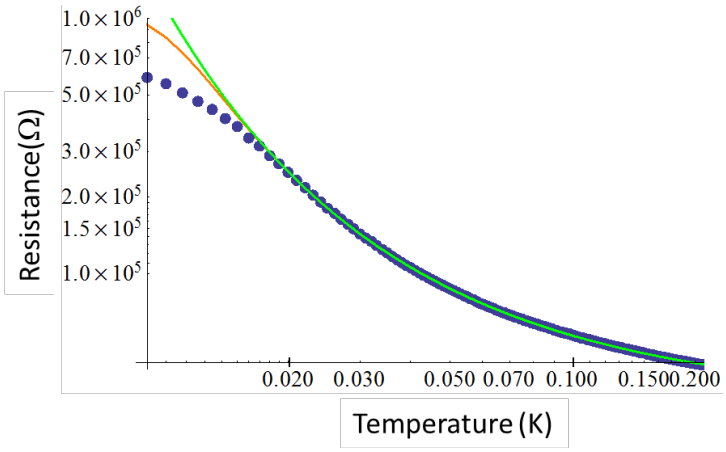

Figure 3.56: Blue points are experimental data, corresponding to the sample presented figure 3.54 measured at 10 pA. The green line is the extrapolation from high temperatures with $R = 33350\, e^{(\frac{0.0472}{T})^{0.83}}$. The orange line is the simulation of the effect of electron-phonon decoupling on the extrapolated green curve, with a current of 10 pA corresponding to the measurement bias, obtained by assuming $g_{e-ph} = 1 \times 10^8$ W.K^{-5}.m^{-3}.

Exclusion of parasitic power

Having excluded that the electrical power injected by the measurement itself could be at the origin of the observed saturations, one can wonder if those could be explained by a constant power arriving on the sample, due to bad IR shielding, or noisy instruments for instance. We have addressed this problem in sections 2.2.3.3 and 3.2.2, but we would here like to provide a more quantitative analysis.

One way of discarding this artefact is to estimate the outside spurious power necessary to produce the resistance saturation observed in the M2 regime. Similarly to what has been done in the previous paragraph, we assume that the conduction law at the lowest temperatures is the continuation of the intermediate temperature conduction law. Then, knowing the electron-phonon coupling constant, we estimate the power required to explain the resistance saturation. Figure 3.57 shows such a simulation for the 50 Å-thick as-deposited a-$Nb_{13.5}Si_{86.5}$ sample : only an external power as high as $P_0 = 2.2\, 10^{-14}$ W can explain the low temperature resistance behaviour. This value is two orders of magnitude higher than the measurement power (of the order of 3×10^{-16} W for this sample). This would correspond to a voltage of $U_{noise} = 25\ \mu$V.

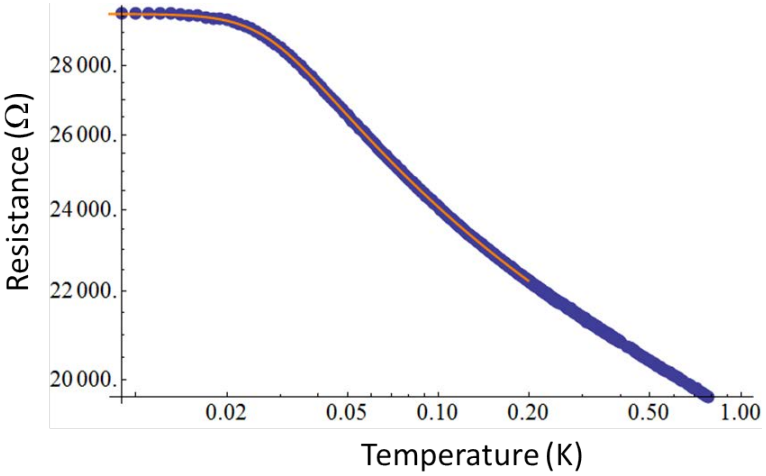

Figure 3.57: Simulation of electron-phonon decoupling on a 50 Å-thick as-deposited a-$Nb_{13.5}Si_{86.5}$ sample, with a constant power $P_0 = 2.2 \times 10^{-15}$ W (orange line).

This is unrealistic. Indeed, such a high voltage noise source would not allow the measurement of both the M1 and the superconducting regimes - which were measured in the same cryostat -. It would alternatively correspond to a current of I_{noise}=800 pA. This is unrealistic as well since such a current noise source would affect more the most insulating samples. A constant incoming power P_0 from the environment is also unlikely : experimentally the temperature at which the resistance plateau appears decreases as the sample becomes more and more resistive. Moreover, insulators have been measured in the same cryogenic environment, without observable electron heating effects.
Finally, let us note that this modelisation yields different values of P_0 for different samples. For instance, $P_0 = 1.4\,10^{-15}$ W for the 45 Å-thick as-deposited a-$Nb_{13.5}Si_{86.5}$ sample. This power corresponds to $U_{noise} = 10$ μV or $I_{noise} = 130$ pA. This confirms that the **resistance plateaus cannot be due to a constant noise source, whether current or voltage. Moreover, it shows that this phenomenon cannot be explained by a constant incoming power either.**

3.4.4.2 Evolution of the saturation as a function of disorder

Having checked that the obtained saturations, even for the highest observed resistances at 10 mK, cannot be explained by electron-phonon decoupling, we can safely use the obtained values of $\sigma_{min} = \sigma_{\square}\,(10mK)$ to complete the evolution of σ_{min} obtained in [Couëdo, 2014] (and presented in section 2.3.3.4). The obtained plot is presented figure 3.58 [23] for all samples identified as being in the M2 phase, grown for this thesis and mentioned in [Marrache-Kikuchi, 2006] [Crauste, 2010] [Couëdo, 2014].
The obtain curve allowed us to find that :

- σ_{min} evolves linearly as a function of σ_{4K} for $\sigma_{4K} > (4.65 \pm 0.65)\,\frac{e^2}{h}$, emphasizing that, for these samples, quantum corrections are small between 10 mK and 4 K.
- σ_{min} does not depend on the tuning parameter (either composition, thickness or heat treatment).
- σ_{min} goes to zero as $\sigma_{4K} \to (3 \pm 0.2)\,\frac{e^2}{h}$.
- As the low temperature correction to conductivity becomes important when we get closer to the MIT, σ_{min} evolves faster (it decreases of 2 orders of magnitude between $\sigma_{4K} = 4.5\,\frac{e^2}{h}$ and $\sigma_{4K} = 3\,\frac{e^2}{h}$), giving rise to a sharp transition.

Let us recall that, according to the Ioffe-Regel criterion, a MIT should occur in the 3D case for $k_F l \sim 1$, with $\sigma_c = \frac{e^2}{h}$. In our case, we found a transition around $\sigma_{4K,c} \sim 3\,\frac{e^2}{h}$, close to this expected value, but slightly higher. This is probably due to the difficulty of determin-

23. To obtain this figure, the 50 Å-thick a-$Nb_{13.5}Si_{86.5}$ sample from [Crauste, 2010] has been omitted. Indeed, an important part of the present thesis has been dedicated to the elimination of noise on the presented experiment. The incriminated sample has been found, a posteriori, to have been affected by a non-optimal filtering of the lines.

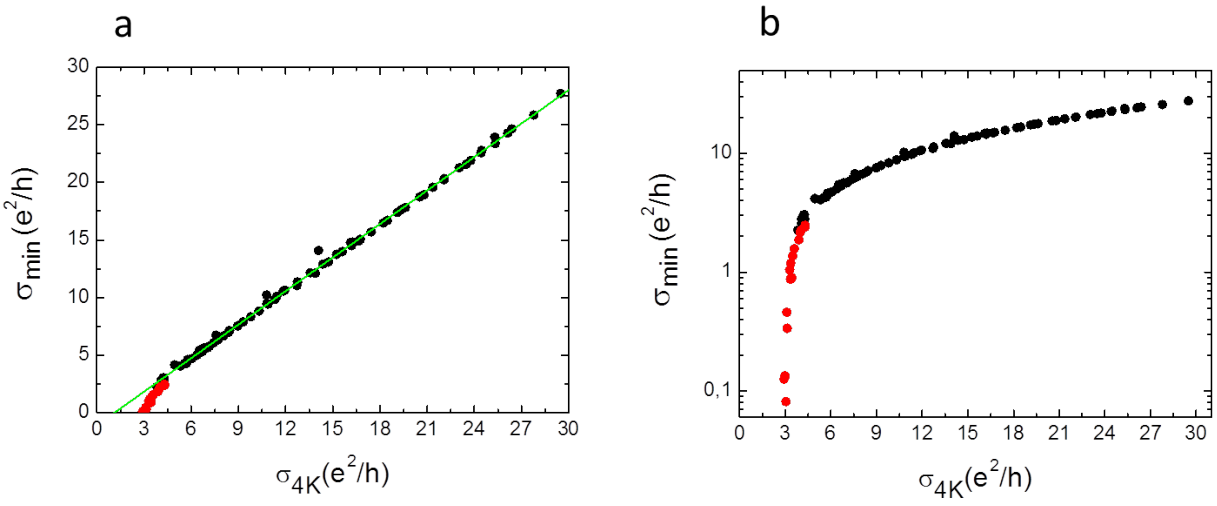

Figure 3.58: σ_{min} as a function of σ_{4K} in linear (a) and semilog (b) scales. In red, σ_{min} obtained from the samples grown for this thesis. In black, σ_{min} obtained from samples of [Marrache-Kikuchi, 2006] [Crauste, 2010] [Couëdo, 2014]. In green, fit of the experimental data with $\sigma_{min} = 0.97\sigma_{4K} - 1.05$ (in $\frac{e^2}{h}$ unit).

ing the absolute value of $k_F l$, in particular in the presence of both localization and interactions [24].

Since σ_{min} (considered as an estimation of the $T \to 0$ conductivity) vanishes near the M2-to-Insulator Transition, it plays a role similar to an order parameter. We can therefore fit the evolution of σ_{min} with the scaling relation :

$$\sigma_{min} \propto |\sigma_{4K} - \sigma_{4K,c}|^{\mu} \tag{3.19}$$

where μ is a critical exponent depending on the universality class of the system. By fitting our data with this scaling law (figure 3.59), we find $\sigma_{4K,c} = 3\frac{e^2}{h}$ and $\mu = 0.7 \pm 0.05$. This value can be compared to those found in other 2D MITs [Popović, 2016] which range from 1 to 3. We clearly belong to another universality class, maybe due to :

1. a much higher carrier density ($\sim 10^{13}$ cm^{-2} vs $\sim 10^{11}$ cm^{-2} in Si-MOSFETs)
2. the proximity of a superconducting state.

To summarize our findings on the M2 phase :

- Close to the M1-to-M2 transition, M2 samples exhibit a 2D weak localization behaviour at intermediate temperatures, with an anomalous dependence of the prefactor α_{WL} with disorder.
- When disorder is increased, deviations from the 2D weak localization law is observed and it gives way to a more localizing behaviour, compatible with an activated conduction law.
- This activated law is identifiable with a 2D Mott-type VRH, except close to the M2-to-Insulator transition where the resistance increases more steeply, until it reaches a simply activated law ($n = \frac{1}{3}$ continuously evolves towards $n \sim 1$). The corresponding characteristic temperatures and resistances increase as the MIT is approached. This evolution is counter-intuitive for R_M (R_n). Moreover, the values for T_M (T_n) are much smaller than expected and they are thickness-dependent as would be expected for a Mott-type VRH.
- At low temperatures, the resistance saturates for all samples in the M2 regime. The corresponding values of σ_{min} are universal and only depend on σ_{4K}. σ_{min} goes to zero at the MIT, as could be expected, although the system is here 2D with respect to all relevant phenomena.

24. Taking the 300 K conductivity as a measure of disorder gives $\sigma_{300K,c} = 9\frac{e^2}{h}$.

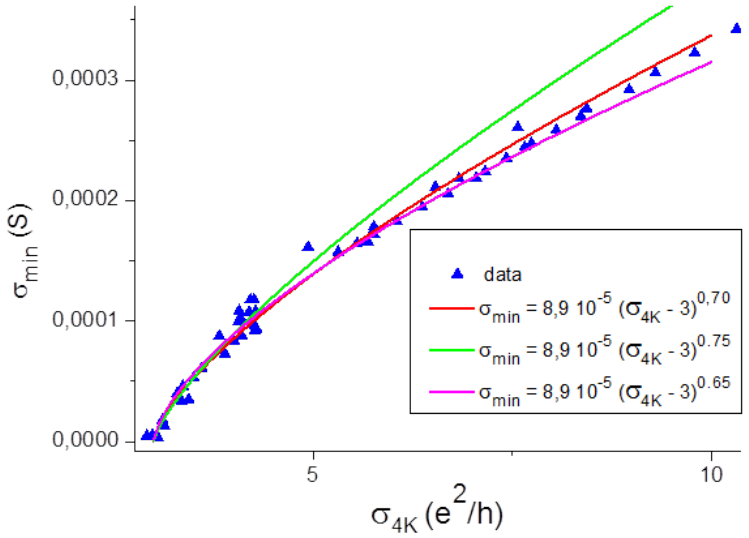

Figure 3.59: Close-up on σ_{min} for $\sigma_{4K} \lesssim 10\frac{e^2}{h}$ with fits using the scaling relation given by equation 3.19 (see laws and parameters in the inset).

3.5 The MIT

In section 3.3, we have analyzed the evolution of the transport properties in insulating films as disorder is varied. In section 3.4, we have done the same for the metallic regime. In this section, we would like to connect both analyzes and examine what happens at the M2-to-Insulator transition. We will infer the necessary conditions to have an insulating sample in a-Nb_xSi_{1-x} alloys. We will then draw the phase diagram for our samples and try to propose an interpretation for the observed phenomena in the next section. But first, let us identify the M2-to-Insulator Transition more precisely.

3.5.1 Identification of the first insulating sample in a series

In order to establish more precisely the criteria for the M2-to-Insulator transition, we would like to examine more closely the case of the 45 Å-thick a-$Nb_{13.5}Si_{86.5}$ film. As seen figure 3.13, a progressive increase in the heat treatment temperature allowed us to sample the transition : we managed to cross the MIT within a single sample via θ. At the same time, the parameter n increases as observed figures 3.49 and 3.60. As n becomes higher than 0.5 at the lowest temperatures, 2 regimes are clearly defined : one with n evolving from 0.5 to 1 (at the lowest temperatures), and an ES VRH regime (at intermediate temperature).

In section 3.4.4.1 (see figure 3.56), we have shown that, for $\theta = 110$ ℃ ($\sigma_{4K} = 2.9\,\frac{e^2}{h}$), this sample still presented an intrinsic saturation of the resistance and therefore was on the M2 side of the transition.
One step hotter in the heat treatment temperature renders the same sample insulating. Indeed, as can be seen figure 3.61, for $\theta = 120$ ℃ ($\sigma_{4K} \sim 2.85\,\frac{e^2}{h}$), the film does not deviate from a simply activated law at low temperature (n extracted through Zabrodskii's method gives $n = 0.98 \pm 0.05$). This activated regime is observed from 12.5 mK to 90 mK, while the resistance varies by a factor 20 from 25 kΩ to 530 kΩ.
Let us emphasize that $n = 1$ (within experimental determination) is only obtained from $\theta = 120$ ℃ and hotter. The intermediate temperature activated regime measured for $\theta = 110$ ℃ corresponded to $n = 0.85$. $n = 1$ **at low temperature therefore signs the emergence of the insulating phase.** We can identify the transition to occur at $\sigma_{4K} = 2.85\,\frac{e^2}{h}$, close to the critical value determined by the evolution of $\sigma_{min}(4K)$ observed figure 3.59.

For this film, the Zabrodskii's plot is given figure 3.63 : the simply activated regime ($T_0 \sim$ 50 mK ; $R_0 \sim$13.5 kΩ) gives way to an ES-type VRH regime for temperatures ranging from 90 mK to 700 mK ($T_{ES} \sim$90 mK ; $R_{ES} \sim$8.6 kΩ) as described in section 3.3. The corresponding

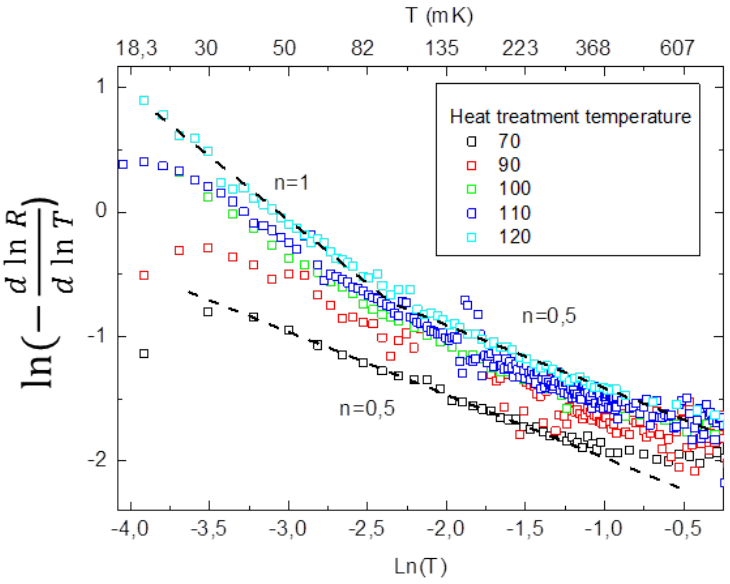

Figure 3.60: Zabrodskii's technique used on a 45 Å-thick sample of a-$Nb_{13.5}Si_{86.5}$ for different heat treatment temperatures θ (in ℃). Only a selection of θ is shown for clarity. For films with $n > 0.5$, a intermediate temperature ES VRH regime is clearly visible.

fits are compared to the experimental data figure 3.62.

3.5.2 Comparison of the laws at both sides of the MIT

In this thesis, we found and characterized strong insulating laws on both sides of the MIT. In each case, we extracted a parameter n (characteristic of the insulating law), a characteristic energy T_i, and a parameter R_i. For all the samples studied in this thesis, including old data sets, these parameters are presented figures 3.64 [25], 3.65 and 3.66.

We saw that, in our **metallic films**,
- For samples such that $5.5 > \sigma_{4K} > 4\,\frac{e^2}{h}$, close to the MIT, we have an insulating regime with $n = \frac{1}{3}$ at intermediate temperatures, larger than those for which the resistance saturates.
- Within our error bars, the extracted parameters T_i and R_i increase continuously as a function of disorder.
- We observe an effect of the thickness on T_M (and T_n), as expected for a 2D Mott regime.

On the **insulating phase**, we saw that :
- We observe different insulating laws ($n \sim 1$, ES and 2D Mott VRH) with $T_0 < T_{ES} < T_{Mott}$ when the three regimes are observed. The hierarchy for T_{ES} and T_{Mott} is what is expected theoretically due to the opening of the Coulomb gap. The T_i are diminishing as we get closer to the TMI.
- We did not observe any visible effects of the thickness on the parameters [26] T_i and R_i.
- R_{Mott} and R_{ES} decrease when disorder is increased, while R_0 increases.

Now, let us look at the MIT. What is remarkable in figures 3.23, 3.65 and 3.66 is the continuity of all measured parameters : The exponents characterizing the strong localization laws continuously evolves from a single $n = \frac{1}{3}$ law in the M2 regime up to 3 exponents of $n = \frac{1}{3}$, $n = \frac{1}{2}$ and $n = 1$ in the insulator. Concomitantly, the characteristic energies T_i all converge close to $\sigma_{4K,c} = 3 \pm 0.2\,\frac{e^2}{h}$, the critical disorder value for the M2-to-Insulator transition. Even more striking is the convergence of all characteristic resistances at the M2IT, whatever their initial evolution with disorder in their respective phases.
These implies a very gradual change in the system, more compatible with a crossover than an

25. Only the lowest temperature regime and the ES regime are represented. Moreover, samples showing $n > 1.2$ (see figure 3.23) are not presented here for clarity. They are addressed in appendix B and section 3.6

26. Such effect is expected in T_{Mott} but is not observed due to a limitation in the choice of samples with different thicknesses in this regime.

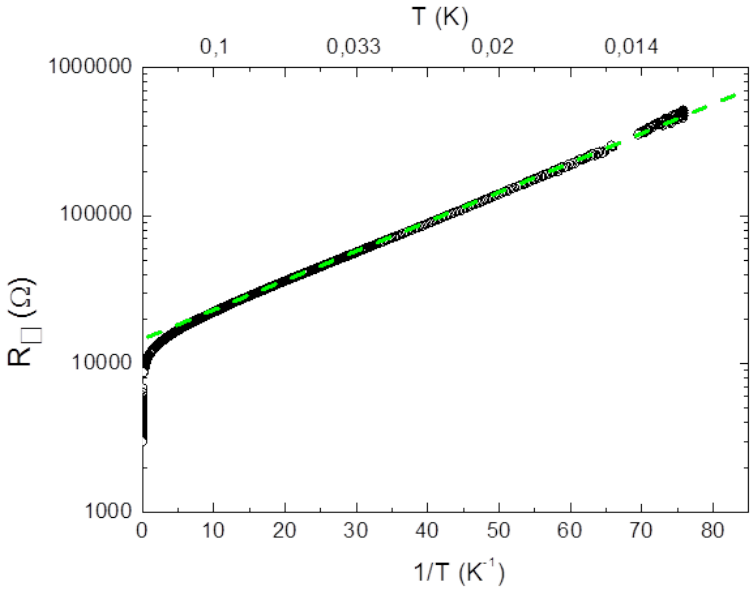

Figure 3.61: $R_{\square}(1/T)$ characteristic of a 45 Å-thick a-$Nb_{13.5}Si_{86.5}$ sample which sustained a heat treatment at 120 ℃. Dashed line : linear fit showing no deviation to the $e^{T_0/T}$ law at low temperatures.

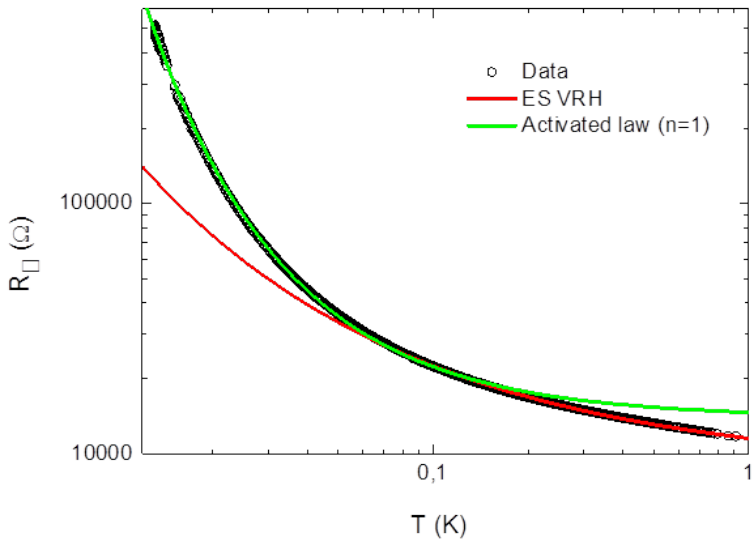

Figure 3.62: $R_{\square}(T)$ characteristic of a 45 Å-thick a-$Nb_{13.5}Si_{86.5}$ sample which sustained a heat treatment at 120 ℃. In addition are plotted the fits for the simply activated regime (in green) and the ES VRH regime (in red). See text for the fitting parameters.

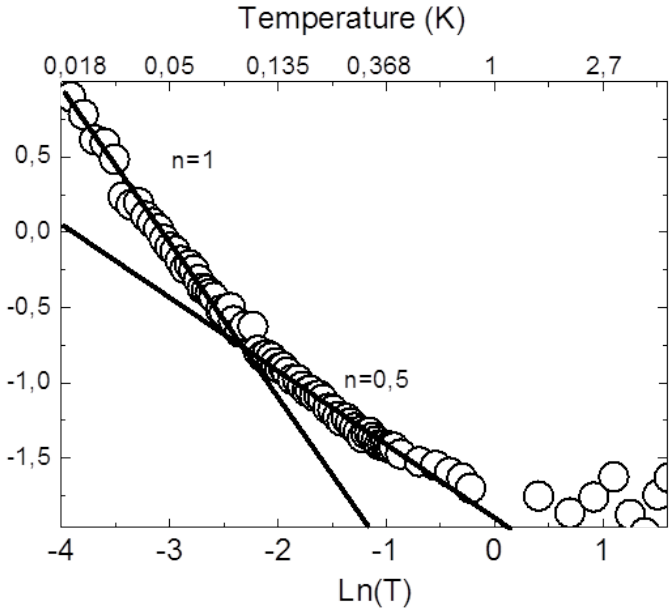

Figure 3.63: Zabrodskii's method applied on the film presented figure 3.62. Both the simply activated and the ES VRH regime are clearly determined.

actual transition at $\sigma_{4K,c} = 3 \pm 0.2 \frac{e^2}{h}$. In particular, the characteristic energies does not vanish at $\sigma_{4K,c}$. In section 3.3.2.4, we also saw that Δ_2^{CG} vanished in the vicinity of $\sigma_{4K} = 4\text{-}5 \frac{e^2}{h}$ rather than at the M2IT. The question then arises on whether the "M2IT" is an actual transition or a crossover.

3.6 Interpretation

The questions listed at the beginning of this work (introduction of section 2.4) and which we tried to address could be summarized by :

- What is the nature of the Metal 2 phase? Is it fermionic or bosonic? Is it 3D or 2D? Are there any precursor signs of the insulating regime in this dissipative phase?
- What is the nature of the Insulating phase? Is it fermionic or bosonic? Can it be fully explained by an activated behavior?
- Is the Metal 2-to-Insulator a phase transition or a crossover? Is the change continuous or abrupt?

In order to try to answer these questions, we have performed a detailed study of the M2-to-Insulator Transition thanks to the three different parameters (x, $d_\perp$ and θ for fine-tuning) that were available to modify the disorder in a-Nb_xSi_{1-x} films. We have focused on characterizing the evolution of the resistance with temperature for different disorder levels, and analyzed accordingly the experimental data obtained both during this thesis and in previous works. We have established that the M2 regime is characterized not only by a saturating resistance at low temperature, but also by a strongly localized behavior, at intermediate temperatures, when close to the M2-to-Insulator Transition. This behavior is highly unusual for metallic phases and we believe it is an important result of this work. Moreover, we have shown that the insulating laws evolve progressively and continuously, not only in the insulating phase, but also in the M2 phase. However, the analysis was carried out without much dwelling on a possible interpretation. This is the object of this paragraph. In the following, we will try to answer these questions by proposing a scenario which could explain the different observed phenomena.

The Metal 2 phase - The Metal 2 phase is characterized by a negative TCR ($\frac{dR}{dT}$) and a saturation of the resistivity at very low temperatures. In the present work, we have been able to refine our analysis of this ground state. Let us summarize the major observations that have to be theoretically explained :

- Close to the M1-to-M2 transition, M2 samples exhibit a 2D weak localization behavior at intermediate temperatures, with an anomalous dependence of the prefactor α_{wl} with

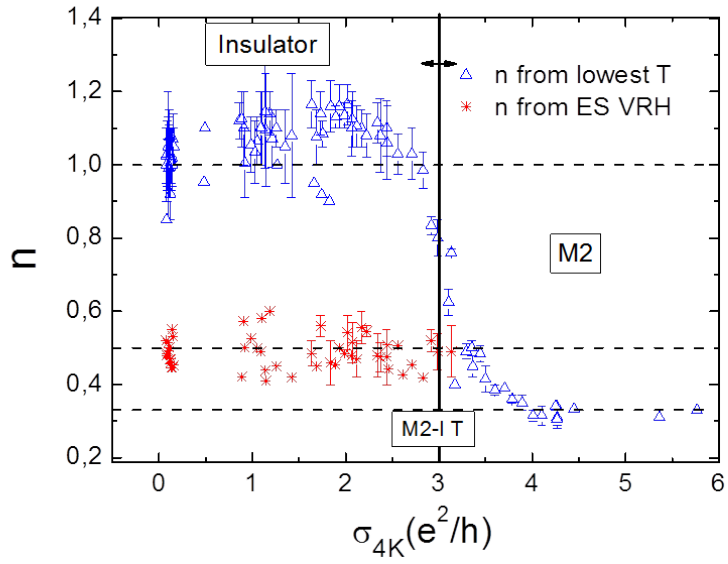

Figure 3.64: Evolution of the parameter n as a function of the 4 K sheet conductivity. Dashed lines correspond to $n = \frac{1}{3}$, $n = \frac{1}{2}$ and $n = 1$. The samples included are from this thesis and from the sets CK15, CK13, CK11, CK10, CK9, CK8 and CK6 of compositions ranging from 8 to 12.5% in Nb and thicknesses from 125 to 250 Å, from [Marrache-Kikuchi, 2006].

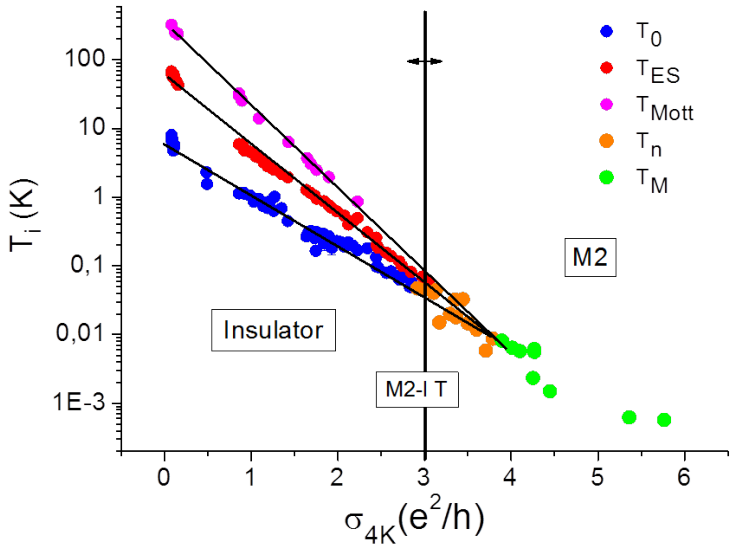

Figure 3.65: Evolution of the characteristic energies of the activated regimes observed for the samples featuring figure 3.64.

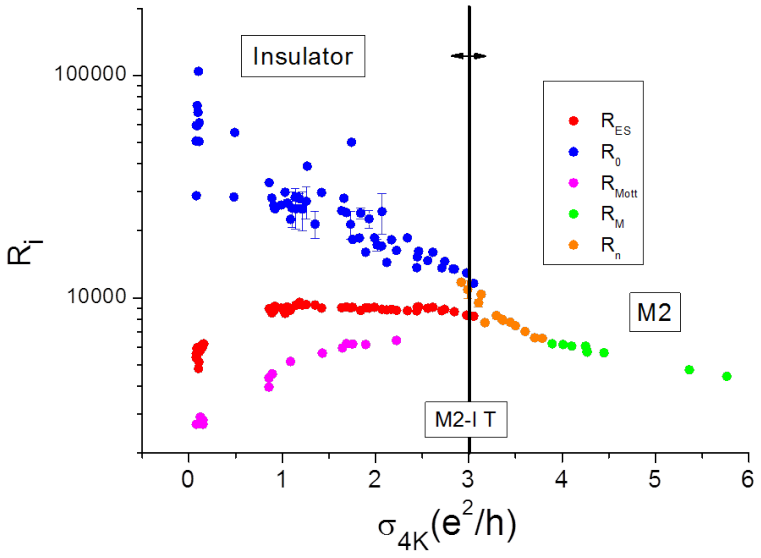

Figure 3.66: Evolution of the prefactors of the activated regimes, for the same samples than figure 3.64.

disorder. In this section, we will refer to this behavior as **M2M**.

- When disorder is increased, deviations from the 2D weak localization law is observed and it gives way to more insulating behaviors, compatible with an activated conduction law. In this section, we will refer to this behavior as **M2I**.
- The observed activated law is compatible with a 2D Mott-type VRH, except close to the M2-to-Insulator transition, which we will consider in a later paragraph. The corresponding characteristic temperatures (T_M) and resistances (R_M) increase as the MIT is approached. This evolution is counter-intuitive for R_M. Moreover, the values for T_M are much smaller than expected and they are thickness-dependent as awaited for a Mott-type VRH.
- At low temperatures, the resistance saturates for all samples in the M2 regime. The corresponding values of σ_{min} are universal and only depend on σ_{4K}. σ_{min} goes to zero at the MIT.

As we have seen section 2.3.3.4, the M2 phase emerges from another metallic phase, the Metal 1, which has been characterized in [Couëdo, 2014] and for which it is reasonable to assume that superconducting fluctuations play an important role at intermediate temperatures, before the resistivity saturates. We propose to describe this phase as metallic islands scattered in a superconducting matrix. In this picture, the proportion of metallic islands is close to the percolation threshold, thus explaining the finite resistance measured at low temperature.

Conversely, **the Metal 2 could then be pictured as superconducting islands scattered in a fermionic matrix**. When disorder is increased, the size of the superconducting islands decreases. Cooper pairs that were localized in these islands are broken and the corresponding electrons contribute to the fermionic matrix.

The following experimental features could then be explained :

- **The weak localization feature -** At high and intermediate temperatures, the fermionic component dominates, and behaves like a regular disordered 2D fermionic system : weak localization explains the $R_\square \propto \ln T$ behavior observed both in the M2M and the M2I phases.
- **Evolution of the weak localization pre-factor α_{wl} -**
  - As disorder is increased in the Metal 1, α_{wl} increases as expected when evolving towards a system where Coulomb interactions are less efficiently screened (section 3.4.2.3).
  - In the M2M phase, as disorder is increased, superconducting puddles are progressively destroyed, inducing an increase of the DOS at the Fermi level $N(E_F)$ which, in turn, could make α_{wl} diminish.
  - In the M2I phase, as disorder is further increased and the number of superconducting puddles diminish, the increase in $N(E_F)$ is no longer sufficient to counterbalance the decrease in the screening efficiency due to disorder. α_{wl} then increases again as disorder is increased.

- **The activated conduction law in the M2I phase -** As disorder becomes important, electrons in the fermionic matrix begin to strongly localize (3.4.3.2), which translates into an activated conduction law at intermediate temperatures.
  - As seen above, in this phase, one would expect the screening becomes less efficient. This would correspond to an Aronov-Altshuler-type anomaly in the density of states. When this feature appears in the DOS, the effect should, at first, be small, so that a Mott-type VRH is possible [Sarachik and Dai, 2002].
  - The characteristic temperature T_M could however be affected by this non-constant DOS [Shafarman et al., 1989], which would explain the small measured values. Indeed, the expression of the VRH characteristic temperatures given section 1.5.1 are only valid well into the insulating regime and breaks down in the vicinity of the metallic phase, and should not be valid close to the MIT [Pollak and Shklovskii, 1991].
  - Whether the fact that the transition from M2M to M2I occurs when Coulomb interactions change in dimensionality is a coincidence or not remains to be investigated.
- **The saturating resistances at low temperature -** Our proposed description of the M2 phase is very similar to a Josephson Junctions Array (JJA) [van der Zant et al., 1996]. These systems are known to, under certain conditions, give rise to metallic states, analogous to those encountered in granular superconductors (see section 1.7.3.4.a). The junctions would, at low temperature, short circuit the fermionic component. The resistance saturations we observe would then fall under the theories developed in section 1.7.3.4. The temperature at which the saturation sets in would then reflect the superconducting critical temperature T_c of each grain.

The M2-to-Insulator Transition - The M2-to-Insulator Transition is characterized by the transition between a finite resistance and a diverging resistance at low temperature. The experimental features that have to be explained are :

- It occurs for $k_F l \sim 3$.
- The activated law at intermediate temperatures in the M2 phase gives way to both an Efros-Shklovskii-type VRH (at intermediate temperature) and a simply activated behavior (at low temperature) on the insulating side.
- The characteristic energy scales on both sides of the transition converge but do not vanish.

Within the developed model, this could be explained as follows. As the screening vanishes, the DOS begins to be unnegligibly affected by Coulomb interactions and a zero-bias dip in the DOS appears (this behavior has been observed in other materials such as Si:B [Lee et al., 1999] or bulk NbSi [Bishop et al., 1985]), providing an increasing value of the activation power n. Eventually, as the DOS becomes almost fully depleted, $n \to 1$. Indeed, it has been observed in 3D Si:P that, as disorder is increased, the parabolic gap ($g(\epsilon) \sim \epsilon^2$) becomes deeper and eventually flattens to zero at low excitations. This would also explain the converge of T_0 and T_{ES} close to the M2IT.

As the Coulomb-induced gap increases, electrons pairing is hindered and superconducting puddles decrease in size and are more scarce. The Josephson tunneling is then suppressed.
The "transition" could then be more appropriately described as a crossover between a regime where the fermionic channel dominates the conduction (the insulator) and a regime where the interplay between the fermionic channel and the superconducting fluctuations give rise to a metallic state.

The insulating regime - The insulating regime is characterized by a simply activated conduction regime at the lowest temperatures which gives way to a VRH-type conduction regime (either a single ES or two successive ES and 2D Mott regimes). Let us summarize our findings on this phase :

- The characteristic energies continuously increase when disorder is increased.
- Close to the M2IT, Mott VRH is no-longer observable.
- The ES-type VRH is always observable.
- Close to the M2IT, the extracted characteristic temperatures are lower than expected for "standard" VRH regimes, and the characteristic resistances R_i all saturate.
- Close to the M2IT, over-activated behaviors are measured.

These could be explained as follows :

- **The over-activated behavior near the M2IT -** This unexpected behavior, observed in some samples in the immediate vicinity of the M2IT, could be explained by superconducting fluctuations. Indeed, in our picture, superconducting fluctuations survive in the M2 phase and could well play a role close to the M2IT. If present, they would lower

the quasi-particle tunneling probability, inducing an increase resistance which can lead to $n > 1$ [Adkins et al., 1980][Kim et al., 1992]. This would explain how, deep in the insulating regime, this over-activated behavior disappears. An alternative interpretation is given in appendix B.

- **The low values for the characteristic temperatures near the M2IT -** As previously stated, these could be explained by a DOS that is not completely depleted close to the M2IT [Shafarman et al., 1989]. Moreover, in Coulomb glasses, Pollack noted that multi-hopping could occur. This glassy behavior would result in a renormalization of the characteristic energies encountered in the insulator, compared with what is encountered for single electron hopping [Pollak and Shklovskii, 1991]. Let us note that this is consistent with the fact that, as NbSi becomes insulating, it behaves like an electron-glass [Delahaye et al., 2014]. Thus, glassy behaviour has been evidenced in this disordered system.
- **The saturating values of R_i near the M2IT -** Saturation of R_i in VRH regimes is often taken as a proof of phononless mechanism of hopping as pointed out in section 3.3.2.3. Pollak has also predicted that multi-hopping mechanism is reflected through a constant characteristic resistance R_M, as observed at low temperature where Coulomb interactions should be larger. This stresses the important influence of electron-electron interactions in the conductivity mechanism.

In this part, we have reported on the low frequency transport measurements that we have performed on two-dimensional disordered films. Indeed, a-Nb_xSi_{1-x} is a model system to study the interplay between quantum interferences, Coulomb interactions and superconductivity. In 2D, these phenomena have to be taken into account on an equal footing, and their competition may give rise to exotic electronic phases that have not yet been completely characterized.

For a-Nb_xSi_{1-x}, the corresponding phase diagram is given figure 3.67. As can be seen, it is more complex than a simple Superconductor-Insulator diagram. Indeed, unpredicted metallic phases set in between the superconducting and the insulating ground states. 2D dissipative states have been observed, notably by Kravchenko and coworkers in Si-MOSFETs [Kravchenko et al., 1994], but our system is in the opposite limit : it is very disordered, with a mean free path of the order of the interatomic distance, and with a large carrier density, more that 2 orders of magnitude over the usual densities in 2DEGs.

Moreover, our study shows that the traditional dichotomy between fermionic and bosonic models for the Superconductor-to-Insulator Transitions can be questioned. Indeed, we believe the different activation laws measured in the insulating phase in a-Nb_xSi_{1-x} films sign a fermionic insulator. However, the observed metallic phases are compatible with a two-fluid model where a fermionic component runs parallel to a bosonic channel. The transition, or , rather, crossover, is therefore nor fermionic nor bosonic. It is the survivance of superconducting fluctuations that renders the dissipative phases possible.

Of course, the sketched scenario would need to be confirmed. In appendix C, we have listed a list of experiments we find would help the understanding of our system, and, more generally, the physics of disordered systems.

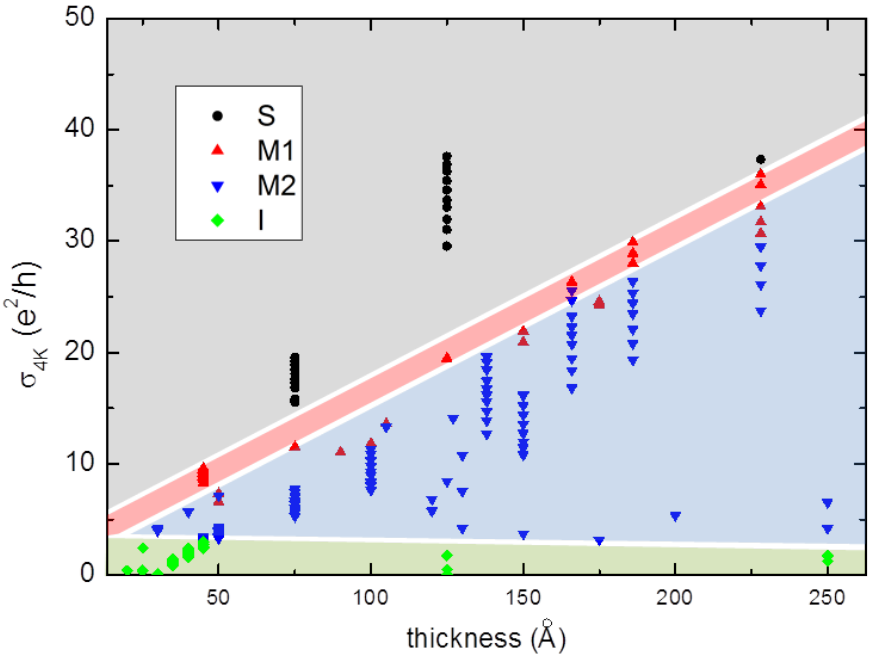

Figure 3.67: Phase diagram of 2D a-Nb_xSi_{1-x} in the disorder-thickness plane. σ_{4K} is tuned by either a change in thickness or composition x, or by heat treatment.

Part II

Microwave measurements

Chapter 4

State of the art : electrodynamics of superconductors

The second part of this manuscript is devoted to the description of the microwave low temperature calibration set-up which we have designed and tested.

Before reporting this new calibration method into more details in chapter 5, we would first like to put this experimental effort into perspective and sketch the state-of-the-art for the measurements of electrodynamic properties of disordered superconductors. We will first recall the theoretical predictions in this domain. We will then describe the main techniques used for the measurement of AC conductivity in superconductors along with some experimental results. We will end this chapter by describing the main goals of our work within this context.

Contrary to classical systems, where dynamics and thermodynamics are separable, in quantum mechanical systems they are intertwined. In fact, they are indissociable. This comes from the fact that time acts as an extra dimension for quantum systems [Sondhi et al., 1997]. In other words, to every characteristic energy scale in the system corresponds a characteristic timescale in the dynamics. As a direct consequence, measuring the AC response of a quantum system is a way to know its relevant thermodynamical quantities and therefore constitutes a very powerful tool to probe the phenomena at play. We will now show how this translates in the case of Quantum Phase Transitions, and more specifically for the Superconductor-to-Insulator Transition.

4.1 Frequency as a probe for Quantum Phase Transitions

As seen in chapter 1, Quantum Phase Transitions (QPT) are transitions between different ground states that are, strictly speaking, defined only at $T = 0$. However, the **manifestations** of QPT are measurable at finite temperatures in the quantum critical region. Indeed, in the vicinity of a QPT tuned by an external parameter K, the correlation length diverges as :

$$\xi \sim |\delta|^{-\nu} \sim |K - K_c|^{-\nu} \tag{4.1}$$

where K_c is the value of the tuning parameter at the transition and ν the correlation length exponent. The characteristic length for imaginary times correlatively diverges as :

$$\xi_\tau \sim \xi^z \tag{4.2}$$

where z is the dynamical scaling exponent. As illustrated figure 4.1, as long as the size of sample in the imaginary time direction, given by $\frac{\hbar}{k_B T}$, is larger than ξ_τ, the system dynamical properties will be determined by ξ_τ and the system will not "notice" that the temperature is finite (figure 4.1.a). The system will then be dominated by quantum fluctuations such that :

$$\hbar\omega \gg k_B T \tag{4.3}$$

Above a certain temperature, ξ_τ will be larger than $\frac{\hbar}{k_B T}$, the dominant fluctuations will be of thermal nature (figure 4.1.c) and the system will behave classically. The cross-over will occur for temperatures such that $\frac{\hbar}{k_B T} \simeq \xi_\tau$ (figure 4.1.b).

Conversely, a fluctuation of characteristic frequency ω will be of quantum nature for a given system if $\hbar\omega \gg k_B T$ and classical otherwise. The system response to an AC excitation at

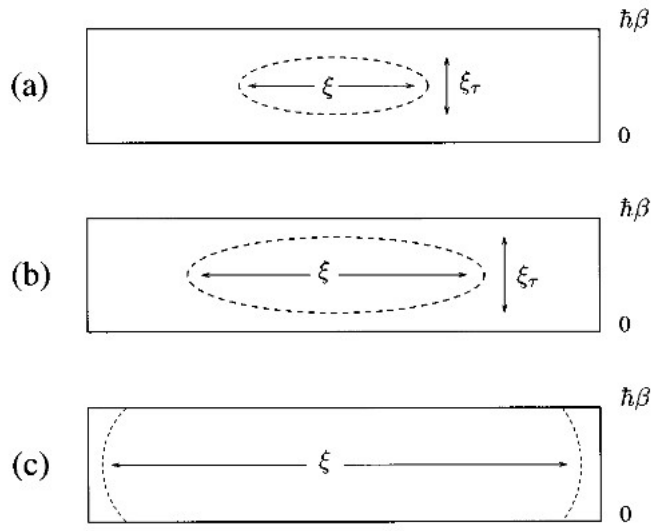

Figure 4.1: Illustration of the effect of the temperature near a QPT. At low temperature, the system is dominated by quantum fluctuations of characteristic timescale ξ_τ (a), whereas, at high temperature, the temperature acts as a cut-off in the imaginary time direction (c). The cross-over takes place when $\xi_\tau \simeq \hbar\beta = \frac{\hbar}{k_B T}$ (c). Taken from [Sondhi et al., 1997].

frequency ω will therefore allow to explore both quantum and classical fluctuations depending on the value of the ratio $\frac{\hbar\omega}{k_B T}$.

The **cross-over from the classical to the quantum fluctuating regimes** has been observed experimentally in bulk metallic NbSi films. As can be seen figure 4.2, the AC conductance σ is solely determined by the frequency ω at low temperatures (quantum regime) but is frequency-independent at high temperatures (classical regime). The cross-over between the two regimes systematically occurs at $\hbar\omega \simeq k_B T$.

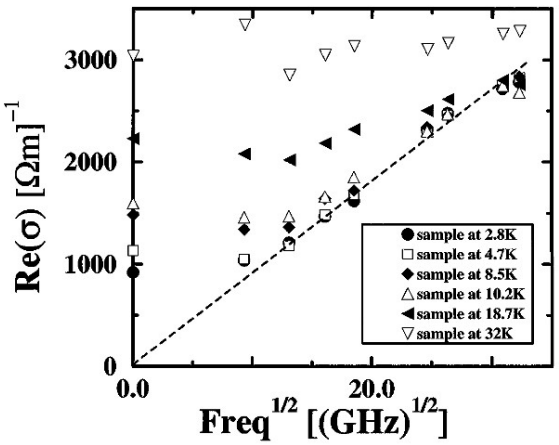

Figure 4.2: Real part of the AC conductance σ of an a-NbSi thin film as a function of $\sqrt{\omega}$ for different temperatures. The straight line emphasizes the $\sqrt{\omega}$ dependence in the quantum regime. Taken from [Lee et al., 1998].

In the quantum regime ($\hbar\omega \gg k_B T$), and close enough to the quantum critical point ($\frac{|K-K_c|}{K_c} \ll 1$), scaling theory for QPT predicts that physical quantities G obey **the finite-size scaling law** [Sondhi et al., 1997] :

$$G(K, T, \omega) \sim f\left(\frac{\hbar\omega}{k_B T}, \frac{|K - K_c|}{K_c T^{\frac{1}{\nu z}}}\right) \tag{4.4}$$

where f is a scaling function. This relation enables, from experimental data, to retrieve the value of the critical exponents ν and z and thus determine the universality class the QPT belongs to.

Scaling laws have been measured for the conductivity in the case of the Metal-to-Insulator

Transition (MIT) for bulk a-NbSi samples [Lee et al., 2000]. As displayed figure 4.3, the conductivity scales in frequency and temperature, provided that the frequency is scaled by a factor $\frac{\hbar}{1.54k_B}$. Three different universal curves are obtained depending on whether the sample is on the metallic or the insulating side of the MIT, or just at criticality. For this transition, the critical exponents obtained from the frequency and temperature dependences are $\nu = 1$ and $z = 2$. In this experiment, the scaling as a function of the distance to the quantum critical point $\frac{|K-K_c|}{K_c}$ has not been tested.

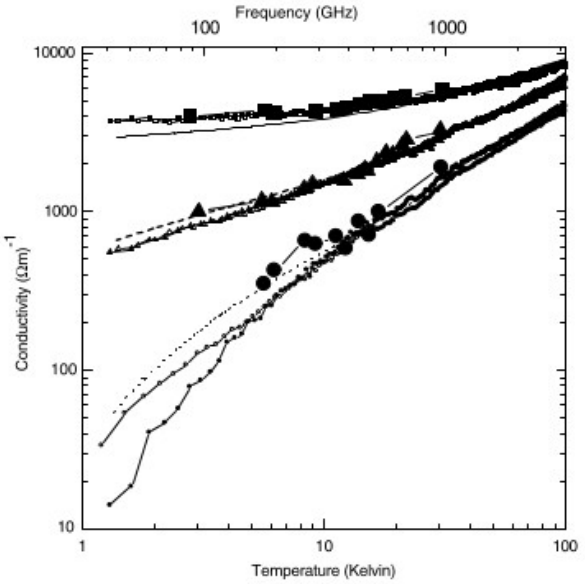

Figure 4.3: Conductivity as a function of temperature or frequency for three samples : the most conducting one is on the metallic side of the MIT, the least conducting one is on the insulating side of the MIT and the third sample sits at the critical point. The lines represent the DC conductivity ; the small symbols were obtained via resonant cavity measurements (solid at 5 GHz, open at 12 GHz) ; the large symbols were obtained in the 80-1000 GHz range with a quasi-optical spectrometer. The frequency has been scaled by a factor of $\frac{\hbar}{1.54k_B}$. Taken from [Lee et al., 2000].

AC measurement is therefore a particularly relevant technique to characterize a QPT. It can both assess the quantum mechanical nature of the transition and establish the critical behavior of the system through the determination of scaling laws and critical exponents. However, finite frequency measurements can also establish the complete electrodynamic response of the system in each of the considered phase. We will now detail the expectations regarding AC conductivity both in the superconducting and the insulating states for disordered superconductors.

4.2 Theory of electrodynamics within the BCS model

The main features of the electrodynamic response of superconductors can be understood within a simple two-fluid model (section 4.2.1). However, to gain a more complete understanding of how collective modes affect AC conductivity, one has to consider the Mattis-Bardeen theory (section 4.2.2) which is based on the BCS description of superconductivity. This model therefore deals with relatively clean superconductors. Disorder effects have an additional contribution which will be outlined in section 4.2.3.

4.2.1 Two-fluid model

The two-fluid model is based on a phenomenological extension of Drude's model where electrons within a superconducting material are described as being either normal - in which case they are scattered on a characteristic timescale τ_n - or superconducting - in which case $\tau_s \to +\infty$ -. The two electronic channels are assumed to run parallel to each other. The resolution of Drude's

conductivity at frequencies much lower than the superconducting gap ($\hbar\omega \ll \Delta$) then yields :

$$\sigma_1(\omega) = \frac{n_s e^2 \pi}{2m}\delta(\omega) + \frac{n_n e^2 \tau_n}{m} \tag{4.5}$$

$$\sigma_2(\omega) = \frac{n_s e^2}{m\omega} \tag{4.6}$$

where σ_1 and σ_2 are respectively the real and imaginary parts of the complex conductivity, n_s is the superfluid density, n_n the normal electron density and m the electron mass. The first term appearing in the expression of σ_1 reflects the fact that, at $\omega = 0$, superconducting electrons short-circuit the normal ones. The second term corresponds to the **dissipative response** due to quasiparticles at finite frequencies. The $\frac{1}{\omega}$ dependence of σ_2 reveals the inductive behavior of a superconductor.

The two-fluid model therefore considers a superconductor at finite frequency to effectively behave like a RL circuit (figure 4.4), with, for a film a thickness $d_\perp$:

$$R_\square = \frac{m}{d_\perp n_n e^2 \tau_n} \qquad \text{the equivalent resistance due to quasiparticles} \tag{4.7}$$

$$L_\square = \frac{m}{d_\perp n_s e^2} \qquad \text{the equivalent inductance due to Cooper pairs (\textbf{kinetic inductance})} \tag{4.8}$$

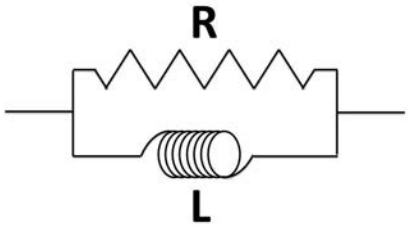

Figure 4.4: Schematic representation of the two-fluid model for a superconductor. Quasiparticles correspond to the dissipative channel, whereas the Cooper pairs response is modeled by an inductance.

In order to have an idea of the finite frequency behavior of a superconductor as a function of temperature, it is often convenient to use the temperature dependence of R and L given by Ginzburg-Landau theory :

$$R(T) = R_n \exp\left(\frac{\Delta_0}{T}\right) \tag{4.9}$$

$$L(T) = \frac{L_0}{\sqrt{1 - \frac{T}{T_c}}} \tag{4.10}$$

where R_n is the normal state resistance, $\Delta_0 = 1.76 k_B T_c$ the superconducting gap, T_c the superconducting critical temperature, and L_0 the Cooper pairs kinetic inductance at zero temperature which can be estimated in the **dirty limit** by :

$$L_0 = \frac{\hbar R_n}{\pi \Delta_0} \tag{4.11}$$

Figure 4.5 gives the frequency and temperature dependence of the conductivity, of the corresponding complex impedance Z and reflectometry signal $|\Gamma|$ for a superconducting film of $R_n = 10,4\ \Omega$ and $T_c = 3,6$ K, in the GHz region. As we will see in the next chapter, these values correspond to the characteristics of a Vanadium film of 100 Å which we will measure. The RL circuit analogy is especially transparent in the dependence of the conductivity with the frequency : the real part being purely resistive, it only depends on the temperature and is frequency-independent ; the imaginary part varies hyperbolically with ω as expected for an inductance.

4.2.2 Mattis-Bardeen theory

The two-fluid model is very practical to gain a sense of the behavior of superconductors under a low frequency ($\hbar\omega \ll \Delta_0$) AC drive. However, this simplistic model does not capture all

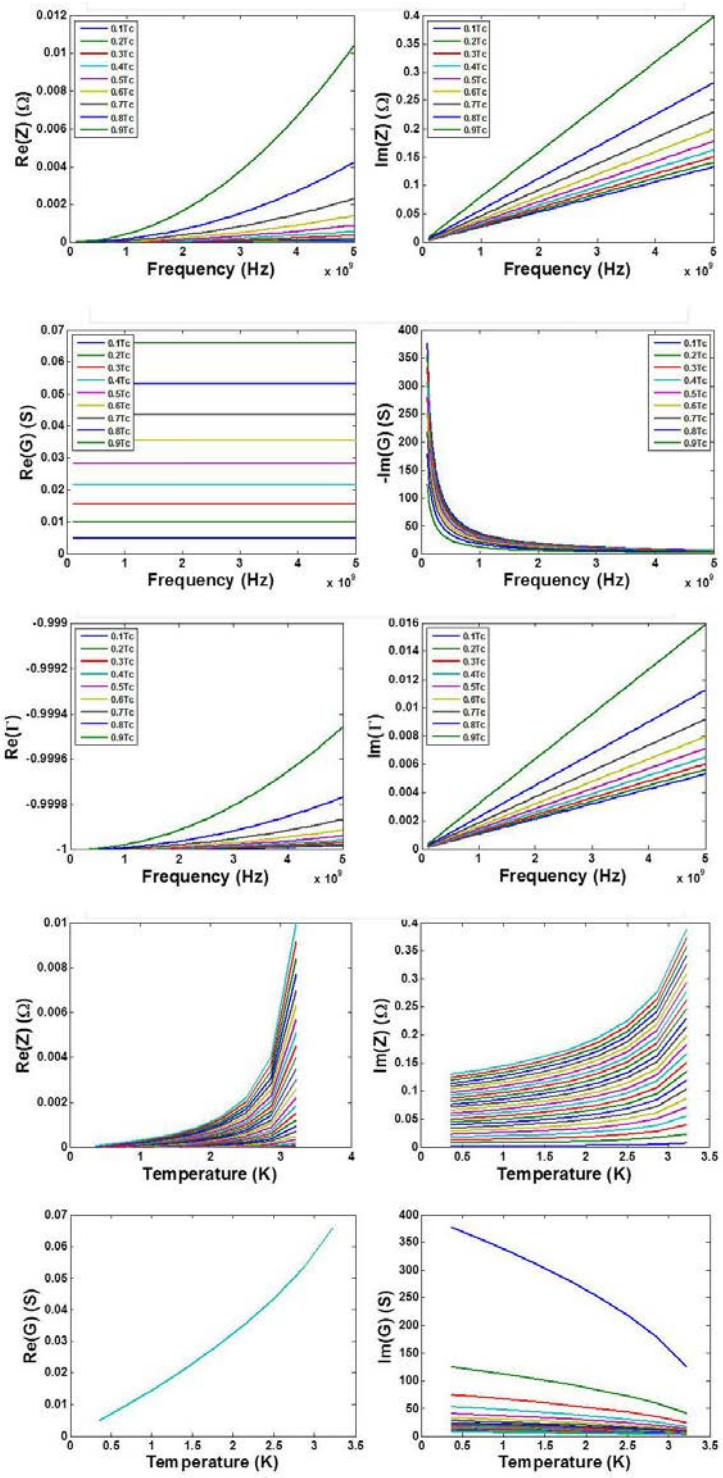

Figure 4.5: Predictions for the temperature and frequency dependence of the complex impedance Z, of the conductance G and of the reflectivity $|\Gamma|$ according to equations 4.9 and 4.10 (two-fluid model) for a superconducting film of $R_n = 10,4\ \Omega$ and $T_c = 3,6$ K. The frequency is here made to vary between 100 MHz and 5 GHz by steps of 200 MHz.

features, and misses in particular the characteristic traits of quantum coherence. A more complete description can be achieved by considering the Mattis-Bardeen theory [Mattis and Bardeen, 1958].

Starting from BCS description, this model describes the electrodynamic response of a superconductor in which electron scattering is also taken into account. The system complex conductivity then is :

$$\begin{aligned}\frac{\sigma_1(\omega,T)}{\sigma_n} =& \frac{2}{\hbar\omega}\int_{\Delta}^{\infty}\frac{[f(E)-f(E+\hbar\omega)]\,(E^2+\Delta^2+\hbar\omega E)}{(E^2-\Delta^2)^{1/2}\left[(E+\hbar\omega)^2-\Delta^2\right]^{1/2}}\mathrm{d}E \\ &+\frac{1}{\hbar\omega}\int_{\Delta-\hbar\omega}^{-\Delta}\frac{[1-2f(E+\hbar\omega)]\,(E^2+\Delta^2+\hbar\omega E)}{(E^2-\Delta^2)^{1/2}\left[(E+\hbar\omega)^2-\Delta^2\right]^{1/2}}\mathrm{d}E\end{aligned} \tag{4.12}$$

$$\frac{\sigma_2(\omega,T)}{\sigma_n} = \frac{1}{\hbar\omega}\int_{\Delta-\hbar\omega,-\Delta}^{\Delta}\frac{[1-2f(E+\hbar\omega)]\,(E^2+\Delta^2+\hbar\omega E)}{(\Delta^2-E^2)^{1/2}\left[(E+\hbar\omega)^2-\Delta^2\right]^{1/2}}\mathrm{d}E \tag{4.13}$$

where σ_n is the normal state conductivity, $f(E,T) = (\exp(E/k_BT)-1)^{-1}$ is the Fermi-Dirac distribution, E the energy and Δ the superconducting gap.

σ_1 describes the dissipative response of quasiparticles. The first term of equation 4.12 corresponds to the effect of thermally excited quasiparticles. It therefore vanishes at zero temperature [Dressel, 2013]. The second term describes the absorption of a photon to excite quasi-particles. Since this process requires the breaking of a Cooper pair, the second term is scarcely relevant unless $\hbar\omega > 2\Delta(T)$.

Equation 4.13 shows that Cooper pairs contribution to the AC response is purely inductive. A simple analytic form can be obtained at low frequency ($\hbar\omega \ll 2\Delta(T)$) and links σ_2 to the superconducting gap [Tinkam, 2004] :

$$\frac{\sigma_2}{\sigma_n} = \frac{\pi\Delta(T)}{\hbar\omega}\tanh\left(\frac{\Delta(T)}{2k_BT}\right) = \begin{cases}\frac{\pi\Delta(0)}{\hbar\omega} & \text{for } T \ll T_c \\ \frac{\pi}{2}\frac{\Delta^2(T)}{k_BT\hbar\omega} & \text{for } T \simeq T_c\end{cases} \tag{4.14}$$

Figures 4.6 and 4.7 give the frequency and temperature dependence of the complex conductivity $\sigma = \sigma_1 - i\sigma_2$ as predicted by the Mattis-Bardeen theory [Dressel, 2013], assuming that the ratio of the zero-temperature coherence length to the mean free path is such that : $\frac{\pi\xi(0)}{l} = 10$.

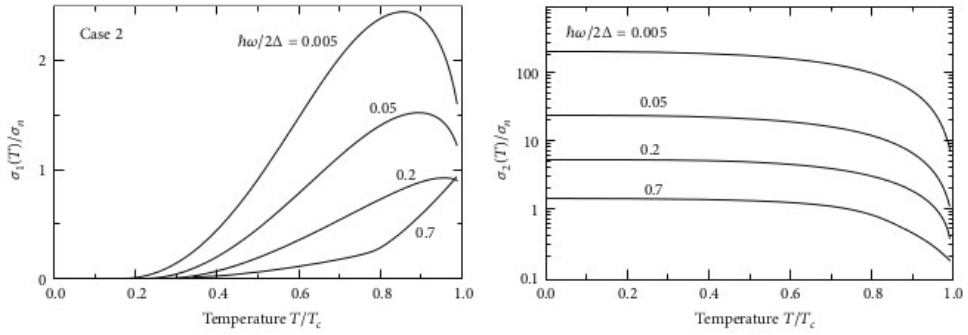

Figure 4.6: Predictions of Mattis-Bardeen theory for the temperature dependence of the complex conductance σ (real part σ_1 and imaginary part σ_2) for different frequencies under the assumption that $\frac{\pi\xi(0)}{l} = 10$. Taken from [Dressel, 2013].

The main difference with the two-fluid model predictions is the peak in the dissipative part of the conductivity, close to $0.8T_c$. This so-called **coherence peak** in σ_1 has a purely quantum mechanical origin and is due to the coherence factors in BCS theory. It is predicted to shift to lower temperatures at lower frequencies, and following :

$$\left(\frac{\sigma_1}{\sigma_n}\right)_{max} \sim \log\left(\frac{2\Delta_0}{\hbar\omega}\right) \tag{4.15}$$

until it completely disappears for $\hbar\omega \geq \frac{\Delta_0}{2}$.

Moreover, $\sigma_1(\omega)$ can be viewed as the sum of two components : one due to photon-activated quasiparticles (visible as the zero temperature contribution in figure 4.7), whereas the diverging component at finite temperatures and low frequency correspond to the thermally activated quasiparticle response. Since the quasiparticle density-of-states vanish at low temperatures for energies such that $\frac{\hbar\omega}{2\Delta} < 1$, the photon-activated component is negligible in this frequency range.

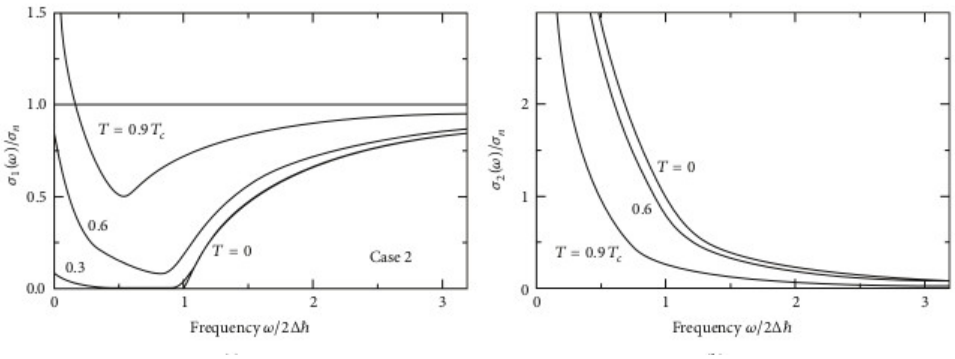

Figure 4.7: Predictions of Mattis-Bardeen theory for the frequency dependence of the complex conductance σ (real part σ_1 and imaginary part σ_2) for different temperatures under the assumption that $\frac{\pi\xi(0)}{l} = 10$. Taken from [Dressel, 2013].

Finally, let us point out that, as Ferrell and Glover have shown [Ferrell and Glover III, 1958], the dissipative and inductive parts of the conductivity are linked by an oscillator-strength **sum rule** :

$$\int_0^\infty \sigma_1(\omega)d\omega = \frac{\pi n e^2}{2m} \tag{4.16}$$

where n is the electron density. This equation translates the fact that the spectral weight due to excitations is conserved on both side of the superconducting transition. At $T = 0$, comparing $\sigma_n(\omega)$ with $\sigma_1(\omega)$, the area missing in the spectrum of σ_1 is, in fact, recovered at zero frequency in the form of a Dirac distribution similar to the one appearing in equation 4.5. At finite temperatures, the Dirac distribution widens to give rise to a low frequency peak.

4.2.3 Electrodynamics of disordered superconductors

Mattis-Bardeen theory has been developed for homogeneous and isotropic superconductors in the $k_F l \gg 1$ limit [Mattis and Bardeen, 1958], that is to say when electron scattering exists but with a large scattering time.

Nam [Nam, 1967b, Nam, 1967a] has shown that the Mattis-Bardeen equations were still qualitatively valid in the presence of some specific disorder. For instance, superconductors containing magnetic impurities have the same electrodynamic response as a pure superconductor, provided the value of the gap is renormalized by the spin-flip relaxation time.

Subsequent work extended these calculations to isotropic superconductors with an arbitrary purity [Nicol et al., 1991, Akis et al., 1991, Zimmermann et al., 1991], characterized by a mean free path time τ. Numerical calculations carried out by Zimmermann et al. [Zimmermann et al., 1991] are reproduced figure 4.8. One of the striking features of these developments is that, a small deviation from the pure case leads to a peak in the dissipative part for frequencies just above $2\Delta(T)$. Moreover, at $T = 0.7\,T_c$ and $\omega \to 0$, which corresponds to the region where the coherence peak is awaited, σ_1 diverges more steeply than in the pure case (figure 4.9). As a result, the coherence peak is expected to be larger in the disordered case.

4.3 Experimental techniques

The complex conductivity of a given system can be accessed through various probes. In order to choose between the different experimental techniques, one has to take into account the different characteristic timescales of the system as well as the regime that one wants to investigate. Indeed, for a specific timescale τ to be studied, the excitation frequency ω must be such that $\omega > \frac{2\pi}{\tau}$. Moreover, as we have seen section 4.1, in order to probe the quantum critical regime of a QPT, the temperature at which the experiment is conducted must be lower than the excitation frequency : $k_B T < \hbar\omega$.

Figure 4.10 summarizes the main experimental techniques which we will briefly overview in this section, each one corresponding to a given frequency range. The reviewed techniques will be limited to those having been used in the study of disordered superconducting thin films. For more complete reviews, see [Armitage, 2009, Basov et al., 2011].

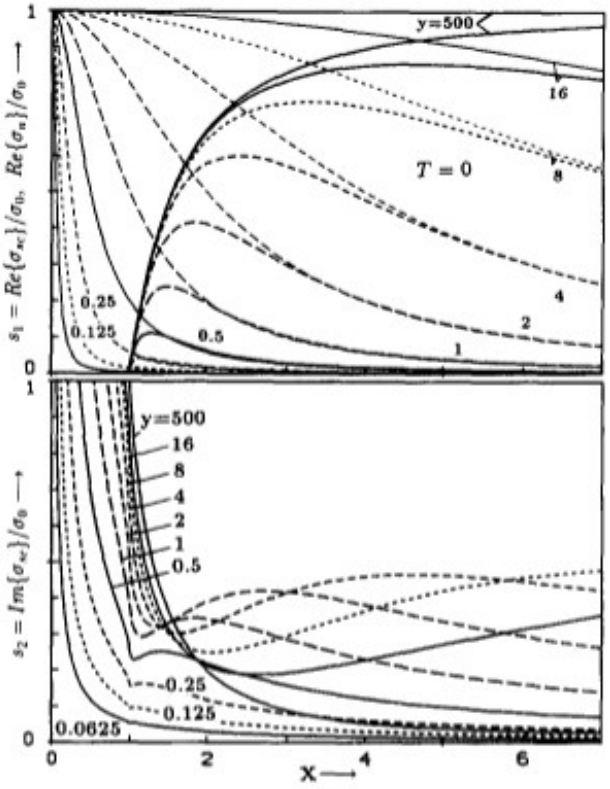

Figure 4.8: Predictions for the $T = 0$ frequency dependence ($x = \frac{\hbar\omega}{2\Delta_0}$) of the real and imaginary parts of the complex conductivity. Here, σ_0 is the DC conductivity, $y = \frac{\hbar}{2\tau\Delta_0}$ is the impurity parameter ($y = 500$ is the impure limit, whereas $y = 0.0625$ is the pure limit). In the top panel, the normal state conductivity σ_n is also shown (the corresponding curves are Lorentzians). Taken from [Zimmermann et al., 1991].

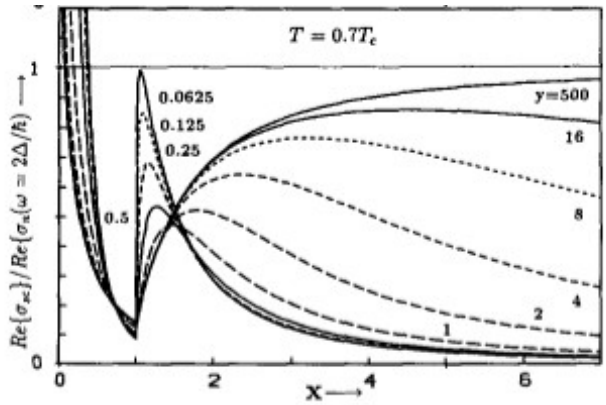

Figure 4.9: Predictions for the $T = 0.7T_c$ frequency dependence ($x = \frac{\hbar\omega}{2\Delta(T)}$) of the real part of the complex conductivity. Here, σ_0 is the DC conductivity, $y = \frac{\hbar}{2\tau\Delta(T)}$ is the impurity parameter ($y = 500$ is the impure limit, whereas $y = 0.0625$ is the pure limit. Taken from [Zimmermann et al., 1991].

4.3.1 Two-coil experiments

The two-coil method, first introduced by Hebard and Fiory [Hebard and Fiory, 1980], consists in placing the sample in a plane transverse to the axis of two coils. The magnetic field created by the primary (drive) coil induces currents in the sample which, in turn, perturbs the mutual inductance between the two coils, measured by the secondary (pickup) coil. A typical setup geometry is shown figure 4.11 [Turneaure et al., 1998]. The typical frequencies of operation range from a few kHz to a few hundreds of MHz.

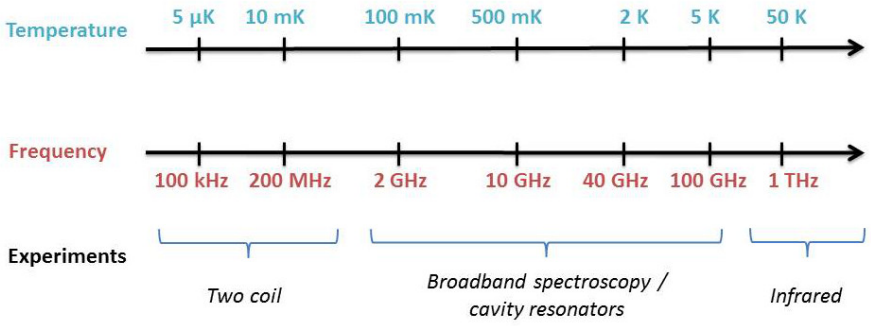

Figure 4.10: Main experimental techniques depending on the excitation frequency range. The energy scale is also converted to equivalent temperature scales.

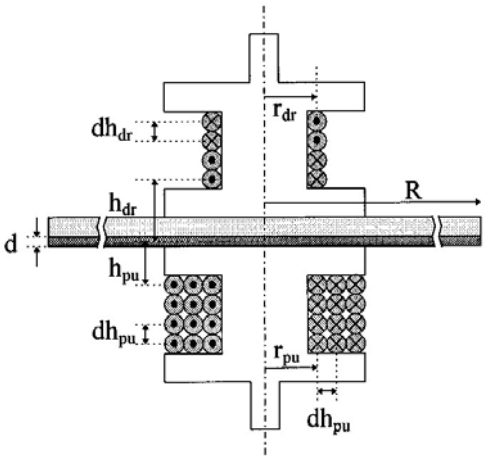

Figure 4.11: Geometry of the two-coil experiment in Thomas Lemberger's group [Turneaure et al., 1998]. The upper coil is the drive, whereas the bottom one is the pickup coil. A sample of thickness d sits in between and perturbs the mutual inductance between the two coils.

The main advantage of this technique lies in its large sensitivity : the magnetic penetration depth can typically be measured with a precision better than 10% [Turneaure et al., 1996]. Moreover, it is relatively simple, non-destructive and does not require any external calibration, as is the case for GHz broadband spectroscopy as we will see.

For the study of disordered superconducting thin films, the main drawback of this technique is that it is limited to low frequency. The method has to be operated at (sometimes prohibitively) low temperature in order to see the influence of quantum fluctuations.

4.3.2 Superconducting cavity resonators

Until recently, measurements in the GHz range had been mainly performed in resonant cavities such as the one depicted figure 4.12.a [Lehoczky and Briscoe, 1971]. Microwaves were created by klystrons and only selected modes could propagate. The introduction of the sample within the cavity changed its resonant features : from the resonance frequency shift and its broadening, the complex conductivity could be inferred.

With the development of lithography techniques and the improvement of microwave components, such resonant techniques were miniaturized as shown figure 4.12.b [Day et al., 2003]. In these cases, a microwave feedline carries the microwave delivered by a Vector Network Analyzer (VNA). The resonant circuit is capacitively coupled to the feedline and affects its transmission when the feedline frequency is close to the resonator's characteristic frequency.

The main advantage of these techniques is their high sensitivity due to the fact that they work close to a resonance. Moreover, they do not require an external calibration.

However, they only work at discrete frequencies. In the case of macroscopic cavities, the frequency was fixed by the klystron source and the geometry of the cavity. In the case of

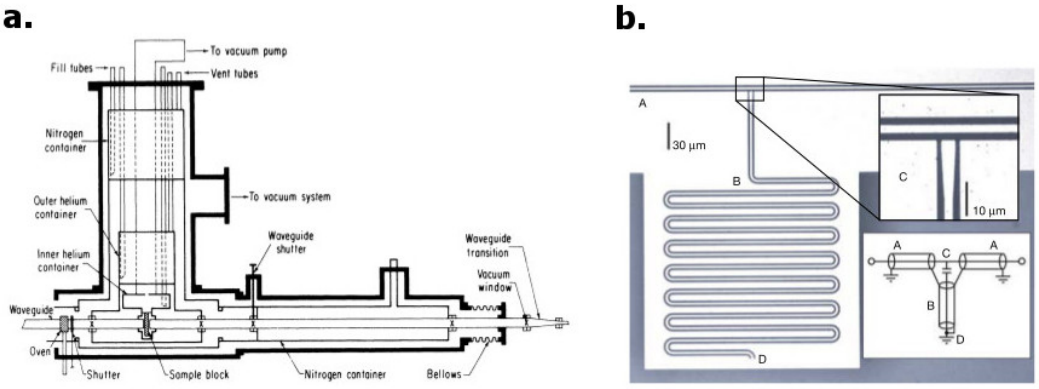

Figure 4.12: **a.** Geometry of a microwave cryostat [Lehoczky and Briscoe, 1971]. **b.** Photography of a mesoscopic resonator [Day et al., 2003]. The white region is covered with Aluminum, whereas the gray region is insulating. The central straight line is the microwave feedline which transmission is affected at the resonant frequency of the capacitively-coupled resonator. The wiggling line (between points C and D) corresponds to the resonator.

lithographed cavities, the geometry and material used for the resonator determines the resonance. In the latter case, the electrokinetic modeling for the ensemble {feedline + resonator} is also crucial to derive the complex conductivity of the sample and is a source of uncertainty.

4.3.3 Broadband spectroscopy

Since the 1990's, broadband GHz spectroscopy has developed as a powerful tool to probe a large spectrum of frequencies. A typical experimental set-up is shown figure 4.13 [Booth et al., 1994]. The microwave, delivered by a VNA, propagates in a coaxial cable until the sample. The sample response can be detected in transmission, in which case a second coaxial cable on the other side of the sample is required to collect the signal, or in reflection, in which case a single coaxial cable is sufficient.

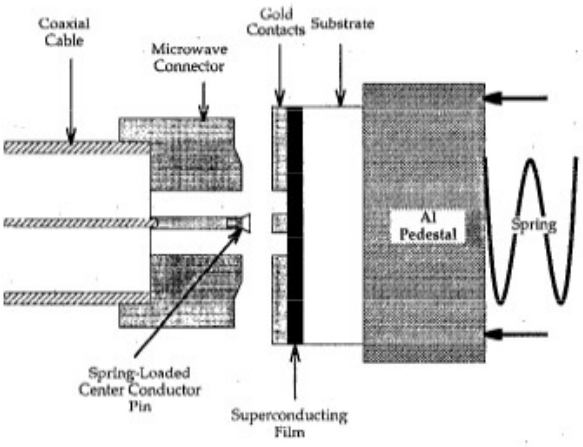

Figure 4.13: Schematic representation of a broadband microwave reflection experiment [Booth et al., 1994] : the microwave arrives on the sample via a coaxial cable. The contact between the sample and the pin is crucial and guaranteed by the force exerted on the Aluminum pedestal by a spring.

The major advantage of this technique is to be broadband. In a single experiment, one can access different ranges of frequencies ranging from a few MHz to tens of GHz. As in the case of cavity resonators, these frequencies correspond precisely to the range of frequencies at which disordered superconductors display some characteristic features : coherence peaks, Kosterlitz-Thouless physics, superconducting fluctuations, ...

However, broadband spectroscopy is extremely sensitive to any imperfection in the circuit. Indeed, any impedance mismatch leads to a partial reflection of the incoming wave, thus inducing errors in the measurement of the sample complex impedance. The set-up has thus to be calibrated before any measurement, by a three-standard point procedure, as we will see in the next chapter.

The ultimate aim behind this thesis work is the determination of the broadband electrodynamic response of superconducting thin films with T_c between a few hundreds of mK to a few K. Moreover, we would want to determine the quantum nature of the Superconductor-to-Insulator (or Superconductor-to-Metal) Transition and the associated timescales. We therefore chose to use a technique which allowed to probe both the $\hbar\omega < k_B T$ and the $\hbar\omega > k_B T$ regimes and could probe the superconducting gap. For this aim, broadband GHz spectroscopy therefore is a suitable technique.

4.3.4 THz spectroscopy

THz spectroscopy is highly interesting for it allows to probe timescales of great interest in solids : scattering times of electrons, characteristic vibration times in crystals, carrier lifetimes in metals and semiconductors, localization peaks, ... However, this technique lies at the interface between optics and microwave electronics, so that the practical realization of such experiments is often difficult. Figure 4.14 gives an example of such a set-up [Pracht et al., 2013], where a monochromatic THz radiation is provided by a frequency-tunable backward-wave-oscillator (BWO). Quasi-optical techniques are then used to measure the transmission signal coming from the sample.

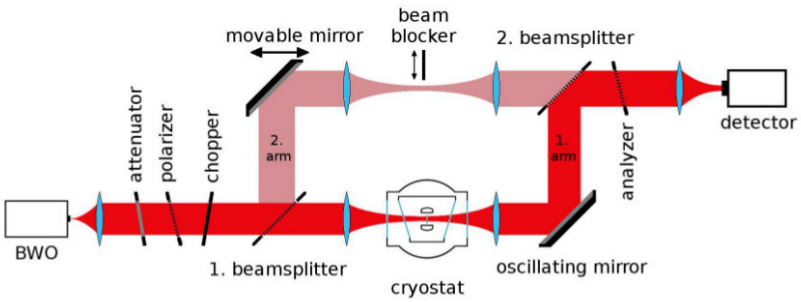

Figure 4.14: Schematic representation of a THz experiment [Pracht et al., 2013] using a Mach-Zehnder-type interferometer : the microwave arrives on the sample via a coaxial cable. The transmission then is measured by a detector sensitive to the magnitude and direction of the electric field.

The main advantage of this technique is, as mentioned above, the timescales it probes. Moreover, it does not require any prior calibration outside determining the transmission signal without the sample in place.

However, as can be seen figure 4.14, when the sample has to be measured at low temperature, the set up is external to the cryostat through which the radiation is shone. Because of the space taken by optics, the setup can hardly be inserted within a cryostat. This introduces some signal loss and is a potential source of uncertainty. Other uncertainty sources include black-body radiation and weak sources [Armitage, 2009].

4.4 Measurements of electrodynamics of superconducting thin films

Having briefly reviewed the main experimental techniques used to characterize the electrodynamic response of superconductors in the previous section, let us now turn to the experimental results obtained in BCS-type superconductors.

4.4.1 Clean superconductors

The complex conductivity of clean superconductors has, for the main part, experimentally been established as early as the 1970s. Indeed, as can be seen by comparing figures 4.15.a and 4.7.a, one can clearly observe the existence of the superconducting gap in the frequency

dependence of the real part of the conductivity σ_1. As temperature is increased, the gap closes, following the BCS prediction, and the spectral weight develops at low frequency. In this case, Mattis-Bardeen theory quantitatively describes the experimental observations.

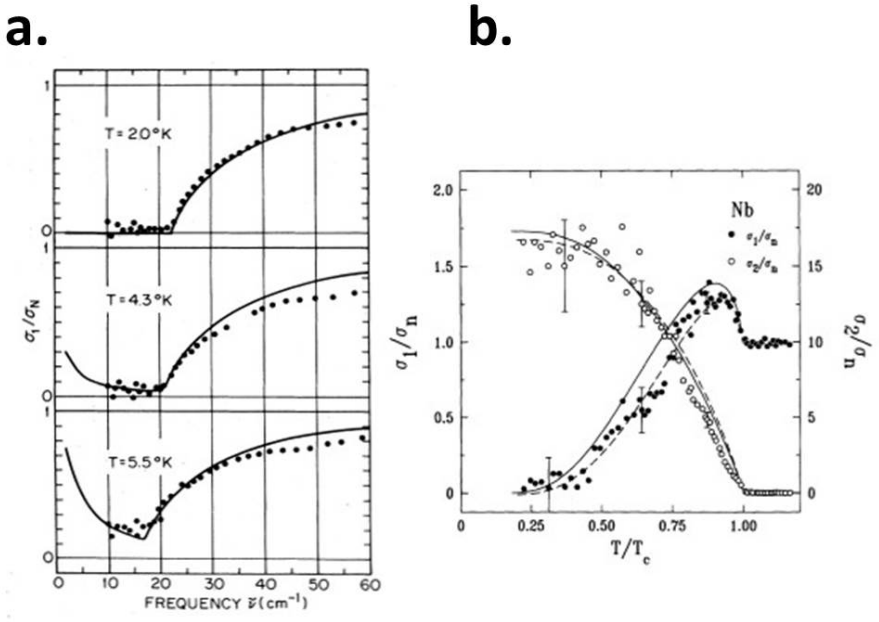

Figure 4.15: (a). Temperature and frequency dependence of the normalized real part of the conductivity $\frac{\sigma_1}{\sigma_N}$ for thin superconducting Lead films (T_c =7.2 K) measured in the THz range by far-infrared spectroscopy [Palmer and Tinkham, 1968]. The points correspond to experimental data and the line to the prediction of Mattis-Bardeen theory. (b). Complex conductivity (real part in black, imaginary part in white dots) as a function of temperature for (weak coupling) Niobium films at 60 GHz, measured by cavity perturbation [Klein et al., 1994]. The solid lines are fit to Mattis-Bardeen theory, whereas the dashed ones correspond to the strong-coupling Eliashberg predictions. Niobium is believed to follow the predictions of Mattis-Bardeen theory.

The temperature dependence of conductivity has also been shown to follow the predictions of Mattis-Bardeen theory (figure 4.6). The coherence factors that appear in the temperature dependence of σ_1 at frequencies much lower than the gap, although measured by ultrasonic attenuation and nuclear spin relaxation beforehand [Tinkam, 2004], had not been measured at microwave frequencies before the 1990s. The first experiment to achieve high enough accuracy in the measurement of the transmission and reflection coefficients in this range is due to Klein et al. on Niobium films [Klein et al., 1994]. As can be seen figure 4.15.b, the results are also in good quantitative agreement with Mattis-Bardeen theory.

Subsequent studies have examined the dependence of these coherence peaks as a function of the mean free path l. As seen figure 4.16, and as expected from Zimmermann's theory (section 4.2.3), the peaks get larger when disorder is increased, indicating that the superconducting gap fully opens up at lower temperatures. Moreover, the peaks get higher for lower l, revealing an increased contribution of quasiparticles to σ_1 within the considered temperature range. In the experiments reported figure 4.16, the mean free path is of the order of a few nanometers.

4.4.2 Superconducting fluctuations

The main advantage of dynamical measurements at frequency f is the fact that they are, by definition, sensitive to transient regimes, or, in other words, to fluctuations occurring at typical timescales of the order of $1/f$. For superconducting samples, this is the case of thermally activated quasiparticles giving rise to the so-called coherence peak, but it can also be seen for other fluctuation phenomena which may not be taken into account in the standard Mattis-Bardeen derivation of the complex conductivity. Indeed, σ_1 directly reflects the rate at which particle-hole pairs are created through the absorption of photons of frequency f. Hence, any quasiparticle scattering mechanism can actually give rise to a peak in the real part of the complex conductivity, be it electron-phonon or electron-electron scattering for instance.

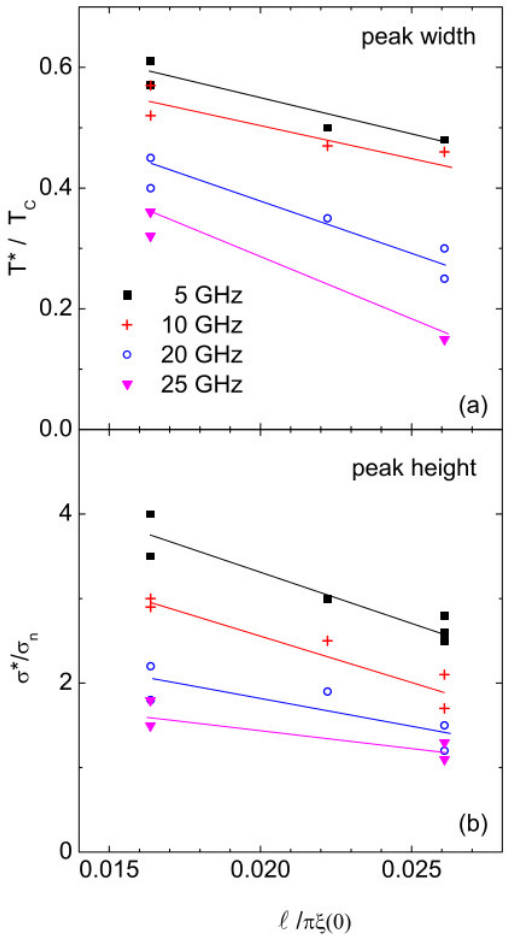

Figure 4.16: Width $\frac{T_c - T_n}{T_c}$ (a.) and height $\frac{\sigma_{max}}{\sigma_n}$ (b.) of the coherence peaks measured from $\sigma_1(T)$ in Aluminum films of different mean free paths l [Steinberg et al., 2008]. T_n is the temperature at which $\sigma_1 = \sigma_n$ again. σ_{max} corresponds to the maximum of the peak. ξ_0 is the zero temperature superconducting coherence length.

The latter case is illustrated figure 4.17.a for a high T_c superconductor. For these $YBa_2Cu_30_{7-\delta}$ films, the peak in σ_1 just below T_c has been measured via far-infrared reflection and transmission experiments, but was absent from NMR measurements, indicating that it cannot be attributed to a Hebel-Slichter (or coherence) peak. Moreover, the peak experimentally appears at 50 cm^{-1}, almost at $\Delta(0)/2$, well above the frequency above which Mattis-Bardeen theory predicts the coherence peak to vanish ($\frac{\omega}{2\Delta(0)} < 0.1$). The existence of this dissipative peak has subsequently been attributed to electron-electron scattering and the scattering rate inferred.

In low-temperature superconducting films, similar dissipation peaks have been observed, for instance in NbN thin films [Mondal et al., 2013] as seen figure 4.17.b. In this case, this feature has been interpreted as the signature of Aslamazov-Larkin-type fluctuations above T_c : the quasiparticle lifetime increases when one approaches the superconducting transition from high temperatures and this results in a characteristic frequency $\omega_0 = \frac{16 k_b T_c}{\pi \hbar} \ln\left(\frac{T}{T_c}\right)$ which, in turn, gives rise to a peak in σ_1 when $f = \frac{\omega_0}{2\pi}$.

As can be seen from these two examples alone, GHz conductivity measurements are a powerful probe to investigate quasiparticle scattering and/or dynamics and its influence on superconductivity.

4.4.3 BKT transition

As we have seen section 1.7.2, thin superconducting films can undergo a Berezinskii-Kosterlitz-Thouless transition due to the dissociation of vortex-antivortex pairs above T_{BKT}. Another way of explaining this phenomenon is to say that, well below the superconducting temperature T_c, the superconducting order parameter phase is fixed and does not vary in space. This can be modeled

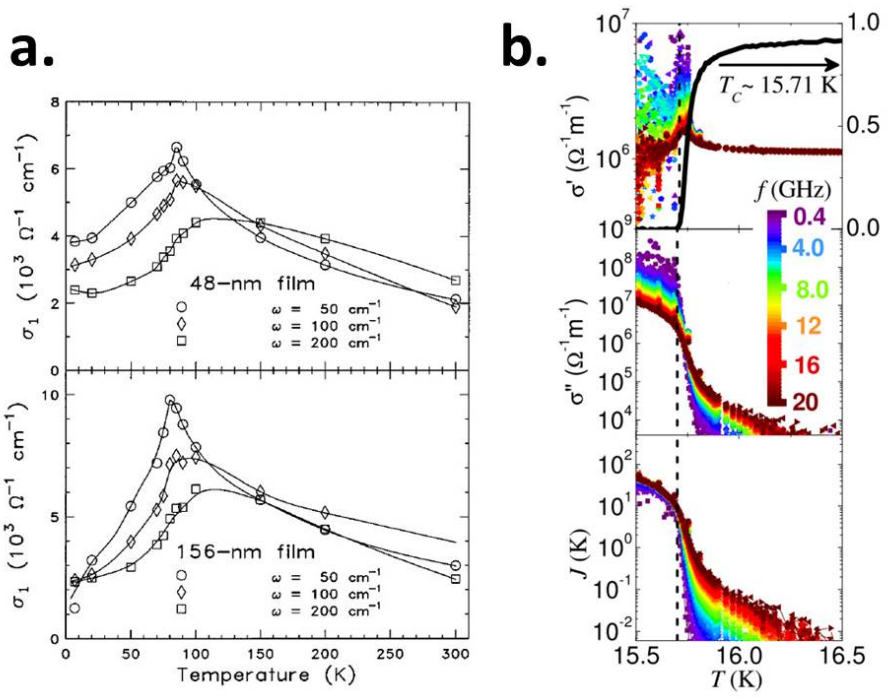

Figure 4.17: (a).Temperature dependence of the real part of the complex conductivity for two $YBa_2Cu_30_{7-\delta}$ films [Gao et al., 1996]. (b). Temperature dependence of the complex conductivity (real part σ' and imaginary part σ'') and superfluid stiffness $J = \frac{\hbar^2 n_s a}{4mk_b}$, with n_s the superfluid density and a the lengthscale associated to fluctuations, for a NbN film of T_c=15.71 K (marked by the vertical dashed line) [Mondal et al., 2013]. The different colors correspond to different frequencies ranging from 0.4 to 20 GHz. The DC resistance is also plotted in the upper panel (thick black line).

by a maximum and constant **phase stiffness** $T_\theta = \frac{n_s(\omega)e^2\hbar d}{k_b m G_Q}$ [1], where $n_s(\omega)$ is the effective superfluid density, d the film thickness and $G_Q = \frac{4e^2}{\hbar}$. Well above T_c, the phase coherence is destroyed and the phase stiffness is therefore zero. For $T_{BKT} < T < T_c$, the phase coherence is maintained, but only on a finite lengthscale which grows larger as temperature decreases. T_θ being proportional to the superfluid density and hence to σ_2, frequency measurements can probe the phase stiffness on a lengthscale given by the vortex diffusion length $\sqrt{\frac{\lambda D}{f}}$, where λ is the penetration depth and D the vortex diffusion coefficient.

As can be seen figure 4.18 in the case of InOx films, T_θ does not exhibit any frequency dependence at low temperature and goes to zero when superconductivity is destroyed. Theoretical predictions give that the discontinuous jump in phase stiffness - at zero frequency - due to the unbinding of vortex-antivortex pairs occurs at a value $T_\theta = 4T_{BKT}$ represented figure 4.18 by the pink dashed line. At finite frequency, this corresponds to the temperature at which T_θ becomes frequency-dependent. From these results, one can see that, in these films, T_{BKT} is actually the temperature at which the DC resistance becomes null.

4.5 Frequency measurements and the Superconductor-to-Insulator Transition

In the previous section, we have seen how frequency measurements could help characterize important features of superconducting thin films such as superconducting fluctuations or the BKT transition. In fact, disordered superconducting films far enough from the Superconductor-to-Insulator Transition (SIT) can reasonably well be accounted for using Mattis-Bardeen theory in which fluctuations are incorporated. However, close to the SIT, this simple model is expected to break down and the electrodynamic response of the system may provide interesting information on the nature of the phases and on the mechanisms at play in this phase transition. In this section,

1. T_θ was called J in figure 4.17.

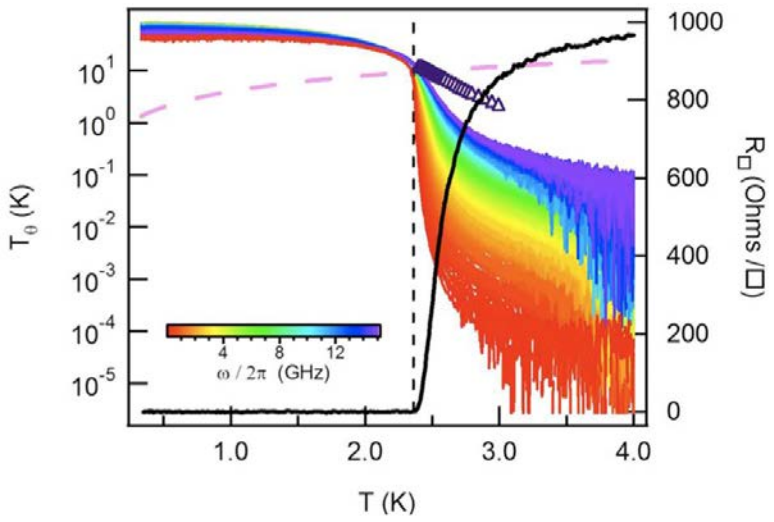

Figure 4.18: Temperature dependence of the phase stiffness T_θ for different frequencies for an InO_x film [Liu et al., 2011]. The black line corresponds to the DC resistance. The dashed pink line depicts the theoretical BKT prediction and the vertical dashed line marks the superconducting temperature.

we will therefore focus on the contribution of AC transport measurements to the understanding of the Superconductor-to-Insulator Transition, although, up to now, experimental data are scarce in this regime.

4.5.1 Electrodynamics of fermionic insulators

Before tackling the issue of the SIT, let us mention results of dynamical conductivity measurements at a closely related transition : the Metal-to-Insulator Transition (MIT). The theory underlying the MIT has been sketched in sections 1.3 and 1.4. Except for superconductivity, the main ingredients are the same as for the SIT : disorder effects, localization and Coulomb interactions.

We have already mentioned the scaling relations that have been observed on both sides of the MIT (section 4.1). We will here concentrate on the AC response measured for a fermionic insulator, on the disordered side of the MIT.

On the insulating side of the MIT, either Mott or Efros-Shklovskii-type Variable Range Hopping (VRH) is expected. In these regimes, the theoretical predictions for the real part of the conductivity are :

$$\sigma_1 = \alpha e^2 N_0^2 \xi^5 \hbar\omega^2 \left(\ln\left(\frac{2I_0}{\hbar\omega}\right)\right)^4 \qquad \text{for Mott-type VRH} \tag{4.17}$$

$$\sigma_1 = \alpha e^2 N_0^2 \xi^5 \omega \left(\ln\left(\frac{2I_0}{\hbar\omega}\right)\right)^4 (\hbar\omega + U(r_w)) \qquad \text{for Efros-Shklovskii-type VRH} \tag{4.18}$$

where α is a constant close to unity, ξ the localization length, I_0 the Bohr energy of the impurities, $U(r_w) = \frac{e^2}{\varepsilon_1 r_w}$ the Coulomb interaction between two sites, and $r_w = \xi \ln\left(\frac{2I_0}{\hbar\omega}\right)$ the most probable hopping distance between pairs [Helgren et al., 2004].

The imaginary part of the dynamical conductance is positive, reflecting a capacitive response due to localization. Due to Kramers-Kronig relation and the fact that $\sigma_1 \propto \omega^\alpha$ ($\alpha = 1$ in the case of Efros-Shklovskii VRH and $\alpha = 2$ for Mott VRH), one has $\sigma_2 \propto \omega^\alpha$, thus yielding [Dyre and Schrøder, 2000, Helgren and Gruner, 2001] :

$$\sigma(\omega) = \sigma_1(\omega) + \sigma_2(\omega) = A\left(-i\frac{\omega}{\omega_0}\right)^\alpha \tag{4.19}$$

This is what is shown figure 4.19 in the case of bulk insulating a-Nb_xSi_{1-x} samples. Due to the rate at which an electron tunnels from one site to the other, VRH-induced AC response is observable at frequencies of the order of 10-1000 GHz.

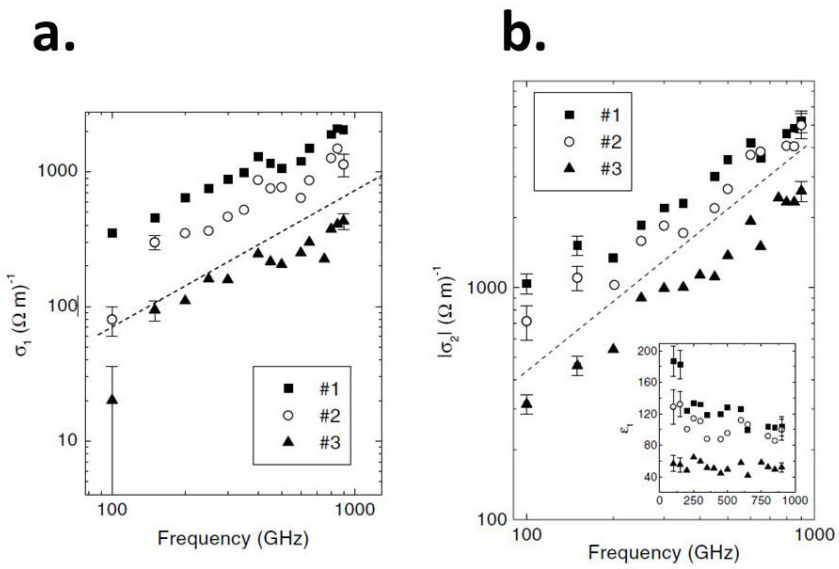

Figure 4.19: Frequency dependence of the real (a) and imaginary (b) parts of the conductivity for a-Nb_xSi_{1-x} samples on the insulating side of the MIT [Helgren and Gruner, 2001]. The three symbols correspond to three different compositions of the alloy.

GHz or even lower frequencies (1 to 100 kHz) measurements enable to access the dielectric response of insulators via the relation :

$$\varepsilon = \varepsilon_1 + i\varepsilon_2 = 1 + i\frac{\sigma}{\epsilon_0 \omega} \tag{4.20}$$

Combined with low frequency (DC) measurement of the conductivity on the metallic side, the divergence of the dielectric susceptibility χ at the transition defines the MIT, as shown figure 4.20 for doping-induced MIT in Si:P samples.

4.5.2 Electrodynamic characterization of Cooper pairs in the non-superconducting regime

As previously explained, using dynamical conductance measurements, one can access short-lived fluctuations, if any. This has been performed, in the framework of the SIT, on InO_x films.

Using microwave cavities (9-22 GHz), Crane et al. have measured a non-zero superfluid stiffness well into the insulating regime [2] of **highly disordered** InO_x films [Crane et al., 2007]. As seen figure 4.21.a, the points in temperature and field where the superfluid stiffness goes to zero are frequency-dependent. The higher the frequency, the longer the superconducting fluctuations persist. This has been interpreted as the signature for Cooper pairs with a finite lifetime surviving in an extensive region of the insulating regime.

In the limit of **low-disorder** films, using microwave spectroscopy (50 MHz-16 GHz), Liu et al. have shown that superconducting fluctuations persist in the magnetic field-tuned SIT above a critical field B_{sm} where the global superconducting phase coherence is lost : the characteristic fluctuation frequency Ω extrapolates to zero at $T = 0$ for $B_{sm} \simeq 4$ T (figure 4.21.b). However for $B_{sm} < B < B_{cross}$ where the SIT is expected by the Dirty Boson Model [3], superconducting fluctuations are still measured. The authors interpret this as the signature for an unconventional 2D metal where Cooper pairing exists without the global phase coherence.

4.5.3 Electrodynamic characterization of Coulomb interactions

Recently, AC conductivity measurements have been shown to be a very interesting probe to tackle Coulomb interactions. Indeed, Sherman et al. compared the DC tunneling spectra and the electrodynamic response of two films on both sides on the SIT : one was measured to be superconducting, with a T_c of about 3 K, by DC resistance measurements and the other

2. The superfluid stiffness still had a finite value when the measured DC resistance was over 10^6 $\Omega/\square$.

3. B_{cross} corresponds to the field where all $R(T)$ curves cross. In other words, it is the point at which the resistance of the sample is constant. The insulator is expected for $B > B_{cross}$.

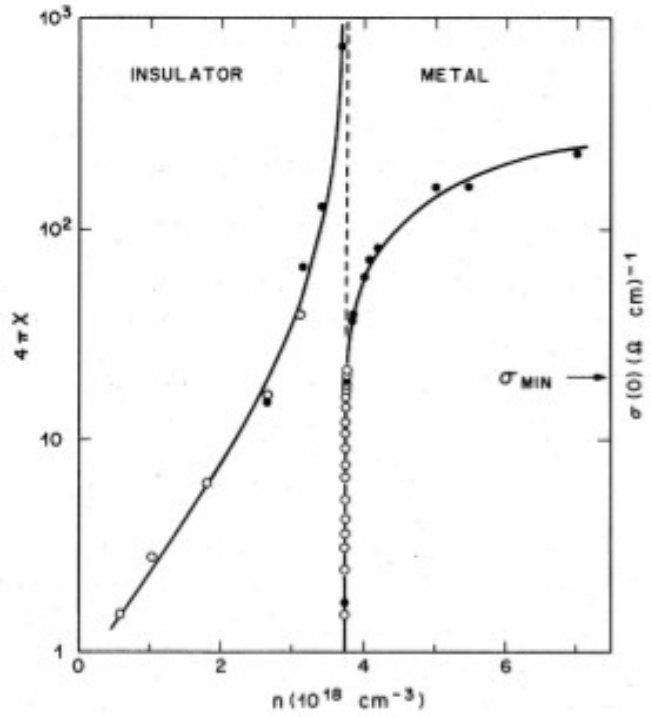

Figure 4.20: Dielectric susceptibility χ and zero temperature conductivity $\sigma(0)$ as a function of the donor concentration n in Si:P samples [Hess et al., 1982]. At the MIT, χ diverges on the insulating side, whereas $\sigma(0)$ goes to zero on the metallic side.

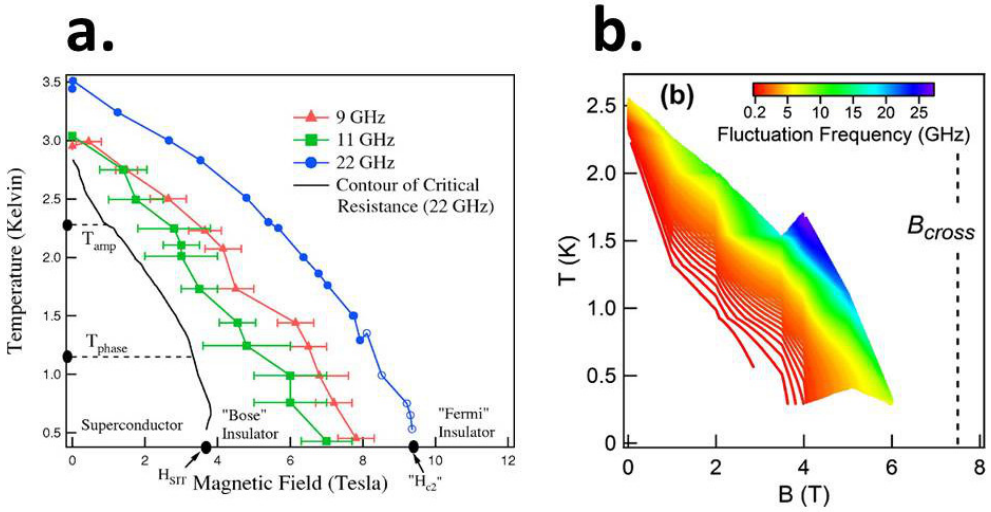

Figure 4.21: Phase diagrams for InO_x thin films as a function of temperature and magnetic field. (a). **High disorder limit** [Crane et al., 2007]. The black line indicates the SIT as defined from DC measurements. The colored lines correspond to the points where the superfluid stiffness goes to zero at 9, 11 and 22 GHz. (b). **low disorder limit** [Liu et al., 2013]. The color lines correspond to different values of the characteristic fluctuation frequency Ω.

was insulating, with an activation energy of about 0.5 K. The comparison is shown figure 4.22. Whereas THz measurements show frequency dependencies that are consistent with each regime (Mattis-Bardeen-type for the superconductor and Drude for the insulator), the tunneling spectra both present a gap at low energy. On the superconducting side, as expected, the gap is of BCS-type. On the insulating side however, this gap - which had, in some cases, been attributed to inhomogeneous superconductivity in such disordered systems - appears as induced by the tunneling technique. Indeed, if there really was a gap in the density-of-states in the insulating

sample, it would have been also measured by THz technique. On the contrary, a gap that is only visible by tunneling spectroscopy could well reflect the importance of Coulomb interactions in this system : the counter-electrode used for tunneling is thought to enhance screening and enable the persistance of superconducting fluctuations at higher disorder.

AC conductivity measurements therefore are a non-perturbative technique which, by comparison with other techniques sensitive to Coulomb interactions, could provide very interesting insight on the relative importance of screening and localisation in disordered superconducting thin films.

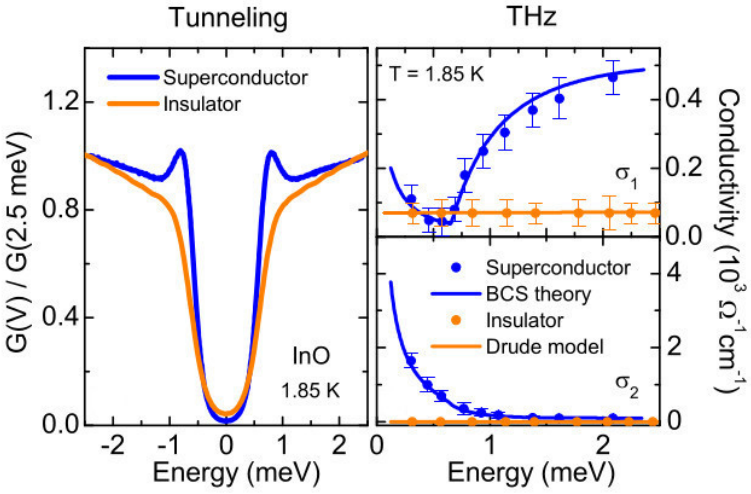

Figure 4.22: Tunneling density-of-states (left) and THz conductance (real part on the upper right panel, imaginary part on the lower right panel) for InO_x films on both sides of the SIT [Sherman et al., 2014].

4.6 Aim of our work

As shown in this chapter, AC transport measurements are extremely powerful to determine the ground state and the different excitations that coexist in a given system. In particular, close to the SIT, one could hope to address issues such as the survival of superconducting fluctuations, the extent of BKT regime, the importance of Coulomb interactions, the universality class of such a transition or the quasiparticle relaxation rate.

Given the energy scales we would like to probe (of the order of 10 mK - 1 K), we chose to work at microwave frequencies (a few GHz). However, as mentioned in section 4.3, these high frequency measurements are extremely sensitive to the sample ... but also to its environment. In order to achieve sufficiently precise measurements, one could choose to work at a given frequency with high-quality resonators. However, to grasp a fuller picture of the system, one would ideally like to perform broadband spectroscopy. This comes at the price a full set-up calibration, in conditions as close as possible to the measurement conditions.

In a previous work [Couëdo, 2014], there has been an attempt to measure the finite frequency response of superconducting a-Nb_xSi_{1-x} films by microwave reflectometry measurements using either a room temperature or a 4 K calibration. At low temperature, the signal they wanted to detect was barely large enough to be extracted from the errors induced by the cooling down [4] so that hypotheses had to be made on the normal and superconducting states [5] in order to extract the response of the sample **at the superconducting transition**. Although this method is extremely powerful for extracting a signal on large temperature scales, it is not entirely satisfactory since it assumes the knowledge of the sample AC conductivity at three different temperatures.

This is the reason for the present work : we wanted to build an **in situ** low temperature calibration set-up. Ideally, in a single cool down and at **all temperatures**, one could have

4. Indeed, at room temperature (or 4K), parasitic reflections and set-up imperfections are compensated thanks to the calibration. However, as detailed in 5.2.2 the reflection due to cables, connections, ... evolve in temperature. At low temperature, the calibration hence no longer counter-balances the electrodynamic response coming from the sample environment. This induces some uncertainty in the measurement.

5. The hypotheses that were made were two-fold. First, the superconducting state was modeled as a pure inductance at $T \ll T_c$. Second, the normal state was modeled as a pure resistor.

an exact set-up calibration and hence extract the sample dynamical conductivity with a good precision.

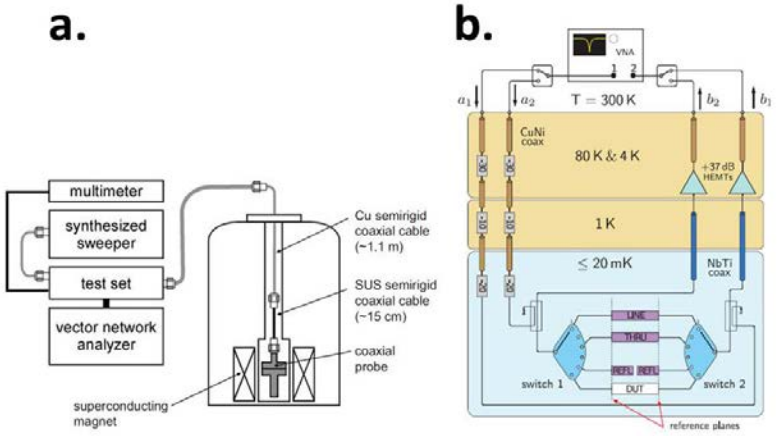

Figure 4.23: (a). Schematic representation of the set-up used in [Kitano et al., 2008]. The different standards used for calibration are successively measured in order to establish the calibration. (b). Schematic representation of the set-up used in [Ranzani et al., 2013b]. The sample and the three standards are measured at all temperatures, using RF electro-mechanical switches.

Different attempts have been made to tackle this problem :

1. One possibility is to successively measure the three standards necessary for a complete calibration of the set-up (Open, Short and Load, usually) at room temperature and at low temperature [Reuss, 2000, Kitano et al., 2008]. From the different obtained spectra, one could theoretically determine a complete calibration at low temperature (figure 4.23.a). The drawback of this method is that it assumes a constant reproducibility of the thermal constraints and electrical contacts between the different cool-downs. In reality, however, the different thermal cycles degrade the reproducibility with time. Moreover, they are extremely time-consuming.
2. Commercially available electromechanical switches could also be used. However, the electrical path for the different switching positions are often not exactly the same, inducing uncertainties in the calibration process [Cano and Artal, 2009]. Recent developments in RF switches [Ranzani et al., 2013b, Ranzani et al., 2013a, Yeh and Anlage, 2013] have overcome this problem, but are made out of solenoids, sensitive to magnetic field. Since the ultimate aim of this work is to be able to study the AC response near the SIT, including the magnetic field-induced transition, we wanted a calibration set-up that could be robust to any small magnetic field (typically up to 1-2 T).

Our aim was therefore to build a robust mechanical switch that could be used at very low temperature, under magnetic field, and which could provide a reliable and precise calibration at all temperatures, in a single cool-down. The developments and tests performed to achieve this goal will be described in the next chapter.

Chapter 5

Experimental results

5.1 Introduction

We have described the aim of the present work in the previous chapter : build an in-situ low temperature calibration setup for GHz broadband measurements which would, in principle, allow us to determine with good precision the absolute value of any sample's complex impedance.

In this chapter we will :
- Give the working principle of broadband measurements, and especially reflectometry measurements, and the sources of uncertainties for these methods.
- Describe the theoretical calibration procedure and how it could be applied in the case of measurements in a cryogenic environment.
- Describe the calibration set-up we have developed.
- Describe the characterisation of Vanadium samples, used for the setup validation.
- Present the first measurements of the GHz response of Vanadium films and qualify the performances of the calibration device.

5.2 Broadband measurement : principle

As previously mentioned, GHz measurements can be obtained though broadband spectrometry or by using high quality factor resonators. We have chosen to favour broadband measurements which can be accessed either through transmission or reflection on the sample. However, as we will see in the following, broadband measurement requires a good knowledge of the setup frequency response.

In this section, we will :
- Explain how broadband measurements are performed.
- Detail the sources of uncertainties linked to the measurement.
- Show how a calibration can, in principle, free the experimentalist from the error sources due to the setup.

5.2.1 Basics of broadband spectrometry

In broadband spectrometry measurements, a multi-frequency microwave is usually synthesized by the source of a Vector Network Analyser (VNA). This wave will propagate through a line of characteristic impedance Z_0 given by :

$$Z_0 = \sqrt{\frac{L_l}{C_l}} \tag{5.1}$$

with L_l the inductance of the line per unit length and C_l its capacitance per unit length. In the case of standard coaxial cables, $Z_0 = 50\,\Omega$. They then are adapted to the VNA output impedance.

In the case of a modification of the characteristic impedance of the line (presented figure 5.1.a.), the signal incoming from port 1 (and of amplitude taken to be 1 for simplicity) is partially and locally reflected with an amplitude Γ. Due to conservation of the wave amplitude, the transmitted signal then has an amplitude given by $T = 1 + \Gamma$. Both Γ and T can then be

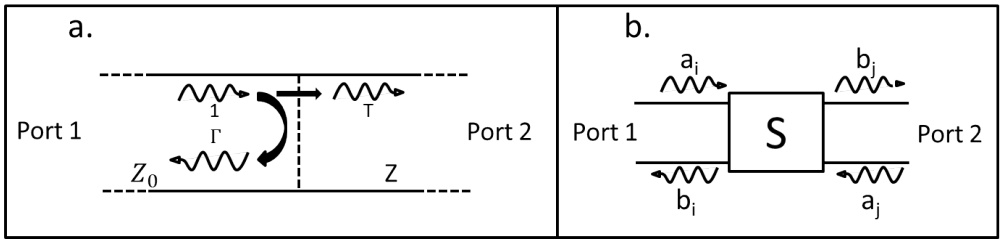

Figure 5.1: Principle of microwave measurements : a modification of the characteristic impedance of the line from Z_0 to Z induces a reflected and a transmitted wave (a.). More generally, any mismatch is represented by a scattering matrix S, characteristic of the mismatch response in frequency (b.). The excitation is incoming from port 1 and the measurement can be performed in port 1 (reflection) or in port 2 (transmission).

measured respectively in port 1 or port 2, which are supposed perfect [1]. In particular, if the characteristic impedance of the cable is Z_0 before the reflexion and Z after it, Γ and T are given by :

$$\Gamma = \frac{Z - Z_0}{Z + Z_0} \tag{5.2}$$

$$T = \frac{2\,Z}{Z + Z_0} \tag{5.3}$$

In a more general case, any element inducing a mismatch of the line can be represented by scattering matrices S, as represented figure 5.1.b., such that

$$\begin{pmatrix} b_i \\ b_j \end{pmatrix} = S \begin{pmatrix} a_i \\ a_j \end{pmatrix} \tag{5.4}$$

where a_k (respectively b_k) with $k = \{i, j\}$ is the amplitude of the incoming (outgoing) signal toward (from) the elements represented by S [2].

Let us note that even if it is theoretically equivalent, measuring either the transmission coefficient or the reflection coefficient affects the experiment sensitivity. As one can observe figure 5.2, **the maximum sensitivity in transmission is obtained in the case of an impedance Z close to 0, whereas the maximum in reflection sensitivity is achieved for Z close to Z_0**. Therefore, combining the two measurement methods should be the best way to have a sensitive measurement in all cases.

As we will see, such measurements require a calibration of the setup. In the case of reflective measurements, the sole characterization of the incoming line will be necessary. In the case of transmission measurements, one needs - in addition - to calibrate a second line as well as the transmission between the lines, without modifying the setup. This is complicated to perform in a low temperature environment. In the following we will therefore mainly describe how to perform reflective measurements, corresponding to the approach we adopted in this work.

5.2.2 The error sources

In the previous paragraph, we have seen what the response of a sample would be in the ideal case where no parasitic reflection or attenuation occurs. In this subsection, we will examine the effects of the setup imperfections and the possible sources of error in a real-life experiment.

Skin effect and propagation

From Maxwell's equations, one can show that - in a conductor - the current is propagating only on a frequency-dependent thickness δ, the **skin depth**, such that :

$$\delta = \sqrt{\frac{2}{\sigma \mu \omega}} \tag{5.5}$$

1. I.e. matched to the line such that there is no reflection at the ports.
2. For perfect ports, and in the absence of other scattering elements, $a_j = 0$.

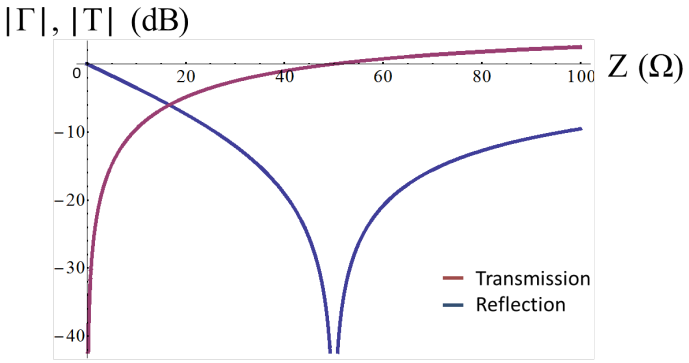

Figure 5.2: Modulus of the reflection and transmission coefficients ($|\Gamma|$ and $|T|$, in dB) as a function of the sample impedance. This curve has been obtained by taking $Z_0 = 50\ \Omega$.

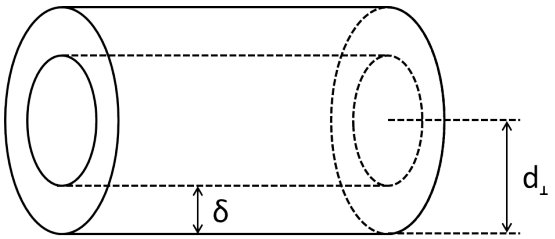

Figure 5.3: Schematic representation of the skin effect on a cylindrical conductor of radius $d_\perp$ and skin depth δ.

with ω the angular frequency of the AC signal, σ the conductivity of the material and μ its magnetic permeability.
As a consequence, for $\delta < d_\perp$, where $d_\perp$ is the thickness of the conductor, only the surface is carrying the signal as represented figure 5.3 for a cylindrical conductor, such as coaxial cables.

The skin effect has two major consequences on the system :
- A conductor has a **resistance which is frequency-dependent**, given by $R_s = \frac{1}{\sigma\delta} = \sqrt{\frac{\omega\mu}{2\sigma}}$.
- Since cables are resistive, the incoming signal partly **dissipates** as it propagates within this medium. For a conductor of length z, the propagating signal a_i is such that $a_i \propto e^{-\alpha z}e^{-ikz}$, where k is the wave vector of the propagating signal and $\alpha = \frac{1}{2}\frac{R_s}{Z_0}$ (if the dielectric loss can be neglected) [Pozar, 2004]. In this expression, e^{-ikz} is the propagation term describing a progressive phase oscillation as the signal travels along the line, and $e^{-\alpha z}$ corresponds to the attenuation factor.

The consequences of the skin effect can be seen figure 5.4 on which we plotted the measured reflection of cables connected in series and terminated by an open ($Z = \infty$). The attenuation occurring along the cable is indeed frequency-dependent due to skin effect. A typical value for the attenuation along the type of coaxial cables used in this work [3] is between -1.5 dB/m and -0.6 dB/m [4] at 1 GHz. Since the cable resistance is temperature-dependent, the attenuation in the signal is also temperature-dependent, so that the frequency response of a cable varies with the temperature. This point will be important when considering how to calibrate the set-up.
One also has to be aware of such an effect when designing the sample. Indeed, if the sample thickness is too large, the electromagnetic field will not penetrate in all the volume of the sample, and the obtained response will only reflect the properties of the sample surface. We will come back to this point when dealing with the choice of an appropriate sample, section 5.4.1.

Multiple impedance mismatches

3. Outer conductor diameter of 2.2 mm and central conductor diameter of 0.5 mm for stainless and copper coaxial cables.
4. Respectively for stainless and copper cables.

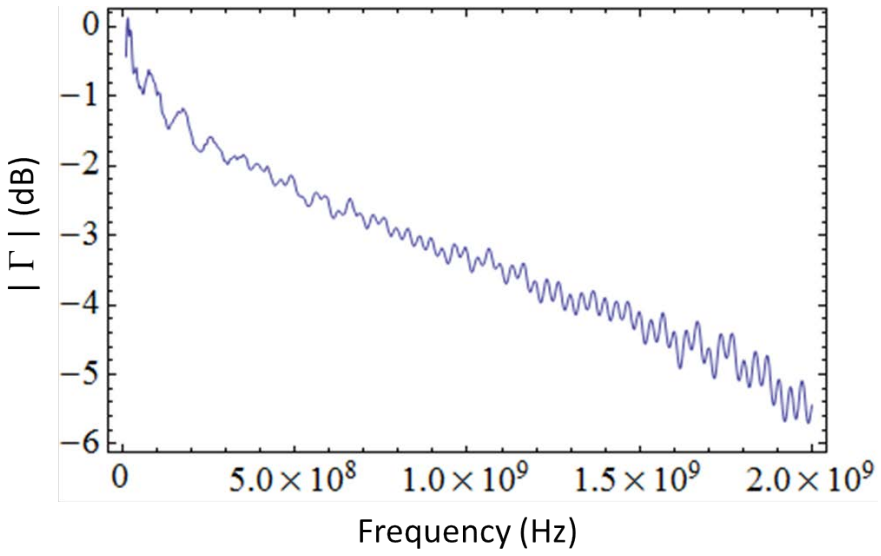

Figure 5.4: Measurement of $|\Gamma|$ (in dB) for coaxial cables terminated with an open, for frequencies ranging from 10 MHz to 2 GHz. The decreasing reflection signal signs the skin effect. The small oscillations are due to the multiple impedance mismatches along the line.

In addition to losses, the lines have unavoidable imperfections which can be intrinsic or due to connections. For instance, any interruption in the line to insert a microwave component such as an amplifier, a directional coupler, or, even more basically, a connection to the sample via SMA-type connectors, induces parasitic reflections that may become a nuisance if not controlled or characterized. The measured overall response is then a function of the electrodynamic response of the sample and of the multiple reflections at each of the line imperfections.

In particular, **impedance mismatches can induce Fabry-Perot oscillations**, observable figure 5.4. These originate from the interferences between the different reflections of the signal. This effect can be illustrated by a simple example : a single line with an extended impedance mismatch of length $l > \lambda$ (systematized figure 5.5). One can show that for such a mismatch, the total measured reflection is :

$$\Gamma_{tot} = \Gamma_1 + \frac{\Gamma_2(1-\Gamma_1^2)}{e^{i\theta} + \Gamma_1\Gamma_2} \tag{5.6}$$

with $\theta = 2kl$, Γ_1 the reflection at the first mismatch and Γ_2 the reflection at the second mismatch. As $\omega = \frac{kc}{n}$ is tuned, Γ_{tot} oscillates with a $\frac{c\pi}{nl}$ periodicity in angular frequency, c being the speed of light and n the refraction index of the medium. Therefore, oscillations in the overall reflected signal appear for each cavity formed by impedance mismatches.

The intrinsic response of the sample can be deconvoluted if the number of resonant cavities is limited in the corresponding frequency range. For the presented example :

$$\Gamma_1 = \frac{\Gamma_2 - e^{i\theta}\Gamma_{tot}}{-e^{i\theta} + \Gamma_2\Gamma_{tot}} \tag{5.7}$$

However, when the number of cavities with different lengths and reflection factors is important, it is complicated to obtain the intrinsic response of the system by using such a deconvolution method.

One would, ideally, like to avoid Fabry-Perot effects due to the spatial extension of the sample. Regarding the incoming wavelength, the sample therefore needs to be considered as a point in space : $\lambda \gg l$, with l the length of the sample. At 10 GHz and considering the substrate we used [5], we find that this condition gives $l \ll 10$ cm. We will see that the typical size of our samples complies with this constraint (section 5.5).

Effect of the temperature

5. TMM10i with $\epsilon = 9.8$.

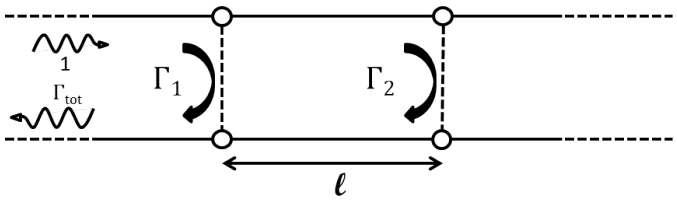

Figure 5.5: Schematic representation of an extended sample to illustrate the Fabry-Perot effect. The section of length l forms a resonant cavity.

As the temperature is modified, the response of the system is modified by two phenomena :
- The **conductivity of the lines is modified** with the above-mentioned consequences on their characteristics.
- **Thermal contraction occurs**. As the different parts of the set-up are made out of different materials, each having its own thermal expansion coefficient, cooling down a microwave circuit is not straightforward. For instance, Teflon has a thermal expansion coefficient of 1.6% between 4 K and 300 K. Therefore, as the RF line is usually of the order of 1 m long [6], Teflon contraction induces a change in the cable length of about 1.6 cm between room temperature and 4 K.

These phenomena have several consequences on the apparatus :
- Applying the characterization of the setup made at high temperature to low temperature measurements induces important errors since both the varying conductivity of the cables changes the attenuation and thermal contractions induce different impedance mismatches at each connections and inside the coaxial cables for instance.
- At each cool down, thermal contractions and thermal gradient distributions change the overall setup response. The lack of reproducibility in the mechanical and electrical properties prevents the definition of a unique response of the setup from cool down to cool down.
- The apparatus is sensitive to temperature changes. More specifically, the helium level and the thermal anchoring of the lines will affect the total reflected signal.

Due to all these reasons, it is important to try to characterize the system at low temperatures, and, whenever possible, within a single cool down.

5.2.3 Calibration

In order to be insensitive (or, at least, less sensitive) to the apparatus and to obtain the frequency-dependent complex impedance of the measured sample with a maximum precision, one needs to fully characterise the response of the system. In the following, we will exclusively focus on the equations for reflectometry measurements as we did not performed transmission measurements during this thesis.

We will first detail the calibration principle before extending the discussion to the different non-standard calibrations used in the literature for such measurements.

5.2.3.1 Mathematical description of calibration

Mathematically, all errors originating from the apparatus can be described by an **error matrix** S_{err} such that :

$$S_{err} = \begin{pmatrix} E_D & E_R \\ 1 & E_S \end{pmatrix} \tag{5.8}$$

Where E_D, E_R and E_S are frequency-dependent complex coefficients, representing respectively the **directivity**, the **reflection tracking** and the **source mismatch** in the apparatus. The equivalent system, for reflection measurements and taking into account these errors, is given figure 5.6. All the imperfections of the apparatus are included into S_{err}. E_D is principally due to mismatches in the transmission line or to the imperfection of additional components used during the experiments (a directional coupler for instance). E_R is principally due to the dissipation of

6. For our experimental set-up, the RF line is of the order of 1.5 m inside the cryostat.

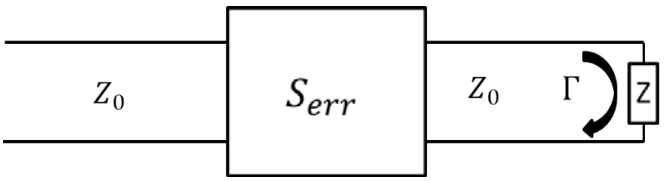

Figure 5.6: Equivalent representation of the imperfect apparatus, with a transmission line of impedance Z_0 and a sample of impedance Z measured in reflectometry.

the lines and dephasing along the lines. Finally, E_S is due to re-reflection of the signal as it goes back to the output of the measurement apparatus.

5.2.3.2 Principle

We saw that the errors due to the apparatus can be taken into account by 3 coefficients, E_D, E_R and E_S. Having 3 different well-known standards therefore allows to fully characterize S_{err} and retrieve the response of the sole sample.

By using the measurement of different standards 1, 2 and 3 (i.e. samples for which the electrodynamic response is perfectly known in the considered frequency range), one can calculate that the error coefficients are given by [Kitano et al., 2008] :

$$E_D(\omega) = \frac{\Gamma_{M1}(\Gamma_{M2}-\Gamma_{M3})\Gamma_{ref2}\Gamma_{ref3} + \Gamma_{M2}(\Gamma_{M3}-\Gamma_{M1})\Gamma_{ref3}\Gamma_{ref1} + \Gamma_{M3}(\Gamma_{M1}-\Gamma_{M2})\Gamma_{ref1}\Gamma_{ref2}}{(\Gamma_{M1}-\Gamma_{M2})\Gamma_{ref1}\Gamma_{ref2} + (\Gamma_{M2}-\Gamma_{M3})\Gamma_{ref2}\Gamma_{ref3} + (\Gamma_{M3}-\Gamma_{M1})\Gamma_{ref3}\Gamma_{ref1}} \tag{5.9}$$

$$E_R(\omega) = \frac{(\Gamma_{M1}-\Gamma_{M2})(\Gamma_{M2}-\Gamma_{M3})(\Gamma_{M3}-\Gamma_{M1})(\Gamma_{ref1}-\Gamma_{ref2})(\Gamma_{ref2}-\Gamma_{ref3})(\Gamma_{ref3}-\Gamma_{ref1})}{[(\Gamma_{M1}-\Gamma_{M2})\Gamma_{ref1}\Gamma_{ref2} + (\Gamma_{M2}-\Gamma_{M3})\Gamma_{ref2}\Gamma_{ref3} + (\Gamma_{M3}-\Gamma_{M1})\Gamma_{ref3}\Gamma_{ref1}]^2} \tag{5.10}$$

$$E_S(\omega) = \frac{\Gamma_{M1}(\Gamma_{ref2}-\Gamma_{ref3}) + \Gamma_{M2}(\Gamma_{ref3}-\Gamma_{ref1}) + \Gamma_{M3}(\Gamma_{ref1}-\Gamma_{ref2})}{(\Gamma_{M1}-\Gamma_{M2})\Gamma_{ref1}\Gamma_{ref2} + (\Gamma_{M2}-\Gamma_{M3})\Gamma_{ref2}\Gamma_{ref3} + (\Gamma_{M3}-\Gamma_{M1})\Gamma_{ref3}\Gamma_{ref1}} \tag{5.11}$$

where Γ_{refi} is the expected reflection for the standard $i \in [1,3]$ and Γ_{Mi} is its actual measurement performed with the setup.

Having determined all error coefficients, one can measure the sample and retrieve its impedance. Indeed, for a sample of reflectivity $\Gamma(\omega)$, the measured reflectivity $\Gamma_{meas}(\omega)$ for the sample with the given setup is obtained through :

$$\Gamma_{meas}(\omega) = E_D(\omega) + \frac{E_R(\omega)\Gamma(\omega)}{1 - E_S(\omega)\Gamma(\omega)} \tag{5.12}$$

This gives us that the signal originating from the sample is :

$$\Gamma(\omega) = \frac{E_D(\omega) - \Gamma_{meas}(\omega)}{-E_R(\omega) + E_S(\omega)(E_D(\omega) - \Gamma_{meas}(\omega))} \tag{5.13}$$

In the standard calibration for reflectometry measurements, the **3 calibration points correspond to : an open, a short and a load** (matched to the RF line) which characteristics are listed below :

Standard	Impedance	Γ_{ref}
Open	∞	1
Short	0	-1
Load	$Z_0 = 50\,\Omega$	0

Figure 5.7: Standard references, as well as their impedance and reflection coefficient Γ_{ref}.

As we saw in section 5.2.2, due to thermal contractions, the lines are modified at each cool down, making calibration by using successive cool downs of the 3 references and of the sample difficult. With some assumptions on the system response, one can lower the number of standards needed. One can for instance calibrate using only two standards and assuming that $E_D \sim 0$. This assumption is equivalent to say that there is no impedance mismatch in the line between the instruments and the sample. Such hypothesis induces :

$$\Gamma(\omega) = \frac{(\Gamma_{M1} - \Gamma_{M2})\Gamma_{meas}\Gamma_{ref1}\Gamma_{ref2}}{-\Gamma_{M2}\Gamma_{meas}\Gamma_{ref1} + \Gamma_{M1}(\Gamma_{M2}(\Gamma_{ref1} - \Gamma_{ref2}) + \Gamma_{meas}\Gamma_{ref2})} \tag{5.14}$$

This strong assumption is usually not commendable due to imperfections of the line. It induces large errors on the retrieved signal $\Gamma(\omega)$. However, it can give some rough indication for debugging the setup.

Usually, instead of using such assumptions, experimentalists use experimental "tricks" to obtain a "good" calibration of the system and limit the number of cool downs.

5.2.3.3 Non standard calibration techniques

Instead of using the usual Open Short Load calibration, one can indeed use some alternative calibration methods :

- Booth et al. [Booth et al., 1994] measured the calibration points at room temperature, assuming that most of the errors, except the losses due to the line (E_R), could be corrected in this way. In addition, and to obtain E_R, **they substituted the measurement of the short at low temperature by the sample in the superconducting state**, assuming a pure inductive response of the superconductor. This requires to know the kinetic inductance of the system, and can be used only in the case of superconducting materials.
- Kitano et al. [Kitano et al., 2008] successively measured all references at low temperature but **substituted the measurement of the load by taking the resistance of the sample in the normal state**, assuming that the resistivity is frequency-independent [7]. This calibration can be used for any system with a metallic state described by Drude's model.
- Couëdo et al [Couëdo, 2014] **used the response of the system in both the superconducting and the normal state to obtain all calibrations points and the response of the system in a single cool down**. To do so, they used two calibration points in the normal state at low temperature, of different resistances, for which they assumed a purely resistive response. The third calibration point has been taken in the superconducting state by assuming a pure kinetic response of the system at the lowest temperatures. These hypotheses have been validated by an usual Open Short Load calibration. However, this method is also limited to superconducting samples, or, at least, to samples for which the frequency response is known at 3 different temperatures.

5.3 Calibration device

To both perform an efficient calibration and limit the number of cool downs, we chose a different approach than the above-cited ones : **we chose to measure standard calibration points (Open, Short and Load) in addition to the sample during a single cool down**. This approach required the development of a compact apparatus [8] allowing such a calibration, while the 3 standards and the sample are measured in conditions as similar as possible.

The idea guiding the design of this device was to use a rotating microwave cable connected to a dial where the standards and the sample are placed. Through successive rotations, the incoming signal is then connected to the corresponding dial line. The experimental challenges are :

- To operate a **mechanically rotating cable at low temperature**, and located 1-1.5 m-deep in a cryostat.

7. As expected for metals described by Drude's model, for frequencies much lower than the scattering time ($\tau = 10^{-13}$ s for a good metal).

8. It needs to enter in a ^{4}He cryostat of diameter $\Phi = 29mm$.

- Design **equivalent dial lines**, so that the incoming wave sees exactly the same environment, except for the nature of the sample or device at the end of each line.
- Ensure that the mechanical rotation of the connector gives **similar transmissions for each of the dial lines**.
- Ensure a **good transmission** between the rotation microwave cable and the other rigid cable.

Several designs have been tested during this thesis. In the following, we will only detail the last one with which the measurements of superconducting vanadium samples have been performed. In the following, we will detail :

- How the dial is designed. We will more particularly detail the structure of the lines and of the different references.
- How the transition between the coaxial cables and the dial is done.
- The switching mechanism between the different standards and sample.
- The validation of the calibration device on a 200 Ω dead resistor.

5.3.1 Design of the lines on the dial

The characteristic output impedance of the VNA and the characteristic impedance of the cables is $Z_0 = 50\ \Omega$. To limit the reflection of the signal during its propagation within the dial lines, these have to be accordingly adapted. To do so, we adopted a Conductor-Backed Coplanar WaveGuide geometry (CBCPW) (presented figure 5.8). It consists in a dielectric of relative permittivity ϵ_r (and thickness h) sandwiched between 2 conducting layers (of thicknesses $d_\perp$). The top layer is patterned with a strip of width $S = 2a$, in the middle of two semi-infinite ground planes at a distance W.

For this geometry, the characteristic impedance Z_0 is given by [Simons, 2001] :

$$Z_0 = \frac{60\pi}{\sqrt{\epsilon_{eff}}} \frac{1}{\frac{K(k_1)}{K(k_1')} + \frac{K(k_2)}{K(k_2')}} \tag{5.15}$$

where $K(k)$ is the complete elliptic integral of the first kind, $k_1 = \frac{a}{2a+2W}$, $k_1' = \sqrt{1-k^2}$, $k_2 = tanh(\frac{\pi a}{2h})/tanh(\frac{\pi b}{2h})$, $k_2' = \sqrt{1-k_2^2}$, and ϵ_{eff} is given by :

$$\epsilon_{eff} = \frac{1 + \epsilon_r \frac{K(k_1')}{K(k_1)} \frac{K(k_2)}{K(k_2')}}{1 + \frac{K(k_1')}{K(k_1)} \frac{K(k_2)}{K(k_2')}} \tag{5.16}$$

Using this geometry presents several advantages :

- It is easy to design the lines by usual lithography or milling techniques.
- The geometry is similar to the one of coaxial cables, with a conductor surrounded by ground planes, which helps the adaptation between the two different geometries.
- The impedance Z_0 of such a line is easily tunable to match the impedance of the coaxial cables (50 Ω), by tuning S and W for given $d_\perp$ and h.
- The radiation losses [9] are low thanks to the proximity of the conducting strip to the ground [10].

For our device, we chose as dielectric a 635 μm-thick TMM10i ceramic ($\epsilon = 9.8$), which is known to have low losses at low temperatures and high frequencies. It is covered on both sides by a 17.5 μm-thick copper layer. The analytical computation of Z_0 being cumbersome, the geometry of the lines have been optimized using AppCAD©. The patterning of the lines has then been performed using a micro-milling machine at the LPS-Orsay.

5.3.2 Design of the calibration dial

The main idea behind this design, presented figure 5.9a., is to be able to measure successively and by staying at low temperatures, all references and the sample, all sitting on a single chip. In addition, we wanted to add a low frequency measurement of the sample by using a bias-Tee [11]

9. Dissipation by the environment.
10. In addition, dielectric loss can be reduced by adequately selecting the dielectric material.
11. A bias-Tee is a passive component allowing to mix low frequency and high frequency measurements, without interferences between them.

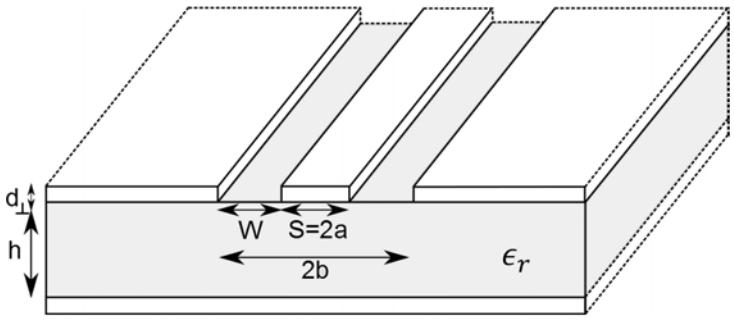

Figure 5.8: Conductor-Backed Coplanar Wave Guide geometry, with a strip line of thickness $d_\perp$ and width S. It is separated from the ground by a distance W on plane and h out of plane. The substrate has a dielectric constant ϵ_r.

(figure 5.9b.).

Several parameters have then to be taken into account to determine the final design of the lines (presented figure 5.10) :

- The **50 Ω adaptation along the line**, addressed in the previous section.
- The **size of the termination gap** : the use of a commercial 50 Ω CMS for our load sets the size of the terminating gap at 200 μm, corresponding approximately to the distance between the metallic pads of the CMS element.
- The **adaptation of the end of the line to the sample to probe** : the width of the line S, and of the gap W is determined by the width of the sample we would like to probe, which should match the width of the line. In our case, we chose to have a line termination with $S = 600$ μm, determining $W = 800$ μm. This choice is has been made to :
  - easily handle samples. Indeed, these are deposited onto a substrate and it is convenient to "flip-chip" (see section 5.5) them onto the dedicated line, so that the film to probe is directly in contact with the microwave line. The sample then is of micro-stipline geometry.
  - have a CBCPW line geometry to stripline (sample geometry) transition at the end of the line, allowing to be less sensitive to imperfections at the edges of the sample [12].
- The **adaptation between the coaxial cable and the calibration device** : it is performed by a right-angle SMP-connector placed in the middle of the chip and presented figure 5.11 [13]. The line at the transition has a width of 350 μm adapted to the size of the pin of the connector. It imposes the size of the gap at the beginning of the line to be 210 μm, to have a 50 Ω adapted transition.
- The **adaptation to a Bias-Tee** [14], which footprint has been reproduced on the line of the sample [15] imposes $S = 490$ μm and $W = 390$ μm [16].
- **A good definition of the ground plane** : it is provided by via [17] distant of 1.5 mm from each other. They have been placed away from the center of the chip in order to avoid interferences with the rotation of the right-angle connector.

To verify there were no resonances due to the modification of the width along the lines, RF simulations have been performed using *Sonnet*©. The resulting design is presented figure 5.12, with a 3D view of the CAD design created on *SolidWorks*© and a picture of the assembled chip. The line dedicated to the measurement of the sample will be detailed in section 5.5.

5.3.3 The reference points

We saw in section 5.2.3.2 that calibration in reflectometry is usually obtained by measuring 3 different standards, which are placed at the end of the lines as represented figure 5.13.a. In the case of perfect calibration points (figure 5.13.b.), the Open is an open line, the Short a direct

12. Such uncontrolled imperfections, due to the cutting process, can engender peak effects of the electric field and disturb the measurement.
13. Radiall R222941700W connector.
14. Marki BT-0024SMG.
15. It has been sufficiently spaced from the center of the sample so that it does not mechanically hinder the motion of the pin of the right-angle connector.
16. To obtain a correct calibration, a small delay due to the bias-Tee has to be taken into account. This delay, measured separately, is assimilable to an additive propagation length (see appendix D.2).
17. Metallic links between the top and the bottom metallic planes.

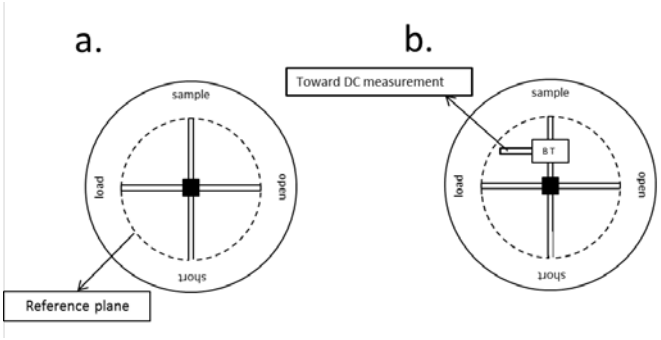

Figure 5.9: (a) Schematic representation of the calibration chip, with the different CBCPW lines addressing the references points and the sample. The reference (or calibration) plane is marked by a dashed line. (b) Schematic representation of the design with a Bias-Tee on the line of the sample.

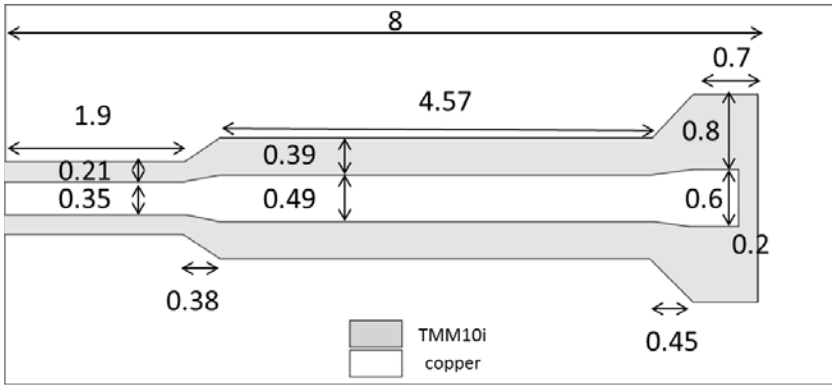

Figure 5.10: Design of the dial lines. The various lengths are given in mm.

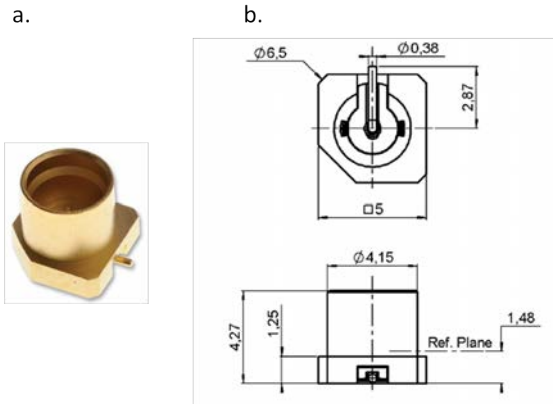

Figure 5.11: (a) Picture of the right angle connector. (b) Schematic representation of the connector. Source : http://www.radiall.com/.

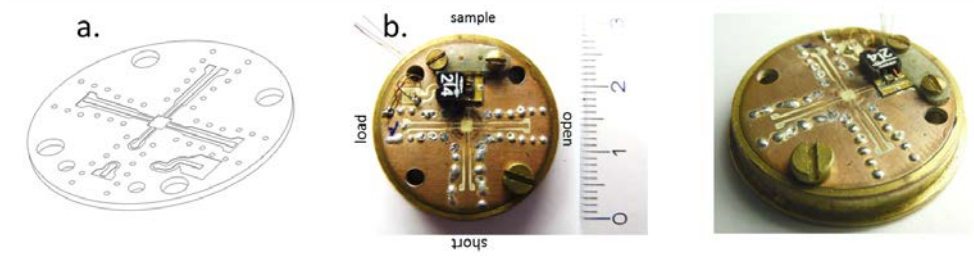

Figure 5.12: (a) 3D view of the final chip design. (b) Pictures of the assembled calibration chip.

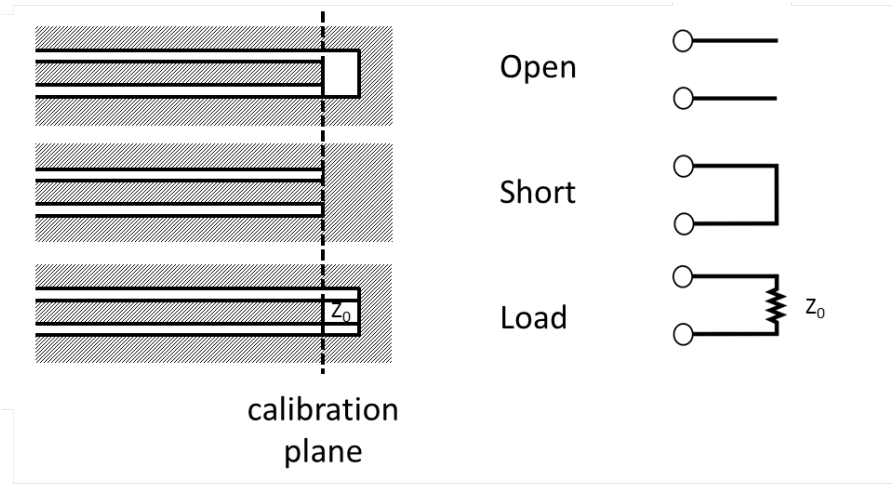

Figure 5.13: (a) Usual realisation of calibration points in reflectometry measurements. The calibration takes into account the setup up to the calibration plane, marked by a dashed line. (b) Representation of the equivalent circuits for ideal calibration points.

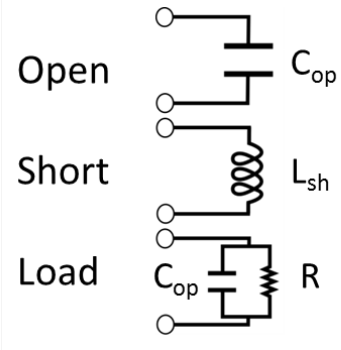

Figure 5.14: Representation of real calibration points. The open is equivalent to a capacity C_{op} between the line and the ground, the short to an inductance L_{sh}, and the load to a parallel RC_{op} circuit.

connection to the ground and the load a $Z_0 = 50\,\Omega$ resistor in which the signal is entirely absorbed.

In our case, the open has been obtained by leaving a gap between the line and the ground plane. The short has been obtained through a direct connection to the ground plane and the load has been obtained by soldering a CMS 50 Ω resistor [18] between a line identical to the open and the ground plane. These can be seen figure 5.12.

We have, up to now, assumed that the reference points were perfect, as shown in table 5.7 and section 5.2.3.2. However, it is usually not the case and they need to be modeled to achieve a good calibration. In general, **the different calibration points can be modeled as following** (figure 5.14):

- The open is modeled by a capacitance C_{op} between the ground and the line, due to the proximity of the ground.
- The short is modeled by a small line of inductance L_{sh}.
- The load is modeled by a resistor $Z \sim Z_0 = 50\,\Omega$ in parallel with a capacitance C_{op}.

Based on this model, one can estimate the parameters L_{sh} and C_{op} by using either analytical formula or simulations.

18. The resistor is a Vishay CH2016-50RGFT, certified to be frequency-independent for frequencies up to ∼ 20 GHz.

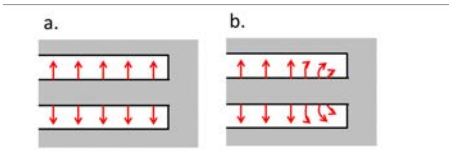

Figure 5.15: (a) Schematic representation of the electric-field lines in the case of a perfect short. (b) Schematic representation of the electric-field lines in the real case.

Open

For a width of the termination gap l_g such that $l_g \lesssim 0.1(S+2W)$, like in our case, an estimation of C_{op} is given by [Simons, 2001]:

$$C_{op} = \frac{2\epsilon_0}{\pi}\{(S+W)[\frac{ln(\eta+\sqrt{1+\eta^2})}{\eta} + ln(\frac{\sqrt{1+\eta^2}+1}{\eta}) - \frac{1}{3}(\frac{1}{1+\sqrt{1+\eta^2}})] - (S+\frac{2}{3}W)\}\epsilon_r \tag{5.17}$$

with $\eta = \frac{l_g}{S+W}$. Calculating the value, we find $C_{op} \sim 0.1\,pF$.

Using the simulation software Comsol©, we find a value of $C_{op} \sim 0.06 \pm 0.02 pF$, in fair agreement with the obtained analytical value. These values, as we will see later, are barely measurable on the reflected signals and can therefore be neglected within our experimental precision.

Short

In the case presented figure 5.13, by definition of the calibration plane, there should be no contribution coming from the short ($L_{sh} = 0$). This would be the case for non-disturbed electric-field lines (figure 5.15.a.). However, due to the presence of the neighbouring ground plane, the electric field lines are deviated as represented figure 5.15.b., leading to $L_{sh} \neq 0$. This can be interpreted as an artificial prolongation of the line, of a length l_{sh} given by [Simons, 2001]:

$$l_{sh} = \frac{L_{sh}}{L_l} \tag{5.18}$$

With $L_l \sim \frac{Z_0}{c}\sqrt{\epsilon_{eff}}$ for CPW geometry [19]. In our case, L_{sh} can be estimated through the analytical formula [Simons, 2001]:

$$L_{sh} = \frac{2}{\pi}\epsilon_0\epsilon_{eff}(S+W)Z_0^2(1 - \frac{1}{cosh(60\pi^2/Z_0\sqrt{\epsilon_{eff}})}) \tag{5.19}$$

Taking into account the characteristic dimensions of our circuit, it gives $L_{sh} \sim 100$ pH and $l_{sh} = 250\ \mu$m. These values have little influence on the measured signals. However, as we would like to measure superconducting materials with impedance lower than 100 pH, it needs to be taken into account in this case to correct our raw data, as we will see in section 5.5.

5.3.4 Rotation mechanism

To be able to address the different lines, we fabricated the rotating device presented figure 5.16. Different elements had to been taken into account to design it:

- **The rotation** : the rotation is provided by a drive shaft, a stainless tube going in straight line from room temperature to the device, ended by gears. The operator can manually rotate the drive shaft outside the cryostat. The rotation is then transmitted through the gears to a copper rotating axis through which runs a microwave cable.
- The **incoming fixed microwave cable has to be adapted to the cable running within the rotating axis** and to the dial lines. A slide-on connector [20] ensures the connection between the fixed microwave cable and the rotating one. Moreover, the transition between the rotating cable with the dial is made through a right-angle SMP-connector.

19. The approximation of a CPW line instead of a CBCPW line can be done as the gap is small compared to the distance from the metallic back ground plane.
20. Made with a 21 MMPX-50-2-1/111 NE and a 11 MMPX-50-2-1/111 NE connector.

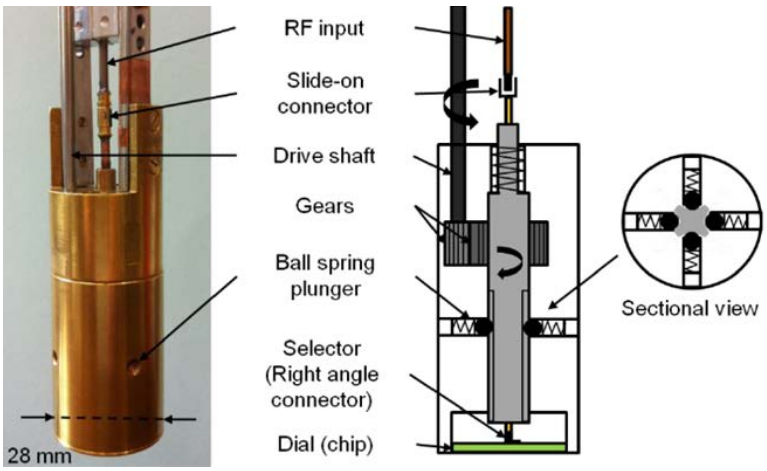

Figure 5.16: Picture of the device allowing the selection of the lines. (b) Schematic representation of the device. Picture from [Diener et al., 2014].

– **The positions of the lines** on the dial should be easy to find : 4 groove slides at 90 ° from each other have been drilled on the rotating axis, determining 4 positions which are locked by ball spring plungers. They define four pre-determined positions corresponding to the different lines.

Moreover, **a good contact between the right-angle connector and the dial lines is of primary importance**. Indeed, due to differential thermal contraction of the different materials composing the lines and the cryostat, a loss of contact can occur. This has been one of the main problems faced during the development of this device. It has been addressed by using springs, forcing the right-angle connector to contact the lines. In addition, a flexible coaxial cable have been added at approximately mid-length of the cryostat, to reduce the rigidity of the incoming cables and allow a little mechanical freedom, thus reducing constraints due to thermal contractions of the RF lines on both the slide-on connector and the setup presented figure 5.16.

5.3.5 Validation of the calibration procedure on a resistor

In order to validate the calibration device, we have tested it at room and cryogenic temperatures, the sample then being a 200 Ω dead resistor. These tests have been perform on a non-final prototype which is slightly different from the one presented section 5.3: the lines have slightly different geometry and the bias-Tee was not included. It therefore does not fully represent the performances found with the definitive calibration chip, which will be discussed in section 5.5. However, it provides a first proof-of-principle.

In this subsection, we will :
– Compare the measurement of the bare calibration points with what is expected.
– Validate the calibration procedure on a 200 Ω dead resistor.

5.3.5.1 Measurement of the reflection coefficients of the different standards

Let us first recall what is expected in the case of perfect calibrations points (summarized in table 5.1). The reflected signal is given by $\Gamma = \frac{Z-Z_0}{Z+Z_0} = |\Gamma|e^{i\theta}$. The phase is therefore defined by $\theta = \frac{180}{\pi} Arg(\Gamma)$ and the attenuation (in dB) by $20Log|\Gamma|$. Therefore, the Short and the Open should give rise to perfect reflections (Γ =1) with respectively, an in-phase and 180 °out-of-phase signal. For the load (50 Ω resistor), as all the incoming signal is absorbed by the resistor, $\Gamma = 0$ and the phase is not defined.

These references have been measured both at room and low temperature (4 K). As the difference between the two measurements is mostly due to a modification of the attenuation of the lines, only the room temperature measurements will be analysed here [21].

21. The differences between the 2 spectra - at room temperature and 4 K - are mainly due to a lower dissipation due to a reduced influence of the skin effect. This also translates into a slight shift in frequency for the oscillations due to impedance mismatches.

Standard	Impedance	$\|\Gamma_{ref}\|$	Attenuation (dB)	θ (°)
Open	∞	1	0	0
Short	0	1	0	180
Load	$Z_0 = 50\,\Omega$	0	$-\infty$	not defined

Table 5.1: Standard references, as well as their impedance, reflection coefficient Γ and corresponding attenuation and phase.

We connected the calibration device directly to the VNA through using coaxial cables as represented figure 5.18. The selection of the reference points or the 200 Ω resistor is driven from the outside of the cryostat.

The raw reflectometry measurements of the different reference points (Open, Short, Load) using the calibration device, as well as the 200 Ω dead resistor, are presented figure 5.17. The phase shift due to propagation has been compensated prior to the measurement by a delay of $\sim$ 10.1 ns, identical for each measurement and corresponding to the effective cable length [22].
The **Short** and the **Open** (figure 5.17.a. and b.) have a near perfect reflection at low frequency. At higher frequency, the signal is attenuated due to skin effect. The obtained phase is flat in frequency. The visible oscillations in both the attenuation and phase are linked to imperfections of the propagation line (see 5.2.2).
The measurement of the **Load** gives an attenuation of about {-30, -35} dB when $f \to 0$, corresponding to a resistance of (52.5 ± 1) Ω, close to the measured DC value (50 ± 1 Ω obtained through a 2 probes measurement). In theory, $Z = 50\,\Omega$ should gives $|\Gamma| \to -\infty$. Experimentally, this is not the case, due to impedance mismatches along the line (upstream the load) which induce parasitic reflections. Measuring the load enables to quantify the setup directivity - i.e. to quantify E_D - (see section 5.2.3.2).
The **dead resistor** should give an attenuation of $20Log(|\frac{200-50}{200+50}|) \sim -4.5$ dB, close to the measured value at low frequency. As $\Gamma > 0$, the phase should be equal to 0, as observed (0 ± 20° [23]).
As for the short and the load, additional dissipation at finite frequency is due to skin effect and oscillations to imperfections of the line.

5.3.5.2 Calibration of the resistor

We applied the calibration procedure detailed in section 5.2.3.1 to test it and to retrieve the value of the 200 Ω dead resistor.

We present figure 5.19 both the measured signal and the signal obtained through calibration [24]. We notice that :
- Attenuation due to propagation through the coaxial cables (skin effect) and the dial lines is corrected.
- The oscillations due to the multiple impedance mismatches along the lines are also suppressed.

The retrieved signal is almost frequency-independent, with small variations at frequencies higher than 1.3 GHz.

One can now find back the impedance by inverting equation 5.2, giving :

$$Z = -Z_0 \frac{\Gamma + 1}{\Gamma - 1} \tag{5.20}$$

By doing so, we obtain figure 5.20. We indeed find the DC value of the resistor (200 Ω) in a range of 10 MHz to 1.3 GHz, within a precision of better than 10 %, and better than 20 % at frequencies up to 2 GHz. At higher frequencies (not shown) the response of the system is more hazardous, possibly due to resonances within the calibrator volume. Indeed, due to the size of the calibrator (typically $\sim$ 2.6 cm), resonances due to eigenmodes of the box are expected close to $f = 2$ GHz [25].

22. $\sim$ 2 meters in the specific case of this experiment.
23. The large uncertainty is due to oscillations because of multiple impedance mismatches.
24. For this calibration, L_{sh} has been taken into account.
25. $\sim$ 1.8 GHz in TMM10i and $\sim$ 5.8 GHz in liquid He or air, by taking into account that $\epsilon_{He} \sim \epsilon_{vaccum} = 1$.

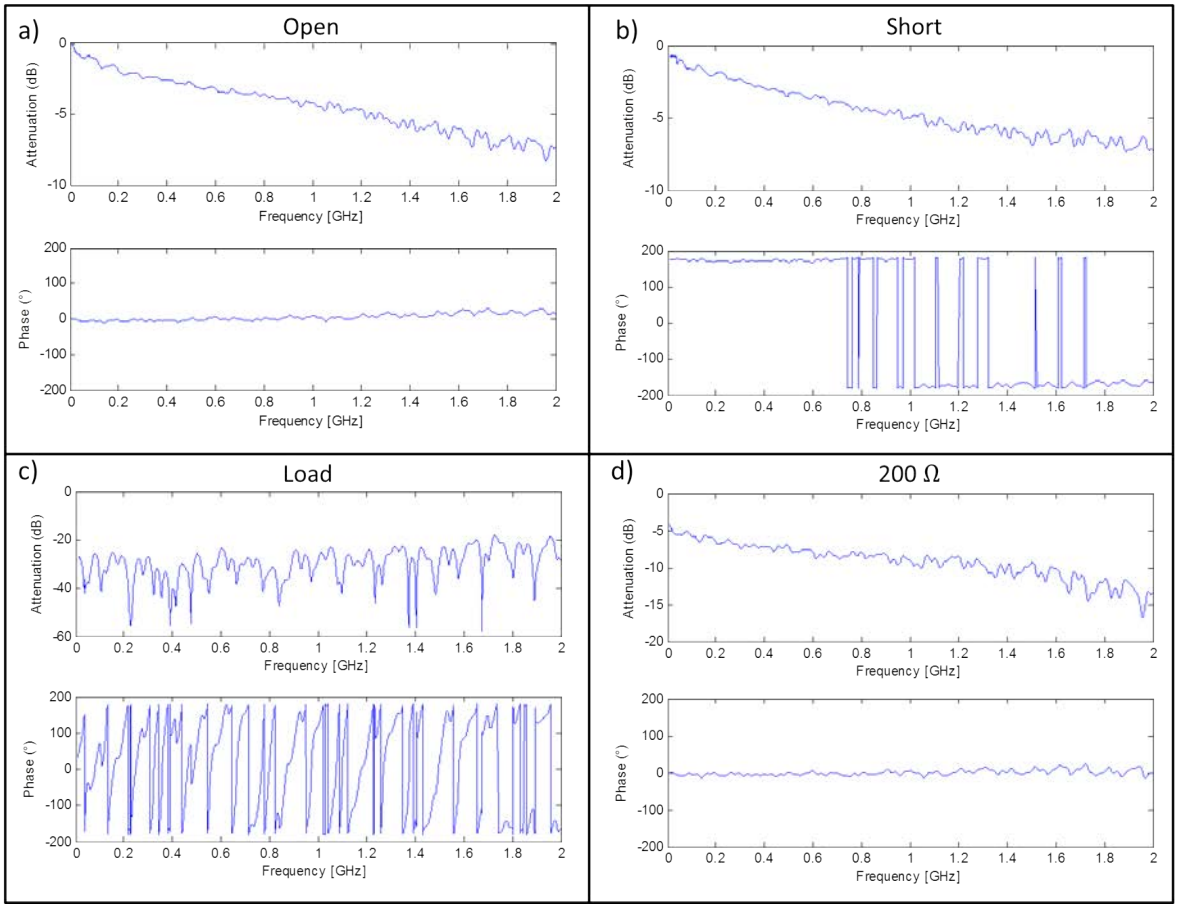

Figure 5.17: Attenuations and phase shifts obtained through the measurement of the reflection coefficients for the Open (a), the Short (b), the Load (c) standards, as well as for a 200 Ω resistor (d).

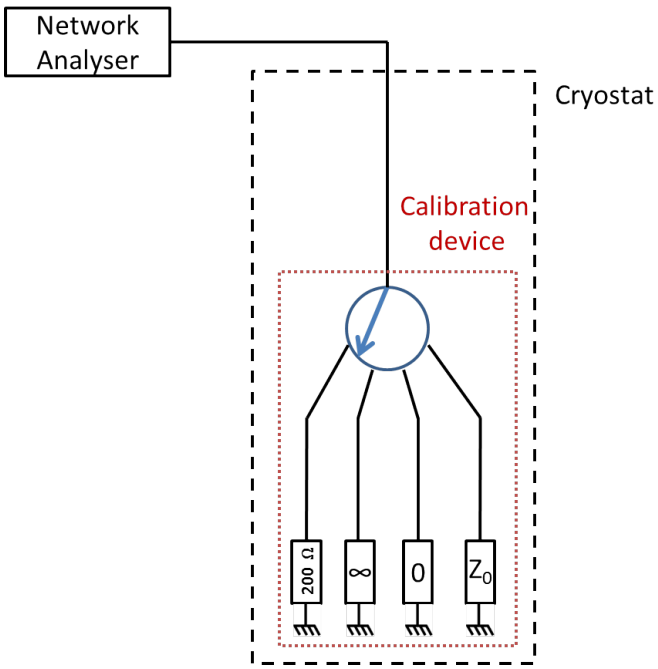

Figure 5.18: Schematic representation of the setup used to calibrate the 200 Ω resistor.

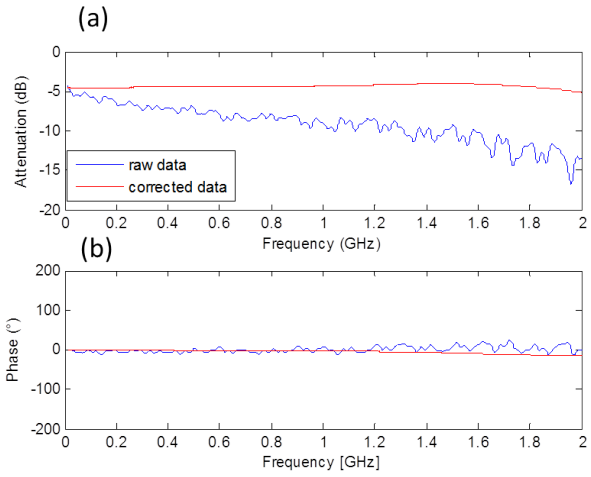

Figure 5.19: Attenuation (a) and phase (b) of the reflected signal of the 200 Ω resistor without (blue) and with (red) applying the calibration procedure.

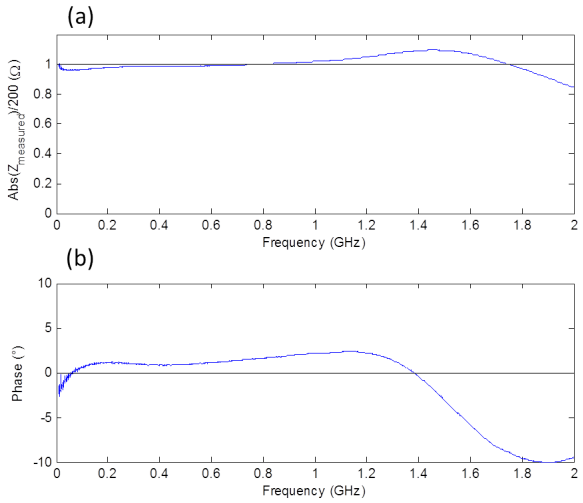

Figure 5.20: Calibrated impedance $|Z|$ (a) and phase (b) obtained through the calibration of a 200 Ω dead resistor.

The developed calibration procedure can therefore be used to find back the impedance of samples in reflectometry measurements. With this first prototype, we indeed were able to measure a 200 Ω dead resistor with a precision on the measured resistance of the order of 10 to 20 %. This proves the feasibility of such a calibration device. The design tested here has then been improved to measure superconducting samples.

5.4 Sample selection

The above-described calibration device has been designed in order to work at cryogenic temperatures (T<4 K). In order to test it, we therefore wanted to probe samples with an important variation of resistance as a function of the temperature (for $T < 4$ K) to test the limits of the apparatus on a single sample. Superconducting materials therefore seemed to be good candidates for such a test.

In this section we will :

- Explain how the material for the test has been selected.
- Show how we tuned the properties of the film to meet our requirements for the test.
- Compare the D.C. properties of the chosen films with the literature.

5.4.1 Possibles candidates

Good candidates to validate the calibration device had to meet the following criteria :

1. The films should be **easily synthesized** with conventional evaporation techniques.
2. The films needed to be **continuous** at the probed thicknesses.
3. They should be superconducting of **BCS weak-coupling** type to avoid corrections due to strong coupling.
4. The **critical temperature** should be such that $2<T_c<4.2$ K to be easily measurable in a ^{4}He cryostat with a large enough range in temperature.
5. The thickness of the films should be such that the electric field penetrates all the sample, i.e. $\lambda_L < d_\perp$, to avoid skin effect.

A list of candidates is presented in the following table : [Ashcroft and Mermin, 1976, Kittel, 1986]

Compound	Tc (K)	$2\Delta/k_BT_c$	Screening length $\lambda_L = \sqrt{\frac{m^*}{n\mu_0 e^2}}$ (Å)
Al	1.2	3.4	160
In	3.40	3.6	220
Nb	9.3	3.8	390
Pb	7.2	4.3	370
Sn	3.7	3.5	340
V	5.4	3.4	530

In order to meet the above criteria, Nb and Pb have been excluded due to their strong coupling. Similarly, In and Sn have been excluded due to small λ_L compared to the film continuity threshold in these materials. **Aluminum samples** seemed to be good candidates, with a T_c that could be enhanced by decreasing the thickness contrary to most other materials and regarding the fact that Al films had already been measured in the GHz range [Steinberg et al., 2008]. We actually performed some preliminary tests with this compound, but it turned out that a very large capacitance appeared between the film and the microwave lines, due to Aluminum-oxide forming at the surface of the sample. This complicated the interpretation of the experimental data and implied the modelling of the electrodynamic response of the oxide layer. In addition, the allowed range in temperature was limited by the T_c of the measured samples, ranging from 1.5 to 1.7 K [26]. We therefore abandoned this lead.

Vanadium films seemed to be good candidates for the considered test as they possess a high enough critical temperature, a weak-coupling superconductivity and a large penetration depth, allowing the electric field to penetrate in the sample. Moreover, it is not so sensitive to oxidation, so that parasitic capacitance effects due to films oxidation could hopefully be avoided.

5.4.2 Superconductivity in Vanadium, probed by low frequency techniques

According to London's penetration depth, any vanadium sample of thickness lower than 500 Å should be a good candidate for microwave measurements. However, the critical temperature for bulk samples is too high to be comfortably used in a ^{4}He cryostat. Furthermore, the resistivity of vanadium is of the order of $\rho_V \sim 4\mu\Omega.cm$, giving a resistance of less than 1 Ω for 500 Å-thick films with the considered film geometry. A value closer to 50 Ω would be preferable to have a good sensitivity, at least in the normal state, and measure the evolution and precision on the evolution of the resistivity as a function of the temperature when the film becomes superconducting. We were therefore interested in modifying the properties [27] of Vanadium films by using the thickness as an experimental knob.

In this subsection, we will see :
– How the films are synthesized.
– How the properties of V are modified by thickness effects.
– How the samples for the calibrator validation have been selected.

26. Obtained by thickness effects.
27. Both the low temperature normal state resistance R_n and T_c.

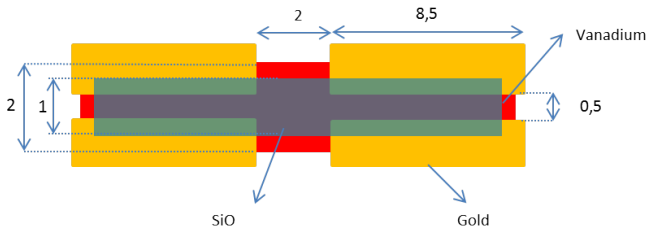

Figure 5.21: Schematic representation of a Vanadium sample.

5.4.2.1 Sample fabrication

All Vanadium samples presented below have been synthesized by e-beam deposition under ultra-high vacuum [28]. The deposition chamber used is similar to the one described section 2.2.1.1.

The deposition sequence is described below :

Compound	Thickness (Å)
SiO	250
V	53 to 406
Au	2000
SiO	250

The vanadium film is deposited onto a silicon substrate covered by a 250 Å-thick SiO coating layer in order to reduce the roughness of the surface. We then use shadow masks to define the geometry of the sample and evaporate Vanadium of the desired thickness, followed by 2000 Å-thick Gold pads for electrical contacts [29]. In reflectometry measurements, the gold pads will enable a good contact between the microwave lines and the flip-chipped sample. A protective 250 Å-thick over-layer of SiO is then evaporated without breaking the vacuum, to prevent the oxidation of the layer. The final geometry is presented figure 5.21.

5.4.2.2 Evolution of the properties of Vanadium films with the film thickness

As we have seen, in order to be used for the validation of the calibration device, vanadium superconducting properties had to be tuned. We therefore seized this opportunity to undertake a preliminary study on the suppression of superconductivity in vanadium thin films, due to a thickness reduction. We therefore synthesized three batches of vanadium films (9 films in total) of thicknesses ranging from 50 to 400 Å of which we studied DC transport characteristics at low temperature.

Transport measurements were carried out using a pumped-^{4}He cryostat, having a base temperature of the order of 1 K, and by using standard low-frequency lock-in techniques with 4 probes-measurements. Measurements have been carried out by applying a low enough polarisation to avoid heating in the normal state and, when superconducting, to be below the critical current. The temperature of the samples is measured by a calibrated Cernox thermistor thermally anchored to the sample holder.

The characterisation of our samples in the normal state as well as their superconducting properties will be detailed below.

The normal state

The characteristics of the different evaporated samples are presented in the table below :

28. With a pressure between 1 and 2×10^{-8} mbar during deposition.
29. This geometry defines 500 μm-long Vanadium strips between the Au pads for RF measurements : the length of Vanadium strips is longer than the gap designed on the calibration device (200 μm) in order to avoid alignment problems.

Batch	Thickness (Å)	R_{300K} (Ω)	ρ_{300K} ($\mu\Omega.cm$)	R_n (Ω)	ρ_n ($\mu\Omega.cm$)
VHRF01	400	6.5	26.0	0.78	3.1
VHRF01	300	9.25	27.7	1.29	3.9
VHRF01	200	14.48	29.0	2.9	5.8
VHRF02	150	19.72	29.6	4.55	6.82
VHRF02	120	26.43	31.7	6.72	8.1
VHRF02	100	34.84	34.8	10.38	10.4
VHRF04	83	42.78	35.5	15.41	12.8
VHRF04	67	57.93	38.8	23.27	15.56
VHRF04	53	80.23	42.5	37.42	19.8

Table 5.2: Thickness, resistance and resistivity (taken at 300 K and 6 K) of the Vanadium films grown for this study,

The resistivities measured in our films are comparable to those found in the literature : at 300 K, $\rho_{300K} \simeq 26-30$ $\mu\Omega$.cm and at low temperature (6 K), $\rho_n \simeq 3-5$ $\mu\Omega$.cm [30]. From these values, the mean-free path time can be estimated via a simple Drude model, using $n \simeq 5\times10^{28}$ m^{-3} [Reale, 1970, Foner, 1957, Laulajainen et al., 2006, Tsai et al., 1981] and the fact that the effective mass m^* is about 10 times the electron mass [Radebaugh and Keesom, 1966]: $\tau = \frac{m^*}{ne^2\rho_{300K}} \simeq 2-3\times10^{-14}$ s for the thickest film. Since the Fermi velocity is of the order of $v_F \simeq 1.8\times10^5$ m.s^{-1}[Gutsche et al., 1994, Williamson, 1970, Sekula and Kernohan, 1972, Moser et al., 1982], this corresponds to an estimate for the mean free path of $l \simeq 40$ Å, comparable to what has been found in similarly grown Vanadium films [Kuzmenko et al., 1978, Teplov et al., 1976, Reale, 1970, Alekseevskii et al., 1976].

Through Matthiessen's rule (see section 1.2.2), the phonon resistivity at 300 K can be estimated as $\rho_{300K} - \rho_n = \rho_{ph}(300K) - \rho_{ph}(6K) \simeq \rho_{ph}(300K) \simeq 23 \pm 1$ $\mu\Omega$.cm (cf table 5.2). This value is compatible with what had been found by Teplov et al. [Teplov et al., 1976].

The sharp increase of the low temperature resistivity for thinner films cannot be explained only by geometry effects. However, they can be accounted for by the Fuchs-Sondheimer law (see section 1.7.1) which takes into account isotropic electron scattering, and both surface and grain-boundary scattering in the case of polycrystalline films. ρ_n is then expected to vary as $1/d$, which is indeed the case, as shown figure 5.22.

All these considerations lead us to think that **our Vanadium films are of comparable quality to the polycrystalline films reported in the literature.** Since no particular precaution was taken during the film deposition (the substrate has not been cooled down), and as is confirmed by the values of the resistivities, it is highly unlikely that our films are either monocrystalline - in which case the resistivity would be of the order of 1 $\mu\Omega$.cm [Gutsche et al., 1994, Laulajainen et al., 2006] - or amorphous - in which case the awaited resistivity is of about 200 $\mu\Omega$.cm [Kuzmenko et al., 1978].

The superconducting state

The R(T) characteristics for the different films are shown figure 5.23. All measured films are superconducting. As expected for disordered films, as $d_\perp$ decreases, the normal sheet resistance is increasing and the critical temperature T_c decreases. The evolution of the critical temperature as a function of the film thickness is presented figure 5.24. T_c have values ranging from 1.56 to 4.9 K and evolve as $1/d_\perp$. As is usual for **homogeneous films** [Gantmakher and Dolgopolov, 2010], all superconducting transitions are sharp and parallel to one another, and no sign of reentrance is observed.

T_c evolves as accounted for by Simonin's model, which takes into account the increasing influence of surfaces in thin films (see section 1.7.1 for details) :

$$T_c = T_{c0}(1 - \frac{d_m}{d_\perp}) \tag{5.21}$$

30. In Teplov et al. [Teplov et al., 1976], $\rho_{300K} \sim 25$ $\mu\Omega$.cm and $\rho_n \sim 4$ $\mu\Omega$.cm for thick polycrystalline films.

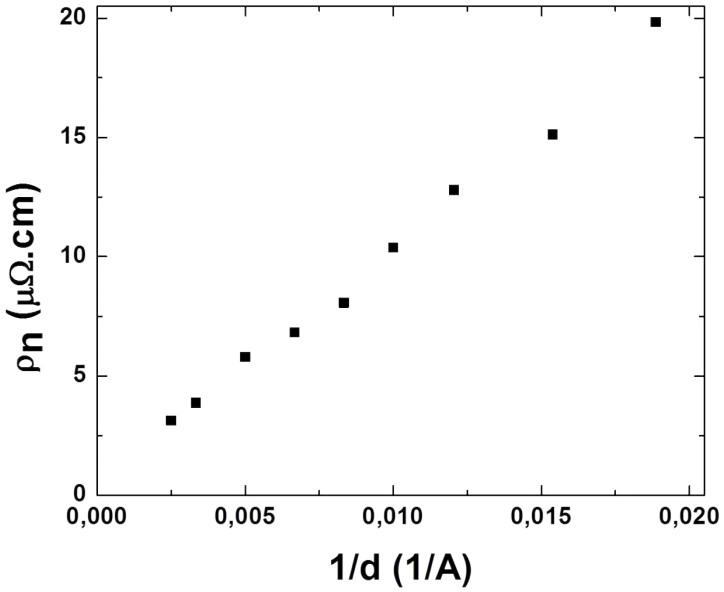

Figure 5.22: Low temperature (6 K) resistivity of Vanadium thin films ρ_n as a function of $1/\mathrm{d}_\perp$. ρ_n varies linearly as accounted for by Fuchs-Sondheimer model.

where T_{c0} is the bulk value of the superconducting critical temperature and d_m is the critical thickness at which superconductivity is destroyed.
By applying equation 5.21 with $T_{c0} \sim 5.4$ K, close to the tabulated value [McMillan, 1968, Ashcroft and Mermin, 1976], one finds $d_m = (3.7 \pm 0.5)$ nm. This minimum thickness for the existence of superconductivity in vanadium thin films is model-independent and is relatively large as far as elemental superconductors are concerned. Indeed, although any interpretation of this effect is beyond the scope of this thesis, it is noteworthy that, if $d_m \simeq 52$ Å for Aluminum, $d_m \simeq 41$ Å for Indium and $d_m \simeq 37$ Å for Lead [Jaeger et al., 1989], elemental superconductors such as Beryllium, Bismuth, Gallium, Molybdenum, Niobium or Tantalum have critical thicknesses of the order of a few angströms, 1 nm at most.

Another way to interpret the effects of a thickness modification on the critical temperature is to consider the change in screening it induces and its influence on superconductivity, as performed in Finkelstein's fermionic model (see section 1.7.3.1.b). In this case, T_c is driven by the variation of the sheet resistance as :

$$\frac{T_c}{T_{c0}} = exp(-\frac{1}{\gamma})[(1 + \frac{\sqrt{t/2}}{\gamma - t/4})(1 - \frac{\sqrt{t/2}}{\gamma - t/4})^{-1}]^{1/\sqrt{2t}} \tag{5.22}$$

with $\gamma = 1/ln(k_B T_{c0}\tau/\hbar)$ and the renormalized sheet resistance $t = R_n e^2/(2\pi^2\hbar)$. For the theory to be valid, the system has to be morphologically homogeneous and such that $5 < -\frac{1}{\gamma} < 10$.
In our case, it would be possible to qualitatively describe our data with such a law, assuming that $\tau \sim 1 \times 10^{-22}$ s (figure 5.25), corresponding to a mean free path of $\sim 2 \times 10^{-17}$ m, well below the inter-atomic distance. This value is therefore highly unlikely. In term of γ, it gives $-\frac{1}{\gamma} \sim 20$, out of the validity limit of Finkelstein's model.

Both Simonin and Finkelstein's models agree qualitatively with our experimental data on the destruction of superconductivity in Vanadium films. Short of any definitive conclusion, let us just say that we are out of the validity range for Finkelstein's model. Whether Simonin's model should hence be favoured is a question that needs to be addressed in a later work.

5.4.2.3 Comparison with the bibliography

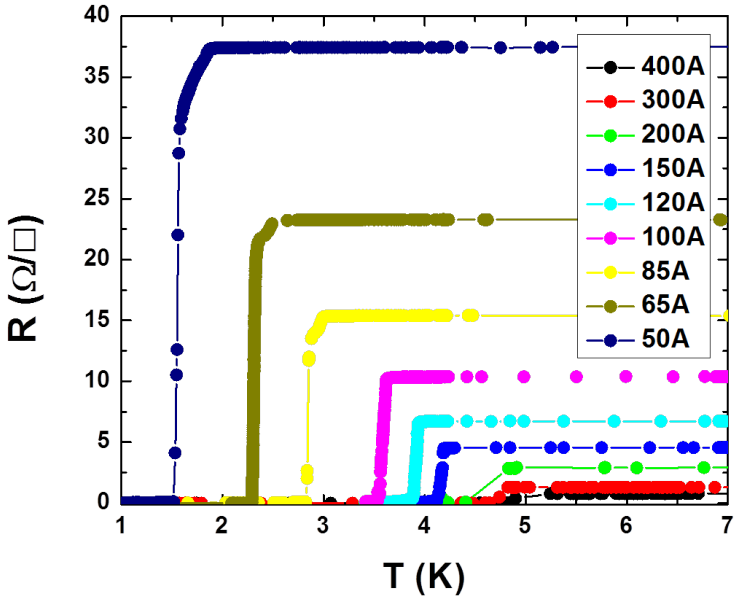

Figure 5.23: Sheet resistance R as a function of temperature for the Vanadium thin films.

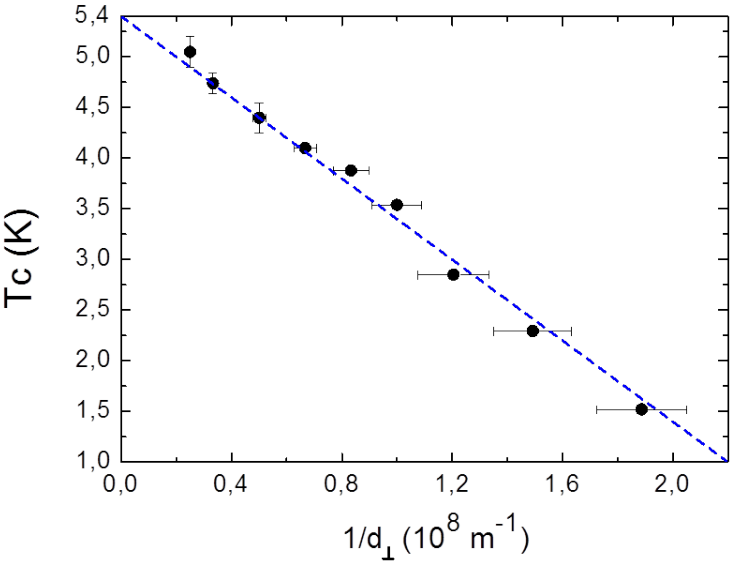

Figure 5.24: Variation of the superconducting critical temperature T_c of Vanadium thin films of different thicknesses. In blue, fit of the data with $T_c(d_\perp) = 5.4 - \frac{2\times10^{-8}}{d_\perp}$.

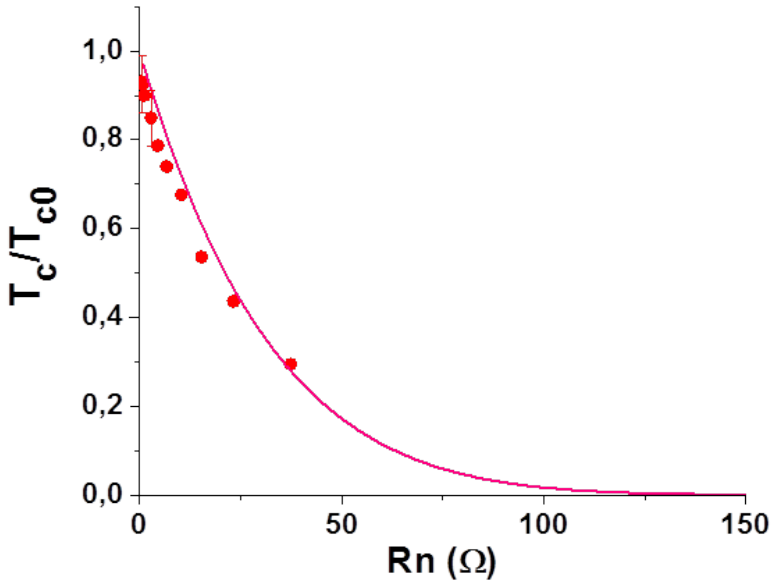

Figure 5.25: Variation of the renormalized superconducting critical temperature T_c/T_{c0} (T_{c0} = 5.3 K) of Vanadium thin films as a function of the sheet resistance R_n. The thick line corresponds to a fit using Finkelstein's equation (equation 5.22) with $\tau = 1 \times 10^{-22}$ s.

The evolution of T_c with the film thickness in Vanadium has been studied exhaustively in the literature [Alekseevskii et al., 1976, Gutsche et al., 1994, Kuz'menko et al., 1975, Kuzmenko et al., 1978, Teplov et al., 1976, Teplov and Mikheeva, 1980]. However, although some authors had pointed out to differences between amorphous and polycrystalline films [Kuz'menko et al., 1975, Kuzmenko et al., 1978], we are not aware of a systematic study on the influence of the structure, and therefore on the nature of disorder, on the destruction of superconductivity in this material.

In order to evaluate the influence of the nature of disorder (here the film structure) on the destruction of superconductivity, we have compiled experimental data available in the literature. The corresponding graph is given figure 5.26. From this plot, there is a clear distinction between crystalline and polycrystalline films on the one hand, and amorphous films on the other. Both have T_c evolving as $\frac{1}{d_\perp}$. However, the bulk values of the superconducting critical temperature, which can be estimated by taking the $\frac{1}{d_\perp} \to 0$ limit, are very different. For mono- or poly-crystalline films, $T_{c,bulk} \simeq 5.4$ K. A contrario, in amorphous films, $T_{c,bulk} \sim 3$ K. This can be related to the fact that Vanadium has its Fermi energy at a maximum of the density-of-states (DOS). In amorphous films, disorder smears the sharp features in the DOS (see section 1.4.1) which, in this case, is lessened, giving rise to a smaller T_{c0} [Crow et al., 1969].
Moreover, the rate at which T_c decreases with $1/d_\perp$ is slower for amorphous films, resulting in a lower critical thickness ($d_m \sim 21$ Å) than in (poly-)crystalline vanadium ($d_m \sim 31$ Å).

One can wonder what happens if we take the normal sheet resistance as a measurement of disorder, as usually performed for thin films. The corresponding evolution is represented figure 5.27. As can be seen, R_n, despite the commonly accepted picture, is not a good parameter to account for the destruction of superconductivity in disordered films [31] : amorphous films and (poly-)crystalline films do not fall on the same trend for $T_c(R_n)$.
In the case of amorphous films, the transition can be described within the framework of Finkelstein's theory. Indeed, we find for amorphous films $\tau \sim 1 \times 10^{-15}$ s, giving $-\frac{1}{\gamma} \sim 7$, within the validity range of the theory. Contrary to what has been found for poly-crystalline films, Finkelstein's model could well explain the $T_c(R_n)$ evolution in amorphous films.

The criterion for the applicability of Finkelstein's theory can be questioned. Indeed, it is

31. The problem of linking R_n with disorder for films of different thicknesses has already been observed in a-Nb_xSi_{1-x} thin films, as reported section 2.3.3.3.

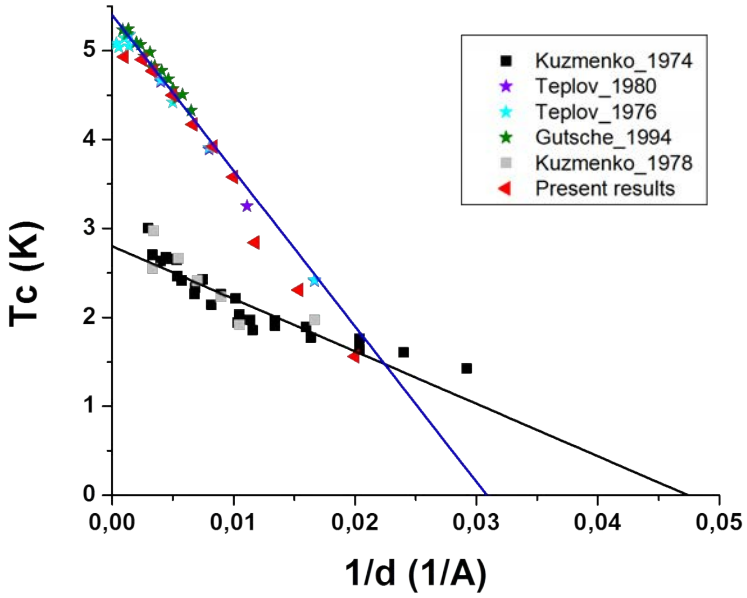

Figure 5.26: Variation of the superconducting critical temperature T_c in Vanadium thin films as a function of $1/d_\perp$.

striking that $T_c(R_n)$ can, in both cases (amorphous and (poly-)crystalline), be qualitatively described by equation 5.22 . One can therefore wonder whether, in the (poly-)crystalline case for instance, the identification of τ with the mean free path time is correct, or, if the existence of crystallites would introduce a renormalization of this parameter. We can however conclude on the fact that the microscopic nature of disorder is important to describe the destruction of superconductivity, at least in this material. It has been indeed found to be dependent on the morphology, even though theories usually predict a similar mechanism for the destruction of superconductivity in all homogeneously disordered films (i.e. amorphous and (poly-)crystalline, see section 1.7).

5.4.2.4 RF sample

To select a suitable sample for RF measurements, we saw that two things had to be taken into account :

- The sample needs to have a T_c in the range easily accessible with our ^{4}He test cryostat.
- As we will measure the reflection of a microwave signal, the impedance of the sample needs to be as close as possible to 50 Ω, for a maximum sensitivity.

Several samples meet these criteria, as can be seen figure 5.28, where they correspond to those enclosed in the green region. Their properties have been summarized in the following table :

Batch	Thickness (Å)	R_n (Ω)	$T_c\,(K)$
VHRF02	120	6.72	3.92
VHRF02	100	10.38	3.58
VHRF04	83	15.41	2.84
VHRF04	67	23.27	2.31

The samples of interest have sheet resistances ranging from 6.7 to 23.2 Ω and T_c varying from 2.31 to 3.92 K. We favored the measurement of one of the thickest ones (100 Å-thick), as it allowed to have a larger range in temperature where the superconducting properties of the film could be measured before attaining our cryostat base temperature.

For microwave measurements, the samples shown figure 5.21 have been scribed with a diamond tip in order to fit within the calibration device. The corresponding sample design is then

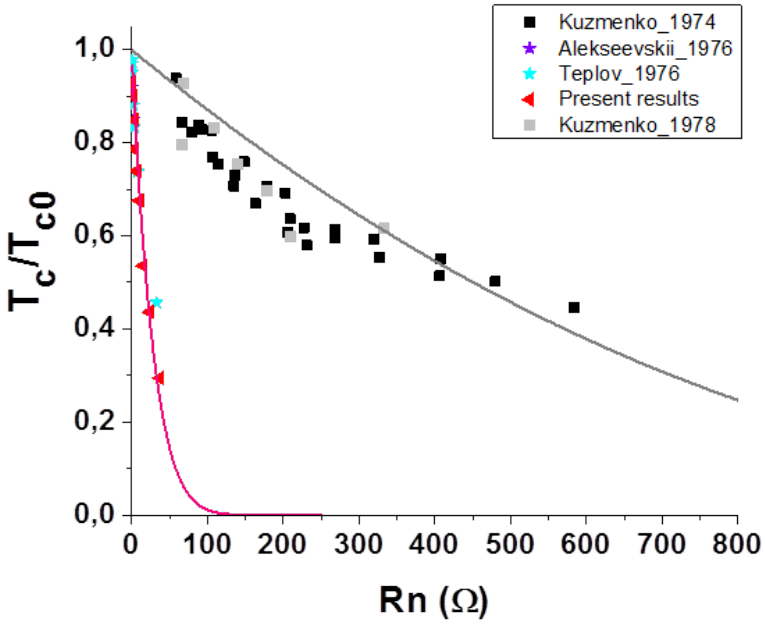

Figure 5.27: Variation of the renormalized superconducting critical temperature T_c/T_{c0} (T_{c0} = 5.3 K for (poly-)cristallyne films and T_{c0} = 3.2 K for amorphous films) in Vanadium thin films as a function of the sheet resistance R_n. The thick lines correspond to fits using Finkelstein's equation (equation 5.22) with $\tau = 1\times10^{-22}$ s (in pink) or $\tau = 1.5\times10^{-15}$ s (in grey), respectively for (poly-)crystalline films and amorphous films.

schematically shown figure 5.28. Let us now examine how these films respond to a microwave excitation.

5.5 Microwave measurement of a Vanadium film

In this section, we will present the high frequency measurement of the 100 Å-thick Vanadium sample. The sample has been put in contact with the measurement line using a flip-chip technique (presented figure 5.30) : the pre-designed sample is directly connected to the measurement line. A PVC strip allows to maintain and press it onto the lines to ensure good electrical contact (see figure 5.12.b.).

During these measurements, we simultaneously measured the high frequency response of the sample and its low-frequency resistance (see figure 5.31):

- The high frequency measurement is provided by a $R\&S^{®}$ ZVA network analyser. The rotation mechanism presented in section 5.3.4 allows to measure successively the different references and the sample. To avoid heating the sample by the noise incoming from the network analyser, 30 dB attenuation has been added along the lines as pictured figure 5.32. By using the internal coupler of the instrument, we avoid any attenuation of the reflected signal during the measurement.
- The low-frequency resistance measurement is performed through the bias-Tee by conventional lock-in techniques [32]. The measurement was of 4-probes type down to the bias-Tee [33]. It was performed at an excitation, given by the lock-in voltage output and the polarisation resistance R_{pola} (typically 1 MΩ), of the order of 1 to 10 μA to avoid heating the film.

In the following, we will :

- Give the awaited response (computed via Mattis-Bardeen equations) of a superconducting film in our experimental conditions as the superconducting transition is crossed.
- Observe the effects of the calibration performed at liquid Helium temperature on the sample.

32. We used a SR560 lock-in amplifier.
33. The bias-Tee induces an additive measured resistance of $\sim 2\ \Omega$ at 300 K and $< 0.1\,\Omega$ at 4 K.

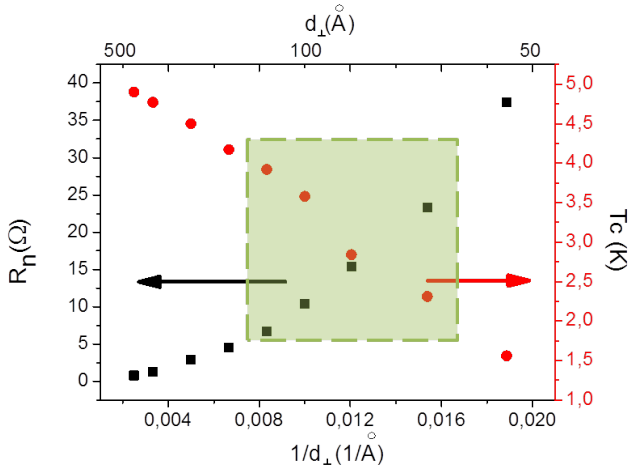

Figure 5.28: R_n and T_c as a function of $1/d_\perp$ in the Vanadium thin films. The green region indicates the suitable samples for microwave measurements.

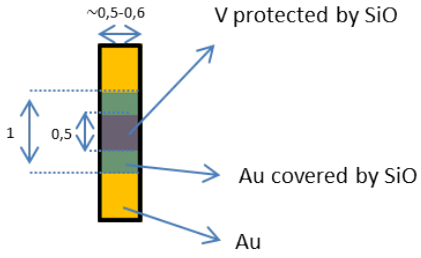

Figure 5.29: Geometry of Vanadium samples probed by microwave measurements.

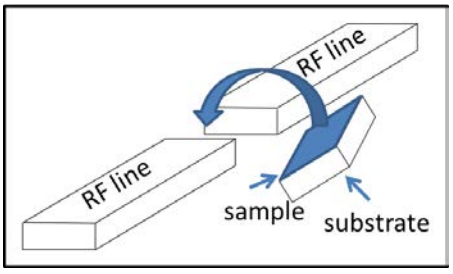

Figure 5.30: Illustration of the flip-chip technique to place the sample between the microwave lines. One is the incoming line. The other is connected to the ground.

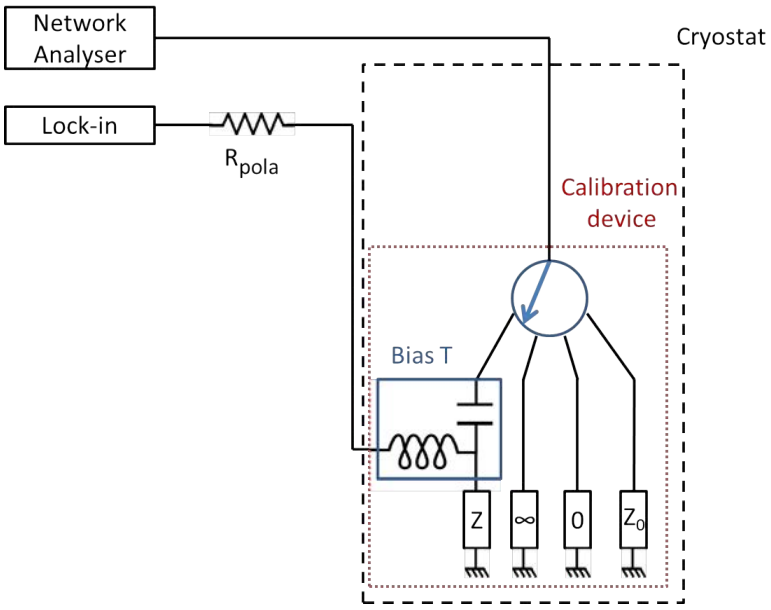

Figure 5.31: Illustration of the measurement setup used to perform both low frequency and high frequency measurements of the sample of impedance Z.

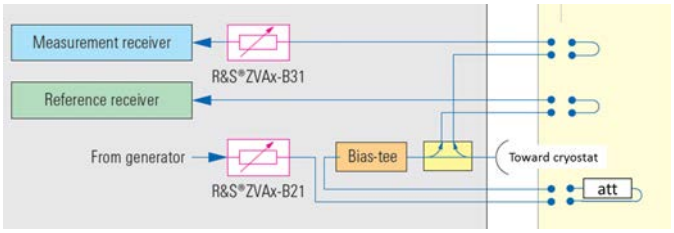

Figure 5.32: Insertion of the attenuator needed to perform RF measurements without heating the superconducting films. The attenuator was placed upstream the directional coupler of the ZVA such that it does not attenuate the reflected signal. As it also is upstream the reference measurement, it has no incidence on the measured attenuation. Adapted from the user guide of the ZVA Network Analyser. Source : https://www.rohde-schwarz.com/.

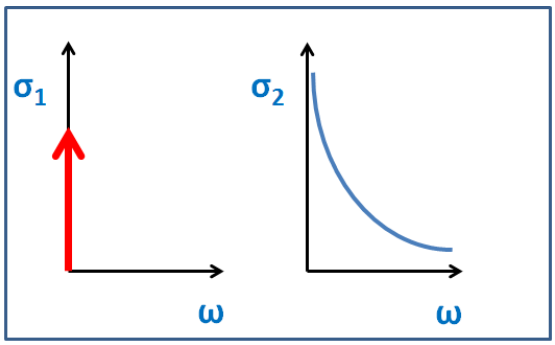

Figure 5.33: $\sigma_1(T=0,\omega)$ and $\sigma_2(T=0,\omega)$ at frequencies $\omega << \Delta_0$. At $T=0$, $\sigma_1(T=0,\omega)$ is described by a δ function and $\sigma_2(T=0,\omega) = -\frac{1}{L_{k0}\omega}$.

– Determine the RF response of the sample as a function of the temperature and frequency, and interpret the corresponding results.

5.5.1 Mattis-Bardeen Predictions

We saw in section 5.4.2.4 that the probed Vanadium film has a superconducting transition with $T_c \sim 3.6$ K. Such system can be described at low temperature by a 2 fluid model but this model cannot describe the data near the transition, and in particular does not predict the coherence peaks. To explain such an effect, one needs to consider Mattis-Bardeen theory (see section 4.2). In the specific case of our film, the probed frequencies are ranging from 10 MHz to 2 GHz. Converted in units of Δ_0, the zero temperature gap , it gives f=[0.0019,0.015]Δ_0, and should therefore not induce pair breaking.

Let us recall what is expected in the case of the probed sample. At zero temperature, following BCS theory, we expect a kinetic inductance of :

$$L_{k0} = \frac{\hbar R_n}{\pi \Delta_0} \sim 5\,pH \tag{5.23}$$

where $R_n \sim 13.5\,\Omega$ is the resistance of the film in the normal state. One can also evaluate L_{k0} using London theory :

$$L_{k0} = \frac{m^*}{n_s e^2} \sim 1.5\,pH \tag{5.24}$$

with $n_s \sim \frac{n}{2} \times d_\perp = 2.5 \times 10^{20}\,m^{-2}$ and $m^* = 10 m_e$ (see section 5.4.2.2). The two values are therefore in rough agreement with each other. We will, in the following, take the value obtained through BCS theory ($L_k \sim 5$ pH) as a reference.
The expected electrodynamic response at $T=0$ is plotted schematically figure 5.33. The quasi-particles are all condensed in a δ peak at zero frequency, giving rise to $Re(\sigma) = \sigma_1 \propto \delta(T)$. On the other hand, the inertial response of Cooper pairs gives rise to a response $Im(\sigma) = -\sigma_2 = \frac{1}{L_{k0}\omega}$. At higher temperature, the electrodynamic response of the sample is given by Mattis-Bardeen theory. The awaited response as a function of both temperature and frequency is plotted figure 5.34 for the probed sample, in the frequency range probed in this experiment.

5.5.2 First calibration

5.5.2.1 Normal state

The raw reflection signal for the 100 Å-thick Vanadium film is given figure 5.35 (blue curve). As we will see, the dephasing due to the Bias-Tee (see annex D.2) and the inductance of the short line linking the sample to the ground (see section 5.3.3) are not taken into account in the calibration procedure. We therefore subtracted these effects from the reflected signal. Once again, the oscillations in $|\Gamma|$ are due to impedance mismatches, and its frequency dependence to skin effect. The frequency dependence of the phase is due to propagation effects.
By applying the calibration procedure, we obtain the red curves presented figure 5.35.

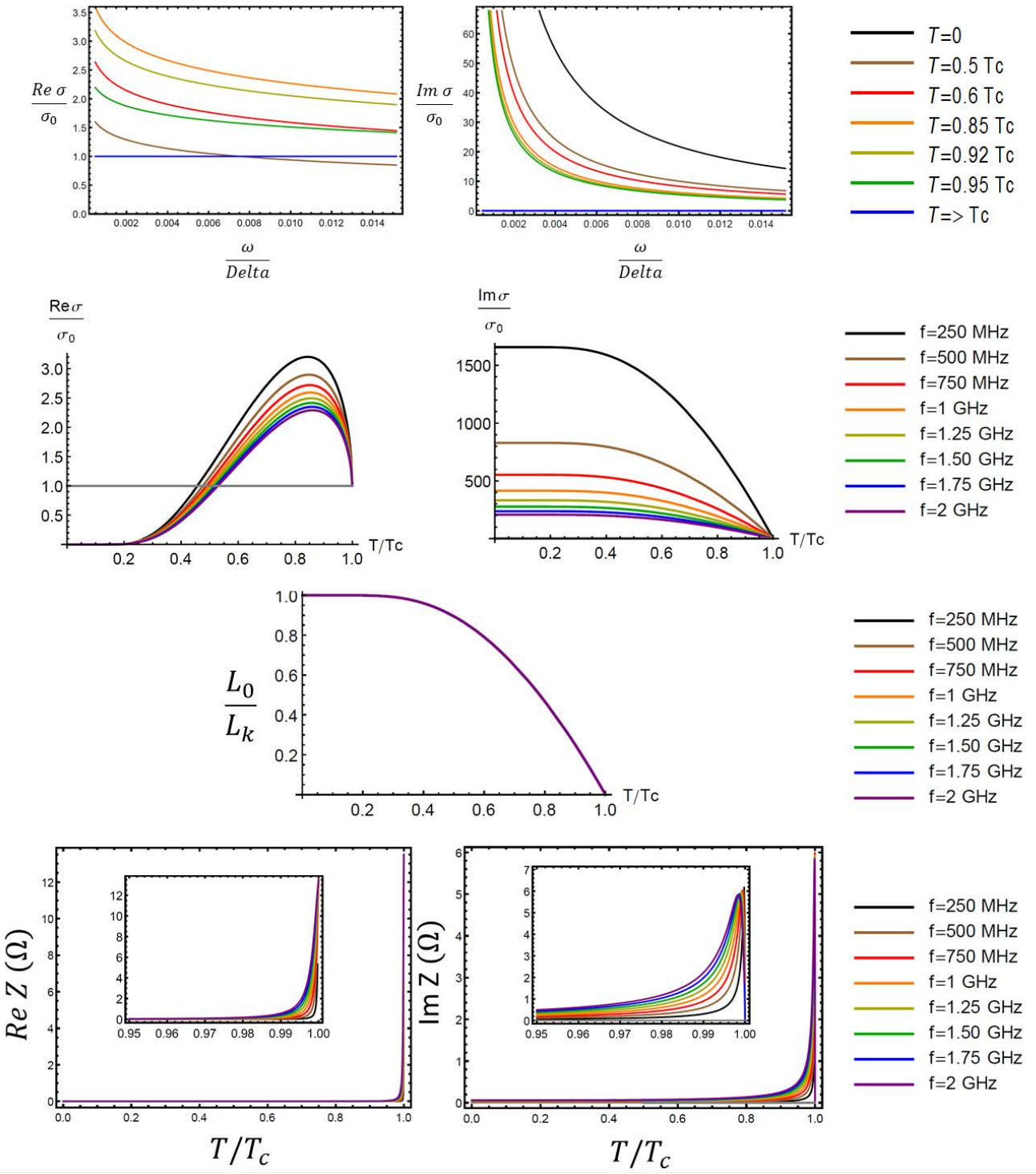

Figure 5.34: Prediction at the considered frequencies (from 10 MHz to 2 GHz) of the complex impedance Z and conductance σ , following Mattis-Bardeen theory, of the 100 Å-thick Vanadium film measured during the presented experiment (L_{k0} = 5 pH, T_c = 3.6 K). Superconducting fluctuations are not taken into account in this model. Adapted from Mattis-Bardeen simulation program, curtesy Y. L. Loh & N. Trivedi.

The real part of the complex impedance as extracted from the reflectometry measurement (figure 5.36) agrees well with the value given by the lock-in measurement performed simultaneously. Indeed, from 45 MHz to 1.3 GHz, the measured difference is lower than 5%. At lower frequencies, the reflectometry measurement gives a lower value of the resistance, probably due to the losses through the bias-Tee inductance (see annex D.2). Between 1.3 and 2 GHz, the

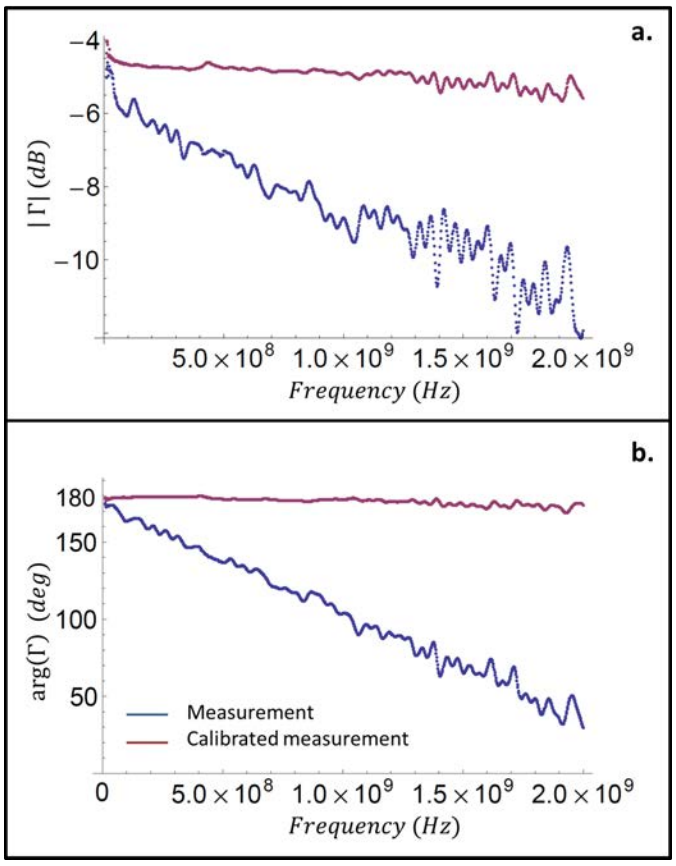

Figure 5.35: Measurement of the attenuation (a.) and phase (b.) obtained by performing reflectometry measurements on the sample in the normal state. The bare measurement is displayed in blue. The calibrated measurement is displayed in red.

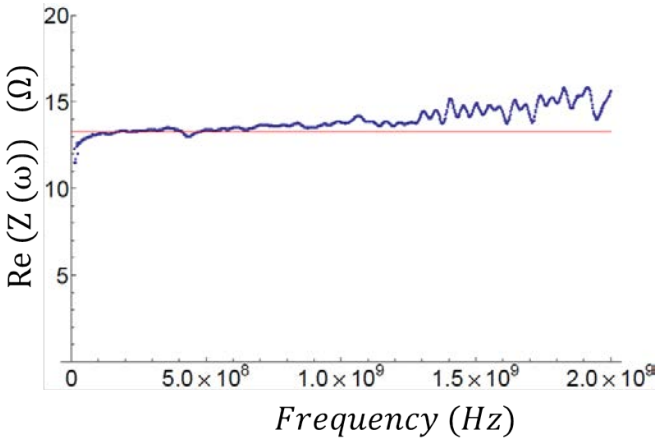

Figure 5.36: Real part of the calibrated impedance of the film. The red line corresponds to the low-frequency measured value.

agreement with the awaited value of the resistance is less good and oscillations appear on the calibrated resistance. This is likely due to a change in the internal amplifier of the VNA.

We measure a linear increase of the calibrated imaginary part of the impedance (figure 5.37). It is due to the geometric inductance of the sample. By fitting this dependence, and by assuming the response of the sample is assimilable to a linear inductance in addition to its resistivity (figure 5.38.a), we find that $L_{geo} \sim (250 \pm 20)$ pH. For a 200μm line of characteristic impedance $Z_0 = 50\ \Omega$, $L_{CPW} = 80$ pH. Adding the inductance due to the short line linking the sample to the ground (see section 5.3.3), we would expect a total geometrical inductance of $L_{geo} \sim 185 + 80 = 265$ pH [34]. This value is therefore in excellent agreement with the experiment and emphasizes how important it is to take into account the inductance of the termination of the line.
In addition to the inductance of the film, an additive capacitance has to be taken into account due to geometrical factor [35] (figure 5.38.b). One can estimate in our case this capacitance to be of the order of $C \sim \frac{2L_{CPW}}{Z_0^2} = 60$ fF [36]. This should not strongly influence our measurement as, at our working frequencies, the corresponding impedance is $Im(Z_C) = \frac{1}{C\omega} > 1000\,\Omega$, which is very large compared to the contribution of the LR circuit (of the order of 10 Ω). The issue of a parallel capacitance will be addressed in section E in which we will see that it can have an influence on the calibration of the normal state but does not modify the calibration results as soon as the resistance of the film decreases.

By lowering the temperature, the film eventually becomes superconducting. We should therefore be able to measure the electrodynamic response of the system due to the presence of Cooper pairs.
The evolution of the probed sheet impedance (respectively the sheet conductance) of the film will be detailed in the following.

5.5.2.2 Evolution of the Impedance as a function of temperature and frequency

By calibrating using the standard procedure (Open, Short, Load), we obtain $Re(Z(\omega))$ displayed figure 5.39 for different temperatures. The normal state, as noticed earlier, is well calibrated until 1.3 GHz. At higher frequencies, oscillations appear in the calibrated measurement. This is the case for all temperatures. Different remarks can be made :

- In the superconducting transition, $Re(Z)$ become highly frequency-dependent due to the presence of Cooper pairs.
- Below the superconducting transition
  - $Re(Z) \to 0$ for $f \to 0$.

34. The substrate of the Vanadium sample is made of SiO on top of the Si substrate. We therefore took $\epsilon_{eff} = \frac{\epsilon_{TMM10i} + \epsilon_{Si}}{2} \sim 10$.
35. The capacitance between the sample and the dial ground plane.
36. As for the estimation of L_{CPW}, the factor 2 comes from the Si substrate.

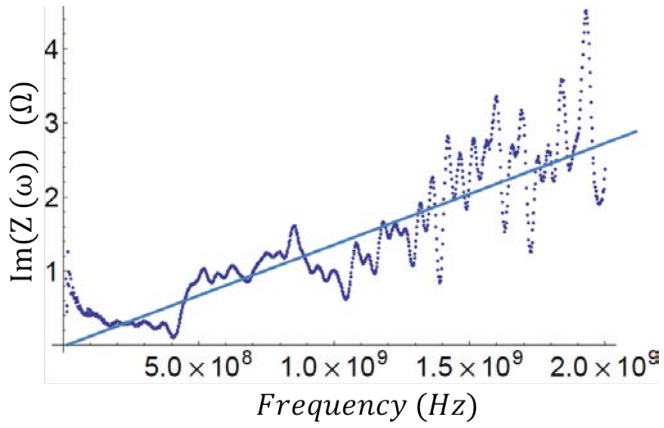

Figure 5.37: Imaginary part of the calibrated impedance of the film. The straight line corresponds to a linear fit such that $y = 2\pi L_{geo} f$, with $L_{geo} = 2.5 \times 10^{-10}$ H.

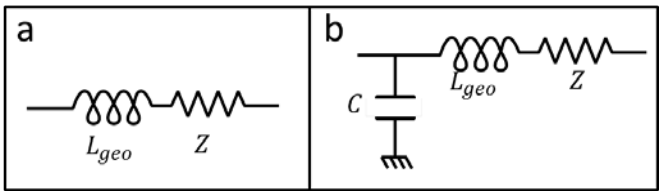

Figure 5.38: (a) Lumped element representation of the sample by supposing it is equatable to an inductance in series with Z. The inductance is due to the finite size of the sample. (b) Lumped element representation of the sample by assuming an additive capacitance.

– The frequency dependence of $Re(Z)$ diminishes when T is lowered far below the superconducting transition as the kinetic inductance diminishes.

These remarks are also observable in figure 5.40 in which we compare the lock-in measurement of $R(T)$, measured at 77 Hz, with the high-frequency measurement performed simultaneously. Both evolutions are similar, except for of the frequency dependence observed just below T_c due to the response of Cooper pairs : the higher the frequency, the higher $Re(Z)$ (inset figure 5.40). By comparing the inset of figure 5.40 with the Mattis-Bardeen theoretical predictions shown figure 5.34, the measured $Re(Z)$ is about 3 to 5 times larger. This may be due to a finite width of the superconducting transition (100 mK in our case). All electrons therefore may not condense at the same temperature.

The imaginary part of the measured impedance is plotted figure 5.41 as a function of frequency. The development of an inductive part is clearly visible below T_c :

– At the superconducting transition, the imaginary part of the impedance increases due to the presence of Cooper pairs and the diverging kinetic inductance.
– As the temperature is lowered below the superconducting transition, the kinetic inductance diminishes along with imaginary part of the impedance.

Looking at the evolution of $Im(Z)$ as a function of the temperature (figure 5.42), we find the expected peak of the Mattis-Bardeen theory. Its dependence as a function of frequency is qualitatively in agreement with theory for $T < T_c$ (see figure 5.34), i.e. the peak is shifted to lower values of $\frac{T}{T_c}$ as the frequency is increased. Furthermore, its amplitude is similar to what has been modeled, with $max(Im(Z)) \sim 6\,\Omega$ theoretically and $\sim 3.5\,\Omega$ measured.
Moreover, as $T \to 0.6\,T_c$, the measured value of $Im(Z(T))$ ($\in$ [0.2,0.6] Ω) does not go to zero as fast as predicted in the Mattis-Bardeen theory. It is however hard to quantify the differences due to noise.

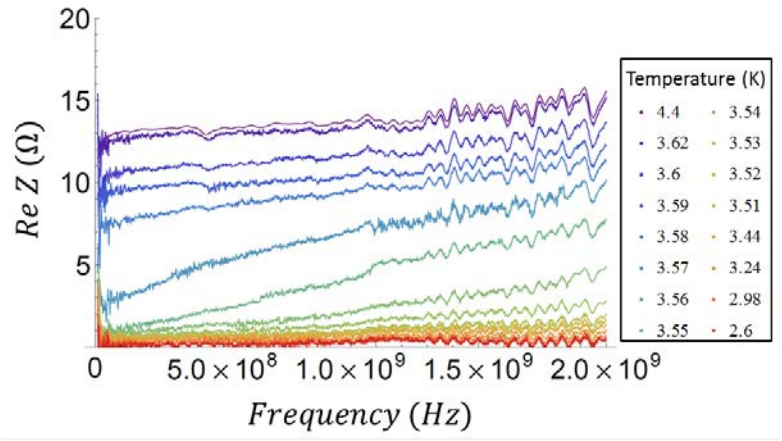

Figure 5.39: Evolution of $Re(Z(\omega))$, plotted for different temperatures ranging from ~ 0.6 to $\sim 1.1\ T_c$, obtained using a standard calibration.

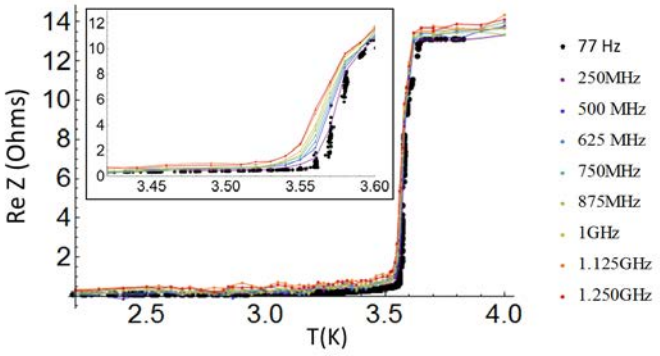

Figure 5.40: Comparison between the resistance measured with the lock-in (77 Hz, in black) and $Re(Z(T))$ obtained in high-frequency measurements using a standard calibration, plotted for different frequencies. A close-up is provided in the inset.

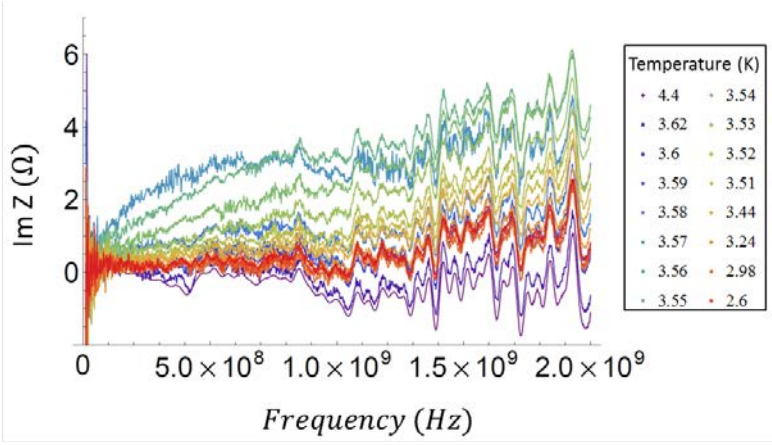

Figure 5.41: Evolution of $Im(Z(\omega))$, plotted for different temperatures ranging from ~ 0.6 to $\sim 1.1\ T_c$, obtained using a standard calibration.

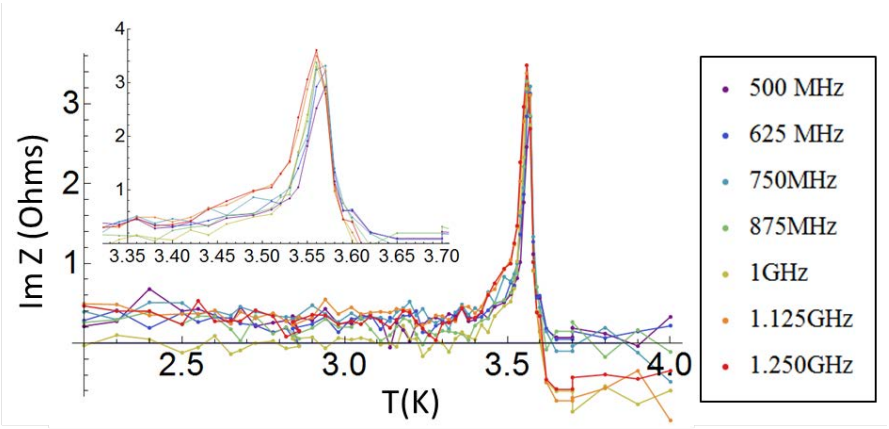

Figure 5.42: $Im(Z(T)$ obtained in high-frequency measurements using a standard calibration, plotted for different frequencies. The negative values of $Im(Z)$ at $T > T_c$ are due to impedance mismatches-induced oscillations of $Im(Z(\omega))$ (see figure 5.41). A close-up is provided in the inset.

5.5.2.3 Evolution of the conductance as a function of temperature and frequency

We will here examine the same results as above, by plotting the conductance $\sigma = \sigma_1 - I\sigma_2 = 1/Z$ for a selection of temperatures close to T_c [37]. This representation is convenient as it allows to de-correlate the contribution of quasi-particles (taken into account by σ_1) and of Cooper pairs (taken into account by σ_2). Furthermore, it allows to evidence the coherence peak and to quantify the kinetic inductance. Indeed, from Drude model, we can define the kinetic inductance L_k such that :

$$L_k = \frac{1}{\sigma_2 \omega} \tag{5.25}$$

$\underline{\sigma(T,\omega)}$

The Real and Imaginary parts of the conductance measured by using a standard calibration are plotted figure 5.43. We will here first make several qualitative remarks :

- $\sigma_1(T,\omega)$ has a temperature and frequency dependence qualitatively similar to what is expected in Mattis-Bardeen theory, due to the broadening of the quasi-particle distribution at finite temperature. $\sigma_1(\omega)$ increases as the temperature is lowered. It would decrease again at very low temperature due to the presence of the coherence peak.
- $\sigma_2(T,\omega)$ evolves as $1/\omega$ as expected. This is confirmed by plotting $\sigma_2(T,\omega) \times \omega$ (figure 5.44), which is frequency-independent for $f > 500$ MHz, except for oscillations which become important for $f \gtrsim 1.3$ GHz. Once again, the frequency-dependence for $f \lesssim 500$ MHz is attributable to the bias-Tee [38].

We therefore observe, at least qualitatively, the same dependence as what is expected in Mattis-Bardeen theory. The exact numerical values do not fit with theory. We will come back on this section 5.5.4.

Coherence peak and kinetic inductance

From the measurement of $\sigma(T,\omega)$, one can try to measure the coherence peak and the kinetic inductance (figure 5.45), to perform a more quantitative comparison with theoretical expectations.

As pictured figure 5.45.a, the dependence of $\sigma(T)$ is similar to what is expected in Mattis-Bardeen theory. As the temperature is lowered below T_c, σ_1 increases until reaching a maximum near 0.9 T_c. However, we saw in figure 5.34 that such coherence peak should have an amplitude $\frac{\sigma_1}{\sigma_0} \in [2;3]$. Taking into account the normal state conductance $\sigma_0 \sim 0.074$ S, we have peaks with

37. Far below T_c, both $Re(Z)$ and $Im(Z)$ are small. In this region, the sensitivity is lessened (see figure 5.2) and Γ is more affected by noise. The uncertainties on σ_1 and σ_2 are thus prohibitively important.

38. The evolution of the cut-off frequency as a function of the impedance of the probed sample is also observable in figure 5.44 : the lower the impedance (the more superconducting the film is), the higher the cut-off frequency.

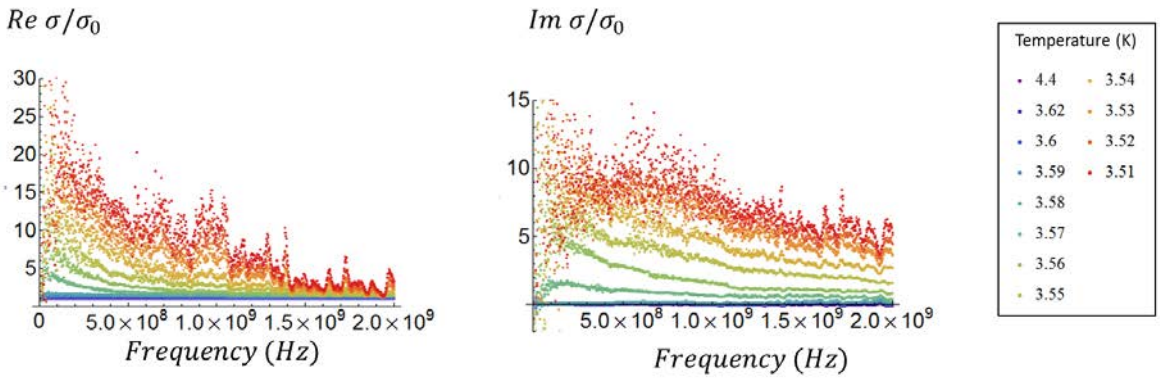

Figure 5.43: $\frac{\sigma_1}{\sigma_0}(\omega)$ and $\frac{\sigma_2}{\sigma_0}(\omega)$ obtained from a standard calibration and plotted for different temperatures. σ_0 is the normal state conductance.

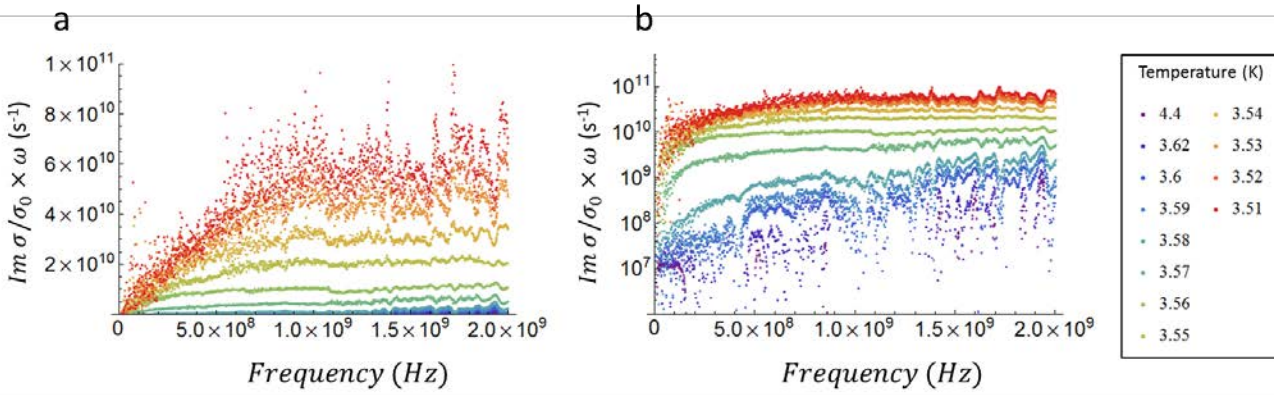

Figure 5.44: $\frac{\sigma_2}{\sigma_0}(\omega) \times \omega$ obtained using a standard calibration and plotted for different temperatures in linear scale (a) and semi-log scale (b).

an amplitude 10 times higher than expected. Again, this will be discussed in section 5.5.4.

We can also obtain the kinetic inductance of the films by extracting $\sigma_2\omega$ as a function of T (figure 5.45.b.). By doing so, we find that L_k has an abrupt increase close to T_c. Due to this feature near T_c, it is impossible to fit it $\sigma_2 \times \omega$ with a simple BCS dependence, where :

$$L_k^{-1} \sim L_{k0}^{-1}(1 - (\frac{T}{T_c})^4) \tag{5.26}$$

We will come back to this point in section 5.5.4. We can however attempt a fit, as shown figure 5.45.b.), to make a first rough estimation of L_{k0}. We thus estimate $L_{k0} \sim 60$ pH. This value is well above the 5 pH awaited from theory. We will come back to a possible explanation for this in section 5.5.4. Furthermore, the tendency breaks down below $0.8\ T_c = 2.8$ K, giving the limit of sensitivity of the experiment as will be discussed in section 5.6.

5.5.3 Improvement of the calibration

5.5.3.1 Using the normal state resistance

In line with of what has been performed by Kitano et al. [Kitano et al., 2008], one can use an improved calibration by using the normal state of the sample instead of the Load reference. In this way, the possible imperfections of the Load standard will not affect the measurement.

By using the normal state of our Vanadium film at Helium temperature ($\sim 1.2\,T_c$) as a calibration point instead of the 50 Ω Load, we have obtained the plot shown figure 5.46. The normal

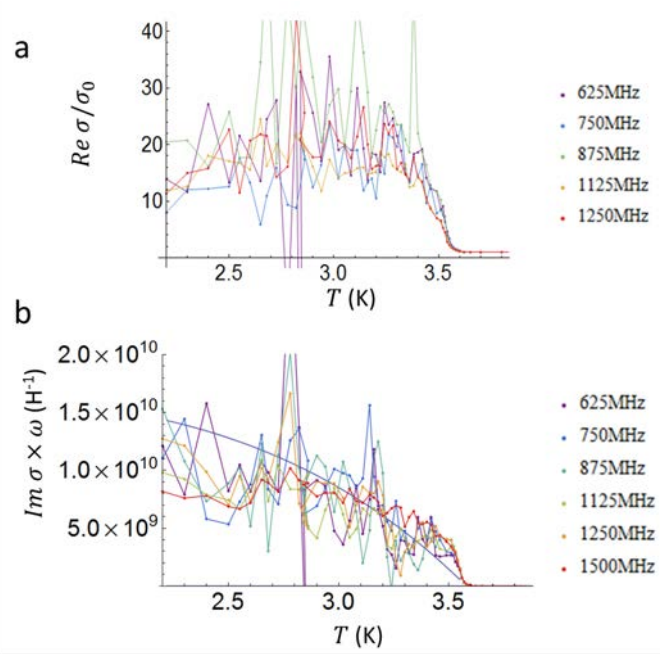

Figure 5.45: $\frac{\sigma_1}{\sigma_0}(T)$ (a) and $\sigma_2(T)\times\omega \propto \frac{1}{L_k}$ (b) plotted for different frequencies and obtained by performing a standard calibration. The BCS fit to $\sigma_2(T)\times\omega$ is given for $L_{k0} = 62.5$ pH.

state is perfectly calibrated [39] since its characteristics are imposed. As temperature is lowered, the size of the oscillations observable in $Re(Z)$ (figure 5.46.a.) are also diminished compared to the standard calibration [40].

Concerning the $Im(Z)$, as the normal state is also perfectly defined. Benefits are also visible for $Re(Z) \lesssim \frac{R_n}{2}$. However, these improvements compared to the standard calibration diminish in the superconducting state and we do not observe much change in the superconducting state. Indeed, the short is dominating the calibration as $|Z| \to 0$, especially when measuring $Im(Z)$ as it is the only inductive reference. **Therefore, such calibration using the normal state as reference, at best, increases sensitivity close to the normal state**.

5.5.3.2 Averaging on the frequency

Another way to improve the calibration is, in addition, to average the reflectivity Γ on a given bandwidth [41]. In this way, the oscillations due to the impedance mismatches are partially averaged out. By averaging the data over a frequency range of 40 MHz, we obtain the plots presented figure 5.47. The uncertainties on each trace remain of the same order as before averaging, but the noise is lessened.

5.5.4 Interpretation

As we have seen, our results on the frequency measurement of Vanadium thin films in the GHz regime are in qualitative agreement with the Mattis-Bardeen predictions. However, two features have to be explained :

- The values of σ_1 and of the kinetic inductance are too large.
- $\sigma_2 \times \omega(T)$ varies abruptly near T_c.

We will here try to explain these two points.

39. The response in the normal state was taken to be purely resistive.

40. Far into the superconducting state, oscillations at 1 GHz are smaller then 0.1 Ω peak to peak instead of 0.2 Ω found by calibrating with the load. At 2 GHz, oscillations stay however important, with a peak to peak oscillations of the order of 0.6 Ω found with both calibration methods.

41. Averaging after calibration does not improve the results as the errors due to the references would be already transmitted in the calibrated response.

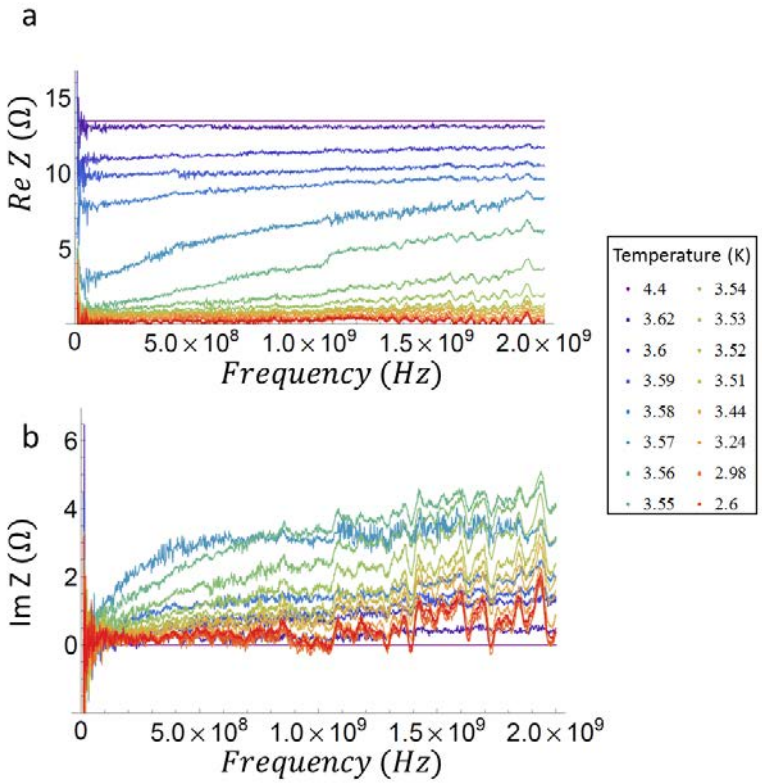

Figure 5.46: $Re(Z)$ and $Im(Z)$ obtained by substituting the measurement of the Load as a reference by the Vanadium sample in its normal state.

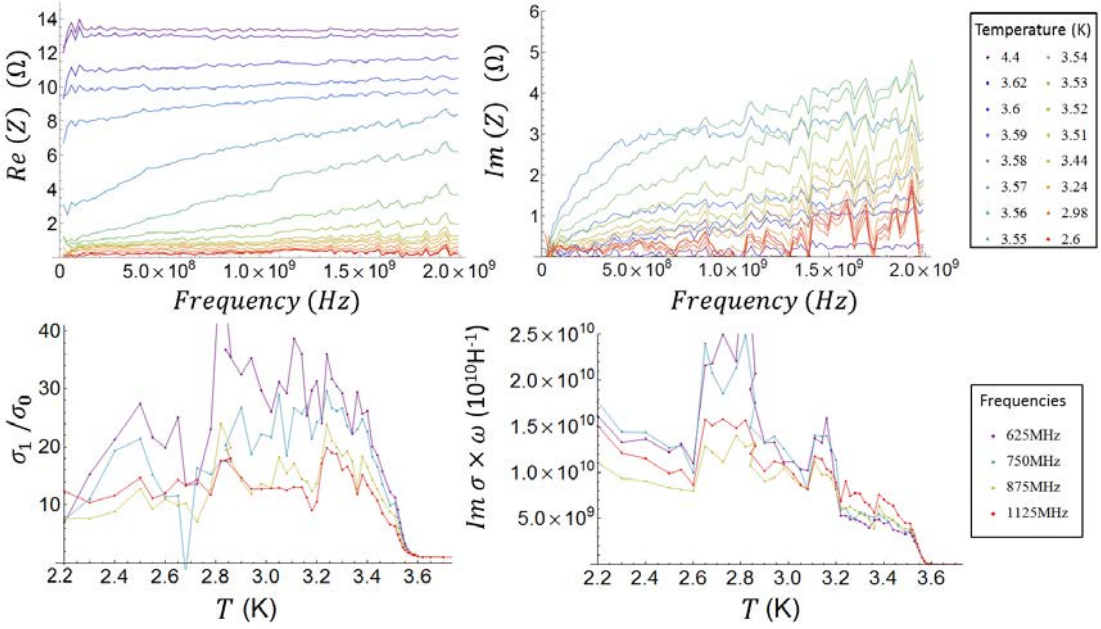

Figure 5.47: $Re(Z)$, $Im(Z)$, σ_1 and $\sigma_2 \times \omega$ obtained by substituting the measurement of the Load as a reference by the Vanadium sample in its normal state, and by averaging on a 40 MHz frequency range.

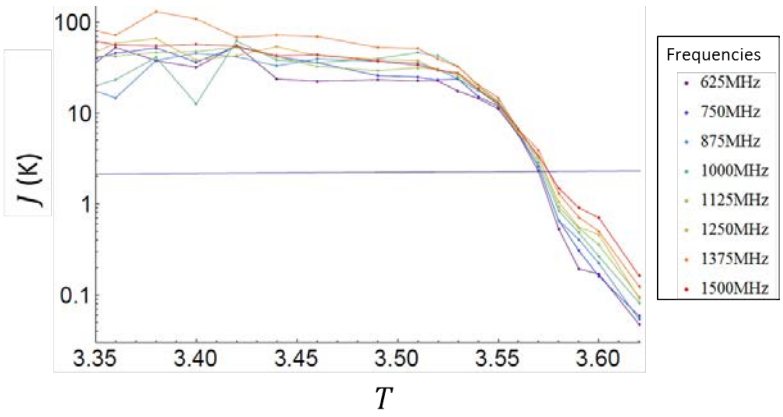

Figure 5.48: Superfluid Stiffness $J(T)$ obtained by using equation 5.28, for frequencies ranging from 0.625 to 1.5 GHz with steps of 125 MHz, and by using an Open, Short, Sample in the normal state calibration. The straight line corresponds to $J(T) = \frac{\pi}{2}T$. The crossing of the two curves at 3.57 K defines T_{BKT}.

Quantitative disagreement with Mattis-Bardeen theory To explain the large values of σ_1 and of the kinetic inductance we have measured, we can evoke two possible explanations. First, higher peaks at temperatures slightly higher than the predicted value, have already been measured, for instance in Aluminum [Steinberg et al., 2008]. It has then been assumed to be linked to a modification of the mean free path both due to disorder and the temperature.

Moreover, as we have seen in section 4, disorder can strongly modify the Mattis-Bardeen response at low frequency. The simulations made by Zimmermann [Zimmermann et al., 1991] give in our case $y = \frac{\hbar}{2\tau\Delta} = 1.9$ (with $\tau = 3 \times 10^{-13}$ s). As can be seen figures 4.8 and 4.9, this brings about a large increase of σ_1 at finite temperature, especially close to the coherence peaks. The second explanation is that all electrons do not condense in Cooper pairs at T_c. This could be the effect of disorder and has been both predicted [Nam, 1997] and observed experimentally [Gao et al., 1996].

BKT physics One can define a characteristic energy linked to the superfluid density called the phase stiffness J (see section 4.4.3). In 2D superconductors, it corresponds to the energy needed for vortex-antivortex pairs to unbind, destroying global phase coherence, and it is linked to the superfluid density as :

$$J = \frac{\hbar^2 n_s^{2D}(T)}{4mk_B} \tag{5.27}$$

By using London's equation for the superfluid density, one therefore finds :

$$J = \frac{\hbar^2 \sigma_2 \omega}{4e^2 k_B} \tag{5.28}$$

As soon as thermal excitations overcome this energy, a dissipative state due to the BKT transition appears due to the motion of vortices, destroying global phase coherence. The BKT temperature can therefore be defined by :

$$T_{BKT} = \frac{\pi}{2} J(T_{BKT}) \tag{5.29}$$

Therefore, one can check if the sudden drop in $\sigma_2 \times \omega$ is linked to BKT physics by plotting $J(T)$ and $\frac{\pi}{2}T$ on the same figure (figure 5.48). At temperatures above the crossing of the two curves, the frequency response of the sample should be altered by vortex motion [42], giving a frequency dependence of J. As can be seen figure 5.48, this is indeed the case. The abrupt jump could therefore be attributed to BKT physics.

This could has another consequence on the definition of T_{BCS} which then does not coincide with the observed superconducting temperature in $R(T)$. By taking into account this deviation

42. This frequency dependence can however be linked to the presence of superconducting fluctuations [Liu et al., 2011].

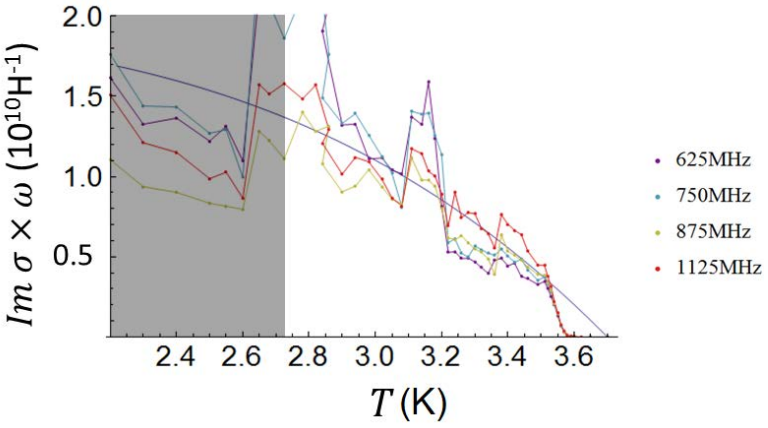

Figure 5.49: Fit of $\sigma_2 \times \omega$ by taking $T_{BCS} = 3.7$ K and $L_{k0} = 5.5 \times 10^{-11}$ H. The grey area corresponds to the temperatures where calibration breaks (see section 5.6).

from BCS theory, T_{BCS} is higher than expected. In this case, we can fit $\sigma_2 \times \omega$ as presented figure 5.49, giving $L_{k0} = 55$ pH.

5.6 Sensitivity of the calibration device

From figures 5.41, 5.39 and 5.46, one can estimate the uncertainties on both the Real and Imaginary parts, in the normal and superconducting regimes. The results are summarized in table 5.6.

As can be seen, taking the sample in the normal state as a reference point improves the sensitivity on $Re(Z)$ when $|Z|$ is finite. The sensitivity on $Im(Z)$ is essentially unchanged. The superconducting state is also mainly unaffected.
Although the full calculation of the propagation of the calibration errors depending on the measured impedance is beyond the scope of this thesis, let us note that the uncertainty depends on Z_{sample}. Indeed, the influence of a reference point is predominant for $Z_{sample} \sim Z_{ref}$ and is therefore non-linear in Z_{sample}. In the normal state, the Load or Sample in the normal state reference is dominant, whereas, in the superconducting state, the Short reference point prevails.

Impedance	Calibration	Frequency range	Uncertainty on $Re(Z)$ (Ω)	Uncertainty on $Im(Z)$ (pH)
13.2 Ω	OSL	0-1 GHz	$\pm$0.35	$\pm$50
	OSL	1-2 GHz	$\pm$1.2	$\pm$70
	OSS	0-1 GHz	$\pm$0.35	$\pm$60
	OSS	1-2 GHz	$\pm$0.35	$\pm$60
300 pH $\times\omega$	OSL	0-1 GHz	$\pm$0.3	$\pm$55
	OSL	1-2 GHz	$\pm$0.6	$\pm$85
	OSS	0-1 GHz	$\pm$0.2	$\pm$50
	OSS	1-2 GHz	$\pm$0.7	$\pm$60

Table 5.3: Uncertainties on both the Real and Imaginary parts, in the normal and superconducting regimes. OSL refers to the Open, Short, Load calibration, whereas OSS refers to the Open, Short, Sample in the normal state calibration.

Due to these values of sensitivity, the experimental data taken for temperatures below $0.75 \times T_c = 2.78$ K are not usable. Indeed, as can be seen from figure 5.49, for $T < 2.78$ K, $L_k < 65$ pH.

Finally, as we have mentioned earlier, the data for $f \gtrsim 1.3$ GHz have large oscillations, probably due to a small defect in the VNA internal amplifier used in this range. Moreover, the data for $f \lesssim 500$ MHz are unreliable due to the cut-off frequency of the bias-Tee. This problem could be solved by a more accurate modeling of the electrokinetic response of the bias-Tee (see

appendix D.2.2). In the present work, we wanted to keep the modeling to a minimum in order to show the validity of the calibration device. We therefore have not pushed this analysis axis.

5.7 Conclusion

We developed a device allowing broadband reflectometry measurements for thin films at low temperatures (T<4 K) and high frequencies (GHz). It allows to measure, in a single cool down, the absolute value of the complex impedance of films by characterizing the microwave environment through successive measurements of known standards.

The originality of this work compared to what can be found in the literature is multiple :
- We can calibrate during a single cooling down, limiting errors due to the non-reproducibility of experimental conditions during successive cool downs.
- We do not have to make assumptions on the impedance of the measured sample : calibration techniques using partially or totally the sample to calibrate assume the knowledge of the sample response and are therefore subject to errors. This should in principle be avoided in our case.
- The geometry of the device can be adapted to the sample geometry.

In order to improve our calibration device, several leads could be explored :
- The influence of the bias-Tee could be taken into account (appendix D.2.2).
- The electrokinetic model for the sample could also be improved (appendix E).
- We have also seen that using the sample as a calibration reference may also improve the measurement. We have checked that, in the case of a purely resistive sample, this calibration method is consistent with the standard Open Short Load calibration.

The validity of the device and the obtained calibration have been tested on a superconducting Vanadium film. The electrodynamic response of the films were found to qualitatively follow BCS dependence. Quantitatively, the kinetic inductance was measured to be 10 times larger than the predicted value. This could reflect the effects of disorder in this system. Moreover, evidence for Berezinskii-Kosterlitz-Thouless physics may have been found for a 10 nm-thick Vanadium film. In the current status, the resolution of our calibration device should be sufficient for numerous applications, such as characterizing disordered thin films close to the Superconductor-to-Insulator Transition.

Conclusion

The goal of this work was to push forward our understanding of the Superconductor-to-Insulator Transition (SIT) and the mechanisms at play at its vicinity. To do so, we studied **low frequency electronic transport properties** in a-Nb_xSi_{1-x} thin films at very low temperatures ($T < 1$ K), to probe the different accessible ground states. We also developed and characterized a setup for **high frequency measurements** which, in the long run, will allow us to shed a complementary light on the SIT and the existing ground states.

More precisely, in the first part of this thesis, the low frequency transport measurement performed in thin a-Nb_xSi_{1-x} films allowed us to measure and characterize the transition between the insulating phase and the neighbouring metallic one. We found that :

- The insulating phase is likely fermionic.
- The neighbouring metallic phase shows precursor signs of this fermionic insulator close to the transition, with an activated regime at intermediate temperatures. In a conventional picture, the existence of these precursor signs should forbid the existence of a *fermionic* metallic ground state at lower temperature.
- The evolution of the characteristic properties of the fermionic precursor with disorder (characteristic energies and pre-factors of the activated regimes) is continuous across the transition between the metal and the fermionic insulator.

In our opinion, these two last points constitute important results of this thesis. Indeed, it confirms that metallic phases in 2D disordered systems may arise, possibly from the persistence of superconducting fluctuations even when long-range coherence is lost. We have qualitatively modeled this situation as the coexistence of a disordered fermionic channel with a bosonic one. In addition, our study shows that the traditional dichotomy between fermionic and bosonic models for the Superconductor-to-Insulator Transitions in homogeneous materials can be questioned as the metallic phases observed would be linked to the coexistence of both bosonic and fermionic excitations in the material, whereas the transition toward the insulator, maybe related to the suppression of bosonic excitations.

In a second part, we have detailed the specificities of an original calibration device, allowing broadband reflectometry measurements for thin films at low temperatures (T<4 K) and high frequencies (GHz) in a single cool down. We were interested in testing it for different sample impedances. Superconducting thin films were good candidates for their potentially large impedance range, within a single sample, at low temperature. The calibration device allowed us to measure the electrodynamic response of a Vanadium film across its superconducting transition, down to $\sim 0.75\,T_c$, with a good sensitivity ($\pm 0.2\,\Omega, \pm 50$ pH) up to 1.3 GHz. Furthermore, the complex impedance qualitatively follows BCS dependence, further assessing the validity of the calibration.
From a more physical point of view, it seems that the qualitative deviations from BCS that have been evidenced in this Vanadium film could be understood by taking into account disorder effects, although this remains to be confirmed. In addition, surprisingly, we found in this pure system a possible manifestation of BKT physics.
With the development and characterization of this apparatus, we achieved an important first step towards the determination of the absolute value of the complex impedance of disordered systems, whether in the superconducting, metallic or insulating phase, as the obtained sensitivity should allow us to comfortably probe such systems where the electrodynamic response is affected by disorder.

The complementarity of the two approaches used during this thesis, with low and high frequency techniques, should allow to deepen our understanding of the SIT to a new level. Indeed, microwave probe, combined with the phase diagram (established by low frequency transport mea-

surements) will allow us to gain new insight on the mechanisms involved close to the different phases observed in a-Nb_xSi_{1-x} at low dimensions, for example by confirming the nature of the 2D metallic states. By going into the quantum regime ($\hbar\omega > k_BT$) we should also have a direct probe of the universality class of these transitions.

Knowing the electrodynamic response of disordered systems cannot however answer all the questions that remain to be addressed when different phenomena such as Coulomb interactions and superconductivity are entangled. Coupling the obtained result with additional techniques may help. We would like in particular to cite two different experimental techniques :

- Tunnel effect will probe how the density-of-states evolves close to the SIT. In particular in the insulating phase close to its destruction, whether excitations are present in the gap would provide much needed informations on the formation of the metallic phases. It should also allow to quantify the effects of Coulomb interactions in the same regime.
- Magnetoresistance measurements used (at high or low frequency) would confirm the presence of superconducting fluctuations in the observed metallic phases.

We believe that these three techniques combined could clarify many unclear issues, notably regarding the role of both superconducting fluctuations and Coulomb interactions, in the emergence of a 2D metallic phase.

Part III

Appendix

Appendix A

Discussion on Zabrodskii's method

A.1 Possible power laws

In the literature, conductivity near the MIT (in a 3D system) is often thought to have a power law dependence as a function of temperature in the metallic regime, when the correlation length diverges [1]. The conductivity then has the form :

$$\sigma_{PL}(T) \sim \frac{e^2 p_F}{\hbar^2}(\frac{k_B T}{E_F})^{\frac{1}{\nu}} = aT^{-\beta} \tag{A.1}$$

where p_F is the Fermi momentum and $1 < \nu < 3$ (or $\frac{1}{3} < \beta < 1$).

One can test the possibility of having a power law near the observed MIT in our films, as expected in a 3D material. To do so, we can use the relation :

$$ln(\sigma_{PL}(T)) \sim ln(a) - \beta ln(T) \tag{A.2}$$

Therefore, by plotting the logarithm of the conductance, one should observe a reasonable range in temperature where the conductivity is proportional to $ln(T)$ in the Quantum Critical Region. Such an attempt is plotted figure A.1 for an as-deposited 45 Å-thick a-$Nb_{13.5}Si_{86.5}$ sample, close to the Metal 2-Insulator Transition. As can be seen, at the lowest temperatures, such a power-law regime cannot reasonably describe our experimental data.

Another argument to push aside such a description of the conduction near the observed M2-to-Insulator transition is the use of Zabrodskii's technique. Indeed, in the case of a conductivity of the form A.1, it gives :

$$ln(-\frac{d\,ln(\sigma_{PL})}{d\,ln(T)}) = ln(\beta) \tag{A.3}$$

Therefore, a power law dependence of σ_{PL} should give with this method a constant, determined by β. As β should be such that $1 \leqslant \beta \leqslant 3$, Zabrodskii's plot should give a constant between 0 and 1.1. As one can observe in figure A.2, the evolution at low temperature of the parameter $ln(-\frac{d\,ln(\sigma)}{d\,ln(T)})$ applied to the sample above presented is clearly not a constant, reinforcing the argument in favour of a conduction mechanism which cannot be described by a simple power-law.

Let us remark that for an arbitrary conductivity of the form :

$$\sigma(T) = \sigma_0 + aT^{\beta} \tag{A.4}$$

The above presented result is valid only in the limit where $\sigma_0 << aT^{\beta}$. In the other limit, the result may be more complicated to interpret and depend on β. For as-deposited 50 Å a-$Nb_{13.5}Si_{86.5}$ films, $\frac{\sigma_0}{aT^{\beta}} \sim \frac{\sigma_0}{\sigma(10\,mK)} \sim \frac{1}{5}$. The approximation is therefore justified in our case.

1. See for instance [McMillan, 1981] [Larkin and Khmel'nitskii, 1982] for theoretical background.

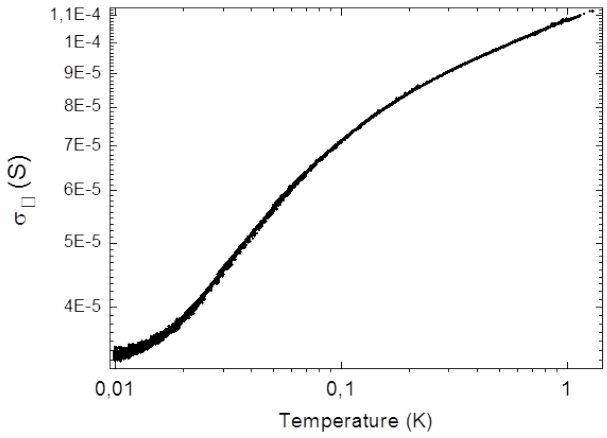

Figure A.1: Conductance of an as-deposited 45 Å-thick a-$Nb_{13.5}Si_{86.5}$ sample as a function of temperature, both in log scale.

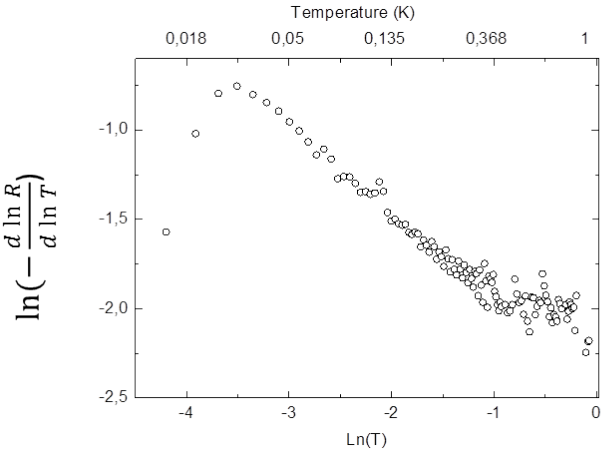

Figure A.2: Zabrodskii plot of an as-deposited 45 Å-thick sample, close to the M2-to-Insulator transition on the M2 side. A pure power-law dependence of the resistance can be excluded as the obtained curve is not constant.

If $\sigma_0 \sim aT^\beta$, we would have obtained the general expression:

$$w = ln(-\frac{d\,ln(1/\sigma(T))}{d\,ln(T)}) = ln(\frac{a\beta T^\beta}{aT^\beta + \sigma_0}) \tag{A.5}$$

which goes to -∞ at low temperature. On the other hand, if $\sigma(T)$ is comparable with σ_0, this expression gives a rounded Zabrodskii plot as a function of temperature due to the relative evolution of aT^β with respect to σ_0. Since this is not what we find in the case of the as-deposited 45 and 50 Å-thick samples, we are quite confident in the fact that our data cannot be described by a power law in the metallic side near the M2-to-Insulator Transition.

A.2 Dependence as a function of temperature of the prefactor in VRH

Strictly speaking, Variable Range Hopping laws are of the form :

$$R(T) = R_0 T^{-m} e^{(T_0/T)^n} \tag{A.6}$$

The derivation performed in this thesis has been done by supposing that the contribution given by T^{-m} is small compared to the one due to the exponential part of the expression. This assumption should be true in the majority of the cases but should be verified.

One can extract m by a simple calculus from the data. Indeed, one can find that

$$\frac{d\,ln(R(T))}{d\,ln(T)} + n(\frac{T_0}{T})^n = -m \tag{A.7}$$

By using the value of n extracted from the analysis, one can therefore obtain the factor m which has not been taken into account.

For an insulating sample just above the M2-to-Insulator Transition, such a fit is performed figure A.3. The obtained value for m is a constant, proof of the quality of the extracted parameters, and allows us to ensure that the absolute value of the parameter $m \sim -0.03$, and can therefore be considered as negligible in this phase.

This is also the case for the intermediate temperature VRH regime in M2 samples : figure A.4 shows that $m \sim 0$ for a sample at the verge of the M2-to-Insulator transition but which still is metallic.

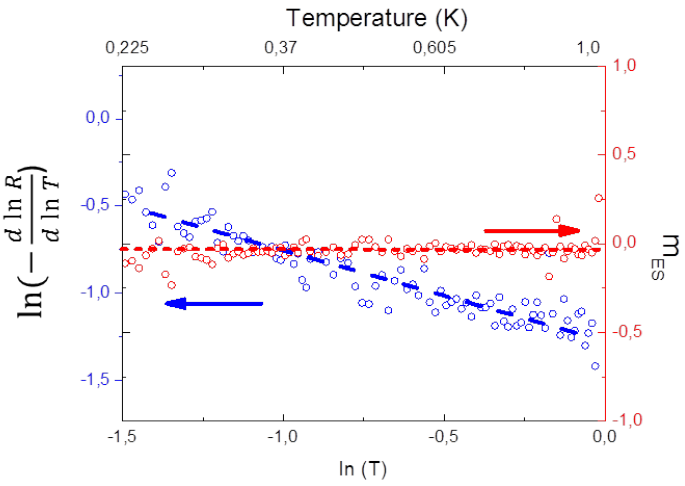

Figure A.3: $\frac{d\,ln(R_\square(T))}{d\,ln(T)}$ (in blue) and the parameter m (in red, defined in the text) for an as-deposited 40 Å-thick a-$Nb_{13.5}Si_{86.5}$ sample. The blue dashed line correspond to an Efros-Shklovskii fit ($n = 1/2$) of the Zabrodskii plot and the red dotted line to the mean value of m in the interval of validity of the fit ($m = -0.03$).

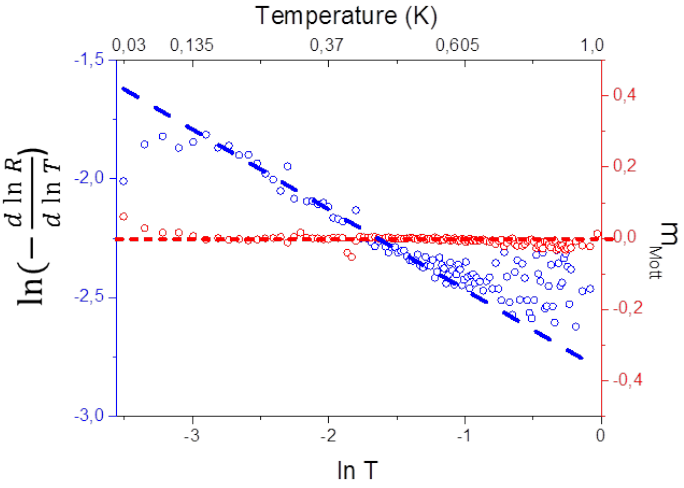

Figure A.4: $\frac{d\,ln(R_\square(T))}{d\,ln(T)}$ (in blue) and the parameter m (in red, defined in the text) for an as deposited 50 Å a-$Nb_{13.5}Si_{86.5}$ sample, on the metallic side but close to the M2-to-Insulator transition. The blue dashed line corresponds to a Mott fit ($n = 1/3$) of the Zabrodskii plot and the red dotted line to $m = 0$.

Appendix B

Over-activated insulating regime

As seen section 3.3.2.3, some of our films near the MIT have been found to be more insulating than an Arrhenius law, with n>1 (figure 3.23). This discrepancy, as discussed in section 3.3.2.3 cannot be associated this experimental errors, and was unexpected in thin film.

A careful analysis of the films grown for previous study in the group showed an even more striking behaviour. Indeed, we found in insulating 25 Å-thick $Nb_{18}Si_{82}$ films an insulating behaviour with $n > 2$ by using Zabrodskii's method, as pictured figure B.1. This strange behaviour may be associate with (electronic or structural) inhomogeneities. Indeed, in the case of the film presented figure B.1, the recrystallisation temperature found by transport measurement is low (of the order of 100 ℃ as pictured figure B.2). It is therefore likely that the migration of Nb inside the amorphous matrix gives birth to Nb-rich clusters, creating structural inhomogeneities similarly to what is encountered in granular systems.

In the case of the films presented in this thesis, we have seen no sign of recrystallisation on the σ_{4K} vs θ characteristic (presented figure 3.8). Therefore, we do not believe that the formation of Nb-rich clusters in our films may be the cause of the observed phenomena. Furthermore, n goes back to the usual value of 1 when disorder is increased further. By analogy with the above-mentioned set of films, we therefore believe that the observed tendency may be explained by electronic inhomogeneities close to the M2-to-Insulator transition. Such an influence of the granularity on the parameter n has also been observed in other systems like in granular In [Kim et al., 1992].

An alternative explanation resides in the Many Body Localization approach. Indeed, recent theoretical developments have shown that disordered, strongly interacting low dimensional systems could undergo a dynamical phase transition towards a non-ergodic localized phase. In this new phase, the strong localization prevents the electronic system to thermalize due to low electron-phonon coupling. Part of the electrons then stay out-of-equilibrium for a measurable time [Basko et al., 2006]. Experimentally, this should manifest itself by a number of phenomena, amongst which:

- A finite-temperature metal-to-insulator transition [Basko et al., 2006, Agarwal et al., 2015, Altshuler et al., 2009]. Experimentally, a finite temperature insulator was reported in InOx thin films [Ovadia et al., 2015] close to the Superconductor-to-Insulator Transition.
- A particular dependence of $\sigma(\omega)$ in the insulating phase, when measured by low frequency techniques [Gopalakrishnan et al., 2015].
- A specific response to electric field through which one could probe the two electronic baths that coexist at distinct temperatures [Basko et al., 2007]. Recently, the experimental signature of this non-equilibrium state in disordered superconductors has been measured by Doron and coworkers [Doron et al., 2016].
- A faster than activated behavior in the insulating phase [Feigel'man et al., 2010] when the localized phase bears Cooper pairs.

This last point should be tested in our a-Nb_xSi_{1-x} films to see if such a phase could explain the $n > 1$ regime we observe close to the M2-to-Insulator Transition.

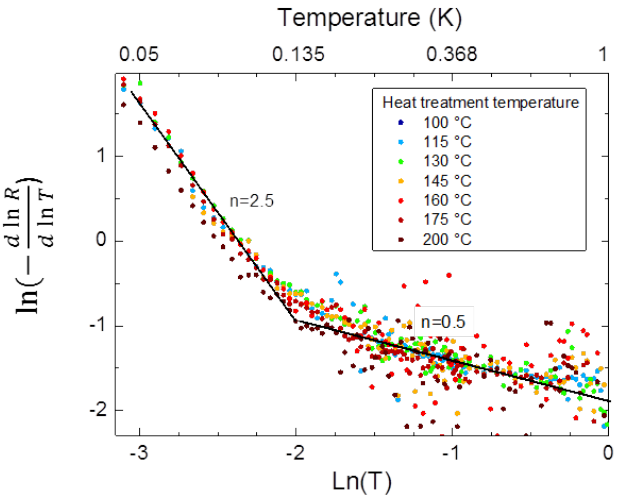

Figure B.1: Application of Zabrodskii's method on a 25 Å-thick $Nb_{18}Si_{82}$ sample from the batch OC6 which sustained a heat treatment. We find a transition between a ES-VRH regime and a regime with $n > 2$ at an almost constant temperature $T \sim 135$ mK.

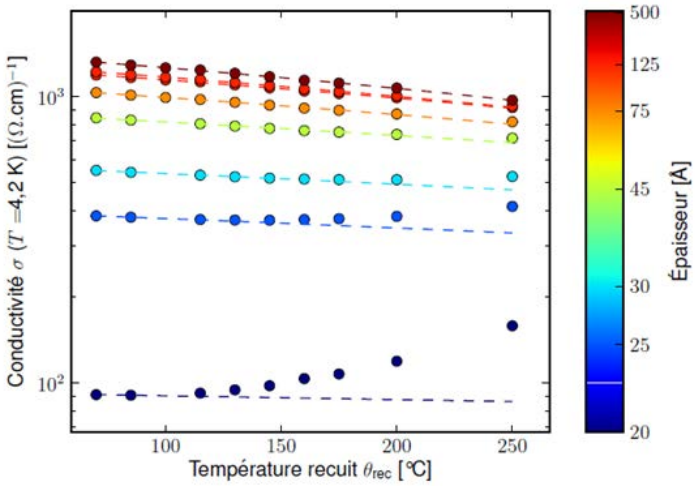

Figure B.2: Evolution of the conductance as a function of the heat treatment temperature for samples of $Nb_{18}Si_{82}$ samples from the batch OC6. Source : [Crauste, 2010]

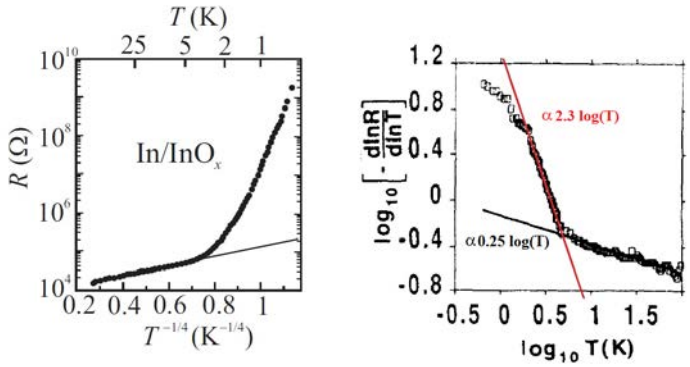

Figure B.3: (left) Resistance as a function of temperature for granular In films. (right) The corresponding Zabrodskii plot shows an over-activated behaviour at low temperatures. Source : [Kim et al., 1992].

Appendix C

Complementary measurements to perform on NbSi films

In the table below, we have listed some of the experiment we feel would be helpful to better understand the effects of disorder in 2D a-Nb_xSi_{1-x} films. Indeed, the interplay between superconducting fluctuations and Coulomb interactions seems particularly important in the vicinity of the observed metallic phases. Complementary measurements could disentangle the various phenomena. For each technique listed, the questions that could thus be tackled are put forward.

Experimental technique	Measured quantity	Questions addressed
Low frequency transport measurements under magnetic field	Magnetoresistance	•Presence of superconducting fluctuations in the different regimes obtained through disorder-driven transitions •Phase diagram of the different ground states as a function of the magnetic field •De-correlation of the effects of Coulomb interactions and localization in the weak-localization regime (quantify Coulomb interaction strength) •Critical exponents of the various transitions
Low frequency transport measurements on crystallising Nb_xSi_{1-x} (driven by heat treatment temperature)	Activation laws in electronic transport	•Are the over-insulating regimes due to superconducting islands and what are the effects of composition/dimensionality/structure ? •Influence of the structure on the destruction of superconductivity in disordered alloys
Low frequency transport measurements of a trilayer NbSi/SiO/Metal	Resistance as a function of d_{SiO} or of an electrostatic gating	Influence of a modification of the screening properties on the different phases by proximity effect to a metal and/or by electrostatic-gating effect
Low frequency transport measurements of a bilayer $Nb_xSi_{1-x}/Nb_{x'}Si_{1-x'}$	Resistance as a function $d_{\mathrm{Nb}_{x'}\mathrm{Si}_{1-x'}}$	•Influence of a modification of the screening properties on the different phases by proximity effect to an Anderson insulator •Superconductivity induced by proximity effect in an Anderson insulator
Specific heat measurements	Heat capacity	Presence of superconducting fluctuations in the different observed regimes
Nano-structured films under magnetic field	Magnetoresistance	Presence of Cooper pairs in the different regimes (Little-Parks oscillations)
Microwave reflectometry measurement	Reflection coefficient Γ	•Nature of the carriers in the different regimes •Mechanisms at play at the transition •Presence of superconducting fluctuations in the different observed regimes •Critical exponents at the various transitions
Two-coil experiment	Penetration length	•Superfluid density •Superconducting fluctuations above T_{BKT}
Noise measurements	Noise spectrum	•Nature of the carriers in the different regimes •Presence of superconducting fluctuations in the different observed regimes
Tunnel effect (STM)	Tunnel conductance (DOS)	•Presence of Cooper pairs in the different phases •Presence of coherence peaks : long range order or local superconductivity •Strength of Coulomb interactions nearby and in the insulating phase •Low energy excitations in the gap (in insulating phases close to the expected SIT and in the neighbouring metals) (•Size of electronic inhomogeneities)

196

Appendix D

The bias-Tee

D.1 Dimensions

The dimensions of the bias-Tee [1] are given figure D.1. They have been taken into account in order to position the bias-Tee on the measurement line without disrupting the rotating parts of the calibration device.

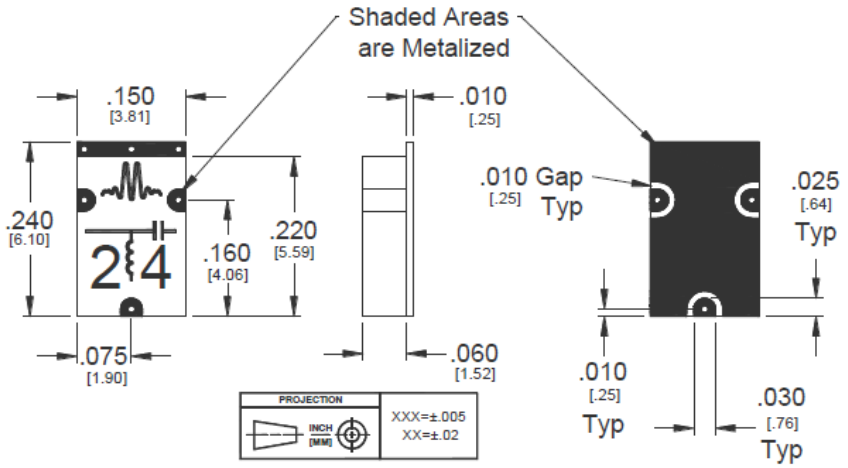

Figure D.1: Dimensions of the bias-Tee. Source : http://www.markimicrowave.com.

D.2 Characterization of the bias-Tee

D.2.1 Modelization of the bias-Tee

The bias-Tee can be modeled by a capacitance C in the line used for high frequency measurements, blocking low frequency signals, and an inductance L on the line used for low frequency measurements, blocking high frequencies. It therefore allows to measure simultaneously the low and high frequency responses of a sample positioned downstream the bias-Tee. A schematic representation of the equivalent electrical circuit is given figure D.2.

From this modelization, one can deduce the transfer function of the bias-Tee :

$$|\frac{V_{out}}{V_{in}}| = \frac{jC\omega Z_L}{1 + Z_L(jC\omega + \frac{1}{jL\omega R})} \tag{D.1}$$

where V_{in} is the voltage at the high frequency end of the bias-Tee and V_{out} the one at its output. The transfer function depends on both the impedance R of the output of the instrument used for low-frequency excitation and the impedance Z_L of the probed sample.

1. Marki BT-0024SMG

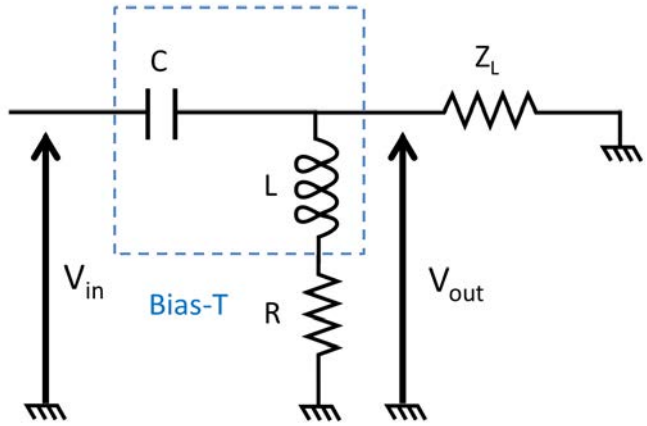

Figure D.2: Equivalent electric circuit of the bias-Tee in a reflectometry measurement configuration. It is composed of the capacitance C on the high frequency line and an inductance L on the low frequency one. R is the characteristic impedance of the instrument used for low-frequency measurements. Z_L is the impedance of the probed device.

For measurements in normal conditions [2], we have :

$$|\frac{V_{out}}{V_{in}}| = \frac{Z_L C\omega}{\sqrt{1+(Z_L C\omega)^2}} \tag{D.2}$$

The cut-off frequency of the bias-Tee is given by :

$$f_c \sim \frac{1}{2\pi C Z_L} \tag{D.3}$$

The constructor data-sheet gives $f_c \sim 500$ kHz. It corresponds to the cut-off value obtained in normal conditions for a sample matched to 50 Ω. We therefore deduced $C \sim 6$ nF.

In addition to this capacitance, which should disturb the measurement at low frequencies, the permittivity seen by the propagating signal is different for a wave propagating inside or outside the bias-Tee (i.e. on the other lines of the calibration chip). The relative permittivity seen by the signal propagating in the bias-Tee is not documented and will induce a dephasing of the signal. We therefore characterized the bias-Tee at low temperature (4 K and 1.5 K) to have both the dephasing and the attenuation due to the bias-Tee.

D.2.2 Measurement of the bias-Tee

To measure the dephasing and reflections due to the bias-Tee, we proceeded by two different means :

- We measured the transmission of a microwave line and compared it with the transmission of the same line in which the bias-Tee had been inserted. The difference between the two measurements characterized the bias-Tee.
- We characterized the bias-Tee directly on the calibration device, by replacing the sample by a copper line, at 300 K and at low temperatures (4 K and 1.5 K).

Both tests yielded the same results. We will therefore only present the measurements made on the device, obtained at 4 K.

To perform this test, we replaced the sample by a short made out of a flip-chipped copper line [3]. We then compared this measurement to the short reference sitting on the dial. Figure D.3 shows the measurement of the phase of the reflection coefficient on the Short and on the group {bias-Tee+ short}, obtained at 4 K. The phase drifts are slightly different. This can be corrected by taking into account a dephasing of 1.65 mm due to the bias-Tee and 0.2 mm due to

2. i.e. for $R \to \infty$. For the SR560 lock-in amplifier we used, $R \sim 1$ MΩ.
3. Cooper line with TMM10i substrate.

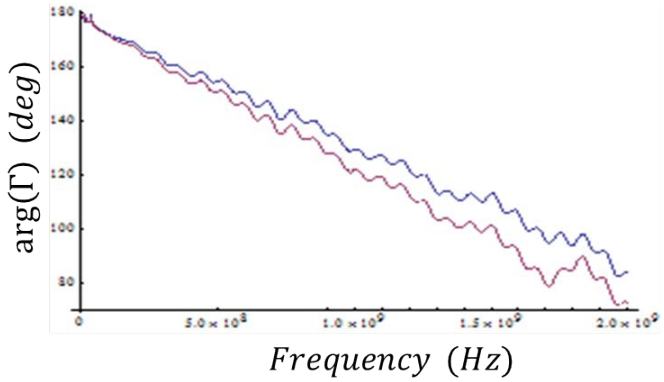

Figure D.3: Phase of the reflected signal measured on the short (red) and on the {BT+short} (blue). The difference between the two can be taken into account by a delay due to the presence of the bias-Tee.

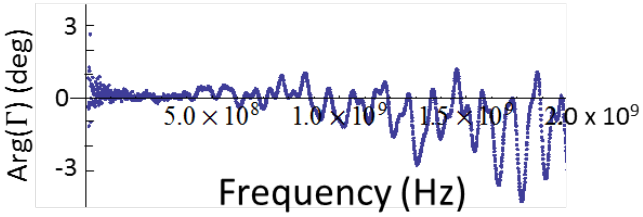

Figure D.4: Correction of the dephasing observed figure D.3 by imposing an extra length of 1.85 mm (1.65 mm corresponding to the bias-Tee and 0.2 mm due to the propagation in the copper strip).

the propagation in the copper line, resulting in a line of (1.85 ± 0.1) mm difference compared to the line containing the short. The correction of the phase, taking into account this dephasing, is plotted figure D.4. This value does not correspond to an actual difference in length, but rather to a change in the dielectric properties of the line. Indeed, the permittivity of the materials within the bias-Tee is not known. A dephasing of 1.65 mm would roughly correspond to a 30 to 40 % difference in ϵ which is realistic.

In addition, we saw in section D.2.1 that the bias-Tee should not be adapted to the measurement of low impedance samples because of a diverging cut-off frequency (equation D.3). The short is a good candidate to test this assertion. The difference of attenuation in Γ between the short and the bias-Tee is plotted figure D.5. Up to 500 MHz, the attenuation observed with the group {bias-Tee+ short} is of the order of ~ 0.15 dB more than with the short only. At higher frequency however, we do not observe any significant difference in attenuation [4]. Therefore, we should not encounter any problem for measuring low impedance samples at frequencies higher than $\sim$ 500 MHz. At frequencies lower than 500 MHz, the excess attenuation should be taken into account to have a correct calibration. It has not been the case in the presented work and will be addressed in the future to increase precision of the calibration at low frequencies.

4. It is less than 0.05 dB.

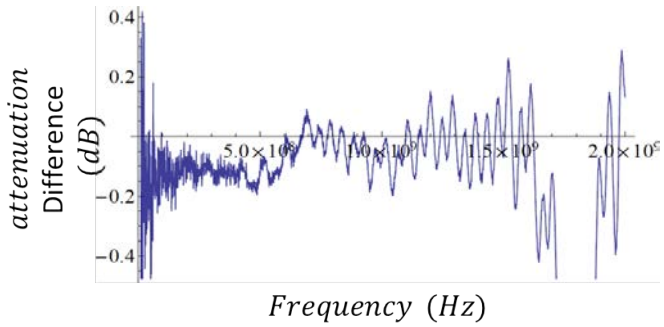

Figure D.5: Losses due to the bias-Tee measured with short terminated lines.

Appendix E

Influence of a parallel capacitance on the calibration

We saw in section 5.5 that the electrokinetic model for the sample should take into account an additive capacitance such as shown figure E.1. We also saw that the capacitance created between the vanadium film and the ground plane on the dial was of the order of 60 fF. This value cannot explain the weak frequency dependence of $Re(Z)$ in the normal state.
An additional capacitance could however come from a slight misalignment of the bias-Tee when it is soldered on the microwave lines. The exact value of this capacitance is however difficult to estimate but could be relatively large as schematically shown figure E.2. Indeed, the distance between the line and the ground plane of the bias-Tee can be arbitrarily small and the surface facing each other comparatively large.

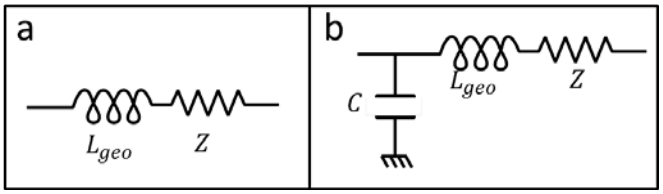

Figure E.1: (a) Lumped element representation of the sample by supposing it is assimilable to an inductance in series with Z. The inductance is due to the finite size of the sample. (b) Lumped element representation of the sample by assuming an additive capacitance.

One can then evaluate the influence of an additional capacitance on the calibration. In the following, we have studied the case of $C = 1$ pF. The influence of this capacitance will be different in the normal and superconducting states.
As can be seen figure E.3, taking into account C enables to explain a frequency-dependence of $Re(Z)$. At the same time, $Im(Z)$ is slightly shifted toward higher values, but is still compatible with a pure resistor within error bars.
On the superconducting side, as can be seen figure E.4, taking into account C does not measurably modify the calibration both for the Real and Imaginary parts of the film impedance.

Although this has not been implemented in this work, taking into account this additional capacitance would improve the sensitivity of the calibration procedure in the normal state.

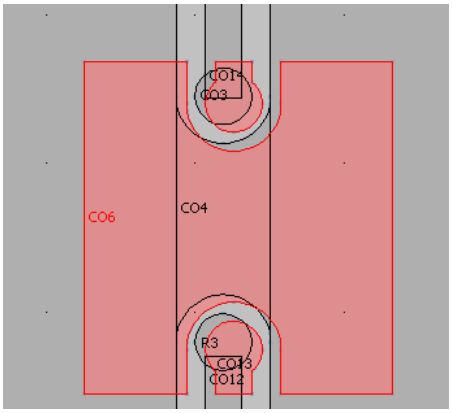

Figure E.2: Schematic representation of a misalignment between the bias-Tee and the microwave lines. The red surface represents the imprint of the bias-Tee.

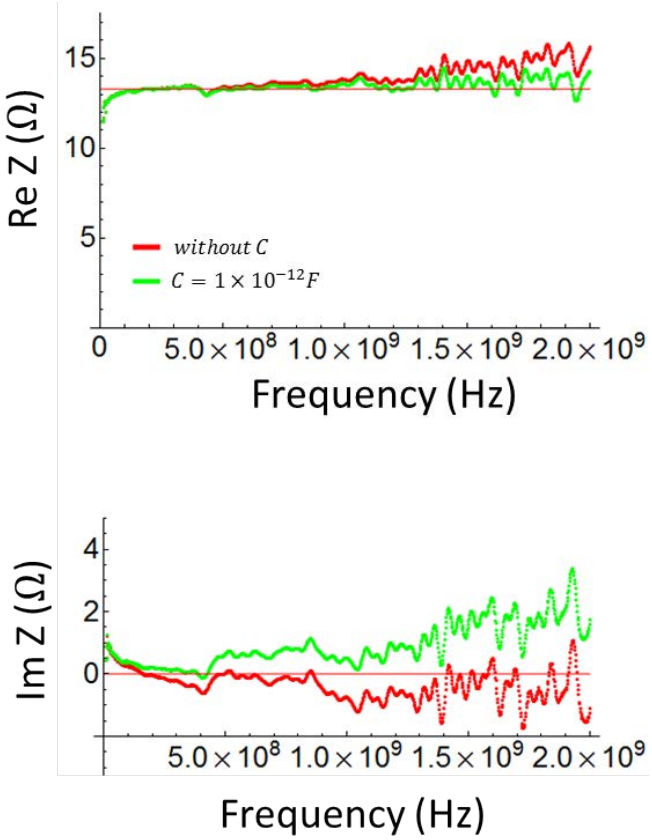

Figure E.3: Real and Imaginary parts of the film impedance in the normal state (4.4 K) as a function of frequency with and without taking into account an additional capacitance $C = 1$ pF. The results have been obtained with a standard Open Short Load calibration. The low frequency resistance is represented by a red line.

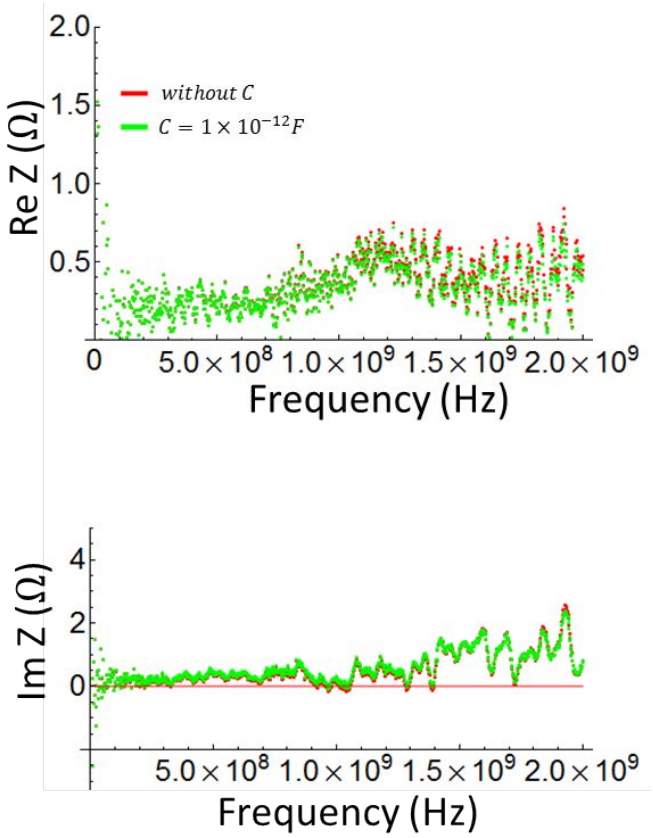

Figure E.4: Real and Imaginary parts of the film impedance in the superconducting state (2.6 K) as a function of frequency with and without taking into account an additional capacitance $C = 1$ pF. The results have been obtained with a standard Open Short Load calibration.

Appendix F

Résumé en Français

F.1 Introduction

Le désordre et ses conséquences sur les propriétés de transport des systèmes électroniques est un problème de longue date en physique de la matière condensée dont la compréhension a un intérêt à la fois théorique et expérimental. Cependant, il n'y a à ce jour aucune théorie permettant de décrire l'ensemble des phénomènes observés. Dans les métaux, lorsque le désordre est augmenté, une **transition Métal-Isolant** (TMI) peut apparaître. En effet, le désordre induit à la fois l'augmentation des interactions Coulombiennes et la localisation des porteurs de charge. L'existence de supraconductivité pour certains matériaux complexifie cette description. En effet, bien que la supraconductivité soit théoriquement insensible au désordre (théorème d'Anderson) la compétition entre condensation des paires de Cooper, interactions Coulombiennes et localisation donne lieu à la destruction de la supraconductivité à fort désordre. La compréhension des mécanismes à l'origine des transitions alors observées reste pour une grande part une question ouverte malgré une importante bibliographie remontant à plus de 50 ans.
Dans les systèmes bidimensionnels, l'existence d'états métalliques est théoriquement interdite par la localisation d'Anderson. Un matériau initialement supraconducteur devrait ainsi présenter une **transition directe supraconducteur-isolant** (TSI). Cependant, la compétition entre interactions Coulombiennes et fluctuations quantiques à basse dimension pourrait modifier ce paradigme. Ainsi, des états non prédits théoriquement pourraient émerger à basse dimension, tels que des états métalliques bi-dimensionnels (2D) entre les états supraconducteurs et isolants.

Ce travail vise à approfondir notre connaissance des phénomènes en jeu dans les films minces désordonnés, en particulier à proximité de la TSI induite par le désordre. Nous avons ainsi commencé par étudier les propriétés de transport électronique de films minces de Nb_xSi_{1-x} amorphe à basse température (T<1 K). Le but est de **comprendre l'origine d'états métalliques 2D observés dans ce système, ainsi que leur destruction par le désordre**. Ce dernier a été modifié en jouant sur l'épaisseur, la composition ou le traitement thermique appliqué aux films (ce dernier moyen expérimental permettant de modifier très progressivement le désordre).
La seconde partie de ce travail s'est concentrée sur la réponse électrodynamique de films supraconducteurs obtenue par réflectométrie micro-onde. Les mesures de transport électronique à haute fréquence sont en effet un moyen efficace de déterminer l'état fondamental et la nature des excitations qui coexistent dans un système donné. Cependant, elles nécessitent une connaissance parfaite de la réponse de l'environnement micro-onde de l'échantillon pour obtenir la conductivité intrinsèque du système mesuré. Il est ainsi nécessaire de calibrer parfaitement le dispositif. C'est le travail que nous avons entrepris au cours de cette thèse.
À terme, la comparaison des deux techniques (basse et haute fréquences) pourrait permettre d'approfondir la compréhension des différents mécanismes en jeu proche de la TSI, et ceci dans chaque phase observée proche de la transition, et à la transition elle même.

Dans ce résumé, nous allons commencer par faire ressortir les problématiques générales inhérentes à ce travail. Nous allons ensuite nous intéresser aux mesures basse fréquence effectuées sur l'alliage de a-Nb_xSi_{1-x} proche de la TSI. Cette étude a permis d'aboutir à une interprétation cohérente des mécanismes à l'origine des phénomènes observés expérimentalement. Enfin, nous allons détailler un nouveau dispositif que j'ai développé pour obtenir la conductivité complexe de films minces. Ce dispositif novateur, validé sur des films minces supraconducteurs de Vanadium, permettra à terme de sonder des films désordonnés proches de la TSI.

F.2 Problématique générale

F.2.1 Localisation dans les métaux

F.2.1.1 Localisation par le désordre

Lorsque le désordre est augmenté dans un matériau initialement métallique, les électrons peuvent, via la diffusion induite par le désordre, interférer avec eux-même. On parle alors de localisation faible. Ce régime induit des corrections à la conductivité et, in fine, la localisation des porteurs. Lorsque le désordre est suffisamment important, ou lorsque les corrections à la conductivité sont trop importantes, un régime fortement localisé émerge. On parle alors de **localisation d'Anderson**. Dans ce régime, la conduction se fait par sauts électroniques thermiquement activés.

Ainsi, le désordre peut induire, par la localisation faible ou la localisation forte, une transition Metal-Isolant. Le matériau passe ainsi, en fonction du désordre, d'un régime conducteur (fonction d'onde délocalisée) à un régime isolant (fonction d'onde localisée).

F.2.1.2 Localisation par les interactions

La modification des interactions dans les métaux peut également induire une transition Metal-Isolant. En effet, l'augmentation du désordre dans un matériau induit une diminution de l'écrantage électrostatique, et donc une augmentation des interactions Coulombiennes.

L'importance croissante de ces interactions avec le désordre donne lieu à une modification des lois de transport. En particulier, l'augmentation progressive des interactions dans un matériau initialement conducteur peut induire une diminution de la densité d'état instantanée au niveau de Fermi, jusqu'à obtenir un gap (**gap de Coulomb**) dans la densité d'état. Cette localisation se greffe aux effets de la localisation par le désordre et a tendance à en renforcer les effets.

F.2.1.3 Théorie de la localisation

Une description globale de la localisation a été proposée par Abrahams, Anderson, Licciardello & Ramakrishnan en 1979 [Abrahams et al., 1979]. Cette description, s'absolvant de modèle microscopique, regarde l'évolution de la conductance microscopique g en fonction de la dimension et de la taille du système.
En traçant l'évolution de $\beta = \frac{d\,ln(g)}{d\,ln(L)}$, caractérisant l'évolution de la conductance en fonction de la taille du système L, en fonction du logarithme de la conductance d'un bloc élémentaire du système $ln(g)$, les auteurs ont obtenu le graphique présenté figure F.1. L'un des résultats majeurs de ce travail est l'impossibilité d'avoir un état métallique 2D. En effet, $\beta < 0$ pour $d \leqslant 2$.

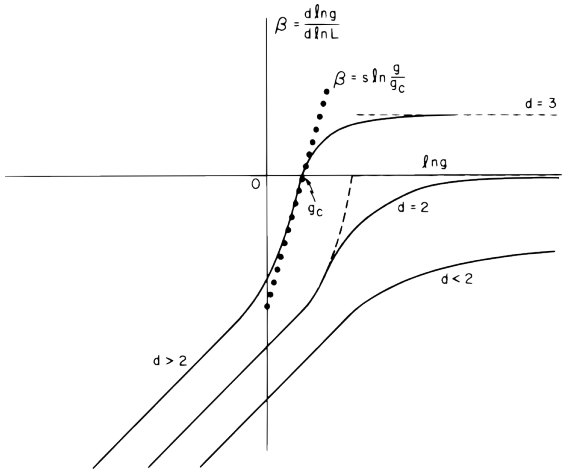

Figure F.1: La fonction de renormalisation β en fonction de la conductance g en dimensions 3, 2 et inférieure à 2 [Abrahams et al., 1979].

Notons que cette théorie s'applique dans le cas d'électrons n'interagissant pas (ou peu) entre eux. En effet, dans les systèmes présentant de fortes interactions Coulombiennes, comme dans les gaz 2D [Kravchenko et al., 1995], des états métalliques 2D ont déjà été observés.

F.2.2 Supraconductivité et désordre dans les systèmes bi-dimensionnels

En présence de supraconductivité, l'image précédemment donnée de la localisation se complexifie de par la **compétition entre l'établissement de la supraconductivité, la localisation et les interactions**. À 3D, les états fondamentaux accessibles dépendent de la position de cette transition supraconductrice par rapport à la transition Metal-Isolant qui apparaitrait en l'absence de supraconductivité.
À 2D, la dimension réduite augmente à la fois les fluctuations et les interactions Coulombiennes. Les états fondamentaux accessibles résultent ainsi de la compétition entre la localisation, interdisant l'établissement d'un état métallique à 2D, et d'autres phénomènes antagonistes qui doivent être considérés comme aussi importants. Du fait de la localisation, il est usuellement considéré que seuls deux états fondamentaux peuvent exister à 2D : un état supraconducteur et un état isolant.
Deux questions se posent alors :

- Quels sont les mécanismes à l'origine de la TSI à 2D ?
- Y a-t-il d'autres états fondamentaux accessibles?

F.2.2.1 Transition Supraconducteur-Isolant à 2D

Différents modèles théoriques se sont attelés à expliquer les mécanismes pouvant être à l'origine de la TSI à 2D. Ils se distinguent par la présence ou l'absence de paires de Cooper dans l'isolant, définissant respectivement des **modèles bosoniques** [Fisher and Lee, 1989] ou **fermioniques** [Maekawa and Fukuyama, 1982, Finkelstein, 1983, Finkel'stein, 1994] de la TSI. Ces modèles supposent généralement que les phases supraconductrice et isolante soient homogènes à proximité de la transition. Une autre possibilité à l'origine de la transition serait, en plus de cette dichotomie, la **présence d'inhomogénéité électronique** proche de la transition donnant lieu à des fluctuations de l'amplitude ou de la phase du paramètre d'ordre supraconducteur. Ces fluctuations seraient liées (mais non corrélées) au désordre [Bouadim et al., 2011] ou à des phénomènes de fluctuations mésoscopiques [Skvortsov and Feigel'man, 2005, Skvortsov, 2008]. Ce dernier phénomène se grefferait à un mécanisme purement fermionique de la TSI. Un matériau homogène deviendrait ainsi inhomogène électroniquement à proximité de la TSI sans pour autant remettre en cause le paradigme d'une transition directe à 2D.

F.2.2.2 D'autre états fondamentaux à 2D ?

Malgré l'interdiction théorique d'états métalliques 2D, de tels états ont été mesurés, notamment dans les matériaux granulaires [Jaeger et al., 1986, Jaeger et al., 1989, Christiansen et al., 2002] puis dans les matériaux homogènes en présence de champ magnétique [Mason and Kapitulnik, 1999].

De tels états métalliques 2D pourraient être liés à l'existence de fluctuations de l'amplitude du paramètre d'ordre supraconducteur mentionnées précédemment. Celles-ci pourraient donner lieu soit à l'existence d'états dans le gap supraconducteur [Feigel'man and Skvortsov, 2012] pouvant donner in fine naissance à un état métallique, soit à la formation d'îlots supraconducteurs [Spivak et al., 2001] qui, en se couplant, pourraient expliquer des saturations de la résistance à basse température [Feigel'man and Larkin, 1998, Das and Doniach, 1999, Dalidovich and Phillips, 2002, Phillips and Dalidovich, 2003].

F.3 Mesures basse fréquences

Au cours de cette thèse, et afin d'étudier les effets du désordre sur la TSI et les états fondamentaux accessibles en sa proximité, nous avons utilisé un alliage de NbSi amorphe (a-Nb_xSi_{1-x}). Ces films, protégés par une couche de SiO, ont été obtenus dans un bâti sous ultra-vide par co-évaporation de Niobium et de Silicium. Ils seront dans cette partie caractérisés par des mesures électroniques basse fréquence ($\lesssim$ 40 Hz). Ces mesures ont été effectuées dans un cryostat à dilution dont la température de base est de 7 mK. Un soin particulier a été apporté au filtrage des lignes électriques et à l'élimination d'effets parasites pouvant perturber le résultat des mesures à basse température.

F.3.1 Travaux préliminaires sur le NbSi

F.3.1.1 Ajustement du désordre dans les films minces

Les films étudiés dans cette thèse sont dans la limite 2D au regard des dimensions d'intéret pour la TSI, i.e. les longueurs relatives à la supraconductivité (longueur de cohérence supraconductrice ξ), aux interactions Coulombiennes (longueur thermique L_T) et à la localisation (longueur de Thouless L_{th}). Nous allons ainsi utiliser la résistance carrée mesurée à 4K $R_{\square,4K}$, notée dans la suite R_{4K}, ou de manière équivalente $\sigma_{4K} = 1/R_{4K}$, pour caractériser le désordre dans nos films. En effet, à 2D, le modèle du gaz de Fermi donne $\sigma_{4K} \propto k_F l$, produit du vecteur d'onde de Fermi et du libre parcours moyen ($k_F l$, paramètre de Ioffe-Regel, est le critère usuel utilisé pour caractériser le désordre).
À 3D, le a-Nb_xSi_{1-x} peut avoir un état fondamental supraconducteur, métallique ou isolant en fonction du désordre [Bishop et al., 1985, Marnieros, 1998]. À 2D, les théories conventionnelles de la TSI prédisent une transition directe entre la phase supraconductrice et isolante pilotée par le désordre.

Afin de traverser la Transition Supraconducteur-Isolant par le désordre, nous pouvons modifier plusieur paramètres expérimentaux :

- Nous pouvons modifier la composition x de films de a-Nb_xSi_{1-x} (figure F.2.a). Pour les films présentés (qui ont une épaisseur fixée de 12.5 nm), l'état fondamental est supraconducteur (au sens de $\frac{dR}{dT} > 0$ et $R = 0$ à basse température, avec une transition supraconductrice) lorsque $x \geqslant 14$ % et isolant (au sens de $\frac{dR}{dT} < 0$ à basse température) pour $x \leqslant 13$ %.
- Nous pouvons modifier l'épaisseur des films (figure F.2.b)). Pour les films présentés (a-$Nb_{18}Si_{82}$), l'état fondamental est supraconducteur lorsque $d_\perp \geqslant 45$Å et isolant (au sens de $\frac{dR}{dT} < 0$) pour $d_\perp \leqslant 30$Å.
- Nous pouvons recuire nos films à une température θ, permettant d'augmenter finement le désordre au sein d'un unique échantillon (figure F.2.c)). Cette procédure est effectuée sous atmosphère d'azote dans un four dédié afin d'éviter la contamination des échantillons.

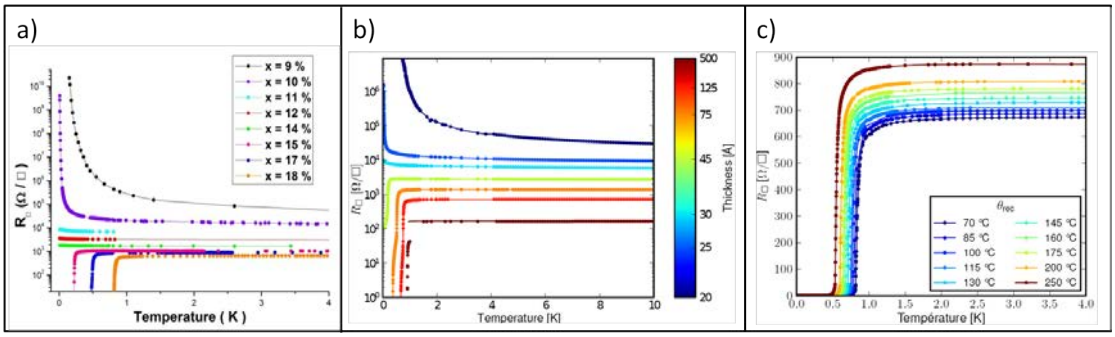

Figure F.2: Évolution de l'état fondamental de films minces de a-Nb_xSi_{1-x} en modifiant a) la composition x, b) l'épaisseur et c) la température de recuit des films.

En modifiant finement le désordre au voisinage de la transition Supraconducteur-Isolant, des états fondamentaux métalliques ont été observés (figure F.3)[Couëdo, 2014]. En effet, en mesurant la résistance carrée d'un film de a-$Nb_{13.5}Si_{86.5}$ de 23 nm initialement supraconducteur et en utilisant la procédure de recuit, l'état fondamental évolue vers des états métalliques (saturation de la résistance à basse température) avant un éventuel état isolant rencontré dans des

films plus désordonnés.

Les phases 2D suivantes ont ainsi été définies :
- **Une phase supraconductrice** présentant une transition supraconductrice à T_c ($R_\square = 0$ aux plus basses températures).
- **Un premier état métallique**, qu'on appellera dans la suite **M1**, qui est caractérisé par une évolution de la résistance comparable à la phase supraconductrice, mais ayant une résistance finie aux plus basses températures (absence de cohérence de phase sur l'ensemble de l'échantillon). Ce métal a des caractéristiques similaires à ce qui a été observé dans des systèmes modèles obtenus en construisant des réseaux 2D de jonctions SNS [Eley et al., 2012, Han et al., 2014].
- **Un second état métallique**, qu'on appellera dans la suite **M2**. Dans cet état métallique, $\frac{dR}{dT} \leqslant 0$ à toute température. La résistance sature cependant à une value finie aux plus basses températures.
- **Un régime isolant**, avec une résistance infinie à température nulle.

Les caractéristiques des différentes phases (ou régimes) obtenues à basses températures sont résumées dans le tableau ci-dessous :

	Résistance (T $\to$ 0)	transition supraconductrice	$\frac{dR}{dT}$ à basse température
Supraconducteur	0	oui	+
M1	constante $\neq 0$	transition partielle	+
M2	constante $\neq 0$	non	-
Isolant	∞	non	-

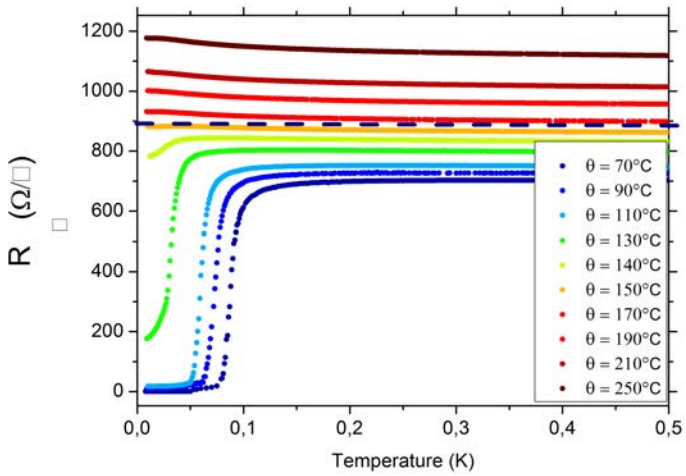

Figure F.3: Évolution de l'état fondamental d'un unique film de a-$Nb_{13.5}Si_{86.5}$ de 23 nm d'épaisseur en fonction de la température de recuit θ appliquée au film.

F.3.1.2 Le diagramme de phase du NbSi à 2D

Au début de ce travail, le diagramme de phase du a-Nb_xSi_{1-x} était tel que présenté figure F.4. Dans ce diagramme, la phase (ou régime) obtenue est présentée en fonction du désordre (mesuré par σ_{4K}, la conductance carrée du film à 4 K) et de l'épaisseur du film. Lorsque le désordre est augmenté (σ_{4K} diminue) à partir d'un état supraconducteur, l'état M1 apparaît. Lorsque le désordre est augmenté à nouveau, cet état transite vers l'état fondamental métallique M2. À plus fort désordre, un état isolant est obtenu.

Les différentes phases ont été caractérisées dans [Couëdo, 2014]. Cependant, bien qu'il semble intuitif que la supraconductivité joue un rôle pour l'état fondamental M1, la nature des différentes phases et transitions restaient, à ce point, à déterminer.

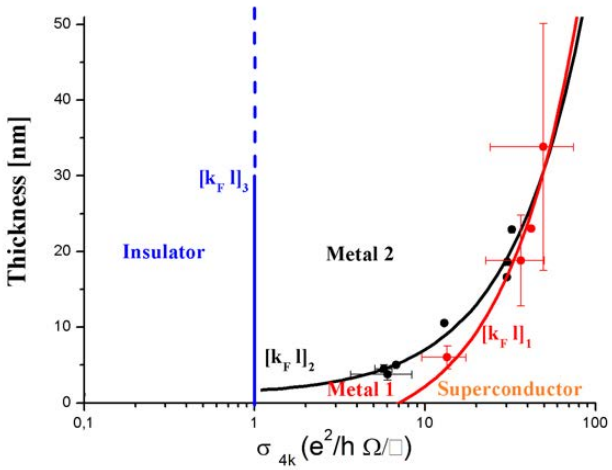

Figure F.4: Diagramme de phase du a-Nb_xSi_{1-x} en fonction de l'épaisseur et du désordre (mesuré par σ_{4K}). Les lignes sont des guides pour les yeux. La ligne bleue correspond au critère de Ioffe-Regel pour la transition Metal-Isolant à 3D. Adapté de [Couëdo, 2014].

F.3.2 Résultat expérimentaux

F.3.2.1 Les phases métalliques

Au cours de cette thèse, nous nous sommes principalement intéressés à la transition M2-Isolant. Nous avons cependant également regardé les loi d'évolution de la résistance en fonction de la température dans les autres régimes.
Dans les échantillons métalliques, nous avons rencontré trois comportements d'évolution de la résistance carrée en fonction de la température :

- **Dans M1** (figure F.5.a), la conductivité suit une loi de localisation faible 2D à basse température ($T \lesssim 1$ K), jusqu'à ce que la résistance diminue probablement due à des fluctuations supraconductrices. À très basses températures, la résistance tend à saturer.
- **Dans M2**,
  - **Proche de la transition M1-M2, dans M2**, la conductivité suit une loi de localisation faible 2D avant la saturation de la résistance aux plus basses températures (figure F.5.b).
  - **Proche de la transition M2-Isolant, dans M2**, la situation devient plus complexe. L'évolution de la résistance avec la température ne peut s'expliquer que par des lois de conduction plus isolantes que la localisation faible aux plus basses températures (typiquement $T \lesssim 300$ mK) avant une saturation de la résistance (observée typiquement à des températures $T \lesssim 30$ mK). Nous avons trouvé que ces lois étaient compatibles avec des lois d'isolantes de la forme $R_\square = R_M e^{(T_M/T)^n}$ dans une gamme de température intermédiaire. On a donc décrit l'évolution de la conductivité dans ce régime par, successivement, une saturation de la résistance, une loi de transport thermiquement activée et, à plus haute température, une évolution de la conductance suivant la localisation faible (figure F.5.c).

Dans cette section, nous allons nous intéresser à ces différents comportements ainsi qu'à l'évolution de la conductivité mesurée à 10 mK en fonction du désordre dans ces régimes.

Localisation faible Dans l'ensemble des métaux 2D mesurés (M1 et M2), un régime de localisation faible 2D a été observé. Dans ce régime, la conductivité est décrite par :

$$\sigma(T) = \sigma_0 + \alpha_{WL} ln(T) \tag{F.1}$$

où σ_0 est la conductivité de Drude et α_{WL} est une constante valant théoriquement $(\beta + (1 - \frac{3}{4}F))\ \frac{e^2}{2\hbar\pi^2}$ où β est une constante lié au phénomène d'interférence électronique en présence de désordre et F est le paramètre de Hartree rendant compte de l'importance des interactions Coulombiennes. Du fait de l'augmentation de ces interactions avec le désordre, α_{WL} est théoriquement une fonction monotone augmentant avec le désordre. Cependant, pour un film unique recuit successivement et présentant les régimes M1 et M2 en fonction du désordre (figure F.6.a.), bien

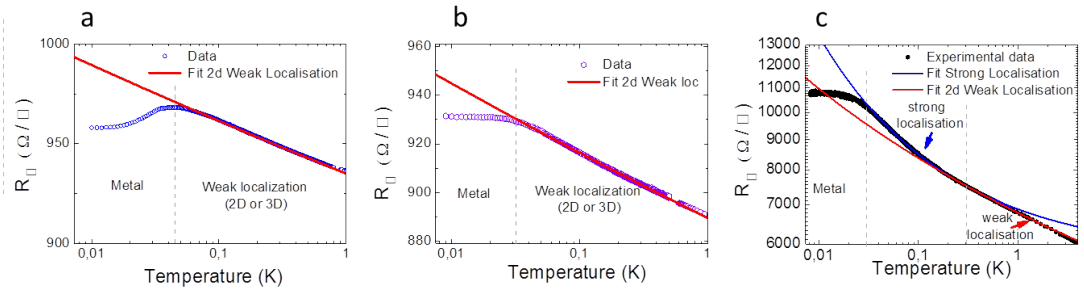

Figure F.5: Présentation des différents régimes observés dans les échantillons métalliques : (a) dans les films M1,(b) dans les films M2 proches de la transition M1-M2 et (c) dans les films M2 les plus désordonnés.

que α_{WL} augmente comme attendu dans le régime M1, la variation de ce paramètre diffère dans le régime M2 (figure F.6.b.). À plus fort désordre, dans le régime M2, α_{WL} diminue lorsque le désordre augmente jusqu'à $\sigma_{4K} \sim 5\,\frac{e^2}{h}$ (figure F.7). Pour les échantillons plus proches de la transition M2-Isolant, α_{WL} semble augmenter de nouveau avec le désordre. Ces derniers échantillons présentent également un régime plus isolant que la localisation faible aux plus basses températures avant saturation de la résistance.

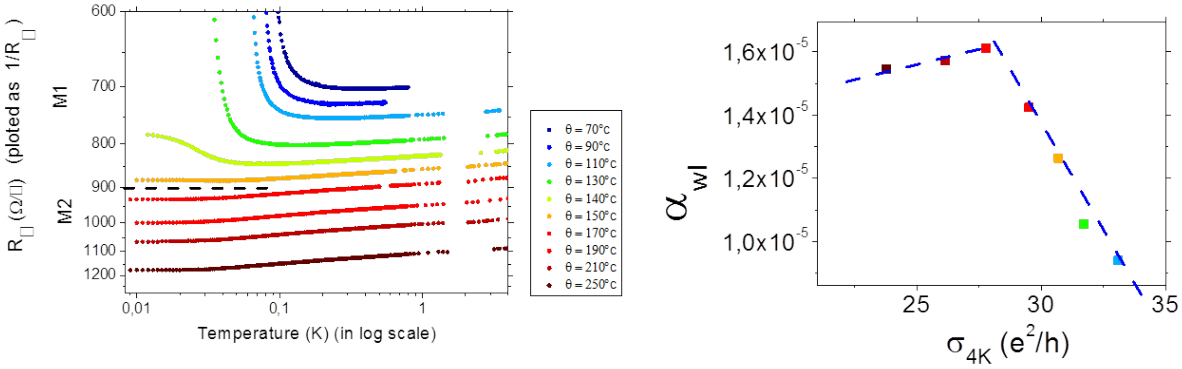

Figure F.6: (Gauche) Conductance d'un film de a-$Nb_{13.5}Si_{86.5}$ de 228 Å pour différentes températures de recuit. La ligne pointillée correspond à la transition M1-M2 telle qu'identifiée dans [Couëdo, 2014].(Droite) Évolution du paramètre α_{wl} en fonction de σ_{4K} pour le même échantillon recuit. La ligne bleue pointillée est un guide pour les yeux.

Précurseur isolant dans l'état Métallique M2 Ce régime plus isolant, observé à des températures intermédiaires, est compatible avec une loi de type 2D Mott VRH ($R_\square = R_M e^{(T_M/T)^n}$ avec $n = \frac{1}{3}$) bien que la résistance sature aux plus basses températures, comme montré par la technique de Zabrodskii (figure sur un échantillon de 50 Å de a-$Nb_{13.5}Si_{86.5}$ ($\sigma_{4K} \sim 4.3\frac{e^2}{h}$) figure F.8). La persistance de la saturation malgré la présence de ce régime fortement isolant pourrait être un signe d'inhomogénéité électronique, et en particulier pourrait être liée à la survie d'îlots supraconducteurs à fort désordre. Ce résultat est l'un des résultats majeur de cette thèse.
En approchant la transition M2-Isolant, nous avons également observé une évolution des lois activées. En effet, en utilisant la technique de Zabrodskii pour suivre l'évolution du paramètre n, nous avons observé son augmentation en fonction du désordre sur différents échantillons proches de la transition (figure F.9 et F.10). Cette évolution s'accompagne par une disparition progressive de la saturation mesurée aux plus basses températures (figure F.9).

Évolution du minimum de conductivité dans la phase métallique M2 Le régime métallique M2 dans le a-Nb_xSi_{1-x} est par ailleurs caractérisé, entre autres, par une saturation de

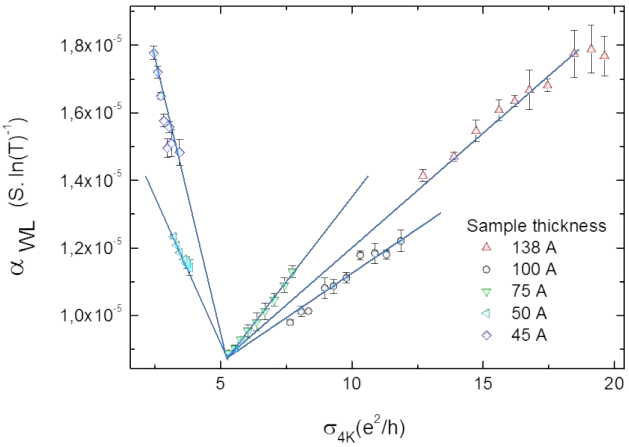

Figure F.7: Évolution de α_{wl} en fonction de σ_{4K} pour des échantillons de a-$Nb_{13.5}Si_{86.5}$ de différentes épaisseurs et températures de recuit. Les lignes bleues sont des guides pour les yeux.

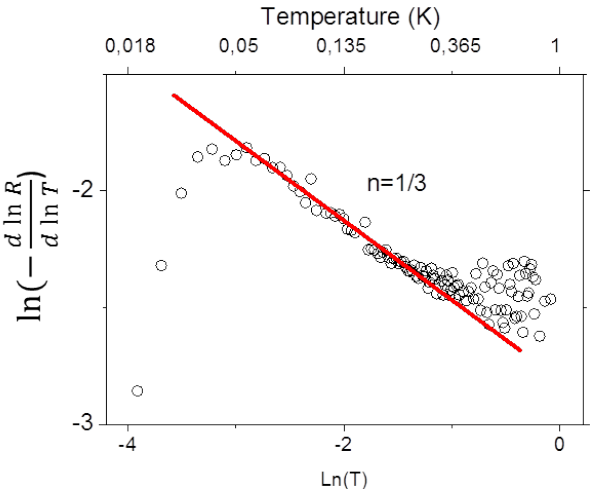

Figure F.8: Application de la méthode de Zabrodskii [Zabrodskii and Zinoveva, 1984] à un échantillon de 50 Å de a-$Nb_{13.5}Si_{86.5}$. La dépendance linéaire sur une décade en température avec une pente de 1/3 (ligne rouge) est le signe d'un régime 2D Mott VRH.

la résistance carrée aux plus basses températures. La valeur de la conductivité carrée correspondante, $\sigma_{min} = \sigma_{\square}(10mK)$, est représentée figure F.11. À faible désordre, $\sigma_{min} \sim \sigma_{4K}$. Proche de la transition M2-Isolant, l'évolution devient plus marquée : σ_{min} évolue plus rapidement et $\sigma_{min}(\sigma_{4K} = 3\frac{e^2}{h}) \to 0$ marque la transition entre les régimes métallique et isolant.

F.3.2.2 Le régime Isolant

Dans le régime de résistance activée, observé dans l'isolant, la résistance prend la forme :

$$R = R_0 e^{(\frac{T_0}{T})^n} \tag{F.2}$$

où R_0, T_0 et n sont des constantes caractéristiques du mécanisme de conduction:
- $n = 1/3$ pour une loi de saut à distance variable (Variable Range Hopping ou VRH) de type Mott 2D (2D Mott VRH).
- $n = 1/2$ pour une loi de saut à distance variable de type Efros-Shklovskii (ES VRH).
- $n = 1$ dans le cas d'une loi simplement activée (comme le saut entre plus proches voisins par exemple).

Dans le régime isolant, nous pouvons identifier en utilisant la méthode de Zabrodskii les differents régimes. Nous observons systématiquement diverses lois isolantes, avec un régime $n \sim 1$ aux plus basses températures (figure F.12) et des régimes de loi de saut à distance variable à plus hautes températures. Nous avons noté que certaines lois étaient plus isolantes que simplement

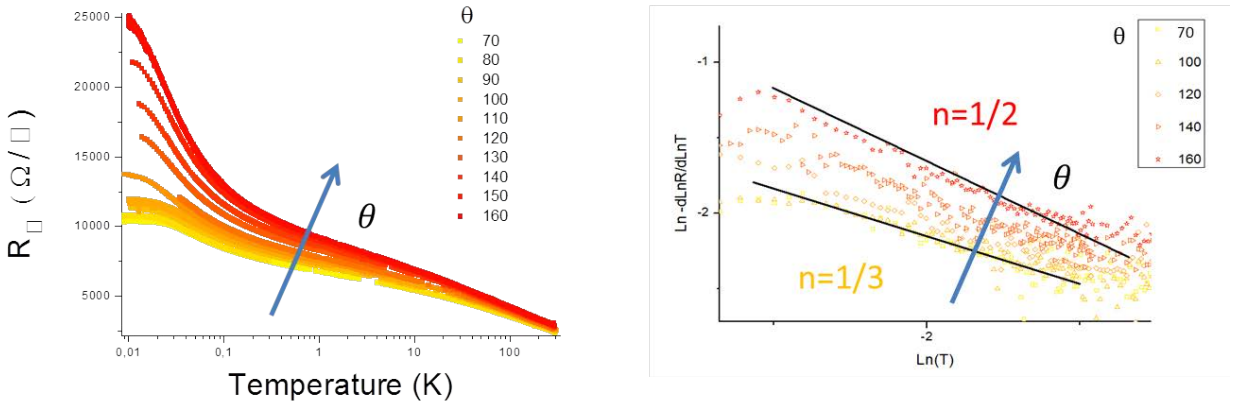

Figure F.9: (Gauche) Évolution de la résistance carrée en fonction de la température d'un film de 50 Å de a-$Nb_{13.5}Si_{86.5}$ recuit à différentes températures θ (en ℃). (Droite) Application de la méthode de Zabrodskii à ce film. Seule une sélection de θ est présentée par soucis de clarté.

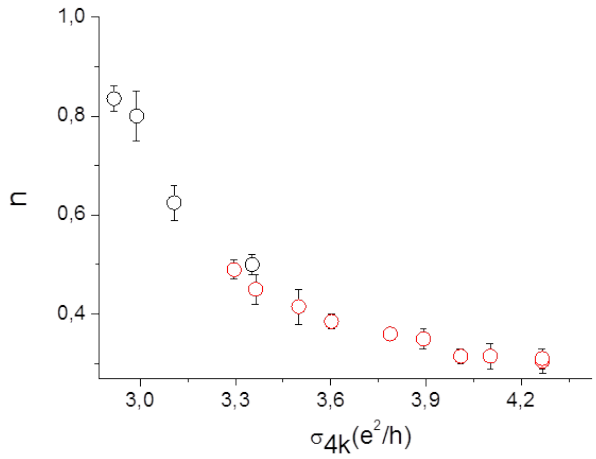

Figure F.10: Évolution du paramètre n en fonction du désordre pour des films de 45 et 50 Å de a-$Nb_{13.5}Si_{86.5}$ recuits à différentes températures.

activé (figure F.13). De telles lois isolantes, avec n>1, n'ont été trouvées que sur des échantillons très proches de la transition M2-Isolant (typiquement $1.5\frac{e^2}{h} < \sigma_{4K} < 3\frac{e^2}{h}$) et pourraient être liés à l'existence d'îlots supraconducteurs dans l'isolant diminuant la probabilité de saut électronique [Kim et al., 1992]. Les échantillons les plus désordonnés montrent un régime avec $n = 1$ (en prenant en compte les barres d'erreur) aux plus basses températures.

Nous définissons les températures de crossover entre les différents régimes comme suit :

- T_{c1} **la plus haute température pour laquelle un régime** $n \sim 1$ **est identifié.**
- T_{c2} **la plus haute température pour laquelle un régime ES VRH est identifié.**
- T_{c3} **la plus haute température pour laquelle un régime Mott VRH est identifié.**

Dépendement du désordre, nous observons ces différents crossovers comme résumé figure F.14. Lorsque le désordre est diminué, i.e. en s'approchant par le côté isolant de la transition M2-Isolant, les différentes températures de crossover diminuent continument. De plus, la température à laquelle le régime simplement activé est observable diminue considérablement à proximité de la transition ($\sigma_{4K} = 3\frac{e^2}{h}$) tout comme la température maximale sur laquelle est observée le régime de Mott. Cet effondrement marque la transition M2-Isolant.

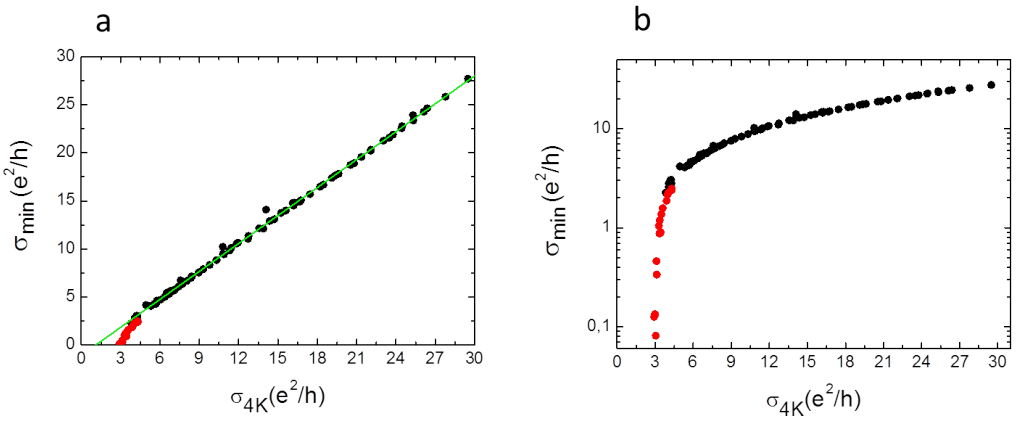

Figure F.11: σ_{min} en fonction de σ_{4K} en échelle linéaire (a) et semilog (b). En rouge, σ_{min} obtenue pour les échantillons fabriqués pour cette thèse. En noir, σ_{min} obtenu à partir d'échantillons de [Marrache-Kikuchi, 2006] [Crauste, 2010] [Couëdo, 2014]. En vert, fit des data expérimentales avec $\sigma_{min} = 0.97\sigma_{4K} - 1.05$ (en unité de $\frac{e^2}{h}$).

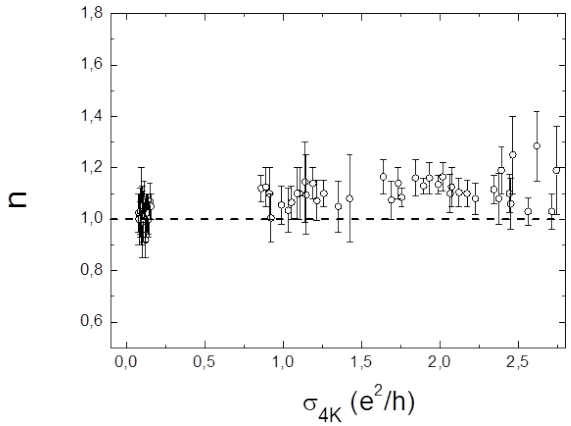

Figure F.12: Paramètre n en fonction de σ_{4K}, extrait en employant la méthode de Zabrodskii dans le régime observé aux plus basses températures dans les échantillons isolants.

F.3.2.3 Continuité des lois entre les régimes M2 et isolant

Nous avons caractérisé dans cette thèse des lois isolantes activées des deux côtés de la transition M2-Isolant. Dans chaque cas, en utilisant la méthode de Zabrodskii, nous avons extrait le paramètre n associé au processus de conduction (figure F.15 [1]). Nous observons une continuité de l'évolution de n des deux côtés de la transition M2-Isolant. En utilisant les paramètres extraits, nous pouvons également extraire les températures et résistances caractéristiques associées à ces lois de conduction (figures F.16 et F.17).

Pour les échantillons métalliques :
- lorsque $5.5 > \sigma_{4K} > 4\frac{e^2}{h}$, $n = 1/3$ dans le régime isolant rencontré à température intermédiaire. La résistance sature aux plus basses températures.
- lorsque $4 > \sigma_{4K} > 3\frac{e^2}{h}$, n augmente avec le désordre bien qu'une saturation de la résistance soit toujours observée aux plus basses températures.
- les paramètres caractéristiques de ce régime isolant (température et résistance caractéristiques du processus de conduction, nommés (R_M, T_M) lorsqu'un régime VRH de type Mott est observé et (R_n, T_n) lorsque le paramètre n évolue) augmentent continument avec le désordre.

1. Dans le régime isolant, seuls les loi isolantes avec $n \sim 1$ et ES VRH sont représentées. De plus, les échantillons présentant $n > 1.2$ ne sont pas représentés.

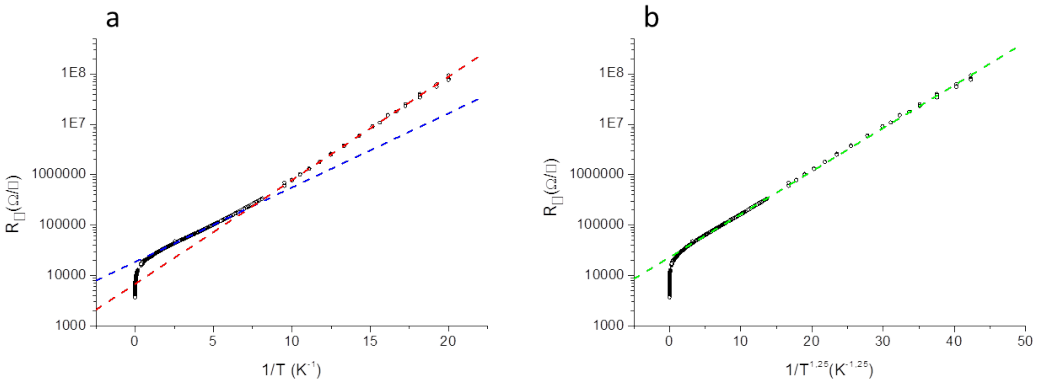

Figure F.13: Résistance carrée d'un film de 45 Å de a-$Nb_{13.5}Si_{86.5}$ isolant recuit à 140℃ représenté en fonction de 1/T (a) et en fonction de $1/T^{1.25}$ (b). Le regime isolant observé pour ce film est plus isolant qu'une loi simplement activé (n=1).

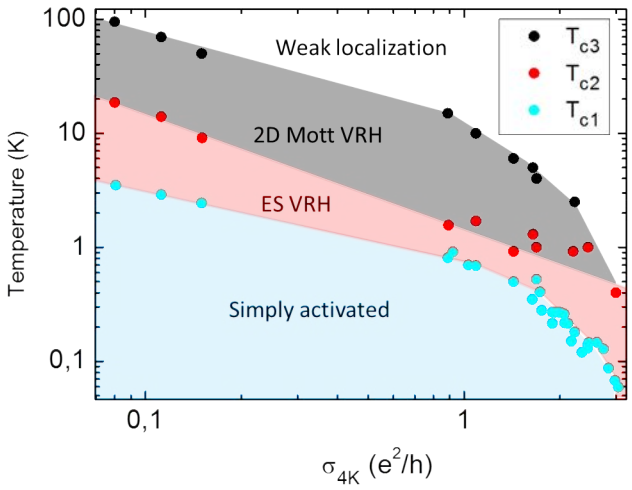

Figure F.14: Températures de crossover T_{c1} (points bleus), T_{c2} (points rouges) and T_{c3} (points noirs) en fonction de σ_{4K} pour les films isolants.

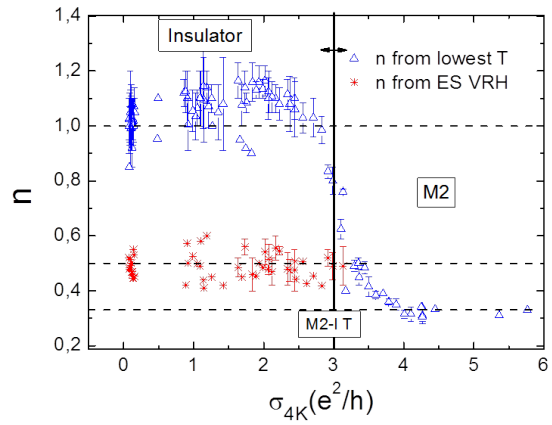

Figure F.15: Évolution du paramètre n en fonction de σ_{4K}. Les lignes discontinues correspondent à $n = \frac{1}{3}$, $n = \frac{1}{2}$ et $n = 1$. Les échantillons utilisés sont issus de cette thèse et de [Marrache-Kikuchi, 2006]. Ils incluent des échantillons de compositions variant entre 8 et 13.5% en composition de Nb, et dont les épaisseurs vont de 30 à 250 Å.

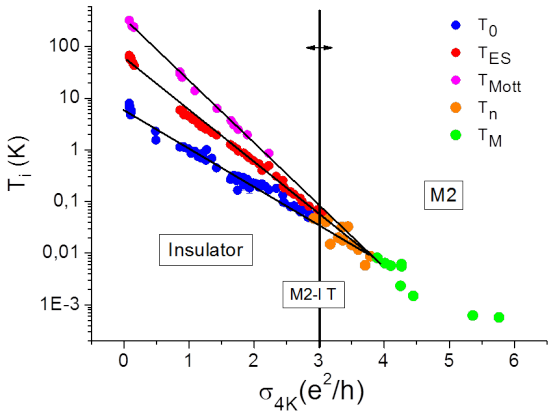

Figure F.16: Évolution des énergies caractéristiques des régimes activés observés dans les échantillons présentés figure F.15. T_0, T_n, T_{ES}, T_{Mott} et T_M correspondent respectivement aux énergies caractéristiques observées dans le régime $n \sim 1$, dans le régime avec n variable, dans le régime ES VRH, dans le régime 2D Mott VRH dans les échantillons isolants, et dans le régime 2D Mott VRH dans les échantillons métalliques.

Pour les échantillons isolants :

- différentes lois isolantes sont observées (avec $n \sim 1$ puis VRH) avec systématiquement $T_0 < T_{ES} < T_{Mott}$ pour les énergies caractéristiques respectivement des régimes avec $n \sim 1$, ES VRH et 2D Mott VRH lorsque ces 3 régimes sont observés. La hiérarchie entre T_{ES} et T_{Mott} est celle attendue du fait de l'ouverture d'un gap de Coulomb dans la densité d'état instantanée au niveau de Fermi.
- T_{ES} et T_0 convergent à proximité de la transition M2-Isolant, marquant une probable relation entre les régimes $n \sim 1$ et ES VRH. Le régime $n \sim 1$ serait lié principalement à la suppression de la densité d'état à basse énergie par les interactions Coulombiennes.
- les différentes résistances caractéristiques des différents régimes observés augmentent lorsque le désordre diminue, et tendent à saturer lorsqu'on s'approche de la transition, marquant l'importance des interactions Coulombiennes dans ce système. Le régime de saut électronique assisté par les phonons deviendrait un régime de saut électronique assisté par les interactions Coulombiennes proche de la transition M2-Isolant.

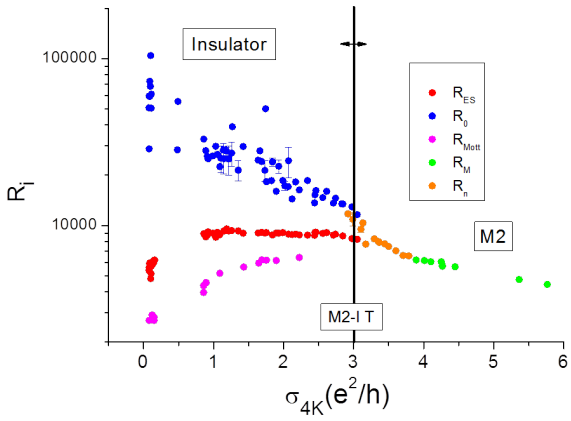

Figure F.17: Évolution des préfacteurs des différentes lois activées pour les échantillons présentés figure F.15.

F.3.2.4 Conclusion des mesures basse fréquence

Les résultats expérimentaux obtenus dans cette partie sont compatibles avec l'établissement d'une phase fortement inhomogène à proximité de la transition. Différents indices pointent en faveur de l'existence d'excitations supraconductrices dans les différents états fondamentaux non supraconducteurs observés (M1, M2 et Isolant proche de la transition M2-Isolant). Ces états fondamentaux seraient composées de 2 fluides comme représenté figure F.18, des îlots supraconducteurs se couplant par effet Josephson pour donner naissance aux régimes métalliques observés. La principale différence entre ces états seraient alors la taille des îlots supraconducteurs et la nature de la matrice dans laquelle ces îlots existent. Ainsi seules les phases supraconductrice à très faible désordre et isolantes à très fort désordre seraient homogènes. La transition Supraconducteur-M1 aurait lieu lorsqu'il n'existerait plus de chemin supraconducteur percolant dans le matériau et les phases M1 et M2 auraient une nature microscopique similaire, avec une matrice (faiblement ou fortement) isolante dans laquelle des îlots supraconducteur persisteraient.

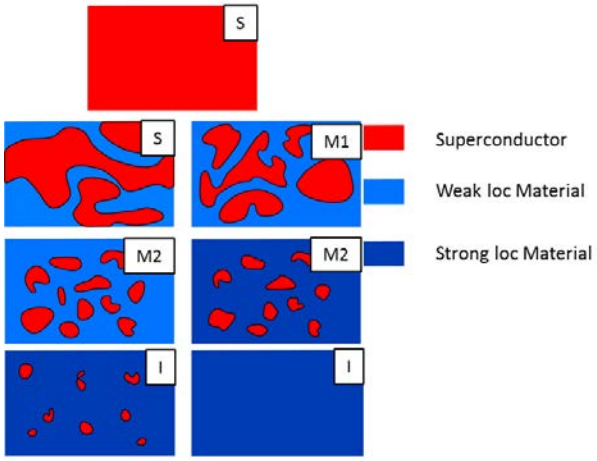

Figure F.18: Représentation schématique des différents états fondamentaux observés durant cette thèse.

F.4 Mesures hautes fréquences

Il existe plusieurs intérêts à utiliser des mesures hautes fréquences pour mesurer les films à proximité de la TSI :

- la présence d'une transition de phase quantique, ou celle d'un crossover, induit une loi d'échelle de la conductivité en fonction de la température. Cette renormalisation permet d'obtenir de précieuses informations sur la nature de la transition et notamment sur sa classe d'universalité. L'influence de la température n'est cependant pas le seul moyen d'obtenir ces informations : on peut également faire varier la fréquence de mesure pour sonder le système sur différentes plages d'énergie. L'obtention d'une loi d'échelle en fréquence permet alors également de sonder la nature de la transition de phase observée lorsqu'on travaille dans le régime quantique, i.e. à des fréquences telles que $\hbar\omega > k_B T$.
- les mesures hautes fréquences sont sensibles à la nature des porteurs de charge dans le régime classique ($\hbar\omega < k_B T$). Dans le cas d'états inhomogènes, et en particulier en présence de supraconductivité comme présenté figure F.18, il est ainsi intéressant d'utiliser des techniques hautes fréquences pour tester la présence d'excitation supraconductrice dans un matériau donné.

Dans un avenir proche, nous aimerions ainsi utiliser les hautes fréquences pour sonder les mécanismes en jeu à proximité de la transition Supraconducteur-Isolant, en particulier dans le a-Nb_xSi_{1-x}. Dans ce matériau, dans la phase supraconductrice proche de la TSI, la transition supraconductrice peut se produire à des températures inférieures à 100 mK. Nous nous sommes donc intéressés au développement d'une technique de mesure permettant d'obtenir directement la conductivité complexe d'un système sur une gamme de fréquences allant jusqu'à 2 GHz, fréquence correspondante en énergie à cette température critique de 100 mK, afin de pouvoir avoir à la fois accès au régime quantique ($\hbar\omega > k_B T$) et classique ($\hbar\omega > k_B T$). L'accès à ces différents régimes permettrait respectivement, à terme, de déterminer la nature de la TSI par la renormalisation en fréquence et d'avoir accès à la nature des porteurs et ainsi de confirmer les hypothèses formulées sur la nature des régimes métalliques observés (voir figure F.18). La réflectométrie micro-onde large bande, permettant un balayage en fréquence sur un unique échantillon, semble particulièrement adaptée à cet usage.

F.4.1 Développement d'un dispositif de calibration pour la réflectométrie micro-onde

L'utilisation de mesures large bande alliées avec des techniques cryogéniques implique cependant un certain nombre de développements expérimentaux pour permettre de s'affranchir de l'environnement micro-onde et de mesurer la réponse intrinsèque de l'échantillon. Pour ce faire, nous avons développé une technique de calibration à basse température basée sur la mesure de 3 standards : un circuit ouvert (Open) de résistance infinie, un circuit fermé (Short) de résistance nulle, et une charge résistive de 50 Ω (Load) adaptée au design de la ligne micro-onde (typ. 50 Ω par construction). Ces références permettent de caractériser le dispositif et de s'affranchir d'effets parasites lors de la mesure.

Pour mesurer toutes ces références lors d'une seule mise à froid, et afin de limiter ainsi les problèmes de reproductibilité liés notamment aux cyclages thermiques des différents éléments du dispositif, j'ai développé un dispositif de rotation à froid (figure F.19) permettant de faire le contact entre des parties fixes du dispositif dans le cryostat et différentes pistes disposées sur un cadran [2] sur lequel sont disposés les différentes références et l'échantillon (figure F.20).

Les éléments clef du dispositif sont :

- un arbre de rotation, actionné à l'extérieur du cryostat, permettant via un jeu d'engrenages de faire tourner une ligne radio-fréquence reliée à un connecteur à angle droit (ce dernier faisant la transition entre la ligne RF et le cadran).
- un connecteur glissant permettant une transition entre les lignes radio-fréquence fixes à l'intérieur du cryostat et la prolongation rotative.
- un ressort, couplé à une portion semi-rigide de câble coaxial radio-fréquence en amont du montage, permettant de forcer le contact du connecteur à angle droit et d'avoir un bon contact électrique avec les pistes électriques du cadran.

2. Le design des lignes a été optimisé en utilisant un logiciel de simulation radio-fréquence.

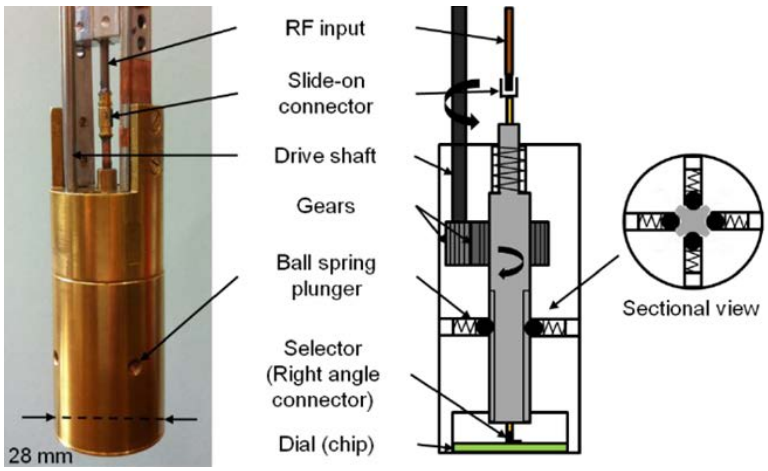

Figure F.19: (Gauche) Photographie du dispositif permettant la sélection des lignes sur le cadran. (Droite) Représentation schématique du dispositif [Diener et al., 2014].

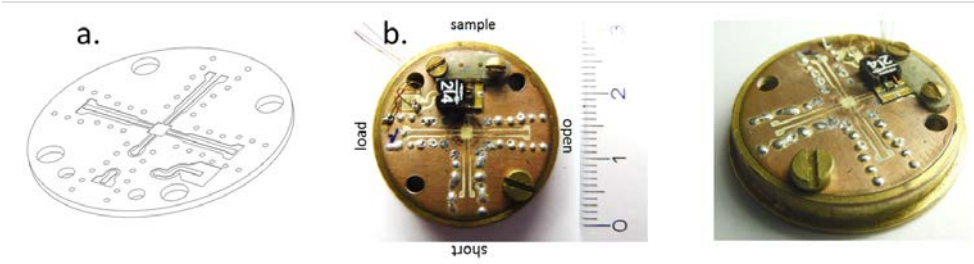

Figure F.20: (a) Représentation 3D du cadran dessiné avec Solidworks©. (b) Photo du cadran une fois assemblé.

- le cadran, sur lequel sont monté les différentes références et l'échantillon.
- l'échantillon, contacté en flip-chip et serré sur la piste de cuivre par une bande de PVC. Ce stratagème permet d'éviter de connecter l'échantillon par des fils de bonding (1 nH/mm de fil, correspondant à une resistance de 6 Ω/mm à 1 GHz, ne permettant pas d'atteindre la résolution recherchée).
- Un bias-Tee, élément passif permettant de mesurer l'échantillon simultanément à haute et à basse fréquence sans perturber les mesures.

F.4.2 Validation du dispositif et mesure de film mince de Vanadium supraconducteur

Pour valider le dispositif, nous avons utilisé un film supraconducteur de Vanadium de 100 Å ayant une transition supraconductrice autour de 3.6 K. L'avantage d'un film supraconducteur est de pouvoir mesurer, sur un même échantillon, un comportement purement résistif (état normal) et purement inductif (état supraconducteur) en fonction de la température.
En utilisant ce film, nous avons été capables de déterminer les incertitudes relatives au dispositif lors d'une mesure à basse température (T <4 K) (tableau F.1). Nous avons caractérisé ces erreurs en calibrant avec les 3 références précédemment citées (Open Short et Load, ou OSL) ainsi qu'en calibrant avec une procédure Open Short Sample (OSS), où la mesure de la référence "Load" est remplacée par celle de l'échantillon dans l'état normal. Cette interversion permet d'augmenter la sensibilité dans le régime purement résistif tout en atténuant les erreurs systématiques, notamment liées à la présence du bias-Tee. Les incertitudes obtenues sont de l'ordre de 0.5 Ω pour la partie réelle est l'inductance et équivalent à $\sim$ 60 pH pour sa partie imaginaire sur la plage de fréquences mesurées.

Impédance	Calibration	Plage de fréquence	incertitude sur $Re(Z)$ (Ω)	incertitude sur $Im(Z)$ (pH)
13.2 Ω	OSL	0-1 GHz	$\pm$0.35	$\pm$50
	OSL	1-2 GHz	$\pm$1.2	$\pm$70
	OSS	0-1 GHz	$\pm$0.35	$\pm$60
	OSS	1-2 GHz	$\pm$0.35	$\pm$60
300 pH $\times\omega$	OSL	0-1 GHz	$\pm$0.3	$\pm$55
	OSL	1-2 GHz	$\pm$0.6	$\pm$85
	OSS	0-1 GHz	$\pm$0.2	$\pm$50
	OSS	1-2 GHz	$\pm$0.7	$\pm$60

Table F.1: Incertitudes des parties réelles et imaginaires de l'impédance complexe mesurée dans les états normaux et supraconducteurs. OSL réfère à une calibration Open, Short, Load, et OSS réfère à une calibration Open, Short, Sample (avec l'échantillon dans l'état normal).

F.4.3 Conductivité complexe d'un échantillon supraconducteur

L'évolution de la résistance et conductivité du film de vanadium supraconducteur mesuré est représenté figure F.21 pour une calibration de type OSS et en moyennant les data sur une plage de fréquence de 40 MHz.

- Dans l'état normal, l'échantillon est purement résistif, avec une impédance $\sim 13.5\,\Omega$.
- Pour $T < T_c$, température de transition supraconductrice du film, la réponse du film peut rapidement être considérée comme purement inductive du fait de l'inductance cinétique des paires de Cooper et de l'augmentation de la résistance de quasi-particule. La réponse mesurée dans Re(Z) devient proche de zero alors que la réponse inductive évolue linéairement avec la fréquence.
- Loin dans l'état supraconducteur (typ. pour $T < 2.7$ K), il devient difficile de mesurer la réponse inductive des paires de Cooper, l'incertitude devenant de l'ordre de ou supérieure au signal mesuré.

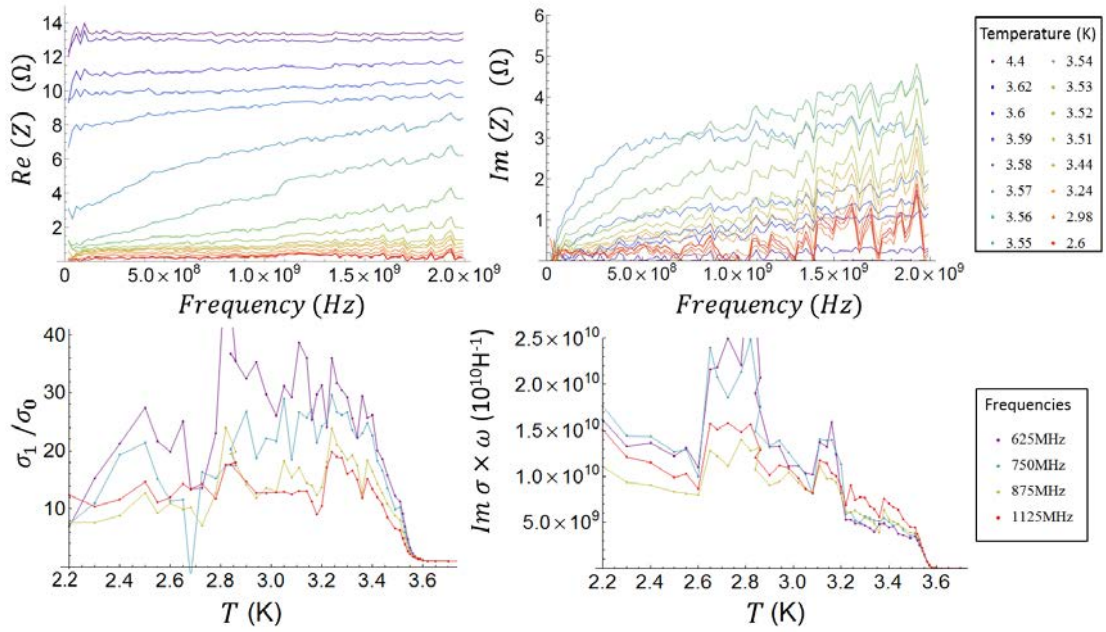

Figure F.21: $Re(Z)$, $Im(Z)$, σ_1 et $\sigma_2 \times \omega$ obtenue par calibration OSS et en moyennant les data sur une plage de fréquence de 40 MHz.

Pour se comparer avec les résultats attendus dans les théories conventionnelles de la supraconductivité en fréquence, et en particulier avec la théorie de Mattis-Bardeen, il est intéressant de tracer les data obtenues en conductivité (σ). Ceci permet de voir la présence d'un "pic" dans $\sigma_1 = Re(\sigma)$, lié au facteurs de cohérence dans la théorie BCS (Bardeen Cooper & Schrieffer),

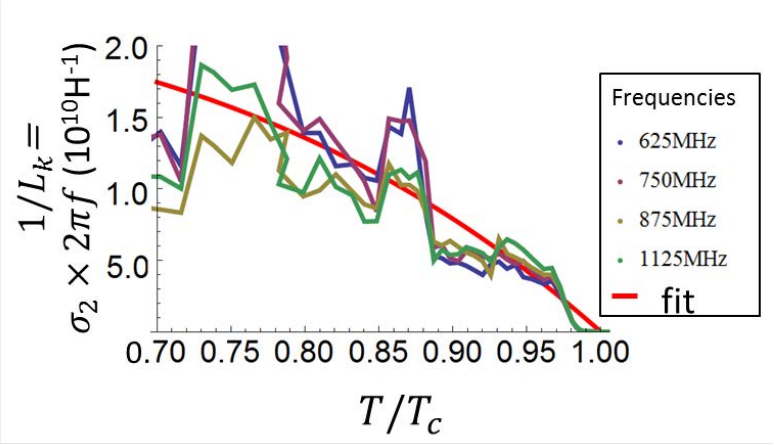

Figure F.22: Fit de la quantité $\sigma_2 \times \omega$, représentée en fonction de la température renormalisée par T_c, avec une loi de type BCS.

et d'observer dans $\sigma_2\omega = -Im(\sigma)\omega$ l'évolution de la densité suprafluide dans le film supraconducteur. En effet, $\sigma_2\omega = \frac{1}{L_k}$, où $L_k \propto \frac{1}{n_s}$, la densité suprafluide. En comparant l'évolution de la densité suprafluide avec ce qui est attendu dans la théorie BCS (figure F.22, obtenue avec un fit de la forme $L_k^{-1} = L_{k0}^{-1}(1 - (\frac{T}{T_c})^4)$ [Tinkam, 2004]), on trouve un bon accord qualitatif avec la théorie BCS. Nous devons cependant souligner que, très proche de T_c, une dépression de la densité suprafluide est observable. Celle-ci pourrait-être attribuée à des fluctuations de phase, possiblement de nature BKT (Berezinsky-Kosterlitz-Thouless).

F.4.4 Conclusion sur les développements effectués pour les mesures RF

J'ai développé un système permettant des mesures de réflectométrie micro-onde large bande (GHz) fonctionnant dans un environnement cryogénique ($T \lesssim 4$ K). Celui-ci permet de mesurer lors d'une unique mise en froid la valeur absolue de l'impédance complexe d'un film mince. Ce travail est original par plusieurs aspects :

- la calibration lors d'une unique mise en froid permet de réduire les erreurs liées à la non-reproductibilité des contraintes liées au cyclage thermique et à la dérive des instruments.
- nous obtenons une calibration sans faire d'hypothèse sur la réponse attendue de l'échantillon.
- la géométrie de l'échantillon peut être adaptée pour maximiser la sensibilité de la calibration.

Ce dispositif a été testé sur un film mince supraconducteur de Vanadium. La réponse électrodynamique du film est qualitativement similaire à ce qui est attendu par la théorie BCS. Notons cependant que la réponse obtenue est quantitativement en désaccord d'un facteur 10 sur la réponse des quasi-particules comme de la densité suprafluide. Cette non-adéquation quantitative pourrait être liée au désordre du film, perturbant les densités de quasi-particule et suprafluide. De plus, proche de la température supraconductrice, nous avons obtenu une signature de la densité suprafluide qui pourrait être liée à des fluctuations supraconductrices et notamment à des fluctuations de phase de type BKT.

En utilisant ce film de Vanadium, nous avons pu caractériser les incertitudes liées à la calibration pour une résistance pure comme pour une inductance pure. Ces incertitudes, relativement faibles, sont bien en dessous de ce qu'il est nécessaire d'atteindre pour mesurer des films très désordonnés comme le a-Nb_xSi_{1-x} proches de la TSI, l'inductance cinétique attendue étant inversement proportionnelle à la température supraconductrice. Ceci est d'autant plus vrai que la présence d'inhomogénéités électroniques pourraient encore augmenter cette réponse.

Bibliography

[A. Kapitulnik and Chakravarty, 2001] A. Kapitulnik, N. Mason, S. K. and Chakravarty, S. (2001). Effects of dissipation on quantum phase transitions. Phys. Rev. B, 63:125322.

[Abrahams et al., 1979] Abrahams, E., Anderson, P., Licciardello, D., and Ramakrishnan, T. (1979). Scaling theory of localization: Absence of quantum diffusion in two dimensions. Phys. Rev. Lett, 42:673.

[Abrikosov and Gor'kov, 1959] Abrikosov, A. and Gor'kov, L. (1959). On the theory of superconducting alloys; i. the electrodynamics of alloys at absolute zero. JETP, 8:1090.

[Adkins et al., 1980] Adkins, C., Thomas, J., and Young, M. (1980). Increased resistance below the superconducting transition in granular metals. Journal of Physics C: Solid State Physics, 13(18):3427.

[Agarwal et al., 2015] Agarwal, K., Gopalakrishnan, S., Knap, M., Müller, M., and Demler, E. (2015). Anomalous diffusion and griffiths effects near the many-body localization transition. Phys. Rev. Lett., 114:160401.

[Akis et al., 1991] Akis, R., Carbotte, J., and Timusk, T. (1991). Superconducting optical conductivity for arbitrary temperature and mean free path. Physical Review B, 43(16):12804.

[Alekseevskii et al., 1976] Alekseevskii, N., Sakosarenko, V., Blüthner, K., and Köhler, H.-J. (1976). Superconducting properties of vanadium films. physica status solidi (a), 34(2):541–546.

[Altshuler, 1985] Altshuler, B. (1985). Fluctuations in the extrinsic conductivity of disordered conductors. JETP lett, 41(12):648–651.

[Altshuler and Aronov, 1979] Altshuler, B. and Aronov, A. (1979). Zero bias anomaly in tunnel resistance and electron-electron interaction. Solid State Communications, 30(3):115–117.

[Altshuler et al., 1980] Altshuler, B. L., Aronov, A. G., and Lee, P. (1980). Interaction effects in disordered fermi systems in two dimensions. Phys. Rev. Lett, 44(19):1288.

[Altshuler et al., 2009] Altshuler, B. L., Kravtsov, V. E., Lerner, I. V., and Aleiner, I. L. (2009). Jumps in current-voltage characteristics in disordered films. Phys. Rev. Lett., 102:176803.

[Anderson, 1958] Anderson, P. (1958). Absence of diffusion in certain random lattices. Phys. Rev., 109:1492.

[Anderson, 1959] Anderson, P. (1959). Theory of dirty superconductors. J. Phys. Chem. Solids, 11:26.

[Armitage, 2009] Armitage, N. (2009). Electrodynamics of correlated electron systems. arXiv preprint arXiv:0908.1126.

[Ashcroft and Mermin, 1976] Ashcroft, N. and Mermin, N. (1976). Solid State Physics. Saunders College, Philadelphia.

[Aubin et al., 2006] Aubin, H., Marrache-Kikuchi, C., Pourret, A., Behnia, K., Berge, L., Dumoulin, L., and Lesueur, J. (2006). Magnetic-field-induced quantum superconductor-insulator transition in nb0.15si0.85. Phys. Rev. B, 73:094521.

[Barber et al., 1994] Barber, R. P., Merchant, L. M., La Porta, A., and Dynes, R. C. (1994). Tunneling into granular pb films in the superconducting and insulating regimes. Phys. Rev. B, 49:3409–3412.

[Bardeen et al., 1957] Bardeen, J., Cooper, L. N., and Schrieffer, J. R. (1957). Theory of superconductivity. Physical Review, 108(5):1175.

[Basko et al., 2006] Basko, D., Aleiner, I., and Altshuler, B. (2006). Metal–insulator transition in a weakly interacting many-electron system with localized single-particle states. Annals of physics, 321(5):1126–1205.

[Basko et al., 2007] Basko, D. M., Aleiner, I. L., and Altshuler, B. L. (2007). Possible experimental manifestations of the many-body localization. Phys. Rev. B, 76:052203.

[Basov et al., 2011] Basov, D. N., Averitt, R. D., Van Der Marel, D., Dressel, M., and Haule, K. (2011). Electrodynamics of correlated electron materials. Rev. Mod. Phys., 83(2):471.

[Baturina et al., 2007] Baturina, T. I., Strunk, C., Baklanov, M. R., and Satta, A. (2007). Quantum metallicity on the high-field side of the superconductor-insulator transition. Phys. Rev. Lett., 98:127003.

[Béal and Friedel, 1964] Béal, M. and Friedel, J. (1964). Relation between local order and interference effects in electrical resistivity for metallic alloys. Phys. Rev., 135:A466.

[Berggren, 1982] Berggren, K. (1982). Weak localisation and the dimensional crossover in disordered metallic films. J. Phys. C : Sol. St. Phys., 15:L843.

[Bergmann, 1971] Bergmann, G. (1971). Eliashberg function $\alpha^2(e)f(e)$ and the strong-coupling behavior of a disordered superconductor. Phys. Rev. B, 3:3797–3801.

[Bergmann, 1976] Bergmann, G. (1976). Amorphous metals and their superconductivity. Phys. Rep., 4:159.

[Bergmann, 1983] Bergmann, G. (1983). Physical interpretation of weak localization: A time-of-flight experiment with conduction electrons. Phys. Rev. B, 28:2914.

[Bishop et al., 1985] Bishop, D., Spencer, E., and Dynes, R. (1985). The metal-insulator transition in amorphous nbsi. Sol. St. Elec., 28:73.

[Booth et al., 1994] Booth, J., Wu, D. H., and Anlage, S. M. (1994). A broadband method for the measurement of the surface impedance of thin films at microwave frequencies. Review of scientific instruments, 65(6):2082–2090.

[Bouadim et al., 2011] Bouadim, K., Loh, Y. L., Randeria, M., and Trivedi, N. (2011). Single- and two-particle energy gaps across the disorder-driven superconductor-insulator transition. Nature Physics, 7(11):884–889.

[Cano and Artal, 2009] Cano, J. L. and Artal, E. (2009). Cryogenic technology applied to microwave engineering. Microwave Journal, 52(12):70.

[Carter et al., 1991] Carter, S., Rosenbaum, T., Honig, J., and Spalek, J. (1991). New phase boundary in highly correlated, barely metallic v 2 o 3. Phys. Rev. Lett, 67(24):3440.

[Castellani et al., 1984] Castellani, C., Di Castro, C., Lee, P. A., and Ma, M. (1984). Interaction-driven metal-insulator transitions in disordered fermion systems. Phys. Rev. B, 30:527–543.

[Christiansen et al., 2002] Christiansen, C., Hernandez, L. M., and Goldman, A. M. (2002). Evidence of collective charge behavior in the insulating state of ultrathin films of superconducting metals. Phys. Rev. Lett., 88:037004.

[Chubov et al., 1969] Chubov, P., Eremenko, V., and Pilipenko, Y. A. (1969). Dependence of the critical temperature and energy gap on the thickness of superconducting aluminum films. SOV PHYS JETP, 28(3):389–395.

[Couëdo, 2014] Couëdo, F. (2014). Transitions de phase quantiques dans les systèmes désordonnés de basse dimension. PhD thesis, Université Paris Sud-Paris XI.

[Crane et al., 2007] Crane, R., Armitage, N. P., Johansson, A., Sambandamurthy, G., Shahar, D., and Grüner, G. (2007). Survival of superconducting correlations across the two-dimensional superconductor-insulator transition: A finite-frequency study. Phys. Rev. B, 75:184530.

[Crauste, 2010] Crauste, O. (2010). Étude des transitions de phases quantiques supraconducteur-isolant, métal-isolant dans des matériaux amorphes désordonnés proches de la dimension 2. PhD thesis, Université Paris-Sud, Orsay.

[Crauste et al., 2014] Crauste, O., Couëdo, F., Bergé, L., Marrache-Kikuchi, C. A., and Dumoulin, L. (2014). Destruction of superconductivity in disordered materials: A dimensional crossover. Phys. Rev. B, 90:060203.

[Crauste et al., 2013] Crauste, O., Gentils, A., Couëdo, F., Dolgorouky, Y., Bergé, L., Collin, S., Marrache-Kikuchi, C., and Dumoulin, L. (2013). Effect of annealing on the superconducting properties of a-nb x si 1- x thin films. Phys. Rev. B, 87(14):144514.

[Crow et al., 1969] Crow, J., Strongin, M., Thompson, R., and Kammerer, O. (1969). The superconducting transition temperatures of disordered nb, w, and mo films. Phys. Lett. A, 30A:161.

[Dalidovich and Phillips, 2002] Dalidovich, D. and Phillips, P. (2002). Phase glass is a bose metal: A new conducting state in two dimensions. Phys. Rev. Lett., 89:027001.

[Das and Doniach, 1999] Das, D. and Doniach, S. (1999). Existence of a bose metal at t=0. Phys. Rev. B, 60:1261.

[Dawson and Tam, 1979] Dawson, P. and Tam, W.-C. (1979). The interaction of oxygen with polycrystalldve niobium studied using aes and low-energy sims. Surface Science, 81(2):464–478.

[Day et al., 2003] Day, P. K., LeDuc, H. G., Mazin, B. A., Vayonakis, A., and Zmuidzinas, J. (2003). A broadband superconducting detector suitable for use in large arrays. Nature, 425(6960):817–821.

[De Gennes, 1999] De Gennes, P. (1999). Superconductivity of Metals and Alloys (Advanced Book Classics). Addison-Wesley Publ. Company Inc.

[Delahaye et al., 2014] Delahaye, J., Grenet, T., Marrache-Kikuchi, C. A., Drillien, A. A., and Bergé, L. (2014). Observation of thermally activated glassiness and memory dip in a-nbsi insulating thin films. EPL (Europhysics Letters), 106(6):67006.

[Devreese and Alexandrov, 2009] Devreese, J. T. and Alexandrov, A. S. (2009). Fröhlich polaron and bipolaron: recent developments. Reports on Progress in Physics, 72(6):066501.

[Diener, 2013] Diener, P. (2013). Private communication.

[Diener et al., 2014] Diener, P., Couëdo, F., Marrache-Kikuchi, C., Aprili, M., and Gabelli, J. (2014). Cryogenic calibration setup for broadband complex impedance measurements. AIP Conference Proceedings, 1610(1).

[Dobrosavljevic et al., 2012] Dobrosavljevic, V., Trivedi, N., and Valles Jr, J. M. (2012). Conductor Insulator Quantum Phase Transitions, volume 16. Oxford University Press.

[Dodson et al., 1981] Dodson, B., McMillan, W., Mochel, J., and Dynes, R. (1981). Metal-insulator transition in disordered germanium-gold alloys. Phys. Rev. Lett, 46:46.

[Doron et al., 2016] Doron, A., Tamir, I., Mitra, S., Zeltzer, G., Ovadia, M., and Shahar, D. (2016). Nonequilibrium second-order phase transition in a cooper-pair insulator. Phys. Rev. Lett., 116:057001.

[Dressel, 2013] Dressel, M. (2013). Electrodynamics of metallic superconductors. Advances in Condensed Matter Physics, 2013.

[Dubi et al., 2006] Dubi, Y., Meir, Y., and Avishai, Y. (2006). Theory of the magnetoresistance of disordered superconducting films. Phys. Rev. B, 73(5):054509.

[Dynes and Garno, 1981] Dynes, R. and Garno, J. (1981). Metal-insulator transition in granular aluminum. Phys. Rev. Lett, 46(2):137.

[Dyre and Schrøder, 2000] Dyre, J. C. and Schrøder, T. B. (2000). Universality of ac conduction in disordered solids. Rev. Mod. Phys., 72(3):873.

[Eley et al., 2012] Eley, S., Gopalakrishnan, S., Goldbart, P. M., and Mason, N. (2012). Fate of global superconductivity in arrays of long sns junctions. arXiv preprint arXiv:1206.5999.

[Feigel'man et al., 2010] Feigel'man, M., Ioffe, L., Kravtsov, V., and Cuevas, E. (2010). Fractal superconductivity near localization threshold. Ann. Phys., 325:1390.

[Feigel'man and Larkin, 1998] Feigel'man, M. and Larkin, A. I. (1998). Quantum superconductor–metal transition in a 2d proximity-coupled array. Chemical physics, 235(1):107–114.

[Feigel'man and Skvortsov, 2012] Feigel'man, M. and Skvortsov, M. (2012). Universal broadening of the bardeen-cooper-schrieffer coherence peak of disordered superconducting films. Phys. Rev. Lett, 109:1347002.

[Ferrell and Glover III, 1958] Ferrell, R. A. and Glover III, R. E. (1958). Conductivity of superconducting films: A sum rule. Physical Review, 109(4):1398.

[Ferry et al., 2009] Ferry, D. K., Goodnick, S. M., and Bird, J. (2009). Transport in nanostructures. Cambridge University Press.

[Finkelstein, 1983] Finkelstein, A. (1983). Influence of coulomb interaction on the properties of disordered metals. JETP, 57:97.

[Finkel'stein, 1984] Finkel'stein, A. (1984). Weak localization and coulomb interaction in disordered systems. Zeitschrift für Physik B Condensed Matter, 56(3):189–196.

[Finkel'stein, 1994] Finkel'stein, A. (1994). Suppression of superconductivity in homogeneously disordered systems. Physica B, 197:636.

[Fiory et al., 1983] Fiory, A., Hebard, A., and Glaberson, W. (1983). Superconducting phase transitions in indium/indium-oxide thin-film composites. Phys. Rev. B, 28(9):5075.

[Fisher, 1990] Fisher, M. (1990). Quantum phase transitions in disordered two-dimensional superconductors. Phys. Rev. Lett, 65:923.

[Fisher and Lee, 1989] Fisher, M. and Lee, D. (1989). Correspondence between two-dimensional bosons and a bulk superconductor in a magnetic field. Phys. Rev. B, 39:2756.

[Foner, 1957] Foner, S. (1957). Hall effect in titanium, vanadium, chromium, and manganese. Physical Review, 107(6):1513.

[Fuchs, 1938] Fuchs, K. (1938). The conductivity of thin metallic films according to the electron theory of metals. In Mathematical Proceedings of the Cambridge Philosophical Society, volume 34, pages 100–108. Cambridge Univ Press.

[Gantmakher, 1998] Gantmakher, V. (1998). Transport properties of normal and quasinormal states of poor superconductors. International Journal of Modern Physics B, 12(29n31):3151–3156.

[Gantmakher and Dolgopolov, 2010] Gantmakher, V. and Dolgopolov, V. (2010). Superconductor-insulator quantum phase transition. Physics-Uspekhi, 53:1.

[Gantmakher and Golubkov, 1996] Gantmakher, V. and Golubkov, M. (1996). Giant negative magnetoresistance in semi-insulating amorphous indium oxide films in strong magnetic fields. Zh. Eksp. Teor. Fiz, 109:1765–1778.

[Gantmakher et al., 2000] Gantmakher, V., Golubkov, M., Dolgopolov, V., Shashkin, A., and Tsydynzhapov, G. (2000). Observation of the parallel-magnetic-field-induced superconductor-insulator transition in thin amorphous ino films. JETP Lett., 71:473.

[Gao et al., 1996] Gao, F., Carr, G., Porter, C., Tanner, D., Williams, G., Hirschmugl, C., Dutta, B., Wu, X., and Etemad, S. (1996). Quasiparticle damping and the coherence peak in yba 2 cu 3 o 7- δ. Phys. Rev. B, 54(1):700.

[Ghosal et al., 1998] Ghosal, A., Randeria, M., and Trivedi, N. (1998). Role of spatial amplitude fluctuations in highly disordered s-wave superconductors. Phys. Rev. Lett, 81(18):3940.

[Ghosal et al., 2001] Ghosal, A., Randeria, M., and Trivedi, N. (2001). Inhomogeneous pairing in highly disordered s-wave superconductors. Phys. Rev. B, 65(1):014501.

[Gopalakrishnan et al., 2015] Gopalakrishnan, S., Müller, M., Khemani, V., Knap, M., Demler, E., and Huse, D. A. (2015). Low-frequency conductivity in many-body localized systems. Phys. Rev. B, 92(10):104202.

[Graybeal and Beasley, 1984] Graybeal, J. and Beasley, M. (1984). Localization and interaction effects in ultrathin amorphous superconducting films. Phys. Rev. B, 29:4167.

[Gutsche et al., 1994] Gutsche, M., Kraus, H., Jochum, J., Kemmather, B., and Gutekunst, G. (1994). Growth and characterization of epitaxial vanadium films. Thin Solid Films, 248(1):18–27.

[Halperin and Nelson, 1979] Halperin, B. and Nelson, D. R. (1979). Resistive transition in superconducting films. J. Low Temp. Phys., 36(5-6):599–616.

[Han et al., 2014] Han, Z., Allain, A., Arjmandi-Tash, H., Tikhonov, K., Feigel'man, M., Sacépé, B., and Bouchiat, V. (2014). Collapse of superconductivity in a hybrid tin-graphene josephson junction array. Nature Physics, 10(5):380–386.

[Haviland et al., 1989] Haviland, D., Liu, Y., and Goldman, A. (1989). Onset of superconductivity in the two-dimensional limit. Phys. Rev. Lett, 62:2180.

[Hebard and Fiory, 1980] Hebard, A. F. and Fiory, A. T. (1980). Evidence for the kosterlitz-thouless transition in thin superconducting aluminum films. Phys. Rev. Lett., 44:291–294.

[Helgren et al., 2004] Helgren, E., Armitage, N., and Grüner, G. (2004). Frequency-dependent conductivity of electron glasses. Phys. Rev. B, 69(1):014201.

[Helgren and Gruner, 2001] Helgren, E. and Gruner, G. (2001). Measurements of the complex conductivity of $\mathrm{nb}_x\mathrm{si}_{1-x}$ alloys on the insulating side of the metal-insulator transition. Phys. Rev. Lett, 87:116602.

[Héritier, 2013] Héritier, M. (2013). Physique de la matière condensée: des atomes froids aux supraconducteurs à haute température critique. EDP sciences.

[Hertel et al., 1983] Hertel, G., Bishop, D., Spencer, E., Rowell, J., and Dynes, R. (1983). Tunneling and transport measurements at the metal-insulator transition of amorphous nb: Si. Phys. Rev. Lett, 50:743.

[Hess et al., 1982] Hess, H. F., DeConde, K., Rosenbaum, T., and Thomas, G. (1982). Giant dielectric constants at the approach to the insulator-metal transition. Phys. Rev. B, 25(8):5578.

[Hsu and Valles, 1995] Hsu, S.-Y. and Valles, Jr., J. M. (1995). Observation of a well defined transition from weak to strong localization in two dimensions. Phys. Rev. Lett., 74:2331–2334.

[Imry and Ovadyahu, 1982] Imry, Y. and Ovadyahu, Z. (1982). Density-of-states anomalies in a disordered conductor: a tunneling study. Phys. Rev. Lett, 49:841.

[Imry and Strongin, 1981] Imry, Y. and Strongin, M. (1981). Destruction of superconductivity in granular and highly disordered metals. Phys. Rev. B, 24:6353.

[Ioffe and Regel, 1960] Ioffe, A. and Regel, A. (1960). Non-crystalline, amorphous and liquid electronic semiconductors. Prog. Semicond, 4:237–291.

[Jaeger et al., 1986] Jaeger, H., Haviland, D., Goldman, A. M., and Orr, B. (1986). Threshold for superconductivity in ultrathin amorphous gallium films. Phys. Rev. B, 34:4920.

[Jaeger et al., 1989] Jaeger, H., Haviland, D., Orr, B., and Goldman, A. M. (1989). Onset of superconductivity in ultrathin granular metal films. Phys. Rev. B, 40:182.

[Jendrzejewski et al., 2012] Jendrzejewski, F., Müller, K., Richard, J., Date, A., Plisson, T., Bouyer, P., Aspect, A., and Josse, V. (2012). Coherent backscattering of ultracold atoms. Phys. Rev. Lett, 109(19):195302.

[Juillard, 1996] Juillard, A. (1996). Etude de couches minces supraconductrices pour la réalisation de bolomètres à très basse température. Master's thesis, École des Mines de Nancy.

[Kamerlingh Onnes, 1911] Kamerlingh Onnes, H. (1911). Further experiments with Liquid Helium G. On the electrical resistance of Pure Metals etc. VI. On the Sudden Change in the Rate at which the Resistance of Mercury Disappears. Koninklijke Nederlandse Akademie van Wetenschappen Proceedings Series B Physical Sciences, 14:818–821.

[Kapitulnik et al., 1985] Kapitulnik, A., Kotliar, G., et al. (1985). Anderson localization and the theory of dirty superconductors. Phys. Rev. Lett, 54(5):473–476.

[Khondaker et al., 1999] Khondaker, S., Shlimak, I., Nicholls, J., Pepper, M., and Ritchie, D. (1999). Two-dimensional hopping conductivity in a δ-doped gaas/al x ga 1- x as heterostructure. Phys. Rev. B, 59(7):4580.

[Kim et al., 1998] Kim, J., Yang, G., and Weiss, A. (1998). Study of the adsorption of hydrogen and oxygen on si (100) using positron-annihilation induced auger electron spectroscopy (paes). Surface science, 396(1):388–393.

[Kim et al., 1992] Kim, J.-J., Kim, J., and Lee, H. J. (1992). Superconductivity effect on electrical conduction in insulating granular films. Phys. Rev. B, 46(18):11709.

[Kitano et al., 2008] Kitano, H., Ohashi, T., and Maeda, A. (2008). Broadband method for precise microwave spectroscopy of superconducting thin films near the critical temperature. Review of Scientific Instruments, 79(7):074701.

[Kittel, 1986] Kittel, C. (1986). Introduction to solid state physics. Wiley.

[Klein et al., 1994] Klein, O., Nicol, E., Holczer, K., and Grüner, G. (1994). Conductivity coherence factors in the conventional superconductors nb and pb. Phys. Rev. B, 50(9):6307.

[Klitzing et al., 1980] Klitzing, K. v., Dorda, G., and Pepper, M. (1980). New method for high-accuracy determination of the fine-structure constant based on quantized hall resistance. Phys. Rev. Lett., 45:494–497.

[Knorr and Barth, 1971] Knorr, K. and Barth, N. (1971). Electron tunneling into disordered thin films. J. Low Temp. Phys., 4(5):469–484.

[Kokanović et al., 1990] Kokanović, I., Leontić, B., and Lukatela, J. (1990). Weak-localization and coulomb-interaction effects in hydrogen-doped zr-ni and zr-cu metallic glasses. Phys. Rev. B, 41(2):958.

[Kotliar and Kapitulnik, 1986] Kotliar, G. and Kapitulnik, A. (1986). Anderson localization and the theory of dirty superconductors. ii. Phys. Rev. B, 33(5):3146.

[Kravchenko et al., 1994] Kravchenko, S., Kravchenko, G., Furneaux, J., Pudalov, V., and D'Iorio, M. (1994). Possible metal-insulator transition at b=0 in 2 dimensions. Phys. Rev. B, 50:8039.

[Kravchenko et al., 1995] Kravchenko, S., Mason, W., Bowker, G., Furneaux, J., Pudalov, V., and D'Iorio, M. (1995). Scaling of an anomalous metal-insulator transition in a two-dimensional system in silicon at b=0. Phys. Rev. B, 51:7038.

[Kuz'menko et al., 1975] Kuz'menko, V., Lazarev, V., Mel'Nikov, V., and Sudovtsov, A. (1975). Superconductivity of amorphous vanadium. Soviet Physics-JETP, 40:396.

[Kuzmenko et al., 1978] Kuzmenko, V., Melnikov, V., and Sudovtsov, A. (1978). Concerning the superconductivity of amorphous vanadium films. Soviet Physics-JETP, 47:1081–1086.

[Larkin and Khmel'nitskii, 1982] Larkin, A. and Khmel'nitskii, D. (1982). Activation conductivity in disordered systems with large localization length. Sov. Phys. JETP, 56(3):647.

[Laulajainen et al., 2006] Laulajainen, M., Callaghan, F., Kaiser, C., and Sonier, J. (2006). Muon spin rotation measurements of the vortex state in vanadium: A comparative analysis using iterative and analytical solutions of the ginzburg-landau equations. Phys. Rev. B, 74(5):054511.

[Lee et al., 1998] Lee, H., Carini, J., and Baxter, D. (1998). Temperature-frequency scaling in amorphous niobium-silicon near the metal-insulator transition. Phys. Rev. Lett, 80:4261.

[Lee et al., 2000] Lee, H. L., Carini, J. P., Baxter, D. V., Henderson, W., and Gruner, G. (2000). Quantum-critical conductivity scaling for a metal-insulator transition. Science, 287:633.

[Lee et al., 1999] Lee, M., Massey, J. G., Nguyen, V. L., and Shklovskii, B. I. (1999). Coulomb gap in a doped semiconductor near the metal-insulator transition: Tunneling experiment and scaling ansatz. Phys. Rev. B, 60:1582–1591.

[Lee and Ramakrishnan, 1985] Lee, P. and Ramakrishnan, T. (1985). Disordered electronic systems. rmp, 57:287.

[Lehoczky and Briscoe, 1971] Lehoczky, S. and Briscoe, C. (1971). Fluctuation effects in the ac conductivity of thin superconducting lead films at microwave frequencies. Phys. Rev. B, 4(11):3938.

[Lesueur et al., 1985] Lesueur, J., Dumoulin, L., and Nedellec, P. (1985). Metal-insulator transition in quench-condensed al_xge_{1-x} : Scaling and tunneling experiments. Phys. Rev. Lett, 55:2355.

[Licciardello and Thouless, 1975] Licciardello, D. C. and Thouless, D. J. (1975). Constancy of minimum metallic conductivity in two dimensions. Phys. Rev. Lett., 35:1475–1478.

[Liu and Giordano, 1991] Liu, J. and Giordano, N. (1991). Electron-phonon scattering times in thin sb films. Phys. Rev. B, 43:3928–3932.

[Liu et al., 2011] Liu, W., Kim, M., Sambandamurthy, G., and Armitage, N. (2011). Dynamical study of phase fluctuations and their critical slowing down in amorphous superconducting films. Phys. Rev. B, 84(2):024511.

[Liu et al., 2013] Liu, W., Pan, L., Wen, J., Kim, M., Sambandamurthy, G., and Armitage, N. (2013). Microwave spectroscopy evidence of superconducting pairing in the magnetic-field-induced metallic state of ino x films at zero temperature. Phys. Rev. Lett, 111(6):067003.

[Löptien et al., 2014] Löptien, P., Zhou, L., Khajetoorians, A., Wiebe, J., and Wiesendanger, R. (2014). Superconductivity of lanthanum revisited: enhanced critical temperature in the clean limit. Journal of Physics: Condensed Matter, 26(42):425703.

[Ma and Lee, 1985] Ma, M. and Lee, P. (1985). Localized superconductors. Phys. Rev. B, 32:5658.

[Maekawa and Fukuyama, 1982] Maekawa, S. and Fukuyama, H. (1982). Localization effects in two-dimensional superconductors. J. Phys. Soc. Jpn., 51:1380.

[Mahan, 2013] Mahan, G. D. (2013). Many-particle physics. Springer Science & Business Media.

[Markovic et al., 1998] Markovic, N., Christiansen, C., and Goldman, A. (1998). Thickness-magnetic field phase diagram at the superconductor-insulator transition in 2d. Phys. Rev. Lett, 81:5217.

[Marnieros, 1998] Marnieros, S. (1998). Couches minces d'isolant d'Anderson. Application à la bolométrie à très basse température. PhD thesis, Paris XI, Orsay.

[Marnieros et al., 2000] Marnieros, S., Bergé, L., Juillard, A., and Dumoulin, L. (2000). Dynamical properties near the metal-insulator transition : evidence for electron-assited variable range hopping. Phys. Rev. Lett, 84:2469.

[Marrache-Kikuchi, 2006] Marrache-Kikuchi, C. (2006). Effets dimensionnels dans un système désordonné au voisinage des transitions métal-isolant et supraconducteur-isolant. PhD thesis, Paris XI, Orsay.

[Marrache-Kikuchi et al., 2008] Marrache-Kikuchi, C., Aubin, H., Pourret, A., Behnia, K., Lesueur, J., Bergé, L., and Dumoulin, L. (2008). Thickness-tuned superconductor-insulator transitions under magnetic field in a-nbsi. Phys. Rev. B, 78:144520.

[Marrache-Kikuchi et al., 2006] Marrache-Kikuchi, C., Berge, L., Collin, S., Dobrea, C., Dumoulin, L., Juillard, A., and Marnieros, S. (2006). Properties of thermometric nbsi thin films and application to detection in astrophysics. Nucl. Instr. and Meth. in Phys. Res. A, 559:579.

[Mason and Kapitulnik, 1999] Mason, N. and Kapitulnik, A. (1999). Dissipation effects on the superconductor-insulator transition in 2d superconductors. Phys. Rev. Lett, 82:5341.

[Mason et al., 1995] Mason, W., Kravchenko, S., Bowker, G., and Furneaux, J. (1995). Experimental evidence for a coulomb gap in 2 dimensions. Phys. Rev. B, 52:7857.

[Matthiessen and Vogt, 1864] Matthiessen, A. and Vogt, C. (1864). On the influence of temperature on the electric conducting-power of alloys. Philosophical Transactions of the Royal Society of London, 154:167–200.

[Mattis and Bardeen, 1958] Mattis, D. and Bardeen, J. (1958). Theory of the anomalous skin effect in normal and superconducting metals. Physical Review, 111(2):412.

[McMillan, 1968] McMillan, W. (1968). Transition temperature of strong-coupled superconductors. Physical Review, 167(2):331.

[McMillan, 1981] McMillan, W. L. (1981). Scaling theory of the metal-insulator transition in amorphous materials. Phys. Rev. B, 24:2739–2743.

[Minkov et al., 2004] Minkov, G., Germanenko, A., and Gornyi, I. (2004). Magnetoresistance and dephasing in a two-dimensional electron gas at intermediate conductances. Phys. Rev. B, 70(24):245423.

[Mobius, 1985] Mobius, A. (1985). The metal-semiconductor transition in three-dimensional disordered systems-reanalysis of recent experiments for and against minimum metallic conductivity. Journal of Physics C: Solid State Physics, 18(24):4639.

[Möbius et al., 1999] Möbius, A., Frenzel, C., Thielsch, R., Rosenbaum, R., Adkins, C. J., Schreiber, M., Bauer, H.-D., Grötzschel, R., Hoffmann, V., Krieg, T., Matz, N., Vinzelberg, H., and Witcomb, M. (1999). Metal-insulator transition in amorphous $si_{1-x}ni_x$: evidence for mott's minimum metallic conductivity. Phys. Rev. B, 60:14209–14223.

[Mondal et al., 2013] Mondal, M., Kamlapure, A., Ganguli, S. C., Jesudasan, J., Bagwe, V., Benfatto, L., and Raychaudhuri, P. (2013). Enhancement of the finite-frequency superfluid response in the pseudogap regime of strongly disordered superconducting films. Scientific Reports, 3.

[Morel and Anderson, 1962] Morel, P. and Anderson, P. W. (1962). Calculation of the superconducting state parameters with retarded electron-phonon interaction. Phys. Rev., 125:1263–1271.

[Moser et al., 1982] Moser, E., Seidl, E., and Weber, H. (1982). Superconductive properties of vanadium and their impurity dependence. J. Low Temp. Phys., 49(5-6):585–607.

[Mott, 1974] Mott, N. (1974). Metal-Insulator Transitions. Taylor & Francis.

[Mott, 1977] Mott, N. (1977). Electrons in glass:[Nobel lecture]. Nobel foundation.

[Mott, 1984] Mott, N. (1984). Metals, nonmetals and metal-nonmetal transitions: some recollections. Reports on Progress in Physics, 47(8):909.

[Mott, 1967] Mott, N. F. (1967). Electrons in disordered structures. Advances in Physics, 16:49–144.

[Mott, 1972] Mott, N. F. (1972). Conduction in non-crystalline systems ix. the minimum metallic conductivity. Philosophical Magazine, 26(4):1015–1026.

[Nam, 1967a] Nam, S. B. (1967a). Theory of electromagnetic properties of strong-coupling and impure superconductors. ii. Physical Review, 156(2):487.

[Nam, 1967b] Nam, S. B. (1967b). Theory of electromagnetic properties of superconducting and normal systems. i. Physical Review, 156(2):470.

[Nam, 1997] Nam, S. B. (1997). Pairing theory of high and low temperature superconductors. arXiv preprint cond-mat/9707017.

[Nava et al., 1986] Nava, F., Psaras, P., Takai, H., Tu, K., Valeri, S., and Bisi, O. (1986). Electrical and structural characterization of nb-si thin alloy film. J. Mater. Res., 1:327.

[Nicol et al., 1991] Nicol, E., Carbotte, J., and Timusk, T. (1991). Optical conductivity in high-t c superconductors. Phys. Rev. B, 43(1):473.

[Noat et al., 2013] Noat, Y., Cherkez, V., Brun, C., Cren, T., Carbillet, C., Debontridder, F., Ilin, K., Siegel, M., Semenov, A., Hübers, H.-W., et al. (2013). Unconventional superconductivity in ultrathin superconducting nbn films studied by scanning tunneling spectroscopy. Phys. Rev. B, 88(1):014503.

[Ovadia et al., 2015] Ovadia, M., Kalok, D., Tamir, I., Mitra, S., Sacépé, B., and Shahar, D. (2015). Evidence for a finite temperature insulator. Scientific Reports, 5(13503).

[Ovadyahu and Imry, 1983] Ovadyahu, Z. and Imry, Y. (1983). On the role of the correlation length near the onset of non-metallic conduction. J. Phys. C : Sol. St. Phys., 16:L471.

[Palmer and Tinkham, 1968] Palmer, L. H. and Tinkham, M. (1968). Far-infrared absorption in thin superconducting lead films. Physical Review, 165(2):588.

[Phillips and Dalidovich, 2003] Phillips, P. and Dalidovich, D. (2003). The elusive bose metal. Science, 302:243.

[Pollak, 1970] Pollak, M. (1970). Effect of carrier-carrier interactions on some transport properties in disordered semiconductors. Discussions of the Faraday Society, 50:13–19.

[Pollak and Shklovskii, 1991] Pollak, M. and Shklovskii, B. (1991). Hopping transport in solids, volume 28. Elsevier.

[Popović, 2016] Popović, D. (2016). Metal-insulator transition in correlated two-dimensional systems with disorder. arXiv preprint arXiv:1603.06525.

[Pozar, 2004] Pozar, D. (2004). Microwave Engineering. Wiley.

[Pracht et al., 2013] Pracht, U. S., Heintze, E., Clauss, C., Hafner, D., Bek, R., Werner, D., Gelhorn, S., Scheffler, M., Dressel, M., Sherman, D., et al. (2013). Electrodynamics of the superconducting state in ultra-thin films at thz frequencies. Terahertz Science and Technology, IEEE Transactions on, 3(3):269–280.

[Punnoose and Finkel'stein, 2005] Punnoose, A. and Finkel'stein, A. (2005). Metal-insulator transition in disordered two-dimensional electron systems. Science, 310:289.

[Radebaugh and Keesom, 1966] Radebaugh, R. and Keesom, P. (1966). Low-temperature thermodynamic properties of vanadium. ii. mixed state. Physical Review, 149(1):217.

[Rammer and Schmid, 1986] Rammer, J. and Schmid, A. (1986). Destruction of phase coherence by electron-phonon interactions in disordered conductors. Phys. Rev. B, 34:1352–1355.

[Ranzani et al., 2013a] Ranzani, L., Spietz, L., and Aumentado, J. (2013a). Broadband calibrated scattering parameters characterization of a superconducting quantum interference device amplifier. Applied Physics Letters, 103(2):022601.

[Ranzani et al., 2013b] Ranzani, L., Spietz, L., Popovic, Z., and Aumentado, J. (2013b). Two-port microwave calibration at millikelvin temperatures. Review of Scientific Instruments, 84(3):034704.

[Reale, 1970] Reale, C. (1970). Electronic structure of the metals of the vanadium and chromium groups. Physics Letters A, 32(3):197–198.

[Reuss, 2000] Reuss, T. (2000). Nouvel étalonnage cryogénique en réflectométrie (0.2 à 18 GHz) et application à l'étude de la dynamique des vortex de supraconducteurs HTc proche de Tc. PhD thesis, Université Joseph-Fourier-Grenoble I.

[Rodríguez et al., 2007] Rodríguez, M., Bonalde, I., and Medina, E. (2007). Consistent hopping criterion in the efros-shklovskii regime. Phys. Rev. B, 75:235205.

[Rosenbaum, 1991] Rosenbaum, R. (1991). Crossover from mott to efros-shklovskii variable-range-hopping conductivity in inox films. Phys. Rev. B, 44:3599.

[Rosenbaum et al., 1980] Rosenbaum, T., Andres, K., Thomas, G., and Bhatt, R. (1980). Sharp metal-insulator transition in a random solid. Phys. Rev. Lett, 45(21):1723.

[Sacépé, 2011] Sacépé, B. (2011). Oral presentation, Workshop : Strongly Disordered Superconductors and Electronic Segregation, Lorentz Center.

[Sacépé et al., 2008] Sacépé, B., Chapelier, C., Baturina, T., Vinokur, V., Baklanov, M., and Sanquer, M. (2008). Disorder-induced inhomogeneities of the superconducting state close to the superconductor-insulator transition. Phys. Rev. Lett, 101:157006.

[Sacépé et al., 2011] Sacépé, B., Dubouchet, T., Chapelier, C., Sanquer, M., Ovadia, M., Shahar, D., Feigel'man, M., and Ioffe, L. (2011). Localization of preformed cooper pairs in disordered superconductors. Nature Physics, 7:239.

[Sarachik and Dai, 2002] Sarachik, M. and Dai, P. (2002). Scaling of the conductivity of insulating si: B: A temperature-independent hopping prefactor. EPL (Europhysics Letters), 59(1):100.

[Sekula and Kernohan, 1972] Sekula, S. and Kernohan, R. (1972). Magnetic properties of superconducting vanadium. Phys. Rev. B, 5(3):904.

[Shafarman et al., 1989] Shafarman, W. N., Koon, D. W., and Castner, T. G. (1989). dc conductivity of arsenic-doped silicon near the metal-insulator transition. Phys. Rev. B, 40:1216–1231.

[Shahar and Ovadyahu, 1990] Shahar, D. and Ovadyahu, Z. (1990). Dimensional crossover in the hopping regime induced by an electric field. Phys. Rev. Lett, 64:2293.

[Shahar and Ovadyahu, 1992] Shahar, D. and Ovadyahu, Z. (1992). Superconductivity near the mobility edge. Phys. Rev. B, 46:10917.

[Sherman et al., 2014] Sherman, D., Gorshunov, B., Poran, S., Trivedi, N., Farber, E., Dressel, M., and Frydman, A. (2014). Effect of coulomb interactions on the disorder-driven superconductor-insulator transition. Phys. Rev. B, 89(3):035149.

[Shklovskii and Efros, 1984] Shklovskii, B. and Efros, A. (1984). Electronic Properties of Doped Semiconductors. Springer-Verlag.

[Shlimak et al., 1999] Shlimak, I., Friedland, K.-J., and Baranovskii, S. (1999). Hopping conductivity in gated δ-doped gaas: universality of prefactor. Solid state communications, 112(1):21–24.

[Simonin, 1986] Simonin, J. (1986). Surface term in the superconductive ginzburg-landau free energy : Application to thin films. Phys. Rev. B, 33:7830.

[Simons, 2001] Simons, R. N. (2001). Coplanar Waveguide Circuits, Components, and Systems. Wiley Series in Microwave and Optical Engineering. Wiley, Newark, NJ.

[Skvortsov, 2015] Skvortsov, M. (2015). Private communication.

[Skvortsov and Feigel'man, 2005] Skvortsov, M. and Feigel'man, M. (2005). Superconductivity in disordered thin films: Giant mesoscopic fluctuations. Phys. Rev. Lett, 95(5):057002.

[Skvortsov, 2008] Skvortsov, M. A. (2008). fluctuation and interference effects in mesoscopic systems (in russian). PhD thesis, Laudau Institute for Theoretical Physics, Chernogolovka.

[Sondheimer, 1952] Sondheimer, E. H. (1952). The mean free path of electrons in metals. Advances in physics, 1(1):1–42.

[Sondhi et al., 1997] Sondhi, S., Girvin, S., Carini, J., and Shahar, D. (1997). Continuous quantum phase transitions. rmp, 69:315.

[Spivak et al., 2001] Spivak, B., Zyuzin, A., and Hruska, M. (2001). Quantum superconductor-metal transition. Phys. Rev. B, 64:132502.

[Spivak and Kivelson, 1991] Spivak, B. I. and Kivelson, S. A. (1991). Negative local superfluid densities: The difference between dirty superconductors and dirty bose liquids. Phys. Rev. B, 43:3740–3743.

[Steinberg et al., 2008] Steinberg, K., Scheffler, M., and Dressel, M. (2008). Quasiparticle response of superconducting aluminum to electromagnetic radiation. Phys. Rev. B, 77(21):214517.

[Stewart et al., 2007] Stewart, M., Yin, A., Xu, J., and Valles, J. M. (2007). Superconducting pair correlations in an amorphous insulating nanohoneycomb film. Science, 318(5854):1273–1275.

[Szabó et al., 2016] Szabó, P., Samuely, T., Hašková, V., Kačmarčík, J., Žemlička, M., Grajcar, M., Rodrigo, J. G., and Samuely, P. (2016). Fermionic scenario for the destruction of superconductivity in ultrathin moc films evidenced by stm measurements. Phys. Rev. B, 93:014505.

[Takagi and Kuroda, 1982] Takagi, H. and Kuroda, Y. (1982). Anderson localization and superconducting transition temperature in two-dimensional systems. Solid State Communications, 41(9):643–648.

[Teplov and Mikheeva, 1980] Teplov, A. and Mikheeva, M. (1980). Parallel critical magnetic fields for superconducting vanadium and technetium films. Sov. Phys. JETP, 52:1165.

[Teplov et al., 1976] Teplov, A., Mikheeva, M., Golyanov, V., and Gusev, A. (1976). Superconducting transition temperature, critical magnetic fields, and the structure of vanadium films. Sov. Phys. JETP, 44(3):587.

[Thomas et al., 1983] Thomas, G., Paalanen, M., and Rosenbaum, T. (1983). Measurements of conductivity near the metal-insulator critical point. Phys. Rev. B, 27(6):3897.

[Thouless, 1974] Thouless, D. (1974). Electrons in disordered systems and the theory of localization. Phys. Rep., 13:93.

[Tinkam, 2004] Tinkam, M. (2004). Introduction to superconductivity. Dover Publications.

[Tsai et al., 1981] Tsai, C., Fagaly, R., Weinstock, H., and Schmidt, F. (1981). Electrical and thermal transport coefficients of pure vanadium. Phys. Rev. B, 23(12):6430.

[Tsigankov and Efros, 2002] Tsigankov, D. N. and Efros, A. L. (2002). Variable range hopping in two-dimensional systems of interacting electrons. Phys. Rev. Lett., 88:176602.

[Turneaure et al., 1998] Turneaure, S. J., Pesetski, A. A., and Lemberger, T. R. (1998). Numerical modeling and experimental considerations for a two-coil apparatus to measure the complex conductivity of superconducting films. Journal of applied physics, 83(8):4334–4343.

[Turneaure et al., 1996] Turneaure, S. J., Ulm, E. R., and Lemberger, T. R. (1996). Numerical modeling of a two-coil apparatus for measuring the magnetic penetration depth in superconducting films and arrays. Journal of applied physics, 79(8):4221–4227.

[Valles et al., 1992] Valles, J., Dynes, R., and Garno, J. (1992). Electron tunneling determination of the order-parameter amplitude at the superconductor-insulator transition in 2d. Phys. Rev. Lett, 69:3567.

[van der Zant et al., 1996] van der Zant, H. S. J., Elion, W. J., Geerligs, L. J., and Mooij, J. E. (1996). Quantum phase transitions in two dimensions: Experiments in josephson-junction arrays. Phys. Rev. B, 54:10081–10093.

[van Keuls et al., 1997] van Keuls, F., Mathur, H., Jiang, H., and Dahm, A. (1997). Localization scaling relation in two dimensions : comparison with experiment. Phys. Rev. B, 56:13263.

[Williamson, 1970] Williamson, S. (1970). Bulk upper critical field of clean type-ii superconductors: V and nb. Phys. Rev. B, 2(9):3545.

[Wolf, 1985] Wolf, E. (1985). Principles of Electron Tunneling Spectroscopy. New-York: Oxford University Press.

[Yazdani and Kapitulnik, 1995] Yazdani, A. and Kapitulnik, A. (1995). Superconducting-insulating transition in two-dimensional a-moge thin films. Phys. Rev. Lett, 74:3037.

[Yeh and Anlage, 2013] Yeh, J.-H. and Anlage, S. M. (2013). In situ broadband cryogenic calibration for two-port superconducting microwave resonators. Review of Scientific Instruments, 84(3):034706.

[Yoon et al., 1994] Yoon, C., Reghu, M., Moses, D., and Heeger, A. (1994). Transport near the metal-insulator transition: polypyrrole doped with pf 6. Phys. Rev. B, 49(16):10851.

[Zabrodskii and Zinoveva, 1984] Zabrodskii, A. and Zinoveva, K. (1984). Low-temperature conductivity and metal–insulator transition in compensate n-ge. Zh. Eksp. Teor. Fiz, 86:742.

[Zavaritskaya and Zavaritskaya, 1987] Zavaritskaya, T. and Zavaritskaya, E. (1987). Metal–insulator transition in inversion channels of silicon mos structures. JETP Lett, 45(10).

[Zimmermann et al., 1991] Zimmermann, W., Brandt, E., Bauer, M., Seider, E., and Genzel, L. (1991). Optical conductivity of bcs superconductors with arbitrary purity. Physica C: Superconductivity, 183(1):99–104.

Titre : Etude des états fondamentaux dans des systèmes supraconducteurs désordonnés de dimension 2

Mots clés : Supraconductivité, Isolant d'Anderson, Systèmes désordonnés à basse dimensionnalité, Transition Supraconducteur-Isolant, Transition Métal-Isolant, Réflectométrie micro-onde.

Résumé : Un matériau 3D, initialement supraconducteur, peut avoir différents états fondamentaux dépendamment de son degré de désordre : supraconducteur, métallique ou isolant. A dimension réduite (2D), la localisation d'Anderson interdit théoriquement tout état métallique. La modification du désordre induit alors une Transition directe Supraconducteur-Isolant (TSI). La présence de fortes interactions électroniques, non prises en compte dans les théories conventionnelles, pourrait cependant remettre en cause ce paradigme et laisser émerger des états métalliques 2D, complexifiant l'image généralement admise de la TSI. Ainsi, des travaux récents ont révélé la présence de deux phases métalliques distinctes dans les films minces de a-NbxSi1-x, s'intercalant entre les états supraconducteur et isolant.
Durant cette thèse, nous avons étudié les propriétés de transport électronique à basse fréquence et à très basse température (T<1K) de films minces de NbxSi1-x amorphes afin de caractériser l'évolution de l'état fondamental en fonction du désordre. Celui-ci a été modifié dans nos films en jouant sur la température de recuit, l'épaisseur et la composition. Nous nous sommes alors attardés sur la destruction de ces états métalliques vers un état isolant. L'analyse des lois de conduction dans le régime isolant nous a permis de quantifier l'évolution de ses propriétés – notamment des énergies caractéristiques – en fonction du désordre. Nous avons alors pu conclure que la phase isolante pouvait être essentiellement décrite par un modèle fermionique. A moindre désordre, dans la phase métallique 2D adjacente à l'isolant, nous avons mis en évidence des signes précurseurs de l'état isolant qui évoluent continument jusqu'à et à travers la Transition Métal 2D-Isolant. Nous proposons une interprétation de l'ensemble de nos résultats impliquant deux canaux parallèles dont l'importance relative est déterminée par le désordre : l'un est fermionique, l'autre gouverné par des fluctuations supraconductrices qui persistent même lorsque la cohérence macroscopique a disparu. L'état métallique est alors dominé par ces dernières, alors que, dans l'isolant, la localisation des excitations fermioniques l'emporte.
Une seconde partie de la thèse s'est concentrée sur le développement expérimental d'un dispositif de calibration large bande dédié à l'étude de films minces en réflectométrie haute fréquence (GHz) à basses températures (T<4K). Ce dispositif a pour but, lors d'une unique mise à froid, de mesurer successivement la réflexion de références connues ainsi que de l'échantillon. La calibration obtenue permet ainsi de s'affranchir de l'environnement micro-onde et d'obtenir la valeur absolue de l'impédance complexe de ces films. Les résultats obtenus sur des films minces supraconducteurs de Vanadium, comparés aux théories de la supraconductivité, permettent une première validation du dispositif et de son principe de fonctionnement en vue d'une utilisation sur des systèmes plus complexes, tels que les films minces proches de la TSI.

Title : Study of accessible ground states in two-dimensional disordered superconductors

Keywords : Superconductivity, Anderson insulator, low dimensional disordered systems, Superconductor-to-Insulator Transition, Metal-to-Insulator Transition, Microwave reflectometry.

Abstract : An initially superconducting 3D material can have different ground states, depending on its disorder : superconducting, metallic or insulating. At lower dimensionality, Anderson localization theoretically forbids any metallic state. A change in disorder then induces a direct Superconductor-to-Insulator Transition (SIT). The presence of strong Coulomb interactions, which are not taken into account in conventional theories, may disrupt this paradigm and enable the emergence of 2D metallic phases, thus complicating the generally admitted picture for the SIT. Indeed, recent work has revealed the existence of two distinct metallic phases in a-NbxSi1-x thin films, in between the superconducting and insulating states.
During this work, we have studied the low frequency transport properties of amorphous NbxSi1-x films at low temperatures (T<1K), in order to characterize the evolution of their ground state with disorder. In our films, disorder has been tuned by varying the heat treatment temperature, the thickness or the composition. We have then focused on the destruction of these metallic states, giving rise to an insulating state. Through the analysis of conduction laws in the insulating regime, we have quantified the evolution of its properties – in particular its characteristic energies – as disorder is varied. We could then conclude that the insulating phase can essentially be accounted for by a fermionic model. At lower disorder level, in the 2D metallic phase neighboring the insulator, we have evidenced precursor signs of the insulating state which continuously evolve until and through the 2D Metal-to-Insulator Transition. We offer an interpretation of all our results implying the existence of two parallel channels which relative importance is determined by the sample disorder level : one is fermionic, the other governed by superconducting fluctuations which persist even when the macroscopic phase coherence is lost. The metallic state is then dominated by the latter, whereas, in the insulator, fermionic excitations prevail.
In a second part, we report on the experimental development of a calibration device for the broadband reflectometry measurement of thin films at microwave frequencies (GHz) and low temperatures (T<4K). This apparatus aims at measuring, during a single cool down, the reflection of known references as well as of the sample. The obtained calibration enables to obtain the absolute value of the films complex impedance, independently of the microwave environment. The results obtained on superconducting Vanadium films, compared with theories of superconductivity, enabled a first validation of the setup and of its working principle. This calibration device is therefore operational to measure more complex systems, such as thin films in the vicinity of the SIT.